Impact of non-neuronal mechanisms on synaptic transmission

Dissertation

zur

Erlangung des Doktorgrades (Dr. rer. nat.)

der

Mathematisch-Naturwissenschaftlichen Fakultät

der

Rheinischen Friedrich-Wilhelms-Universität Bonn

vorgelegt von

Natascha Sarah Vana

aus

Wien

Bonn 2025

Angefertigt mit Genehmigung der Mathematisch-Naturwissenschaftlichen Fakultät
der Rheinischen Friedrich-Wilhelms-Universität Bonn

Gutachter/Betreuer: Prof. Dr. Dirk Dietrich
Gutachter: Prof. Dr. Michael Pankratz

Tag der Promotion: 16. Mai 2025
Erscheinungsjahr: 2025

Table of content

1 Introduction

1.1 Signal transmission in the central nervous system (CNS)

1.1.1 Synapses as means of communication

The adult human brain contains about 86 billion neurons and roughly the same number of non-neuronal cells, i.e. glial cells (Azevedo et al., 2009; Bahney and Von Bartheld, 2014; von Bartheld et al., 2016), which all participate in creating our daily feelings, thoughts and sensations. Together with the spinal cord it forms the CNS controlling most of the body functions. The main computational units in the CNS are neurons, which communicate via chemical or electrical synapses with each other.

Synapses are specialized structures between one cell and another consisting of the presynaptic membrane and the postsynaptic structure, which either communicate with each other via gap junctions (electrical synapse) or via neurotransmitters (chemical synapse). In electrical synapses gap junctions are formed by channel-forming proteins, so-called hemichannels, which allow intercellular flow of ions, nutrients, metabolites and second messengers from one neuron to the other (Söhl et al., 2005). Chemical synapses on the other hand are characterized by a presynaptic and postsynaptic specialization, in which the presynaptic part transmits information via a complex machinery that regulates the release of synaptic vesicles containing neurotransmitters (Nosov et al., 2020). The postsynaptic cell receives the incoming signal when neurotransmitters bind to the receptors clustered at the postsynaptic membrane. Information received by a given neuron gets integrated and when reaching a sufficient threshold eventually forwarded to the next neuron along its axon. Axons are electrically excitable neuronal processes that relay information and depending on its target cell or structure can vary greatly in length between neuronal types ranging from a few millimeters to more than a meter (Muzio and Cascella, 2022).

1.1.2 Structure and function of the chemical synapse

The most common type of synapse in the mammalian brain is the chemical synapse, which follows a general blueprint of a presynaptic and postsynaptic specialization. A neuron's nerve terminal that forms a synapse with another neuron is characterized by an electron-dense structure, the presynaptic active zone (Akert, 1971). Central synapses display active zones as disc-like structures with diameter of 200 – 500 nm (Südhof, 2012). The active zone contains several proteins, amongst others the five core active zone proteins, RIM, Munc13, RIM-BP, α-liprin and ELKS. Those scaffolding proteins form an active zone protein complex that docks and primes synaptic vesicles and recruits Ca^{2+} channels involved in vesicle release. Other important proteins present but not exclusive to the active zone are SNARE proteins and their regulators essential for synaptic vesicle fusion, channels and receptors and cytoskeletal proteins. (Emperador-Melero and Kaeser, 2020; Südhof, 2012)

Synaptic vesicles have a diameter of approximately 40 nm (Zuber et al., 2005) and are packed with neurotransmitters ready to be released in the synaptic cleft. Depending on the type of neurotransmitter enclosed in the synaptic vesicles two types of cells can be identified. Inhibitory cells reduce neuronal activity via secretion of γ-aminobutyric acid (GABA) or glycine, while excitatory cells increase neuronal activity through release of glutamate. There are 3 to 9 times more excitatory neurons in the brain than inhibitory ones (Alreja et al., 2022). Inhibitory synapses typically target the cell body or proximal dendrites of neurons, while excitatory synapses are typically found more distally along the dendritic tree of a neuron (Peters and Palay, 1996). Generally, excitatory (asymmetric) synapses are larger in size and display a more prominent postsynaptic membrane thickening (postsynaptic density, PSD) than inhibitory (symmetric) synapses (Colonnier, 1968). Thus, PSDs are typically found in excitatory synapses, which can be identified in images of electron microscopy by a thick PSD opposed to a less electron-dense presynapse and appear therefore asymmetric compared to the symmetric synapses, which have a PSD similar in thickness to the presynapse (Okabe, 2007; Peters and Palay, 1996).

When the presynaptic membrane releases neurotransmitters they bind to the receptors clustered at the PSD. The PSD has a disc-like shape with a diameter of 200 - 500 nm (Harris et al., 1992), similar to the presynaptic active zone. The proteins that make up the PSD are scaffolding proteins like PSD-95, Homer and Shank, membrane receptors like glutamate receptors, signaling molecules like CAMKII and cytoskeletal proteins. At excitatory synapses both, metabotropic and ionotropic receptors can be found, but the majority of fast, basal transmission is mediated by the later one. The major mediator of excitatory signals in the mammalian CNS is glutamate, which can bind to each of the three types of ionotropic glutamate receptors α-amino-3-hydroxy-5-methyl-4-isoxazolepropionic acid (AMPA), N-methyl-D-aspartate (NMDA) or kainate receptors. Accordingly, NMDA receptors (NMDARs) and the AMPA receptors (AMPARs) alongside with transmembrane AMPAR regulatory proteins (TARPs) (Payne, 2008) have been found to be enriched in the PSD. (Okabe, 2007; Scheefhals and MacGillavry, 2018)

At the intercellular junction, the so-called synaptic cleft cell adhesion molecules bridge the presynaptic terminal and the postsynaptic neuron. The width of the synaptic cleft in the CNS has in the past been described to be around 20 nm (Südhof, 2021; Zuber et al., 2005), newer studies using less harsh treatments suggest that it is more close to 24 nm (Lučić et al., 2005; Zuber et al., 2005). Cell adhesion molecules (CAMs) are actively involved in synapse formation and keep the active zone protein complex and the postsynaptic receptors perfectly aligned (Emperador-Melero and Kaeser, 2020; Südhof, 2012).

An incoming electrical signal depolarizes the membrane, upon which voltage-gated calcium channels open. This leads to an influx of Ca^{2+}, which causes neurotransmitters to be released in the synaptic cleft and in turn leads to a local peak in the glutamate concentration found in the synaptic cleft for a brief period of time (approximately 100 µs) before excess neurotransmitters get taken up and recycled by perisynaptic glial cells. In this short time window neurotransmitters, in case of the ionotropic glutamate receptors AMPA, NMDA and kainate receptors glutamate bind to the receptors at the postsynapse. Binding of a ligand to a

receptor causes the receptor to open and allows ions to enter the cell, which eventually affects downstream signaling molecules (Reiner and Levitz, 2018; Scheefhals and MacGillavry, 2018). In this way synapses are used as relay sites for information transfer between one cell to another, where this information gets processed, encoded and retrieved. Signal transmission between cells is not static but can be altered via several plasticity mechanisms (Citri and Malenka, 2008), which eventually shapes neuronal responses to a variety of stimuli, being key for the control of bodily functions and perception.

1.1.3 A complex system of neurons, glial cells, the extracellular matrix and the neurovascular unit influence synaptic transmission

Since electrical signals are passed on from one neuron to another early research focused heavily on neuron functions. Glial cells including oligodendrocytes (OLs), astrocytes and microglia were successively discovered around 1900, but the importance of glial cells for normal brain functions was not noted immediately. Eventually, around the year 2000 OL precursor cells (OPCs), which serve as precursors for OLs and as a distinct class of glial cells in the brain were identified. Research conducted in the last 30 years started to reveal the many ways in which glial cells not only protect and support but even actively control synaptic transmission (Liu et al., 2023). In recent years the impact of the extracellular matrix and the neurovascular unit on synaptic function and plasticity have added another layer of complexity to signal transmission in the brain (De Luca et al., 2020).

An obvious example for glial control of synaptic transmission are OLs, the only source for myelin in the CNS (Hirano, 1968; Sherman and Brophy, 2005). To ensure fast and reliable signal propagation between neurons especially over long distances loss of electrical signal along axons is minimized by myelin sheets wrapped around them essentially insulating them. At a given axon insulated sections are separated by non-insulated axon sections, the nodes of Ranvier, where ion channels are highly enriched and action potentials are regenerated. In this way action potentials occur only at the nodes of Ranvier, seemingly jumping from one gap

to another, which is known as saltatory conduction. Myelin is a poorly hydrated structure with a high lipid content (Simons and Nave, 2016), which gives the heavily myelinated nerve fiber tracts (white matter) the whitish appearance compared to the grey matter consisting mainly of neurons, glial cells and neuropil. Myelination of axons is crucial for the brain as it not only speeds up conduction velocity, which might save some energy but also provides important metabolic, trophic and structural support for the neurite, which directly influences information processing (Moore et al., 2020; Nave, 2010; Nave and Werner, 2014; Saab and Nave, 2017; Saab et al., 2016; Simons and Nave, 2016; Stadelmann et al., 2019). OLs represent the most numerous glial cell in the brain (Pelvig et al., 2008; Valério-Gomes et al., 2018). Thus, aberrations in OL and OPC function can have serious consequences for the organism, which can be seen for example in neurological and psychiatric diseases such as multiple sclerosis (MS) and schizophrenia (Raabe et al., 2019; Tepavčević and Lubetzki, 2022; Yu et al., 2022). In cases of myelin-related disease and OL loss research focus has turned to OPCs in aspiration to make up for the loss of OLs by recruiting their progenitors. As OPCs are the only other cell in the CNS apart from neurons that receive direct synaptic input, and synaptic input is believed to trigger differentiation of OPCs into OLs, we investigated the excitatory/glutamatergic input to OPCs during embryonic development (see Chapter 2.1 and Vana et al., 2023).

Another important player in synaptic transmission are astrocytes, which ensheath the perisynaptic area with their processes, and form the the tripartite synapse (Araque et al., 1999). Astrocytes possess several neurotransmitter receptors and ion channels through which they can sense neuronal activity (Olsen et al., 2015; Seifert and Steinhauser, 2004; Verkhratsky, 2008) and respond to it via release of gliotransmitters (Araque et al., 2014; Durkee and Araque, 2019). In addition, they have been found to be essential modulators of synaptic plasticity by influencing both, long-term potentiation (LTP) and long-term depression (LTD) (Cavaccini et al., 2020; Henneberger et al., 2010). Another essential function of astrocytes is clearing the synaptic cleft and essentially all extracellular fluid from excess neurotransmitters via transporters, which they recycle and return to neurons (Danbolt, 2001; Verkhratsky et al.,

2015). This resets the stage for any following synaptic event, but also influences the time course and spatial extent of each synaptic transmission. We looked at this mechanism more closely in two different aspects. First, we analyzed how glutamate uptake correlates with spine size (see Chapter 2.2 and Herde et al., 2020) and second, we assessed the glutamate spread in the neuropil, the synaptic-dense region consisting of glial and neuronal processes and fibrils in the grey matter of the CNS (see Chapter 2.3 and Matthews et al., 2022).

Since glutamate plays such a pivotal role in synaptic transmission glutamate concentrations in the brain need to be tightly regulated to ensure normal brain function and in the most severe cases prevent excitotoxicity. Albeit glutamate concentrations in the brain (10,000–12,000 µmol/L) are high compared to blood plasma levels (50–100 µmol/L), most of the glutamate is found inside nerve terminals. In comparison, extracellular fluid (ECF) levels need to be kept at a fraction of it (0.5–5 *µ*mol/L) (Danbolt, 2001; Featherstone and Shippy, 2008; Hawkins, 2009). Functional integrity of the brain is maintained by the blood-brain barrier (BBB), a tightly regulated border between the vascular system and the CNS. The BBB is made up of endothelial cells, pericytes and astrocytes and maintains the brain's metabolic requirements while keeping it free from pathogens. (Bergers and Song, 2005; Kadry et al., 2020). Despite its important role many questions regarding its dynamic control are still unanswered and the models available to study the BBB pose different limitations. We developed a new approach, which allowed us to study different properties of the BBB *in situ* (see Chapter 2.4 and Hanafy et al., 2023).

In the present work we contributed to the expanding field of non-neuronal mechanisms influencing synaptic transmission by investigating embryonic OPCs, astrocytes, the spread of glutamate in the extracellular space and BBB function, which will be expanded on in the following sections.

1.2 Oligodendrogenesis and myelination depend on neuronal activity

1.2.1 OPCs generate OLs

During development as well as in adulthood OLs arise from OPCs (Guo et al., 2021), which are typically characterized by the expression of both, the proteoglycan neuron-glial antigen 2 (NG2, also known as chondroitin sulfate proteoglycan 4 (CSPG4) or AN2) and platelet-derived growth factor receptor α (PDGFRα) (Dawson et al., 2003; Li et al., 2017; Nishiyama et al., 1996, 2009; Rivers et al., 2008; Wilson et al., 2006). As both, a resident cell type of the adult brain and a progenitor cell to OLs, they carry a multitude of unique properties that separates them from other cell types (Ffrench-Constant and Raff, 1986; Nishiyama et al., 1996, 2009; Reynolds and Hardy, 1997; Zhu et al., 2011).

First of all, OPCs represent a discrete glial cell population of the adult mammalian brain that can be found in all brain regions investigated so far, grey and white matter (Dawson et al., 2003; Levine and Card, 1987; Levine et al., 1993; Nishiyama et al., 1996; Passlick et al., 2016; Ziskin et al., 2007). Most neural progenitor cells will cease to exist after development, and the few that can be found in the adult brain seem to be restricted to the subgranular zone of the dentate gyrus and the adult subventricular zone, at least in non-human mammals (Ghosh, 2019; Hagihara et al., 2019; Martínez-Cerdeño and Noctor, 2018; Mira and Morante, 2020). OPCs however, make up a significant 5% of the of the total number of cells in the mammalian adult brain (Dawson et al., 2003).

Next, postnatal OPCs retain their ability to proliferate and differentiate into grey and white matter OLs (Ffrench-Constant and Raff, 1986; Hughes et al., 2013, 2018; Kang et al., 2010; Levine et al., 1993; Trapp et al., 1997). In the postnatal brain OPCs divide largely symmetrical giving rise to two daughter OPCs, the majority of which become OLs within a few days (Hill et al., 2014; Kukley et al., 2008; Zhu et al., 2008, 2011). Thus, OPCs represent the major cycling cell population of the adult CNS (Dawson et al., 2003; Dimou et al., 2008; Psachoulia et al., 2009; Simon et al., 2011). Despite differentiation or cell death OPCs have been shown to keep their numbers constant and are evenly distributed across CNS regions (Dawson et al., 2003;

Hughes et al., 2013; Kirby et al., 2006; Miller, 2002; Rivers et al., 2008). This is achieved by constantly scanning their environment with their motile processes and quickly filling up space that has become devoid of OPCs (Haberlandt et al., 2011; Hughes et al., 2013; Kirby et al., 2006; Simons and Trotter, 2007).

Third, OPCs are the only glial cells that receive direct synaptic input from neurons (Bergles et al., 2010). These neuron-OPC synapses can be found in all grey and white matter regions of the postnatal brain investigated so far (Bergles et al., 2000; De Biase et al., 2010; Kukley et al., 2007; Müller et al., 2009; Sun and Dietrich, 2013) and at all ages (Bergles et al., 2000; Kukley et al., 2008; Passlick et al., 2016; Ziskin et al., 2007). Synaptic transmission in OPCs *in situ* is largely mediated by AMPA/kainate receptors (Bergles et al., 2000; Kukley and Dietrich, 2009; Lin et al., 2005) and GABARs (Kukley et al., 2008; Lin and Bergles, 2004; Vélez-Fort et al., 2010; Zonouzi et al., 2015), while NMDARs contribute to glutamatergic transmission in OPCs only to a limited extent (De Biase et al., 2010; Ziskin et al., 2007). Ultrastructural studies certified the neuron-OPC synapse to be structurally similar to classical neuron-neuron synapses with OPCs usually being at the receiving end (Bergles et al., 2000; Haberlandt et al., 2011; Kukley et al., 2007; Lin et al., 2005; Ziskin et al., 2007), but see (Zhang et al., 2021). Compared to neurons, which are believed to carry up to hundreds of thousands of synapses each cell (DeFelipe et al., 2002; Silbereis et al., 2016), estimates for the number of synapses per OPC range between 10 to 100 (Haberlandt et al., 2011; Kukley et al., 2008; Mount et al., 2019). Even within the OL lineage synapses are exclusive to OPCs since they gradually loose the synaptic input as soon they differentiate into OLs (De Biase et al., 2010; Kukley et al., 2010). Loss of synaptic input is accompanied by a downregulation of the rich set of channels and receptors found in OPCs when they undergo differentiation to become myelinating OLs (De Biase et al., 2010; Cahoy et al., 2008). Thus, OPCs can be well differentiated from OLs by their morphological and electrophysiological properties, as well as their protein markers and gene expression profile.

1.2.2 Developmental origin of OPCs

During development it's a long way from the neural tube until the first OPCs appear and an even longer way until the first myelinating OLs are generated

In the mammalian embryo radial glial cells act as neural stem cells giving rise to most of the cells in the CNS like neurons, astrocytes, ependymal cells and OPCs/OLs via asymmetric cell division (Barragán-Álvarez et al., 2022; Rowitch and Kriegstein, 2010). In an early phase of neuronal development neurons are the first cells to be produced by radial glia cells (neurogenesis), which is followed by a later phase marked by predominant glia cell production (gliogenesis) (Miller and Gauthier, 2007). While the change in tone between those phases is referred to as the neurogenic-to-gliogenic switch, even more sensitive techniques like fate mapping and single-cell RNA sequencing have shown that it's not so much a program that suddenly stops and starts another one as it is a gradual transition. In the same way OPCs are not generated from one day to another but precursor cells in both, spinal cord and brain sequentially acquire OPC/OL lineage markers, PDGFRα for example being usually expressed earlier than NG2 (Nishiyama et al., 2009; Spassky et al., 2001). The earliest OPCs found in the rodent CNS emerge from the ventral ventricular zone in the spinal cord at around embryonic day (E) 14/15 ($PDGFR\alpha^+$ $NG2^+$ cells at E15 (Nishiyama et al., 1996); ($PDGFR\alpha^+$ cells at E14 (Lu et al., 2000; Pringle and Richardson, 1993; Yeh et al., 1993); $NG2^+$ cells at E14 (Dawson et al., 2000); $AN2^+$ cells at E14 (Diers-Fenger et al., 2001)). From there they migrate and populate the whole spinal cord before differentiating into OLs and around E18 meet up with another source of OPC-derived OLs originating in the dorsal spinal cord (Cai et al., 2005; Pringle and Richardson, 1993; Vallstedt et al., 2005; Warf et al., 1991). OL lineage precursors in the forebrain are also generated in several waves starting from ventrally derived Nkx2.1-expressing precursors, which are followed by Gsh-expressing progenitors originating in the lateral and/or caudal ganglionic eminence to Emx1-expressing cortical progenitors (Kessaris et al., 2006; Richardson et al., 2006). At birth OLs and OPCs derived from Nkx2.1-expressing precursors have largely been replaced by the subsequent waves in most brain areas, and Emx1-expressing lineage cells dominate the cortical OL lineage population in the

cortex (Kessaris et al., 2006; Winkler et al., 2018). While Nkx2.1-expressing precursors can be found as early as E13, Sánchez-González et al. (2020) showed that OL lineage precursors at E16 were mostly committed to become OPCs or OLs, but more than 70% of all OL lineage progenitors at E12 or E14 gave rise to astrocytes and neurons instead of OL lineage cells highlighting the only gradual fate-restriction. In the rodent forebrain the dorsal cortex is the last area to be populated by OPCs appearing around E16/17 ($PDGFR\alpha^+$ cells (Kessaris et al., 2006; Pringle et al., 1992; Yeh et al., 1993); $PDGFR\alpha^+$ $NG2^+$ cells (Nishiyama et al., 1996); $Olig2^+$ cells (Winkler et al., 2018) ; CNP^+ $NG2^+$ cells (Tognatta et al., 2016)).

OPCs in the embryonic brain show the strongest proliferative (Bribián et al., 2020; Calver et al., 1998; Gao and Raff, 1997; van Heyningen et al., 2001; Levine et al., 1993; Wolswijk and Noble, 1989) and migratory activity (Bribián et al., 2020; Gao and Raff, 1997; Wolswijk and Noble, 1989) in a mouse's lifetime eventually occupying the entire parenchyma by the time of birth (Pringle et al., 1992). In this way OPCs are being able to colonize the whole brain as a permanent glial type of the adult CNS, and to differentiate into myelin-forming OLs (Dawson et al., 2003; Dimou et al., 2008; Kang et al., 2010; Levine et al., 1993; Pepper et al., 2018; El Waly et al., 2014).

1.2.3 Plasticity of myelination and OL generation

Myelination can be viewed as a fine-tuning process occurring relatively late and over a long period of time compared to other developmental processes in the CNS. In rodents OLs and thus myelination appear only after birth (Barrera et al., 2013; Campagnoni, 1988; Cohen and Guarnieri, 1976; Kristensson et al., 1986; Trapp et al., 1997; Verity and Campagnoni, 1988). The initial time of onset and rate of myelination strongly depends on the neuronal area, whereby the optic nerve is one of the first areas to be fully myelinated and the brain stem one of the last (Cohen and Guarnieri, 1976). The majority of myelination in rodents is achieved within 1-2 months but can last well over 4 months of age (Barrera et al., 2013; Baumann and Pham-Dinh, 2001; Chen et al., 2018; Cohen and Guarnieri, 1976; Verity and Campagnoni,

1988). That said, myelination is a life-long process, as studies verified the generation of new myelinating OLs (Hughes et al., 2018; Psachoulia et al., 2009; Rivers et al., 2008; Young et al., 2013) as well as myelin (Bartzokis et al., 2012; Sturrock, 1980) throughout life.

Myelination is a complex and protracted process, which not only follows an innate developmental plan, but also has to meet ever-changing demands throughout adulthood and disease to either replace OLs that die or respond to requirements for additional myelination (Monje, 2018). Studies employing fractional anisotropy measures in humans suggest that motoric or cognitive training can induce white matter changes from childhood to adulthood and were associated with better performance (Bengtsson et al., 2005; Hu et al., 2011; Scholz et al., 2009; Takeuchi et al., 2010; Taubert et al., 2010). Animal studies demonstrated that myelin is dynamically regulated by social experience during development, and adulthood, which has behavioral and functional consequences for the individual (Kikusui et al., 2007; Liu et al., 2012; Makinodan et al., 2012; Sánchez et al., 1998). When it comes to sensory experience, it was shown that whisker trimming for the first month of life can cause a reduction in myelinated axon density in the mouse barrel cortex (Barrera et al., 2013). Conversely, sensory enrichment in adult mice increases the amount of myelinating OLs in the somatosensory cortex, compared to control or sensory deprived animals, which were on par with each other (Hughes et al., 2018). While physical exercise per se does not seem to influence myelination (Krityakiarana et al., 2010; Tomlinson et al., 2018) motor learning does (Bacmeister et al., 2020; Gibson et al., 2014; Keiner et al., 2017). Further studies showing that skilled reaching training (Keiner et al., 2017; Sampaio-Baptista et al., 2013), water maze learning (Steadman et al., 2020) and contextual fear conditioning (Pan et al., 2020) all lead to changes in myelination suggesting that the learning aspect is the necessary trigger for adaptive myelination. Early on it was also shown that blocking or enhancing neuronal activity via drugs *in vivo/in situ* decreases or increases the number of myelinated axons respectively (Demerens et al., 1996; Fannon et al., 2015; From et al., 2014). Furthermore, Gibson et al. (2014) demonstrated that optogenetic stimulation of the premotor cortex *in vivo* causes enhanced myelin sheet thickness in the

corpus callosum (CC). Pharmacogenetic stimulation of a subset of somatosensory axons increases myelination in the CC exclusively in stimulated axons (Mitew et al., 2018).

Since OPCs receive synaptic input from neurons throughout life it was speculated that they would be in the perfect position to sense an axon's demand for myelination and conform to it by proliferating and generating new OLs that provide additional myelination where needed. Although the OL population in the adult rodent and human brain is very stable (Hughes et al., 2018; Yeung et al., 2014) and most of the newly generated OLs fail to successfully integrate in the adult cortex (Hughes et al., 2018), learning indeed requires the production of new OLs (McKenzie et al., 2014; Pan et al., 2020; Steadman et al., 2020; Wang et al., 2020; Xiao et al., 2016). Since OLs derive from differentiating OPCs several studies attempted to show that proliferation and differentiation of OPCs were dependent on synaptic activity. Blocking neurotransmission by botulinum neurotoxin A injection decreased the OPC density in the hippocampus of adult mice (Chacon-De-La-Rocha et al., 2021), while enhancing neuronal activity in the callosal axons *in vivo* using a DREADD system (Roth, 2016) increased OPCs proliferation and differentiation in juvenile and adult mice (Mitew et al., 2018). Furthermore, electrical stimulation of corticospinal axons in the adult rat for 10 days *in vivo* increased the proliferation and differentiation of OPCs in the dorsal corticospinal tract (Li et al., 2010). Similarly, 30 minutes of optogenetic stimulation of the premotor cortex in adult mice *in vivo* stimulated OPC proliferation in grey and white matter as well as differentiation in white matter (Gibson et al., 2014). Electrical stimulation of the CC in adult mice for several days increased the fraction of proliferating cells among OPCs and the fraction of newly generated OLs (Nagy et al., 2017). Whisker trimming in early postnatal life causes an increase in OPC death underlying a reduction in OL and OPC density (Hill et al., 2014), while fear learning in adult mice induced OPC proliferation and their maturation into myelinating OL in the mPFC (Pan et al., 2020). When it comes to motor learning, running on a complex wheel stimulated the generation of OLs, but reduced the number of OPCs in adult mice (McKenzie et al., 2014; Xiao et al., 2016). In contrast to this, one study failed to show that voluntary running in adult mice induces OPC differentiation, but not proliferation in the area investigated, the grey matter of

the cerebral cortex (Simon et al., 2011). In a recent study employing forelimb reach assay in mice induced an increased propensity for OPC differentiation and generation of OLs after training, but showed no indication for OPC proliferation 1-3 weeks after learning (Bacmeister et al., 2020). In accordance with this adult mice trained in a water-maze experienced pronounced formation of new OLs, but OPC proliferation could only be confirmed in one of the four areas investigated, i.e. the retrosplenial cortex, but not in the anterior cingulate cortex, the prelimbic/infralimbic cortex, or the CA1 region of the hippocampus (Steadman et al., 2020). Taken together studies altering synaptic activity directly or via changes to sensory experience or triggering learning mechanisms reliably induces the generation of new OLs and changes in myelin, but are inconsistent in respect to OPC proliferation, even when only considering *in situ* and *in vivo* studies in healthy rodents.

1.2.4 OPC as a reserve pool for myelinating OLs in demyelinating diseases

Apart from physical axotomy such as spinal cord injury or peripheral nerve trauma pathological loss of myelination can occur in a number of instances. It can either be the result of a primary demyelination, in which genetic defects such as leukodystrophies or inflammation as seen in MS (Dobson and Giovannoni, 2019; Reich et al., 2018) damage OLs, or occur due to an infection or metabolic disease (Love, 2006). In any case the lack of an insulating membrane around the axon causes the electrical signal to slow down or stop completely eventually resulting in loss of neurological function (Alizadeh et al., 2015). From all demyelinating diseases MS is the most common one affecting about 3 million people worldwide (Walton et al., 2020). The etiology of the disease is believed to be multifactorial, but currently there is no treatment fully preventing or reversing the progressive neurological deterioration typically presenting itself as monocular visual loss, limb weakness or sensory loss, double vision or ataxia eventually leading to impaired mobility and cognition (Coggan et al., 2015; Reich et al., 2018). Although MS is rarely fatal, people affected have a 7-year shorter life expectancy

(Lunde et al., 2017) and suffer from a lower health-related quality of life compared to people without the disease (Berrigan et al., 2016).

In an attempt to counteract CNS demyelination the body sets a process called remyelination in motion, which has attracted considerable interest by its potential use to fight demyelinating diseases. Remyelination is a process by which new myelin sheaths are formed, which are typically shorter and thinner than the original myelin sheaths, but importantly restore saltatory conduction and reverse functional deficits (Franklin and Goldman, 2015). Similar to the myelination processes during development, the principal cells involved in remyelination are OPCs, which upon demyelination migrate, proliferate and differentiate into myelinating OLs (Foerster et al., 2020; Franklin and Goldman, 2015; Gensert and Goldman, 1997; Levine and Reynolds, 1999; Zawadzka et al., 2010). Recently, it has been shown that even surviving mature OLs can participate in remyelination (Bacmeister et al., 2020) and both mechanisms are influenced by neuronal activity (Bacmeister et al., 2020; Etxeberria et al., 2010; Gautier et al., 2015; Li et al., 2013). Importantly, de- and subsequent remyelination is not restricted to white matter areas of the brain and remyelination seems to work even more efficient in grey matter than white matter in both, experimental models (Merkler et al., 2006; Skripuletz et al., 2008) and clinical studies (Albert et al., 2007).

However, in demyelinating diseases remyelination fails to balance out the extend of demyelination. Analysis of chronic stage MS tissue revealed that OPCs are present at lesion sites, but apparently fall short to generate functional myelinating OLs (Chang et al., 2000, 2002; Wolswijk, 1998). Because remyelination models have shown that endogenous remyelination is possible common efforts are made to unravel the mechanisms of myelination and remyelination and by understanding the cause of remyelination failure being able to enhance endogenous remyelination in patients. Accumulating work suggests that a variety of endogenous like cell properties and exogenous factors such as a non-permissive environment governing the diseased brain underlies the deficiency in remyelination (Franklin and Goldman, 2015). One reason is that like all regenerative processes remyelination efficiency decreases

with age, which manifests itself in a lower OPC recruitment and differentiation rate (Sim et al., 2002). This age-related decline in rate of colonization is dictated by intrinsic properties of OPCs and independent of the inflammatory environment at a given age (Chari et al., 2003). Apart from enhancing endogenous remyelination a lot of effort has been made to explore the potential of OPC transplantation, which is especially relevant for diseases involving loss of OLs and OPCs like ischemic and traumatic demyelination or chemotherapy and radiotherapy (Franklin and Goldman, 2015). In order to work as an efficient means to deliver myelination, mitotically active OPCs with the capacity to differentiate into myelinating OLs must be selected or generated. Thus, understanding intrinsic properties of OPCs and their relationship with neuronal synapses might help to find new strategies to combat a variety of demyelinating diseases.

1.3 Astrocytes influence synaptic crosstalk by controlling the extracellular glutamate concentration

1.3.1 Structure and function of astrocytes

Astrocytes are a class of glial cells that can be found in many different regions and can take on a variety of functions depending on developmental stage and region. The two most common astrocytic subtypes are the protoplasmic and fibrous astrocytes found in grey or white matter respectively. The protoplasmic astrocytes in the grey matter of the brain and the spinal cord have several primary processes extending from the soma, which quickly branch off giving rise to an array of higher order branch classes. Their most terminal processes are called peripheral astrocytic processes (PAPs) with which they contact synapses and are challenging to visualize because of their delicate structure (Reichenbach et al., 2010). Perivascular astrocytes contact with their terminal processes (end feet), nearby blood vessels, where they are essential for brain homeostasis, while reactive astrocytes, a result of an insult to the brain cause inflammation and/or repair (Hart and Karimi-Abdolrezaee, 2021). Furthermore, they are essential for the formation and function of neuronal synapses (Ullian et al., 2001), provide

energy to neurons (Magistretti et al., 1999) and regulate blood flow (MacVicar and Newman, 2015; Marina et al., 2020). Several studies also showed the involvement of astrocytes in synaptic mechanisms like LTP, LTD and spatial learning (Cavaccini et al., 2020; Henneberger et al., 2010; Hösli et al., 2022a; Perea et al., 2009).

1.3.2 Astrocytes are part of the tripartite synapse

Astrocytes control neuronal activity and synaptic transmission via PAPs contacting synapses, also referred to as astroglial perisynaptic sheaths, which together form the tripartite synapse (Araque et al., 1999; Perea et al., 2009). The majority of synapses in the CNS are tripartite (Verkhratsky and Nedergaard, 2014). In this configuration astrocytes are able to not only modulate synapse formation and synapse function, but also keep extracellular levels of glutamate in balance (Hart and Karimi-Abdolrezaee, 2021). Extracellular glutamate levels, which are low at rest 0.5–5 μmol/L (Danbolt, 2001; Featherstone and Shippy, 2008; Hawkins, 2009) surge during an synaptic event up to 1 mM (Bergles et al., 1999; Clements et al., 1992). Studies trying to assess the time course of free glutamate in the cleft indicated that glutamate is cleared within 1 ms after exocytosis (Clements, 1996; Clements et al., 1992; Diamond and Jahr, 1997; Otis et al., 1996). This is achieved partly by diffusion and partly by glutamate transporters acting in the first few hundred µs of a response (Diamond and Jahr, 1997; Tzingounis and Wadiche, 2007). Maintaining extracellular glutamate levels is not only essential for proper brain function (Marcaggi and Attwell, 2004) but also prevents excitotoxicity through continuous depolarization of neurons, a mechanism seen in neurological and neurodegenerative diseases like Huntington's disease, Alzheimer's disease or Parkinson's disease (Dong et al., 2009; Pajarillo et al., 2019). In the healthy CNS, glutamate is actively removed by excitatory amino acid transporters (EAATs) of which five different ones (EAAT1-5) are known to date. Astrocytes are mainly equipped with EAAT1 (GLAST), responsible for most of the glutamate uptake in the cerebellum (Chaudhry et al., 1995; Rothstein et al., 1994) and EAAT2 (GLT-1), which mediates the bulk uptake of glutamate in the forebrain (Danbolt,

2001; Rothstein et al., 1994; Tanaka et al., 1997). Moreover, glutamate transporters are specifically enriched at astrocytic PAPs (Benediktsson et al., 2012; Chaudhry et al., 1995; Lehre and Danbolt, 1998), which limits both, glutamate entering and exiting the synaptic cleft (Diamond, 2001; Huang and Bordey, 2004; Rusakov and Kullmann, 1998; Wu et al., 2012). However, it is not known whether astrocytes have means to influence the efficiency of glutamate uptake at individual synapses.

1.4 The BBB creates a highly regulated extracellular environment in the brain ensuring proper neuronal function

1.4.1 The BBB in vertebrates

The traditional focus on neurons in neuroscience has been increasingly shifted to glial cells that not only support but actively control a lot of brain functions. Recently, the microvasculature, an aspect of neuroscience that for a long time attracted interest primarily for its pharmacological consequences for the brain, has gained momentum since the concept of the neurovascular unit was established in 2001 (Iadecola, 2017).

There are two essential requirements of the brain in regard to the vasculature, the first being protection of the brain from harmful substances or pathogens and the second meeting the energetic demands during ever changing physiological states of the brain. This ensures the functional integrity of the brain, which is maintained by the BBB, a tightly regulated border between the vascular system and the brain. The BBB is formed by endothelial cells, which together with pericytes, astrocytes, neurons, microglia and the basement membrane form a functional unit, called the neurovascular unit. The neurovascular unit regulates blood flow, vascular function, neuroimmune response and waste clearance and therefore is essential for the maintenance of brain homeostasis. (Bergers and Song, 2005; Kadry et al., 2020)

Different from endothelial cells in other parts of the body, microvascular endothelial cells in the brain are interconnected by tight junctions, which control and restrict the flow of drugs and

exogenous compounds from the blood into the brain (Liebner et al., 2011). The endothelium allows free exchange of oxygen and carbon dioxide and the free diffusion of small lipophilic molecules, while nutrients usually need to be taken up via transporters (Kadry et al., 2020).

Another important constituent of the neurovascular unit are pericytes, which form a second line of defense around the vasculature. Pericytes form close contacts with endothelial cells via N-cadherin and connexins allowing the exchange of ions, metabolites, second messengers and ribonucleic acids between these two cell types. Furthermore, pericytes have been shown to be involved in angiogenesis, microvascular stability, regulation of capillary diameter an cerebral blood flow and possess phagocytic abilities. (Kadry et al., 2020)

Again, astrocytes play a special role at the BBB contacting the vasculature with their end feet (perivascular endfeet). In fact, every astrocyte in all brain regions investigated with exception of the hippocampus contacts at least one blood vessel (Hösli et al., 2022b). In this way astrocytes actively control blood flow (Attwell et al., 2010; Gordon et al., 2008; Otsu et al., 2015) and are involved in nutrient uptake and waste clearance (Díaz-Castro et al., 2023). In fact, astrocytes are required for BBB maintenance as ablation of astrocytes in adult mice lead to vascular leakage and a reduction in tight junctions (Heithoff et al., 2021).

Importantly, because astrocytes contact both, synapses and blood vessels and are interconnected with each other via gap junctions they are in the perfect position to link neurons to the BBB. Many components of the BBB like tight junctions, transporters or transcytotic mechanisms can be modulated (Abbott et al., 2006; Daneman and Prat, 2015). The BBB adapts to the state and requirements of the body for example to stress, diet or exercise (Segarra et al., 2021). Albeit the exact mechanisms are still subject of ongoing research, it is the complex interaction between all the cells present at the neurovascular unit and probably the neurovascular complex that regulate vascular changes (Schaeffer and Iadecola, 2021). The importance of an intact BBB is best seen when things go awry. Alterations in the neurovascular unit, like weakening of tight junctions, increased transcytosis and an impairment of the capillary basement membrane have been linked to several diseases like Alzheimer’s

disease (Kirabali et al., 2020; Zlokovic, 2011), MS (Cashion et al., 2023) and leukodystrophies (Zarekiani et al., 2022). Furthermore, a dysfunctional BBB is present in epilepsy and accompanied by increased glutamate levels as well as changes in astrocytic functions (Barker-Haliski and Steve White, 2015; Heinemann et al., 2012). More than 70 million patients worldwide suffer alone from epilepsy (Ngugi et al., 2010). It is therefore of vital importance to be able to study the involvement of all players present at the neurovascular unit.

2 Publication summaries

2.1 Embryonic OPCs represent a unique developmental stage unaffected by neuronal signaling

The following section summarizes the article “Early cortical oligodendrocyte precursor cells are transcriptionally distinct and lack synaptic connections” by Vana, N.S., van Loo, K.M.J., van Waardenberg, A.J., Tießen, M., Cases-Cunillera, S., Sun, W., Quatraccioni, A., Schoch, S., and Dietrich, D. published 2023 in Glia 2210–2233. DOI 10.1002/glia.24388.

In both, the developing and the adult brain OLs, the only cells producing myelin in the brain, arise through differentiation of OPCs (Guo et al., 2021). Moreover, oligodendrogenesis and myelination can be modified by neuronal activity as discussed in section 1.2.3. Since OPCs but not OLs, form synapses with neurons (De Biase et al., 2010; Kukley et al., 2010) they are believed to be the mediators for the activity-dependent generation of OLs and myelin, which in turn affects information processing and synaptic plasticity. As OPCs demonstrate their peak performance in respect to proliferation (Bribián et al., 2020; Calver et al., 1998; Gao and Raff, 1997; van Heyningen et al., 2001; Levine et al., 1993; Wolswijk and Noble, 1989) and migration (Bribián et al., 2020; Gao and Raff, 1997; Wolswijk and Noble, 1989) before birth, we wondered whether this is a cell-intrinsic property or governed by synaptic input from neurons.

While the electrophysiological properties of postnatal and adult OPCs have been extensively investigated, little is known about them at the embryonic stage. It was recently reported that OPCs in the forebrain of E18 mice express functional glutamate receptors and several ion channels also found in postnatal OPCs, which represent a prerequisite to synaptic responsivity (Spitzer et al., 2019). However, single-cell RNA sequencing studies on OL lineage cells suggested that the transcriptomic profile of embryonic OPCs resembles rather early progenitor

cells than postnatal OPCs (Hochgerner et al., 2018; La Manno et al., 2021; Marques et al., 2018; Yuzwa et al., 2017).

In order to pin-point the nature of embryonic OPCs and their interaction with neuronal synapses in the brain we conducted immunohistochemical, electrophysiological, morphological and RNA sequencing experiments and found that embryonic OPCs are distinct from postnatal OPCs (Vana et al., 2023). Recording mPSCs in the presence of Ruthenium Red in the intermediate zone of E18.5 mouse brain slices revealed that embryonic OPCs of the cortex are not receptive to synaptic input from nearby neurons, which cannot be explained by low release rates and/or a less branched dendritic tree. The electrophysiological properties of embryonic OPCs tend to be different from those of postnatal OPCs and resemble properties known from immature neurons. Bulk RNA sequencing showed that embryonic OPCs isolated via magnetic-activated cell sorting for CD140a (PDGFRα) express some synaptically relevant proteins but the expression of cell adhesion molecules, ion channels and receptors strongly increases between prenatal and postnatal stages, whereby the strongest changes can be found at the postsynapse. We deconvolved our bulk RNA sequencing data with previously published single-cell RNA sequencing data and found that our postnatal OPC data set matches well with the cells previously identified as OPC, while our embryonic OPC data set locates to both, cells previously attributed as OPCs and neuronal progenitors. Single-cell RNA sequencing of specifically cortical OPCs corroborated that embryonic OPCs form clusters distinct from postnatal OPCs and show lower expression levels of synaptic genes.

Thus, compared to postnatal OPCs that require synaptic input to proliferate and differentiate, OPC development, proliferation and migration during prenatal stages do not require synaptic connections. Furthermore, embryonic OPCs represent a distinct yet not recognized class of cells different from neuronal progenitors and OPCs. Apart from the direct findings of this publication future work will also benefit from the transcriptomics data, which were generated in the course of the study and are now freely accessible online to use for everybody.

For this work I performed and analysed all electrophysiological, immunohistochemical and imaging experiments, whereby Anne Quatraccioni helped me with the acquisition of confocal images. Together with Karen van Loo I analysed the bulk RNA sequencing data and with the support of Silvia Cases-Cunillera I isolated OPCs for single-cell RNA sequencing. I wrote the draft for the manuscript to which all authors contributed.

2.2 Astrocytic coverage inversely correlates with spine size, which likely influences synaptic crosstalk

The following section summarizes the article “Local Efficacy of Glutamate Uptake Decreases with Synapse Size” by Herde, M.K., Bohmbach, K., Domingos, C., Vana, N., Komorowska-Müller, J.A., Passlick, S., Schwarz, I., Jackson, C.J., Dietrich, D., Schwarz, M.K., Henneberger, C. published 2020 in Cell Reports 32, 108182. DOI 10.1016/j.celrep.2020.108182.

Glutamate is the primary excitatory neurotransmitter at the synapse in the CNS and requires regulated clearance from the extracellular space upon a synaptic event to retain the fidelity of the signal and avoid excitotoxicity (Andersen et al., 2021). Astrocytic glutamate transporters, which specifically locate to the membrane of perisynaptic processes take up residual glutamate and can therefore influence the time course of a synaptic event (Murphy-Royal et al., 2015). Furthermore, not only the distribution of glutamate transporters in the astrocytic membrane varies, but also the amount of astrocytic membrane covering a synapse, also called astrocytic coverage is not uniform. In fact, astrocytic coverage varies depending on region (Grosche et al., 1999; Špaček, 1985; Ventura and Harris, 1999) and spine size (Gavrilov et al., 2018; Witcher et al., 2007) and is subject to change (Bernardinelli et al., 2014a; Genoud et al., 2006; Hirrlinger et al., 2004; Oliet and Bonfardin, 2010) implying a functional relevance. Computational models suggested that less synaptic coverage and thus a delayed uptake of

glutamate could allow for glutamate spillover and extrasynaptic receptor activation (Gavrilov et al., 2018) but so far the functional implications for differential spine coverage have remained elusive.

To assess how glutamate uptake correlates with astrocytic coverage and spine size, we employed expansion microscopy, glutamate imaging, glutamate uncaging and glutamate iontophoresis as well as Ca^{2+} imaging (Herde et al., 2020). Detailed resolution of the fine PAP structure in hippocampal astrocytes was achieved by visualization of the glutamate transporter GLT-1 outlining astrocytic processes as well as CA1 pyramidal cells with the help of expansion microscopy. We found that the relative GLT-1 coverage is lower at bigger than smaller spines. This observation was reproduced when the PSD instead of the spine via labeling of the presynaptic protein bassoon and the postsynaptic protein shank2 was analyzed. The intensity-based glutamate-sensing fluorescent reporter (iGluSnFR) in combination with Two-photon (2P) imaging was used to visualize glutamate transients in acute hippocampal slices upon electrical stimulation. Blocking glutamate transporters with TBOA had a stronger effect on smaller than bigger spines suggesting that astrocytes execute a tighter control of glutamate levels at smaller spines. Next, we recorded NMDAR-mediated currents in CA1 pyramidal cells elicited upon 2P glutamate uncaging directly adjacent to a given spine head and 500 nm away from it. The attenuation of the NMDAR-mediated response upon release of glutamate at a greater distance was stronger in small than big spines. Furthermore, NMDAR-mediated Ca^{2+} transients in spines were monitored upon iontophoretic application of glutamate. Blocking glutamate uptake via application of TBOA increased the decay time constant of Ca^{2+} transients at small but not large spines. Both experiments suggest that small spines are better shielded from invading or lingering glutamate by GLT-1 expressed on PAPs than larger spines, resulting in a more efficient glutamate clearance and therefore tighter control of glutamate at smaller spines.

We therefore propose that variable degrees of spine coverage by astrocytes processes depict a functional correlate for local glutamate uptake.

For this work I performed and analyzed the 2P glutamate uncaging experiments that I conducted in conjunction with electrophysiological recordings and imaging of CA1 pyramidal neuron spines. Like the other authors I contributed to writing the manuscript.

2.3 Astrocytes limit spread of glutamate in the neuropil

The following section summarizes the article “Optical Analysis of Glutamate Spread in the Neuropil” by Matthews, E.A., Sun, W., McMahon, S.M., Doengi, M., Halka, L., Anders, S., Müller, J.A., Steinlein, P., Vana, N.S., van Dyk, G., Pitsch, J., Becker, A.J., Pfeifer, A., Kavalali, E.T., Lamprecht, A., Henneberger, C., Stein, V., Schoch, S., and Dietrich, D. published 2022 in Cerebral Cortex 1–21. DOI 10.1093/cercor/bhab440.

As stated previously limiting glutamate spread in the extracellular space through glutamate transporters does not only prevent excitotoxicity, but also minimizes unspecific signaling in the CNS. Considering that the nearest neighbor distance at hippocampal synapses is around 500 nm (Mishchenko et al., 2010; Rusakov and Kullmann, 1998; Ventura and Harris, 1999) and synaptic coverage by PAPs and therefore glutamate transporters varies, we wondered how well synaptic glutamate receptors are indeed shielded from extrasynaptic glutamate during a neighboring event. Importantly, the two glutamate receptors conferring most of excitatory synaptic transmission, AMPARs and NMDARs demonstrate very different properties. NMDARs activate slower, but have a higher affinity for glutamate than AMPARs (Clements et al., 1998; Hansen et al., 2021) and are therefore more affected when synaptic cross-talk occurs (Armbruster et al., 2016; Asztely et al., 1997; Hanson et al., 2015; Romanos et al., 2019). Several studies demonstrated that the inhibition of glutamate uptake had no effect on AMPAR-mediated currents, but increased NMDAR responses (Barbour, 2001; Rusakov and Kullmann,

1998; Scimemi et al., 2009; Thomas et al., 2011). Furthermore, it is not known at which distance glutamate can still elicit AMPAR- or NMDAR-mediated responses. We therefore used activated optical glutamate reporter proteins and 2P glutamate uncaging to quantify the spatial extent glutamate can spread and act on glutamate receptors.

We found that glutamate released by a single mossy fiber synapse of a granule cell either upon electrical stimulation or spontaneously spreads around 1.5 µm from the bouton when visualized employing iGluSnFR. Similarly, combining iGluSnFR expression in CA1 pyramidal neurons with 2P glutamate uncaging to mimic a synaptic event allowed the detection of glutamate at a distance of ~1.5 µm from the uncaging spot. To assess whether the spread of glutamate also evokes a physiological response in cells we whole-cell patch-clamped CA1 pyramidal neurons and uncaged MNI-glutamate at different distances from a given spine. Again, even releasing glutamate at a distance of 2 µm produced clearly detectable NMDAR-mediated responses in the recorded cells. Activation of NMDARs was accompanied by Ca^{2+} entry as revealed by the calcium indicator GCaMP6f. A single uncaging pulse elicited Ca^{2+} transients in spines of several neurons more than 2 µm away and thus produced a physiologically relevant signal in many neighboring synapses. As to be expected, AMPAR demonstrated a shorter detection range for glutamate but produced a response even when glutamate was released more than 600 nm away. Blocking glutamate transporters increased the distance 1.8-fold at which glutamate was still detectable for the AMPARs at a given synapse showed that astrocytic glutamate transporters play a pivotal role in controlling local glutamate spread in the brain. Interestingly, increasing the temperature to 32°C only slightly decreased the range at which glutamate caused AMPAR activation suggesting that glutamate transporters exert their immediate function on synaptic transmission rather via rapid binding than translocation of glutamate. Furthermore, glutamate spread in adult mice (5-7 weeks of age) was more restricted than in younger mice and increased in a kainic acid model of temporal lobe epilepsy. We also discovered a supra-additive summation of simultaneously activated glutamate release sites, which is likely caused by facilitated travel of glutamate in the extracellular space.

Taken together, we found that both, AMPARs and NMDARs can be activated by glutamate released as far as 800 and 2000 nm distant from the synapse, respectively. Different from the point-to-point communication usually attributed to synapses our findings show that consistent cross-talk can be expected during a synaptic event. Moreover, our experiments demonstrate that astrocytic glutamate transporters limit further diffusion of glutamate in the extracellular space.

For this project I recorded and analysed mEPSCs in the presence of 1 µM TTX, 100 µM AP5 and 10 µM Gabazine in CA1 pyramidal neurons at different time points before and after the perfusion system for the recording chamber was stopped. We wanted to test whether downtime in perfusion leads to changes in the electrophysiological state of the cells, which could affect the integrity of our data during 2P glutamate uncaging experiments. I showed that neither amplitude nor frequency of AMPAR-mediated mEPSCs changed over a time course of 35 minutes (not included in the manuscript). I also contributed to writing the manuscript.

2.4 Studying the brain vasculature *in situ* allows the detection of acute impairments of the BBB and monitoring the effect of vascular substance delivery on synaptic activity

The following section summarizes the article “Subcellular analysis of blood-brain barrier function by micro-impalement of vessels in acute brain slices” by Hanafy, A.S., Steinlein, P., Pitsch, J., Silva, M.H., Vana, N., Becker, A.J., Graham, M.E., Schoch, S., Lamprecht, A., and Dietrich, D. published 2023 in Nature Communications 14. DOI 10.1038/s41467-023-36070-6.

Albeit a vast amount of models exist that allow the study of the BBB, most of them focus on *in vitro* models that represent simplified versions of the BBB (Jackson et al., 2019; Łach et al., 2023). However, these models do not allow to neither draw conclusions between BBB function and neuronal activity (Kaplan et al., 2020) nor to consider systemic factors on neurovascular function (Schaeffer and Iadecola, 2021). *In vivo* models on the contrary fall short in terms of accessibility and controllability. We therefore developed a new *in situ* model for probing BBB functions, in which single vessels of acute brain slices can be micro-perfused and imaged using multiphoton microscopy. The usefulness of the model was demonstrated by visualizing endothelial cell properties, probing endothelial transporter function and assessing the integrity of the BBB upon introduction of physical and chemical lesions as well as in temporal lobe epilepsy (Hanafy et al., 2023).

We used dye-filled glass pipettes under visual control of a microscope equipped with a 2P laser to penetrate cortical vessels in mouse brain slices. This permitted the visualization of several vascular branches around the injection site, while maintaining the integrity of the BBB. Probing the vascular lumen with the styryl dye FM1-43, which becomes fluorescent once it inserts into the cell membrane, suggested that FM1-43 diffuses across intercellular junctions between endothelial cells. We also demonstrated that both, FM1-43 and Tomato lectin could be used to trace the outline of endothelial cells and determine their surface area. Furthermore, our model allows to study the ATP-binding cassette (ABC) transporters of endothelial cells. Employing the membrane-permeable dye rhodamine123 and Hoechst33342 showed that under normal conditions ABC transporters prevent accumulation of the dye in mitochondria of ECs. Similarly, calcein-AM accumulation in endothelial cells is prevented as long as ABC transporter functions, mainly of ABCB1 was not blocked. Local laser-induced damage to a capillary branch showed extravasation of the dye biocytin-tetra-methylrhodamine (TMR), which normally stayed confined to the vascular lumen. Chemical lesion upon DMSO injection into the vessel showed that fluorescent-labeled bovine serum albumin was able to cross the BBB, potentially by passing through weakened tight junctions, where they were phagocytosed by perivascular macrophages. Brain slices of mice treated with pilocarpine, a model of temporal

lobe epilepsy and tissue samples from human epileptic hippocampi, suggested that the integrity of tight junctions in epilepsy might be affected as seen by TMR leakage in mice, but no intrusion of BSA in the brain parenchyma in neither mouse nor human was detected. Moreover, the pilocarpine model demonstrated an increased functionality of transporters extruding calcein-AM from endothelial cell. Synaptic transmission in the form of field excitatory postsynaptic potentials (fEPSPs) was recorded at the Schaffer collateral-CA1 synapse while vessels were simultaneously perfused with TMR. Inhibiting synaptic transmission via an A1-receptor agonist reduced the fEPSP, which was antagonized by application of caffeine both by bath application or injection in the vascular system.

We established a new model to study the BBB and demonstrated its versatile fields of application. Compared to other models of the BBB our *in situ* model offers a unique feature in investigating the integrity and functionality of the BBB and its players and allows to assess changes to neuronal activity upon local manipulation.

For this project I assisted in the experiments that required 2P-excitation microscopy and Dodt image acquisition and contributed to writing the manuscript.

3 Discussion

In the present publications several aspects of non-neuronal mechanisms, that influence synaptic transmission of neurons were investigated ranging from OPC generation during development and astrocytic regulation of glutamate spread in the neuropil to the cellular constituents of the BBB ensuring proper brain function.

It is a long-standing concept that neuronal activity regulates OPC proliferation, differentiation into OLs and eventually myelination (de Faria et al., 2019; Yang et al., 2013). We and others have shown that OPCs at all ages (Kukley et al., 2008; Passlick et al., 2016; Ziskin et al., 2007) and in all brain regions (Bergles et al., 2000; De Biase et al., 2010; Kukley et al., 2007; Müller et al., 2009; Sun and Dietrich, 2013) investigated so far received synaptic input from neurons, even at postnatal day 4 (P4) (Kukley et al., 2008). So far, communication between neurons and OPCs has been almost exclusively investigated at postnatal stages when myelination takes place. Therefore it was unknown whether OPCs before birth, a period which is marked by a peak in proliferative (Bribián et al., 2020; Calver et al., 1998; Gao and Raff, 1997; van Heyningen et al., 2001; Levine et al., 1993; Wolswijk and Noble, 1989) and migratory (Bribián et al., 2020; Gao and Raff, 1997; Wolswijk and Noble, 1989) activity in OPCs, receive the same synaptic input as their postnatal counterparts. Recently, it has been reported that OPCs in E18 mice already express some voltage-gated ion channels and can react to kainate application (Spitzer et al., 2019). In 2.1 (Vana et al., 2023) we performed a combined electrophysiological, morphological and transcriptional analysis of OPCs in the dorsal embryonic forebrain to investigate the properties of prenatal OPCs and the impact of synaptic signaling on OPC development.

Electrophysiological and RNA sequencing data of E18.5 OPCs demonstrated the expression of ion channels and receptors confirming that prenatal OPCs fulfill the basic prerequisites to receive neuronal signals. Furthermore, neurogenesis starts around E11-12 in mice (Costa et al., 2009; Gao et al., 2014).) and functional synaptic contacts on cortical neurons can be detected as soon as E16 in mice (Kilb et al., 2011). Despite the presence of synapses as

detected by the presence of SV2B in embryonic brain slices, miniature postsynaptic currents (mPSCs) were virtually absent in E18.5 OPCs. We demonstrated that the lack of functional synaptic connections from neurons during prenatal development could not be explained by their reduced dendritic length and thus is not a by-product of their smaller size. Given that OPCs develop in absence of synaptic input, we conclude that synaptic input is not required at this developmental stage. Interestingly, developmental synapse formation of neurons has also been found to be mostly activity-independent (Sando et al., 2017; Sigler et al., 2017; Verhage et al., 2000), suggesting a conserved mechanism, shared by neurons and OPCs alike. Furthermore, the input-independent development of OPCs is in accordance with a previous study that showed that interfering with AMPAR-mediated signaling in postnatal OPCs did not affect their proliferation or number but oligodendrocyte survival (Kougioumtzidou et al., 2017). While prenatal OPC proliferation and development is independent of synaptic input, it cannot be ruled out that it might be influenced by ion channel activity such as DR-type potassium channels. Interestingly, DR-type channels, which have been shown to be involved in OPC proliferation (Gallo et al., 1996; Yuan et al., 2002) were not differentially expressed neither on a functional nor a transcriptional level in embryonic and P7 OPCs. Moreover, it is still possible that the activation of extrasynaptic glutamate receptors could influence OPC development in some other way. It was recently shown, for example, that Gria4, which was already highly expressed at E16.5 OPCs, regulates OPC migration in spinal cord of zebrafish (Piller, Werkman, Brown, Latimer, & Kucenas, 2021).

Embryonic OPCs mimic the same developmental program neurons undergo, in which a prenatal high Rm and low Cm, Na^+ current and peak K^+ current become postnatally reversed (Picken Bahrey and Moody, 2003). Different to neurons, the limited number of synaptic events that were recorded in prenatal OPCs suggests that GABAergic innervation does not proceed glutamatergic innervation as known for neuronal development (Carleton et al., 2003; Hennou et al., 2002; Tyzio et al., 1999). GABA receptor-mediated currents upon electrical stimulation could be recorded in hippocampal OPCs as early as P4 (Kukley et al., 2008) and all three GABAA receptor subunits GABRA3, GABRB2 and GABRG1 subunits identified to confer the

majority of GABAAR signaling in PDGFRα^{+} cells (Ordaz et al., 2021) were significantly up-regulated between E16.5 and P12. Thus, synaptic innervation of OPCs likely happens during a narrow time window after birth.

Our data suggests that the initial proliferation, migration and development of OPCs relies mainly on cell-intrinsic mechanisms, which might be limited only by density-dependent feedback inhibition (Hughes et al., 2013; Zhang and Miller, 1996). Pcdh15 for example, which mediates daughter cell repulsion and dispersion in OPCs (Huang et al., 2020), was highly expressed in E16.5 OPCs and also highly upregulated between prenatal and postnatal OPCs. Thus, it can be concluded that synaptic signaling influences OPC fate not earlier than after birth, when it becomes an essential cue for OPC differentiation (Call et al., 2020; Paez and Lyons, 2020; Trapp et al., 1997).

The fact that neither prenatal OPCs nor OLs are synaptically innervated underscores the very unique stage that the postnatal OPCs represent. Different from OLs (De Biase et al., 2010; Kukley et al., 2010) embryonic OPCs have a similar morphology to postnatal OPCs and demonstrate a comparatively lower but some degree of voltage-gated ion channel currents. Analysis of the bulk RNA sequencing data obtained from E16.5, P4 and P12 brains revealed that several proteins relevant to the postsynapse are differentially expressed between embryonic and postnatal stages. It has to be noted that both, the bulk and the single-cell RNA sequencing data of the two postnatal age groups were comparable. The lack of neuron-glia synapses in the embryonic brain can be partially explained by a lower expression of ion channels and receptors in embryonic OPCs compared to postnatal OPCs like Kcnj10 (Maldonado et al., 2013), Gria1 and Gria3 (Perez-Gianmarco et al., 2023). Furthermore, synapse establishment, maintenance and plasticity strongly depends on synaptic CAMs (Missler et al., 2012; Südhof, 2021; De Wit and Ghosh, 2016), which were lower expressed at E16.5 than at P4 and P12 in the single-cell RNA sequencing data. Presynaptic CAMs were not affected by changes in expression level between E16.5 and P12 as expected for OPCs, which receive input but do not signal themselves. In a recent preprint it was stated that astrocytic

Gpc5 regulates synapse maturation and stabilization (Bosworth et al., 2023). Interestingly, Gpc5 was the CAM experiencing the highest upregulation between E16.5 and P12 in OPCs hinting to a possible role in OPCs too. Taken together his suggests that embryonic OPCs are simply ill-equipped to engage with neurons at this point.

During brain development OPCs appear around the same time as neurons around E11.5 and have already spread throughout the entire telencephalon at E14.5 (Kessaris et al., 2006; Naruse et al., 2017; Rowitch and Kriegstein, 2010). Our electrophysiological and immunohistochemical (PDGFRα$^+$ and NG2$^+$) analysis confirmed that the targeted cells were indeed OPCs. Both, bulk RNA sequencing and single-cell transcriptomic analysis showed that the cells isolated from all age groups are characteristic of OPCs but that E18.5 cells represent a group distinct from P4 and P12 OPCs. The comparative analysis of our data with the data of a study by Marques (Marques et al., 2018) showed that embryonic OPCs more closely aligned with neuronal progenitors than postnatal OPCs. We propose that at E16.5 there are OPCs present in the cortex that were based on their close transcriptional fingerprint previously identified as neuronal progenitors due to their common origin (La Manno et al., 2021). This conclusion is supported by our bulk RNA sequencing data of PDGFRα$^+$ brain cells, which aligned well with the neuronal progenitor clusters identified by Marques (Marques et al., 2018), but replotting those data as a UMAP-based similarity matrix brought the putative neuronal progenitor clusters closer to the cycling OPCs and depicted an overall more clear trajectory from OPCs to oligodendrocytes.

There is still much to learn and understand about the different roles of OPCs in the brain. Recent studies have shed light on other OPC functions in the brain by influencing the remodeling of the neuronal circuit or via phagocytosis of synaptic connections (thoroughly reviewed in (Buchanan et al., 2023)). Different to other studies on murine OPCs, which focused almost exclusively on transcriptional data (Beiter et al., 2022; Dennis et al., 2024; La Manno et al., 2021; Marques et al., 2016, 2018; Weng et al., 2019) and rarely compared pre- and postnatal stages, we took a comprehensive approach investigating physiological, anatomical

and transcriptional data not only to verify the nature of the cells isolated, but also to provide a comprehensive view on early OPC development that could be useful for future studies.

While synaptic innervation of OPCs mainly influences myelination (at least according to the current state of knowledge) and therefore efficiency of information processing (de Faria et al., 2019), astrocytes have been shown to influence synaptic signaling, information processing and cognitive mechanisms via several different mechanisms (Santello et al., 2019). One particular feature of astrocytes is that they are part of the tripartite system, but spine coverage of astrocytic processes does not only vary from synapse to synapse, but is also subject to change (Lushnikova et al., 2009; Santello et al., 2019). In 2.2 (Herde et al., 2020) we investigated the functional relevance of astrocytic spine coverage using expansion microscopy, visualization of glutamate transients via the optical glutamate sensor iGluSnFR, 2P imaging and glutamate uncaging and monitoring of NMDAR-mediated Ca^{2+} transients. Smaller spines were relative to their volume more covered by astrocytic processes as indicated by EAAT2 expression than bigger spines indicating that glutamate will be more efficiently removed from the extracellular space at smaller spines. Both, iGluSnFR and glutamate uncaging experiments demonstrated that glutamate is more tightly controlled at smaller spines than at larger spines and inhibiting glutamate uptake affected the time course of Ca2+ transients at small but not large spines. These data show that variable levels of astrocytic coverage at individual spines are a direct readout of how well synaptic as well as extrasynaptic glutamate levels are controlled. Overall, smaller spines were better shielded from invading or lingering glutamate levels.

It was previously shown that larger spines are in general more stable than smaller spines (Holtmaat et al., 2005) and that changes in astrocytic coverage correlated inversely with spine size (Haber et al., 2006). Smaller and thus immature spines might need more astrocytic coverage to protect them for example from potential harmful postsynaptic calcium increase (Verkhratsky, 2007), which small spines cannot handle as well as bigger spines (Hayashi and Majewska, 2005). Furthermore, our data suggest that smaller spines are subjected to tighter control of extracellular glutamate levels than bigger spines, in which less extensive shielding

of glutamate by glutamate transporters can permit synaptic cross-talk (DiGregorio et al., 2002; Scimemi et al., 2004; Witcher et al., 2007; Zheng et al., 2008).

While the 2P glutamate uncaging experiments show that invading glutamate is more efficiently shielded from small spines than from bigger spines it does not allow to draw a conclusion on how this is achieved. Using TBOA to inhibit glutamate transporters in the iGluSnFR and Ca^{2+} imaging experiments demonstrated that astrocytes limit glutamate accumulation at the synapse by removing it from the extracellular space. This does however not exclude other ways in which astrocytes influence synaptic glutamate transmission, for example by simply acting as a physical barrier to glutamate diffusion (Piet et al., 2004; Rusakov and Kullmann, 1998). There are, however, even more layers to astrocytic control of glutamate diffusion. It was demonstrated that astrocytes in the frontal cortex can adapt their glutamate uptake capacity as a function of activity and brain region (Murphy-Royal et al., 2015; Romanos et al., 2019). Furthermore, because both, spine morphology and spatial configuration of astrocytic processes are subject to plasticity-related changes (Bernardinelli et al., 2014a; Bourne et al., 2013; Matsuzaki et al., 2004; Perez-Alvarez et al., 2014; Wenzel et al., 1991) local glutamate uptake seems to be dynamically modifiable.

Electron microscopy studies do not only show that astrocytic coverage of synapses is variable but also that the distance between neighboring spines can be quite short (Špaček, 1985; Ventura and Harris, 1999). Studies in the hippocampal CA1 area consistently found an average density of approximately 2 synapses per μm^3 and a distance of approximately 450 nm (Bourne et al., 2013; Mishchenko et al., 2010; Rusakov and Kullmann, 1998; Santuy et al., 2020). Earlier studies on synaptic crosstalk focused heavily on glutamate transients and because of their localization and affinity to glutamate on NMDAR function (Armbruster et al., 2016; Hanson et al., 2015; Romanos et al., 2019). However, the distance between the glutamate release site and the spine required to cause a synaptic event has not been established yet. In 2.3 (Matthews et al., 2022) we took advantage of iGluSnFR and 2P glutamate uncaging to mimic a synaptic event with known spatial distance from a given synapse to determine the spread of

glutamate in the neuropil. We found that glutamate released up to 800 and 2000 nm distant from the synapse can still be detected by AMPA or NMDA receptors respectively.

Previously, theoretical models predicted that glutamate transients beyond the synaptic cleft would essentially affect NMDARs exclusively and if only to a minimal extent or when glutamate transporters are not fully functional or overloaded (Barbour, 2001; Rusakov and Kullmann, 1998). However, theoretical models strongly depend on the entered values. Beyond the increasing complexity of the models in recent time, the constants chosen in a given model are critical determinants of the conclusions that can be drawn from them. The estimated glutamate diffusion coefficient in synaptic models for example increased over the years from 0.3 μm^2/ms (Barbour, 2001) over 0.32 μm^2/ms (Zheng et al., 2008) to 0.46 μm^2/ms (Zheng et al., 2017) and was recently even set to 0,76 μm^2/ms (Shuvaev et al., 2024). It can be argued that higher diffusion coefficient could aid faster clearance of neurotransmitters from the synaptic cleft and therefore cessation of the signal, our data however indicate that it leads to a farther spread of glutamate in the neuropil facilitating spillover to neighboring synapses during multivesicular events. Technical advances also delivered new values for other parameters that need to be considered in theoretical models, for example the glutamate content of synaptic vesicles (Wang et al., 2019) or the width of the synaptic cleft (Lučić et al., 2005; Zuber et al., 2005).

The glutamate transporters present on astrocytic processes are involved in limiting the spread of glutamate in the neuropil and to neighboring synapses (Asztely et al., 1997; Diamond, 2005; DiGregorio et al., 2002; Hanson et al., 2015; Herde et al., 2020). Indeed, blocking glutamate transporters increased the distance up to which glutamate release could evoke a response in AMPARs. Earlier studies demonstrated an increase in glutamate transporter efficiency with temperature (Asztely et al., 1997; Bergles and Jahr, 1998). However, the action range of glutamate on AMPAR-mediated currents only slightly increased at elevated temperatures indicating that the recorded responses are not shaped by the slow neurotransmitter translocation process (Otis et al., 1996), but by the fast component of glutamate binding (Diamond and Jahr, 1997). Since the quantity and proximity of glutamate transporters to the

synapse depend on their expression and distribution along the individual astrocytic processes, our findings suggest that astrocytes can not only control neuronal transmission at a single synapse, but at several synapses at once.

While astrocytic processes in close contact to synapses can be found in all brain regions, the degree of ensheathment can vary considerably depending on region and synapse type (Bernardinelli et al., 2014b). It was for example shown that hippocampal mossy fiber synapses experienced a high degree of astrocytic coverage but little overlap at their active zones (Rollenhagen et al., 2007), while astrocytes in the calyx of Held fully encased individual synapses with their processes (Sätzler et al., 2002). We investigated the spatial range of glutamate diffusion at synapses located in the hippocampal CA1 region. Approximately half of the synapses in the CA1 region are contacted by astrocytic processes, which also only partially ensheath those synapses (Ventura and Harris, 1999). Future studies concerning the role of astrocytes in actively modifying synaptic transmission, could first directly correlate astrocytic coverage and glutamate signaling distance at different synapse types and second assess the spread of glutamate in further brain regions and to which degree this can be modified by the structural plasticity of astrocytic processes.

Establishing micro-perfusion of vesicles in acute brain slices in combination with 2P imaging allowed us to study the BBB *in situ*, a model well-known and well-used in electrophysiological studies. Several aspects of the BBB remained intact over a time frame of several hours and functionality was enhanced to previous *in vitro* findings, e.g. the activity of ABC transporters (Kuo and Lu, 2012; Puech et al., 2018; Voirin et al., 2020). The reduced activity of ABC transporters in cell cultures is likely a consequence of ATP shortage, indicating that brain slices not to mention many other aspects such as cellular composition, circulating actors or solution stream are a more accurate representation of the native situation. Furthermore, *in vitro* models struggle to get meaningful results regarding complex or incompletely understood diseases. *In vivo* models on the other hand suffer from a lack in experimentally controllable timing, localization, concentration or accessibility. All those obstacles are overcome in *in vivo*

microperfusion of capillaries, which we demonstrated for example by investigating BBB properties in temporal lobe epilepsy in tissue samples of both, a mouse model and human patients.

Astrocytes contact with the processes not only synapses as discussed above, but also completely ensheath the brain vasculature (Mathiisen et al., 2010) and have been shown to be able to recover vessels upon laser ablation (Kubotera et al., 2019). Astrocytic endfeet influence the permeability of the endothelial cell layer via the secretion of different factors affecting the expression or function of tight junction proteins (Verkhratsky and Pivoriūnas, 2023). Recently, it was found that the molecular composition of perivascular astrocytic endfeet forming the perivascular unit, specifically the CAMs expressed by astroytes, differ depending on the size of the blood vessel (Kameyama et al., 2023). Our model would be well suited to explore such heterogeneity in astrocyte function at the neurovascular unit and its consequences for neuronal transmission in more detail.

Since a disrupted BBB causes a whole array of problems for proper brain function eventually resulting in synaptic and neuronal dysfunction (Zlokovic, 2008) and is a known player in several neurodegenerative diseases our *in situ* BBB model could be a useful tool to identify and study disease-related mechanisms and interactions. On the other hand, our model could also aid the further development of brain-targeted drug delivery in cases, in which a CNS disorder such as glioma ask for pharmacological treatment, but the intact BBB represents an obstacle for drug delivery to the brain (Wu et al., 2023).

In the present studies we have demonstrated the impact and significance of non-neuronal mechanisms influencing synaptic transmission on which further research can build on and deepen our understanding of this complex system shaping the synapse and therefore CNS function.

4 Abstract

The brain receives, encodes and shares information between neurons via synaptic transmission. This kind of communication is generally exclusive to neurons, and was soon found to be activity-dependent and therefore plastic. Numerous mechanisms by which synaptic activity can be modulated by the signaling partners themselves such as changes to the firing rate or release of retrograde messengers have been described. However, an increasing number of studies revealing the many ways in which other players in the brain, primarily glial cells but also the extracellular matrix and the neurovascular unit can influence synaptic transmission, shift this neuron-centered perspective towards a more complex system. To shed further light on this topic we used high-resolution microscopy, 2P glutamate uncaging, electrophysiological methods and RNA sequencing in mouse brain slices to investigate the role of OPCs, astrocytes and the BBB in modulating synaptic activity.

OPCs are the single source for oligodendrocytes in the CNS, constitute the only glial cell type that receives synaptic input from neurons and remain present throughout the entire lifespan. Neuronal activity is believed to play a key role in adult oligodendrogenesis and myelination, which renders neuron-OPC crosstalk central to a field of intense research for therapeutic approaches. We found that embryonic OPCs exhibit a unique transcriptional profile different from both, neuronal precursors and postnatal OPCs, and do not require synaptic innervation from neurons to develop.

Astroglial perisynaptic sheaths in close contact with the synapse make up the so-called tripartite synapse and modulate synaptic activity via several different functions like transmitter secretion as well as generation of a local extracellular microenvironment. Astrocytic coverage varies between brain regions and individual synapses and can change. We demonstrated that astrocytic coverage inversely correlates with spine size and that smaller spines were better shielded from invading glutamate than bigger spines. Furthermore, we experimentally assessed the glutamate spread in the neuropil. Glutamate diffused further than previously thought and could regularly lead to synaptic cross-talk. Our experiments identified astrocytic

glutamate transporters as an essential regulator for the spread of glutamate, which together with differential coverage of individual synapses could control synaptic signaling.

The BBB is part of the neurovascular unit permitting the controlled entry of substances from the blood stream into the brain and ensuring brain homeostasis for proper functioning of synaptic mechanisms. We developed a new approach to study the BBB by combining guided micropipette perfusion of brain vesicles with multiphoton imaging, which unlike previously existing models of the BBB allows spatially and temporally controlled experiments. This offers new ways to deepen our understanding of how changes to the neurovascular unit modify neuronal function and synaptic transmission.

5 References

Abbott, N.J., Rönnbäck, L., and Hansson, E. (2006). Astrocyte-endothelial interactions at the blood-brain barrier. Nat. Rev. Neurosci. *7*, 41–53. 10.1038/nrn1824.

Akert, K. (1971). Struktur und Ultrastruktur von Nervenzellen und Synapsen. Klin. Wochenschr. *49*, 509–519. 10.1007/BF01487987.

Albert, M., Antel, J., Brück, W., and Stadelmann, C. (2007). Extensive cortical remyelination in patients with chronic multiple sclerosis. Brain Pathol. *17*, 129–138. 10.1111/j.1750-3639.2006.00043.x.

Alizadeh, A., Dyck, S.M., and Karimi-Abdolrezaee, S. (2015). Myelin damage and repair in pathologic CNS: Challenges and prospects. Front. Mol. Neurosci. *8*, 1–27. 10.3389/fnmol.2015.00035.

Alreja, A., Nemenman, I., and Rozell, C.J. (2022). Constrained brain volume in an efficient coding model explains the fraction of excitatory and inhibitory neurons in sensory cortices. PLoS Comput. Biol. *18*, 1–19. 10.1371/journal.pcbi.1009642.

Andersen, J. V, Markussen, K.H., Jakobsen, E., Schousboe, A., Waagepetersen, H.S., Rosenberg, P.A., and Aldana, B.I. (2021). Glutamate metabolism and recycling at the excitatory synapse in health and neurodegeneration. Neuropharmacology *196*, 108719. 10.1016/j.neuropharm.2021.108719.

Araque, A., Parpura, V., Sanzgiri, R.P., and Haydon, P.G. (1999). Tripartite synapses: Glia, the unacknowledged partner. Trends Neurosci. *22*, 208–215. 10.1016/S0166-2236(98)01349-6.

Araque, A., Carmignoto, G., Haydon, P.G., Oliet, S.H.R., Robitaille, R., and Volterra, A. (2014). Gliotransmitters travel in time and space. Neuron *81*, 728–739. 10.1016/j.neuron.2014.02.007.

Armbruster, M., Hanson, E., and Dulla, C.G. (2016). Glutamate clearance is locally modulated by presynaptic neuronal activity in the cerebral cortex. J. Neurosci. *36*, 10404–10415. 10.1523/JNEUROSCI.2066-16.2016.

Asztely, F., Erdemli, G., and Kullmann, D.M. (1997). Extrasynaptic glutamate spillover in the hippocampus: Dependence on temperature and the role of active glutamate uptake. Neuron *18*, 281–293. 10.1016/S0896-6273(00)80268-8.

Attwell, D., Buchan, A.M., Charpak, S., Lauritzen, M., MacVicar, B.A., and Newman, E.A. (2010). Glial and neuronal control of brain blood flow. Nature *468*, 232–243. 10.1038/nature09613.

Azevedo, F.A.C., Carvalho, L.R.B., Grinberg, L.T., Farfel, J.M., Ferretti, R.E.L., Leite, R.E.P., Filho, W.J., Lent, R., and Herculano-Houzel, S. (2009). Equal numbers of neuronal and nonneuronal cells make the human brain an isometrically scaled-up primate brain. J. Comp. Neurol. *513*, 532–541. 10.1002/cne.21974.

Bacmeister, C.M., Barr, H.J., McClain, C.R., Thornton, M.A., Nettles, D., Welle, C.G., and Hughes, E.G. (2020). Motor learning promotes remyelination via new and surviving oligodendrocytes. Nat. Neurosci. *23*, 819–831. 10.1038/s41593-020-0637-3.

Bahney, J., and Von Bartheld, C.S. (2014). Validation of the isotropic fractionator: Comparison with unbiased stereology and DNA extraction for quantification of glial cells. J. Neurosci. Methods *222*, 165–174. 10.1016/j.jneumeth.2013.11.002.

Barbour, B. (2001). An evaluation of synapse independence. J. Neurosci. *21*, 7969–7984. 10.1523/jneurosci.21-20-07969.2001.

Barker-Haliski, M., and Steve White, H. (2015). Glutamatergic mechanisms associated with seizures and epilepsy. Cold Spring Harb. Perspect. Med. *5*, 1–15. 10.1101/cshperspect.a022863.

Barragán-Álvarez, C.P., Flores-Fernandez, J.M., Hernández-Pérez, O.R., Ávila-Gónzalez, D., Díaz, N.F., Padilla-Camberos, E., Dublan-García, O., Gómez-Oliván, L.M., and Diaz-Martinez, N.E. (2022). Recent advances in the use of CRISPR/Cas for understanding the early development of molecular gaps in glial cells. Front. Cell Dev. Biol. *10*, 1–15. 10.3389/fcell.2022.947769.

Barrera, K., Chu, P., Abramowitz, J., Steger, R., Ramos, R.L., and Brumberg, J.C. (2013). Organization of myelin in the mouse somatosensory barrel cortex and the effects of sensory deprivation. Dev. Neurobiol. *73*, 297–314. 10.1002/dneu.22060.

von Bartheld, C.S., Bahney, J., and Herculano-Houzel, S. (2016). The search for true numbers of neurons and glial cells in the human brain: A review of 150 years of cell counting. J. Comp. Neurol. *524*, 3865–3895. 10.1002/cne.24040.

Bartzokis, G., Lu, P.H., Heydari, P., Couvrette, A., Lee, G.J., Kalashyan, G., Freeman, F., Grinstead, J.W., Villablanca, P., Finn, J.P., Mintz, J., Alger, J.R., and Altshuler, L.L. (2012). Multimodal magnetic resonance imaging assessment of white matter aging trajectories over the lifespan of healthy individuals. Biol. Psychiatry *72*, 1026–1034. 10.1016/j.biopsych.2012.07.010.

Baumann, N., and Pham-Dinh, D. (2001). Biology of oligodendrocyte and myelin in the mammalian central nervous system. Physiol. Rev. *81*, 871–927. 10.1152/physrev.2001.81.2.871.

Beiter, R.M., Rivet-Noor, C., Merchak, A.R., Bai, R., Johanson, D.M., Slogar, E., Sol-Church, K., Overall, C.C., and Gaultier, A. (2022). Evidence for oligodendrocyte progenitor cell heterogeneity in the adult mouse brain. Sci. Rep. *12*, 1–15. 10.1038/s41598-022-17081-7.

Benediktsson, A.M., Marrs, G.S., Tu, J.C., Worley, P.F., Rothstein, J.D., Bergles, D.E., and Dailey, M.E. (2012). Neuronal activity regulates glutamate transporter dynamics in developing astrocytes. Glia *60*, 175–188. 10.1002/glia.21249.

Bengtsson, S.L., Nagy, Z., Skare, S., Forsman, L., Forssberg, H., and Ullén, F. (2005). Extensive piano practicing has regionally specific effects on white matter development. Nat. Neurosci. *8*, 1148–1150. 10.1038/nn1516.

Bergers, G., and Song, S. (2005). The role of pericytes in blood-vessel formation and maintenance. Neuro. Oncol. *7*, 452–464. 10.1215/S1152851705000232.

Bergles, D.E., and Jahr, C.E. (1998). Glial contribution to glutamate uptake at Schaffer collateral- commissural synapses in the hippocampus. J. Neurosci. *18*, 7709–7716. 10.1523/jneurosci.18-19-07709.1998.

Bergles, D.E., Diamond, J.S., and Jahr, C.E. (1999). Clearance of glutamate inside the synapse and beyond. Curr. Opin. Neurobiol. *9*, 293–298. 10.1016/S0959-4388(99)80043-9.

Bergles, D.E., Roberts, J.D., Somogyi, P., and Jahr, C.E. (2000). Glutamatergic synapses on oligodendrocyte precursor cells in the hippocampus. Nature *405*, 187–191. 10.1038/35012083.

Bergles, D.E., Jabs, R., and Steinhäuser, C. (2010). Neuron-glia synapses in the brain. Brain Res. Rev. *63*, 130–137. 10.1016/j.brainresrev.2009.12.003.

Bernardinelli, Y., Randall, J., Janett, E., Nikonenko, I., König, S., Jones, E.V., Flores, C.E., Murai, K.K., Bochet, C.G., Holtmaat, A., and Muller, D. (2014a). Activity-dependent structural plasticity of perisynaptic astrocytic domains promotes excitatory synapse stability. Curr. Biol. *24*, 1679–1688. 10.1016/j.cub.2014.06.025.

Bernardinelli, Y., Muller, D., and Nikonenko, I. (2014b). Astrocyte-synapse structural plasticity. Neural Plast. *2014*. 10.1155/2014/232105.

Berrigan, L.I., Fisk, J.D., Patten, S.B., Tremlett, H., Wolfson, C., Warren, S., Fiest, K.M., McKay, K.A., and Marrie, R.A. (2016). Health-related quality of life in multiple sclerosis. Neurology *86*, 1417–1424. 10.1212/WNL.0000000000002564.

De Biase, L.M., Nishiyama, A., and Bergles, D.E. (2010). Excitability and synaptic communication within the oligodendrocyte lineage. J. Neurosci. *30*, 3600–3611. 10.1523/JNEUROSCI.6000-09.2010.

Bosworth, A., Contreras, M., Weiser Novak, S., Sancho, L., Salas, I., Manor, U., and Allen, N. (2023). Astrocyte glypican 5 regulates synapse maturation and stabilization. BioRxiv - Prepr. 1–23. 10.1101/2023.03.02.529949.

Bourne, J.N., Chirillo, M.A., and Harris, K.M. (2013). Presynaptic ultrastructural plasticity along CA3→CA1 axons during long-term potentiation in mature hippocampus. J. Comp. Neurol. *521*, 3898–3912. 10.1002/cne.23384.

Bribián, A., Medina-Rodríguez, E.M., Josa-Prado, F., García-Álvarez, I., Machín-Díaz, I., Esteban, P.F., Murcia-Belmonte, V., Vega-Zelaya, L., Pastor, J., Garrido, L., and de Castro, F. (2020). Functional Heterogeneity of Mouse and Human Brain OPCs: Relevance for Preclinical Studies in Multiple Sclerosis. J. Clin. Med. *9*, 1681. 10.3390/jcm9061681.

Buchanan, J.A., da Costa, N.M., and Cheadle, L. (2023). Emerging roles of oligodendrocyte precursor cells in neural circuit development and remodeling. Trends Neurosci. *46*, 628–639. 10.1016/j.tins.2023.05.007.

Cahoy, J.D., Emery, B., Kaushal, A., Foo, L.C., Zamanian, J.L., Christopherson, K.S., Xing, Y., Lubischer, J.L., Krieg, P.A., Krupenko, S.A., Thompson, W.J., and Barres, B.A. (2008). A transcriptome database for astrocytes, neurons, and oligodendrocytes: A new resource for understanding brain development and function. J. Neurosci. *28*, 264–278. 10.1523/JNEUROSCI.4178-07.2008.

Cai, J., Qi, Y., Hu, X., Tan, M., Liu, Z., Zhang, J., Li, Q., Sander, M., and Qiu, M. (2005). Generation of oligodendrocyte precursor cells from mouse dorsal spinal cord independent of Nkx6 regulation and Shh signaling. Neuron *45*, 41–53. 10.1016/j.neuron.2004.12.028.

Call, C.L., De Biase, L.M., and Bergles, D.E. (2020). Neuron–glial interactions and neurotransmitter signaling to cells of the oligodendrocyte lineage (Elsevier Inc.). 10.1016/b978-0-12-814405-3.00036-9.

Calver, A.R., Hall, A.C., Yu, W.P., Walsh, F.S., Heath, J.K., Betsholtz, C., and Richardson, W.D. (1998). Oligodendrocyte population dynamics and the role of PDGF in vivo. Neuron *20*, 869–882. 10.1016/S0896-6273(00)80469-9.

Campagnoni, A.T. (1988). Molecular Biology of Myelin Proteins from the Central Nervous System. J. Neurochem. *51*, 1–14. 10.1111/j.1471-4159.1988.tb04827.x.

Carleton, A., Petreanu, L.T., Lansford, R., Alvarez-Buylla, A., and Lledo, P.M. (2003). Becoming a new neuron in the adult olfactory bulb. Nat. Neurosci. *6*, 507–518. 10.1038/nn1048.

Cashion, J.M., Young, K.M., and Sutherland, B.A. (2023). How does neurovascular unit dysfunction contribute to multiple sclerosis? Neurobiol. Dis. *178*, 106028. 10.1016/j.nbd.2023.106028.

Cavaccini, A., Durkee, C., Kofuji, P., Tonini, R., and Araque, A. (2020). Astrocyte signaling gates long-term depression at corticostriatal synapses of the direct pathway. J. Neurosci. 10.1523/JNEUROSCI.2369-19.2020.

Chacon-De-La-Rocha, I., Fryatt, G.L., Rivera, A.D., Restani, L., Caleo, M., Gomez-Nicola, D., and Butt, A.M. (2021). The synaptic blocker botulinum toxin A decreases the density and complexity of oligodendrocyte precursor cells in the adult mouse hippocampus. J. Neurosci. Res. 1–12. 10.1002/jnr.24856.

Chang, A., Nishiyama, A., Peterson, J., Prineas, J., and Trapp, B.D. (2000). NG2-positive oligodendrocyte progenitor cells in adult human brain and multiple sclerosis lesions. J. Neurosci. *20*, 6404–6412. 10.1523/jneurosci.20-17-06404.2000.

Chang, A., Tourtellotte, W.W., Rudick, R., and Trapp, B.D. (2002). Premyelinating Oligodendrocytes in Chronic Lesions of Multiple Sclerosis. N. Engl. J. Med. *346*, 165–173. 10.1056/nejmoa010994.

Chari, D.M., Crang, A.J., and Blakemore, W.F. (2003). Decline in rate of colonization of oligodendrocyte progenitor cell (OPC)-depleted tissue by adult OPCs with age. J. Neuropathol. Exp. Neurol. *62*, 908–916. 10.1093/jnen/62.9.908.

Chaudhry, F.A., Lehre, K.P., Lookeren Campagne, M. van, Ottersen, O.P., Danbolt, N.C., and Storm-Mathisen, J. (1995). Glutamate transporters in glial plasma membranes: Highly differentiated localizations revealed by quantitative ultrastructural immunocytochemistry. Neuron *15*, 711–720. 10.1016/0896-6273(95)90158-2.

Chen, T.J., Kula, B., Nagy, B., Barzan, R., Gall, A., Ehrlich, I., and Kukley, M. (2018). In Vivo Regulation of Oligodendrocyte Precursor Cell Proliferation and Differentiation by the AMPA-Receptor Subunit GluA2. Cell Rep. *25*, 852–861. 10.1016/j.celrep.2018.09.066.

Citri, A., and Malenka, R.C. (2008). Synaptic Plasticity: Multiple Forms, Functions, and Mechanisms. Neuropsychopharmacology *33*, 18–41. 10.1038/sj.npp.1301559.

Clements, J.D. (1996). Transmitter timecourse in the synaptic cleft: its role in central synpatic function. Trends Neurosci. *19*, 163–171.

Clements, J.D., Lester, R.A.J., Tong, G., Jahr, C.E., and Westbrook, G.L. (1992). The Time Course of Glutamate in the Synaptic Cleft. Science (80-.). *258*, 1496–1501.

Clements, J.D., Feltz, A., Sahara, Y., and Westbrook, G.L. (1998). Activation kinetics of AMPA receptor channels reveal the number of functional agonist binding sites. J. Neurosci. *18*, 119–127. 10.1523/jneurosci.18-01-00119.1998.

Coggan, J.S., Bittner, S., Stiefel, K.M., Meuth, S.G., and Prescott, S.A. (2015). Physiological dynamics in demyelinating diseases: Unraveling complex relationships through computer modeling. Int. J. Mol. Sci. *16*, 21215–21236. 10.3390/ijms160921215.

Cohen, S.R., and Guarnieri, M. (1976). Immunochemical measurement of myelin basic protein in developing rat brain: An index of myelin synthesis. Dev. Biol. *49*, 294–299. 10.1016/0012-1606(76)90276-1.

Colonnier, M. (1968). Synaptic patterns on different cell types in the different laminae of the cat visual cortex. An electron microscope study. Brain Res. *9*. 10.1016/0006-8993(68)90234-5.

Danbolt, N.C. (2001). Glutamate uptake. Prog. Neurobiol. *65*, 1–105. 10.1016/S0301-0082(00)00067-8.

Daneman, R., and Prat, A. (2015). The Blood–Brain Barrier. Cold Spring Harb. Perspect. Biol. *7*, a020412. 10.1101/cshperspect.a020412.

Dawson, M.R.L., Levine, J.M., and Reynolds, R. (2000). NG2-expressing cells in the central nervous system: Are they oligodendroglial progenitors? J. Neurosci. Res. *61*, 471–479. 10.1002/1097-4547(20000901)61:5<471::AID-JNR1>3.0.CO;2-N.

Dawson, M.R.L., Polito, A., Levine, J.M., and Reynolds, R. (2003). NG2-expressing glial progenitor cells: An abundant and widespread population of cycling cells in the adult rat CNS. Mol. Cell. Neurosci. *24*, 476–488. 10.1016/S1044-7431(03)00210-0.

DeFelipe, J., Alonso-Nanclares, L., and Arellano, J.I. (2002). Microstructure of the neocortex: Comparative aspects. J. Neurocytol. *31*, 299–316. 10.1023/A:1024130211265.

Demerens, C., Stankoff, B., Logak, M., Anglade, P., Allinquant, B., Couraud, F., Zalc, B., and Lubetzki, C. (1996). Induction of myelination in the central nervous system by electrical activity. Proc. Natl. Acad. Sci. U. S. A. *93*, 9887–9892. 10.1073/pnas.93.18.9887.

Dennis, D.J., Wang, B.S., Karamboulas, K., Kaplan, D.R., and Miller, F.D. (2024). Single-cell approaches define two groups of mammalian oligodendrocyte precursor cells and their evolution over developmental time. Stem Cell Reports *19*, 654–672. 10.1016/j.stemcr.2024.03.002.

Diamond, J.S. (2001). Neuronal Glutamate Transporters Limit Activation of NMDA Receptors by Neurotransmitter Spillover on CA1 Pyramidal Cells. J. Neurosci. *21*, 8328–8338. 10.1523/JNEUROSCI.21-21-08328.2001.

Diamond, J.S. (2005). Deriving the glutamate clearance time course from transporter currents in CA1 hippocampal astrocytes: Transmitter uptake gets faster during development. J. Neurosci. *25*, 2906–2916. 10.1523/JNEUROSCI.5125-04.2005.

Diamond, J.S., and Jahr, C.E. (1997). Transporters Buffer Synaptically Released Glutamate on a Submillisecond Time Scale. J. Neurosci. *17*, 4672–4687.

Díaz-Castro, B., Robel, S., and Mishra, A. (2023). Annual Review of Neuroscience Astrocyte Endfeet in Brain Function and Pathology: Open Questions. Annu. Rev. Neurosci. *46*, 101–121.

Diers-Fenger, M., Kirchhoff, F., Kettenmann, H., Levine, J.M., and Trotter, J. (2001). AN2/NG2 protein-expressing glial progenitor cells in the murine CNS: Isolation, differentiation, and association with radial glia. Glia *34*, 213–228. 10.1002/glia.1055.

DiGregorio, D.A., Nusser, Z., and Silver, R.A. (2002). Spillover of Glutamate onto Synaptic AMPA Receptors Enhances Fast Transmission at a Cerebellar Synapse. Neuron *35*, 521–533. 10.1016/S0896-6273(02)00787-0.

Dimou, L., Simon, C., Kirchhoff, F., Takebayashi, H., and Götz, M. (2008). Progeny of Olig2-expressing progenitors in the gray and white matter of the adult mouse cerebral cortex. J. Neurosci. *28*, 10434–10442. 10.1523/JNEUROSCI.2831-08.2008.

Dobson, R., and Giovannoni, G. (2019). Multiple sclerosis – a review. Eur. J. Neurol. *26*, 27–40. 10.1111/ene.13819.

Dong, X., Wang, Y., and Qin, Z. (2009). Molecular mechanisms of excitotoxicity and their relevance to pathogenesis of neurodegenerative diseases. Acta Pharmacol. Sin. *30*, 379–387. 10.1038/aps.2009.24.

Durkee, C.A., and Araque, A. (2019). Diversity and Specificity of Astrocyte–neuron Communication. Neuroscience *396*, 73–78. 10.1016/j.neuroscience.2018.11.010.

Emperador-Melero, J., and Kaeser, P.S. (2020). Assembly of the presynaptic active zone. Curr. Opin. Neurobiol. *63*, 95–103. 10.1016/j.conb.2020.03.008.

Etxeberria, A., Mangin, J.M., Aguirre, A., and Gallo, V. (2010). Adult-born SVZ progenitors receive transient synapses during remyelination in corpus callosum. Nat. Neurosci. *13*, 287–289. 10.1038/nn.2500.

Fannon, J., Tarmier, W., and Fulton, D. (2015). Neuronal activity and AMPA-type glutamate receptor activation regulates the morphological development of oligodendrocyte precursor cells. Glia *63*, 1021–1035. 10.1002/glia.22799.

de Faria, O., Gonsalvez, D.G., Nicholson, M., and Xiao, J. (2019). Activity-dependent central nervous system myelination throughout life. J. Neurochem. *148*, 447–461. 10.1111/jnc.14592.

Featherstone, D.E., and Shippy, S.A. (2008). Regulation of synaptic transmission by ambient extracellular glutamate. Neuroscientist *14*, 171–181. 10.1177/1073858407308518.

Ffrench-Constant, C., and Raff, M.C. (1986). Proliferating bipotential glial progenitor cells in adult rat optic nerve. Nature *319*, 499–502. 10.1038/319499a0.

Foerster, S., Neumann, B., McClain, C., Di Canio, L., Chen, C.Z., Reich, D.S., and Franklin, R.J.M. (2020). Proliferation is a requirement for differentiation of oligodendrocyte progenitor cells during CNS remyelination. BioRxiv.

Franklin, R.J.M., and Goldman, S.A. (2015). Glia Disease and Repair—Remyelination. Cold Spring Harb. Perspect. Biol. *7*, a020594. 10.1101/cshperspect.a020594.

From, R., Eilam, R., Bar-Lev, D.D., Levin-Zaidman, S., Tsoory, M., Lopresti, P., Sela, M., Arnon, R., and Aharoni, R. (2014). Oligodendrogenesis and myelinogenesis during postnatal development effect of glatiramer acetate. Glia *62*, 649–665. 10.1002/glia.22632.

Gallo, V., Zhou, J.M., McBain, C.J., Wright, P., Knutson, P.L., and Armstrong, R.C. (1996). Oligodendrocyte progenitor cell proliferation and lineage progression are regulated by glutamate receptor-mediated K+ channel block. Int. J. Dev. Neurosci. *14*, 67. 10.1016/0736-5748(96)80263-2.

Gao, F.B., and Raff, M. (1997). Cell size control and a cell-intrinsic maturation program in proliferating oligodendrocyte precursor cells. J. Cell Biol. *138*, 1367–1377. 10.1083/jcb.138.6.1367.

Gautier, H.O.B., Evans, K.A., Volbracht, K., James, R., Sitnikov, S., Lundgaard, I., James, F., Lao-Peregrin, C., Reynolds, R., Franklin, R.J.M., and Karadottir, R.T. (2015). Neuronal activity regulates remyelination via glutamate signalling to oligodendrocyte progenitors. Nat. Commun. *6*, 1–15. 10.1038/ncomms9518.

Gavrilov, N., Golyagina, I., Brazhe, A., Scimemi, A., Turlapov, V., and Semyanov, A. (2018). Astrocytic Coverage of Dendritic Spines, Dendritic Shafts, and Axonal Boutons in Hippocampal Neuropil. Front. Cell. Neurosci. *12*, 1–16. 10.3389/fncel.2018.00248.

Genoud, C., Quairiaux, C., Steiner, P., Hirling, H., Welker, E., and Knott, G.W. (2006). Plasticity of astrocytic coverage and glutamate transporter expression in adult mouse cortex. PLoS Biol. *4*, 2057–2064. 10.1371/journal.pbio.0040343.

Gensert, J.A.M., and Goldman, J.E. (1997). Endogenous progenitors remyelinate demyelinated axons in the adult CNS. Neuron *19*, 197–203. 10.1016/S0896-6273(00)80359-1.

Ghosh, H.S. (2019). Adult Neurogenesis and the Promise of Adult Neural Stem Cells. J. Exp. Neurosci. *13*. 10.1177/1179069519856876.

Gibson, E.M., Purger, D., Mount, C.W., Goldstein, A.K., Lin, G.L., Wood, L.S., Inema, I., Miller, S.E., Bieri, G., Zuchero, J.B., Barres, B.A., Woo, P.J., Vogel, H., and Monje, M. (2014). Neuronal activity promotes oligodendrogenesis and adaptive myelination in the mammalian brain. Science (80-.). *344*, 1252304. 10.1126/science.1252304.

Gordon, G.R.J., Choi, H.B., Rungta, R.L., Ellis-Davies, G.C.R., and MacVicar, B.A. (2008). Brain metabolism dictates the polarity of astrocyte control over arterioles. Nature *456*, 745–750. 10.1038/nature07525.

Grosche, J., Matyash, V., Möller, T., Verkhratsky, A., Reichenbach, A., and Kettenmann, H. (1999). Microdomains for neuron-glia interaction: Parallel fiber signaling to Bergmann glial cells. Nat. Neurosci. *2*, 139–143. 10.1038/5692.

Guo, Q., Scheller, A., and Huang, W. (2021). Progenies of NG2 glia: What do we learn from transgenic mouse models ? Neural Regen. Res. *16*, 43–48. 10.4103/1673-5374.286950.

Haber, M., Zhou, L., and Murai, K.K. (2006). Cooperative Astrocyte and Dendritic Spine Dynamics at Hippocampal Excitatory Synapses. J. Neurosci. *26*, 8881–8891. 10.1523/JNEUROSCI.1302-06.2006.

Haberlandt, C., Derouiche, A., Wyczynski, A., Haseleu, J., Pohle, J., Karram, K., Trotter, J., Seifert, G., Frotscher, M., Steinhäuser, C., and Jabs, R. (2011). Gray Matter NG2 Cells Display Multiple Ca2+-Signaling Pathways and Highly Motile Processes. PLoS One *6*, e17575. 10.1371/journal.pone.0017575.

Hagihara, H., Murano, T., Ohira, K., Miwa, M., Nakamura, K., and Miyakawa, T. (2019). Expression of progenitor cell/immature neuron markers does not present definitive evidence for adult neurogenesis. Mol. Brain *12*, 1–6. 10.1186/s13041-019-0522-8.

Hanafy, A.S., Steinlein, P., Pitsch, J., Silva, M.H., Vana, N., Becker, A.J., Graham, M.E., Schoch, S., Lamprecht, A., and Dietrich, D. (2023). Subcellular analysis of blood-brain barrier function by micro-impalement of vessels in acute brain slices. Nat. Commun. *14*. 10.1038/s41467-023-36070-6.

Hansen, K.B., Wollmuth, L.P., Bowie, D., Furukawa, H., Menniti, F.S., Sobolevsky, A.I., Swanson, G.T., Swanger, S.A., Greger, I.H., Nakagawa, T., McBain, C.J., Jayaraman, V., Low, C.-M., Dell'Acqua, M.L., Diamond, J.S., Camp, C.R., Perszyk, R.E., Yuan, H., and Traynelis, S.F. (2021). Structure, Function, and Pharmacology of Glutamate Receptor Ion Channels. Pharmacol. Rev. *73*, 1469–1658. 10.1124/pharmrev.120.000131.

Hanson, E., Armbruster, M., Cantu, D., Andresen, L., Taylor, A., Danbolt, N.C., and Dulla, C.G. (2015). Astrocytic glutamate uptake is slow and does not limit neuronal NMDA receptor activation in the neonatal neocortex. Glia *63*, 1784–1796. 10.1002/glia.22844.

Harris, K.M., Jensen, F.E., and Tsao, B. (1992). Three-Dimensional Structure of Dendritic Spines and Synapses in Rat Hippocampus (CAI) at Postnatal Day 15 and Adult Ages: Implications for the Maturation of Synaptic Physiology and Long-term Potentiation. J. Neurosci. *12*, 2685–2705.

Hart, C.G., and Karimi-Abdolrezaee, S. (2021). Recent insights on astrocyte mechanisms in CNS homeostasis, pathology, and repair. J. Neurosci. Res. *99*, 2427–2462. 10.1002/jnr.24922.

Hawkins, R.A. (2009). The blood-brain barrier and glutamate. Am. J. Clin. Nutr. *90*, 867S-874S. 10.3945/ajcn.2009.27462BB.

Hayashi, Y., and Majewska, A.K. (2005). Dendritic spine geometry: Functional implication and regulation. Neuron *46*, 529–532. 10.1016/j.neuron.2005.05.006.

Heinemann, U., Kaufer, D., and Friedman, A. (2012). Blood-brain barrier dysfunction, TGFβ signaling, and astrocyte dysfunction in epilepsy. Glia *60*, 1251–1257. 10.1002/glia.22311.

Heithoff, B.P., George, K.K., Phares, A.N., Zuidhoek, I.A., Munoz-Ballester, C., and Robel, S. (2021). Astrocytes are necessary for blood–brain barrier maintenance in the adult mouse brain. Glia *69*, 436–472. 10.1002/glia.23908.

Henneberger, C., Papouin, T., Oliet, S.H.R., and Dmitri, A. (2010). Long term potentiation depends on release of D-serine from astrocytes. Nature *463*, 232–236. 10.1038/nature08673.Long.

Hennou, S., Khalilov, I., Diabira, D., Ben-Ari, Y., and Gozlan, H. (2002). Early sequential formation of functional GABAA and glutamatergic synapses on CA1 interneurons of the rat foetal hippocampus. Eur. J. Neurosci. *16*, 197–208. 10.1046/j.1460-9568.2002.02073.x.

Herde, M.K., Bohmbach, K., Domingos, C., Vana, N., Komorowska-Müller, J.A., Passlick, S., Schwarz, I., Jackson, C.J., Dietrich, D., Schwarz, M.K., and Henneberger, C. (2020). Local Efficacy of Glutamate Uptake Decreases with Synapse Size. Cell Rep. *32*, 108182. 10.1016/j.celrep.2020.108182.

van Heyningen, P., Calver, A.R., and Richardson, W.D. (2001). Control of progenitor cell number by mitogen supply and demand. Curr. Biol. *11*, 232–241. 10.1016/S0960-9822(01)00075-6.

Hill, R.A., Patel, K.D., Goncalves, C.M., Grutzendler, J., and Nishiyama, A. (2014). Modulation of oligodendrocyte generation during a critical temporal window after NG2 cell division. Nat. Neurosci. *17*, 1518–1527. 10.1038/nn.3815.

Hirano, A. (1968). A confirmation of the oligodendroglial origin of myelin in the adult rat. J. Cell Biol. *38*, 637–640. 10.1083/jcb.38.3.637.

Hirrlinger, J., Hülsmann, S., and Kirchhoff, F. (2004). Astroglial processes show spontaneous motility at active synaptic terminals in situ. Eur. J. Neurosci. *20*, 2235–2239. 10.1111/j.1460-9568.2004.03689.x.

Hochgerner, H., Zeisel, A., Lönnerberg, P., and Linnarsson, S. (2018). Conserved properties of dentate gyrus neurogenesis across postnatal development revealed by single-cell RNA sequencing. Nat. Neurosci. *21*, 290–299. 10.1038/s41593-017-0056-2.

Holtmaat, A.J.G.D., Trachtenberg, J.T., Wilbrecht, L., Shepherd, G.M., Zhang, X., Knott, G.W., and Svoboda, K. (2005). Transient and Persistent Dendritic Spines in the Neocortex In Vivo. Neuron *45*, 279–291. 10.1016/j.neuron.2005.01.003.

Hösli, L., Binini, N., Ferrari, K.D., Thieren, L., Looser, Z.J., Zuend, M., Zanker, H.S., Berry, S., Holub, M., Möbius, W., Ruhwedel, T., Nave, K.A., Giaume, C., Weber, B., and Saab, A.S. (2022a). Decoupling astrocytes in adult mice impairs synaptic plasticity and spatial learning. Cell Rep. *38*. 10.1016/j.celrep.2022.110484.

Hösli, L., Zuend, M., Bredell, G., Zanker, H.S., Porto de Oliveira, C.E., Saab, A.S., and Weber, B. (2022b). Direct vascular contact is a hallmark of cerebral astrocytes. Cell Rep. *39*. 10.1016/j.celrep.2022.110599.

Hu, Y., Geng, F., Tao, L., Hu, N., Du, F., Fu, K., and Chen, F. (2011). Enhanced white matter tracts integrity in children with abacus training. Hum. Brain Mapp. *32*, 10–21. 10.1002/hbm.20996.

Huang, H., and Bordey, A. (2004). Glial glutamate transporters limit spillover activation of presynaptic NMDA receptors and influence synaptic inhibition of Purkinje neurons. J. Neurosci. *24*, 5659–5669. 10.1523/JNEUROSCI.1338-04.2004.

Huang, W., Bhaduri, A., Velmeshev, D., Wang, S., Wang, L., Rottkamp, C.A., Alvarez-Buylla, A., Rowitch, D.H., and Kriegstein, A.R. (2020). Origins and Proliferative States of Human Oligodendrocyte Precursor Cells. Cell *182*, 594-608.e11. 10.1016/j.cell.2020.06.027.

Hughes, E.G., Kang, S.H., Fukaya, M., and Bergles, D.E. (2013). Oligodendrocyte progenitors balance growth with self-repulsion to achieve homeostasis in the adult brain. Nat. Neurosci. *16*, 668–676. 10.1038/nn.3390.Oligodendrocyte.

Hughes, E.G., Orthmann-Murphy, J.L., Langseth, A.J., and Bergles, D.E. (2018). Myelin remodeling through experience-dependent oligodendrogenesis in the adult somatosensory cortex. Nat. Neurosci. *21*, 696–706. 10.1038/s41593-018-0121-5.

Iadecola, C. (2017). The Neurovascular Unit Coming of Age: A Journey through Neurovascular Coupling in Health and Disease. Neuron *96*, 17–42. 10.1016/j.neuron.2017.07.030.

Jackson, S., Meeks, C., Vézina, A., Robey, R.W., Tanner, K., and Gottesman, M.M. (2019). Model systems for studying the blood-brain barrier: Applications and challenges. Biomaterials *214*, 119217. 10.1016/j.biomaterials.2019.05.028.

Kadry, H., Noorani, B., and Cucullo, L. (2020). A blood–brain barrier overview on structure, function, impairment, and biomarkers of integrity. Fluids Barriers CNS *17*, 1–24. 10.1186/s12987-020-00230-3.

Kameyama, T., Miyata, M., Shiotani, H., Adachi, J., Kakuta, S., Uchiyama, Y., Mizutani, K., and Takai, Y. (2023). Heterogeneity of perivascular astrocyte endfeet depending on vascular regions in the mouse brain. IScience *26*, 108010. 10.1016/j.isci.2023.108010.

Kang, S.H., Fukaya, M., Yang, J.K., Rothstein, J.D., and Bergles, D.E. (2010). NG2+ CNS glial progenitors remain committed to the oligodendrocyte lineage in postnatal life and following neurodegeneration. Neuron *68*, 668–681. 10.1016/j.neuron.2010.09.009.

Kaplan, L., Chow, B.W., and Gu, C. (2020). Neuronal regulation of the blood–brain barrier and neurovascular coupling. Nat. Rev. Neurosci. *21*, 416–432. 10.1038/s41583-020-0322-2.

Keiner, S., Niv, F., Neumann, S., Steinbach, T., Schmeer, C., Hornung, K., Schlenker, Y., Förster, M., Witte, O.W., and Redecker, C. (2017). Effect of skilled reaching training and enriched environment on generation of oligodendrocytes in the adult sensorimotor cortex and corpus callosum. BMC Neurosci. *18*, 1–13. 10.1186/s12868-017-0347-2.

Kessaris, N., Fogarty, M., Iannarelli, P., Grist, M., Wegner, M., and Richardson, W.D. (2006). Competing waves of oligodendrocytes in the forebrain and postnatal elimination of an embryonic lineage. Nat. Neurosci. *9*, 173–179. 10.1038/nn1620.

Kikusui, T., Kiyokawa, Y., and Mori, Y. (2007). Deprivation of mother-pup interaction by early weaning alters myelin formation in male, but not female, ICR mice. Brain Res. *1133*, 115–122. 10.1016/j.brainres.2006.11.031.

Kilb, W., Kirischuk, S., and Luhmann, H.J. (2011). Electrical activity patterns and the functional maturation of the neocortex. Eur. J. Neurosci. *34*, 1677–1686. 10.1111/j.1460-9568.2011.07878.x.

Kirabali, T., Rust, R., Rigotti, S., Siccoli, A., Nitsch, R.M., and Kulic, L. (2020). Distinct changes in all major components of the neurovascular unit across different neuropathological stages of Alzheimer's disease. Brain Pathol. *30*, 1056–1070. 10.1111/bpa.12895.

Kirby, B.B., Takada, N., Latimer, A.J., Shin, J., Carney, T.J., Kelsh, R.N., and Appel, B. (2006). In vivo time-lapse imaging shows dynamic oligodendrocyte progenitor behavior during zebrafish development. Nat. Neurosci. *9*, 1506–1511. 10.1038/nn1803.

Kougioumtzidou, E., Shimizu, T., Hamilton, N.B., Tohyama, K., Sprengel, R., Monyer, H., Attwell, D., and Richardson, W.D. (2017). Signalling through AMPA receptors on oligodendrocyte precursors promotes myelination by enhancing oligodendrocyte survival. Elife *6*, e28080. 10.7554/eLife.28080.

Kristensson, K., Zeller, N.K., Dubois-Dalcq, M.E., and Lazzarini, R.A. (1986). Expression of myelin basic protein gene in the developing rat brain as revealed by in situ hybridization. J. Histochem. Cytochem. *34*, 467–473. 10.1177/34.4.2419396.

Krityakiarana, W., Espinosa-Jeffrey, A., Ghiani, C.A., Zhao, P.M., Gomez-Pinilla, F., Yamaguchi, M., Kotchabhakdi, N., and Vellis, J. de (2010). Voluntary exercise increases oligodendrogenesis in spinal cord. Int. J. Neurosci. *120*, 280–290. 10.3109/00207450903222741.VOLUNTARY.

Kubotera, H., Ikeshima-Kataoka, H., Hatashita, Y., Allegra Mascaro, A.L., Pavone, F.S., and Inoue, T. (2019). Astrocytic endfeet re-cover blood vessels after removal by laser ablation. Sci. Rep. *9*, 1–10. 10.1038/s41598-018-37419-4.

Kukley, M., and Dietrich, D. (2009). Kainate receptors and signal integration by NG2 glial cells. Neuron Glia Biol. *5*, 13. 10.1017/S1740925X09990081.

Kukley, M., Capetillo-Zarate, E., and Dietrich, D. (2007). Vesicular glutamate release from axons in white matter. Nat. Neurosci. *10*, 311–320. 10.1038/nn1850.

Kukley, M., Kiladze, M., Tognatta, R., Hans, M., Swandulla, D., Schramm, J., and Dietrich, D. (2008). Glial cells are born with synapses. FASEB J. *22*, 2957–2969. 10.1096/fj.07-090985.

Kukley, M., Nishiyama, A., and Dietrich, D. (2010). The fate of synaptic input to NG2 glial cells: neurons specifically downregulate transmitter release onto differentiating oligodendroglial cells. J. Neurosci. *30*, 8320–8331. 10.1523/JNEUROSCI.0854-10.2010.

Kuo, Y.C., and Lu, C.H. (2012). Expression of P-glycoprotein and multidrug resistance-associated protein on human brain-microvascular endothelial cells with electromagnetic stimulation. Colloids Surfaces B Biointerfaces *91*, 57–62. 10.1016/j.colsurfb.2011.10.035.

Łach, A., Wnuk, A., and Wójtowicz, A.K. (2023). Experimental Models to Study the Functions of the Blood–Brain Barrier. Bioengineering *10*, 1–30. 10.3390/bioengineering10050519.

Lehre, K.P., and Danbolt, N.C. (1998). The number of glutamate transport subtype molecules at glutamatergic synapses: Chemical and stereological quantification in young adult rat brain. J. Neurosci. *18*, 8751–8757. 10.1523/jneurosci.18-21-08751.1998.

Levine, J.M., and Card, J.P. (1987). Light and electron microscopic localization of a cell surface antigen (NG2) in the rat cerebellum: association with smooth protoplasmic astrocytes. J. Neurosci. *7*, 2711–2720. 10.1523/jneurosci.07-09-02711.1987.

Levine, J.M., and Reynolds, R. (1999). Activation and proliferation of endogenous oligodendrocyte precursor cells during ethidium bromide-induced demyelination. Exp. Neurol. *160*, 333–347. 10.1006/exnr.1999.7224.

Levine, J.M., Stincone, F., and Lee, Y. -S (1993). Development and differentiation of glial precursor cells in the rat cerebellum. Glia *7*, 307–321. 10.1002/glia.440070406.

Li, C., Xiao, L., Liu, X., Yang, W., Shen, W., Hu, C., Yang, G., and He, C. (2013). A functional role of NMDA receptor in regulating the differentiation of oligodendrocyte precursor cells and remyelination. Glia *61*, 732–749. 10.1002/glia.22469.

Li, P., Li, H., Jiang, H., Zhu, L., Wu, H., Li, J., and Lai, J. (2017). Expression of NG2 and platelet-derived growth factor receptor alpha in the developing neonatal rat brain. Neural Regen. Res. *12*, 1843–1852. 10.4103/1673-5374.219045.

Li, Q., Brus-Ramer, M., Martin, J.H., and McDonald, J.W. (2010). Electrical stimulation of the medullary pyramid promotes proliferation and differentiation of oligodendrocyte progenitor cells in the corticospinal tract of the adult rat. Neurosci. Lett. *479*, 128–133. 10.1016/j.neulet.2010.05.043.

Liebner, S., Czupalla, C.J., and Wolburg, H. (2011). Current concepts of blood-brain barrier development. Int. J. Dev. Biol. *55*, 467–476. 10.1387/ijdb.103224sl.

Lin, S.C., and Bergles, D.E. (2004). Synaptic signaling between GABAergic interneurons and oligodendrocyte precursor cells in the hippocampus. Nat. Neurosci. *7*, 24–32. 10.1038/nn1162.

Lin, S.C., Huck, J.H.J., Roberts, J.D.B., Macklin, W.B., Somogyi, P., and Bergles, D.E. (2005). Climbing fiber innervation of NG2-expressing glia in the mammalian cerebellum. Neuron *46*, 773–785. 10.1016/j.neuron.2005.04.025.

Liu, J., Dietz, K., Deloyht, J.M., Pedre, X., Kelkar, D., Kaur, J., Vialou, V., Lobo, M.K., Dietz, D.M., Nestler, E.J., Dupree, J., and Casaccia, P. (2012). Impaired adult myelination in the prefrontal cortex of socially isolated mice. Nat. Neurosci. *15*, 1621–1623. 10.1038/nn.3263.

Liu, Y., Shen, X., Zhang, Y., Zheng, X., Cepeda, C., Wang, Y., Duan, S., and Tong, X. (2023). Interactions of glial cells with neuronal synapses, from astrocytes to microglia and oligodendrocyte lineage cells. Glia *71*, 1383–1401. 10.1002/glia.24343.

Love, S. (2006). Demyelinating diseases. J. Clin. Pathol. *59*, 1151–1159. 10.1136/jcp.2005.031195.

Lu, Q.R., Yuk, D.I., Alberta, J.A., Zhu, Z., Pawlitzky, I., Chan, J., McMahon, A.P., Stiles, C.D., and Rowitch, D.H. (2000). Sonic hedgehog-regulated oligodendrocyte lineage genes encoding bHLH proteins in the mammalian central nervous system. Neuron *25*, 317–329. 10.1016/S0896-6273(00)80897-1.

De Luca, C., Colangelo, A.M., Virtuoso, A., Alberghina, L., and Papa, M. (2020). Neurons, Glia, Extracellular Matrix and Neurovascular Unit: A Systems Biology Approach to the Complexity of Synaptic Plasticity in Health and Disease. Int. J. Mol. Sci. *21*, 1539. 10.3390/ijms21041539.

Lučić, V., Yang, T., Schweikert, G., Förster, F., and Baumeister, W. (2005). Morphological characterization of molecular complexes present in the synaptic cleft. Structure *13*, 423–434. 10.1016/j.str.2005.02.005.

Lunde, H.M.B., Assmus, J., Myhr, K.M., Bø, L., and Grytten, N. (2017). Survival and cause of death in multiple sclerosis: A 60-year longitudinal population study. J. Neurol. Neurosurg. Psychiatry *88*, 621–625. 10.1136/jnnp-2016-315238.

Lushnikova, I., Skibo, G., Muller, D., and Nikonenko, I. (2009). Synaptic potentiation induces increased glial coverage of excitatory synapses in CA1 hippocampus. Hippocampus *19*, 753–762. 10.1002/hipo.20551.

MacVicar, B.A., and Newman, E.A. (2015). Astrocyte regulation of blood flow in the brain. Cold Spring Harb. Perspect. Biol. *7*, 1–15. 10.1101/cshperspect.a020388.

Magistretti, P.J., Pellerin, L., Rothman, D.L., and Shulman, R.G. (1999). Energy on Demand. Science (80-.). *283*, 496–497. 10.1126/science.283.5401.496.

Makinodan, M., Rosen, K.M., Ito, S., and Corfas, G. (2012). A critical period for social experience-dependent oligodendrocyte maturation and myelination. Science (80-.). *337*, 1357–1360. 10.1126/science.1220845.

Maldonado, P.P., Velez-Fort, M., Levavasseur, F., and Angulo, M.C. (2013). Oligodendrocyte Precursor Cells Are Accurate Sensors of Local K+ in Mature Gray Matter. J. Neurosci. *33*, 2432–2442. 10.1523/jneurosci.1961-12.2013.

La Manno, G., Siletti, K., Furlan, A., Gyllborg, D., Vinsland, E., Mossi Albiach, A., Mattsson Langseth, C., Khven, I., Lederer, A.R., Dratva, L.M., Johnsson, A., Nilsson, M., Lönnerberg, P., and Linnarsson, S. (2021). Molecular architecture of the developing mouse brain. Nature *596*, 92–96. 10.1038/s41586-021-03775-x.

Marcaggi, P., and Attwell, D. (2004). Role of glial amino acid transporters in synaptic transmission and brain energetics. Glia *47*, 217–225. 10.1002/glia.20027.

Marina, N., Christie, I.N., Korsak, A., Doronin, M., Brazhe, A., Hosford, P.S., Wells, J.A., Sheikhbahaei, S., Humoud, I., Paton, J.F.R., Lythgoe, M.F., Semyanov, A., Kasparov, S., and Gourine, A. V. (2020). Astrocytes monitor cerebral perfusion and control systemic circulation to maintain brain blood flow. Nat. Commun. *11*, 1–9. 10.1038/s41467-019-13956-y.

Marques, S., Zeisel, A., Codeluppi, S., Van Bruggen, D., Falcão, A.M., Xiao, L., Li, H., Häring, M., Hochgerner, H., Romanov, R.A., Gyllborg, D., Muñoz-Manchado, A.B., La Manno, G., Lönnerberg, P., Floriddia, E.M., Rezayee, F., Ernfors, P., Arenas, E., Hjerling-Leffler, J., et al. (2016). Oligodendrocyte heterogeneity in the mouse juvenile and adult central nervous system. Science (80-.). *352*, 1326–1329. 10.1126/science.aaf6463.

Marques, S., van Bruggen, D., Vanichkina, D.P., Floriddia, E.M., Munguba, H., Väremo, L., Giacomello, S., Falcão, A.M., Meijer, M., Björklund, Å.K., Hjerling-Leffler, J., Taft, R.J., and Castelo-Branco, G. (2018). Transcriptional Convergence of Oligodendrocyte Lineage Progenitors during Development. Dev. Cell *46*, 504-517.e7. 10.1016/j.devcel.2018.07.005.

Martínez-Cerdeño, V., and Noctor, S.C. (2018). Neural progenitor cell terminology. Front. Neuroanat. *12*, 1–8. 10.3389/fnana.2018.00104.

Mathiisen, T.M., Lehre, K.P., Danbolt, N.C., and Ottersen, O.P. (2010). The perivascular astroglial sheath provides a complete covering of the brain microvessels: An electron microscopic 3D reconstruction. Glia *58*, 1094–1103. 10.1002/glia.20990.

Matsuzaki, M., Honkura, N., Ellis-Davies, G.C.R., and Kasai, H. (2004). Structural basis of long-term potentiation in single dendritic spines. Nature *429*, 761–766. 10.1038/nature02617.

Matthews, E.A., Sun, W., McMahon, S.M., Doengi, M., Halka, L., Anders, S., Müller, J.A., Steinlein, P., Vana, N.S., van Dyk, G., Pitsch, J., Becker, A.J., Pfeifer, A., Kavalali, E.T., Lamprecht, A., Henneberger, C., Stein, V., Schoch, S., and Dietrich, D. (2022). Optical Analysis of Glutamate Spread in the Neuropil. Cereb. Cortex 1–21. 10.1093/cercor/bhab440.

McKenzie, I.A., Ohayon, D., Li, H., De Faria, J.P., Emery, B., Tohyama, K., and Richardson, W.D. (2014). Motor skill learning requires active central myelination. Science (80-.). *346*, 318–322. 10.1126/science.1254960.

Merkler, D., Ernsting, T., Kerschensteiner, M., Brück, W., and Stadelmann, C. (2006). A new focal EAE model of cortical demyelination: Multiple sclerosis-like lesions with rapid resolution of inflammation and extensive remyelination. Brain *129*, 1972–1983. 10.1093/brain/awl135.

Miller, R.H. (2002). Regulation of oligodendrocyte development in the vertebrate CNS. Prog. Neurobiol. *67*, 451–467.

Miller, F.D., and Gauthier, A.S. (2007). Timing Is Everything: Making Neurons versus Glia in the Developing Cortex. Neuron *54*, 357–369. 10.1016/j.neuron.2007.04.019.

Mira, H., and Morante, J. (2020). Neurogenesis From Embryo to Adult – Lessons From Flies and Mice. Front. Cell Dev. Biol. *8*, 1–20. 10.3389/fcell.2020.00533.

Mishchenko, Y., Hu, T., Spacek, J., Mendenhall, J., Harris, K.M., and Chklovskii, D.B. (2010). Ultrastructural analysis of hippocampal neuropil from the connectomics perspective. Neuron *67*, 1009–1020. 10.1016/j.neuron.2010.08.014.

Missler, M., Südhof, T.C., and Biederer, T. (2012). Synaptic cell adhesion. Cold Spring Harb. Perspect. Biol. *4*. 10.1101/cshperspect.a005694.

Mitew, S., Gobius, I., Fenlon, L.R., Mcdougall, S.J., Hawkes, D., Xing, Y.L., Bujalka, H., Gundlach, A.L., Richards, L.J., Kilpatrick, T.J., Merson, T.D., and Emery, B. (2018). Pharmacogenetic stimulation of neuronal activity increases myelination in an axon-specific manner. Nat. Commun. *9*, 1–16. 10.1038/s41467-017-02719-2.

Monje, M. (2018). Myelin plasticity and nervous system function. Annu. Rev. Neurosci. *41*, 61–76. 10.1146/annurev-neuro-080317-061853.

Mount, C.W., Yalc, B., Cunliffe-koehler, K., Sundaresh, S., and Monje, M. (2019). Monosynaptic tracing maps brain-wide afferent oligodendrocyte precursor cell connectivity. Elife *8*, 1–17.

Müller, J., Reyes-haro, D., Pivneva, T., Nolte, C., Schaette, R., Lübke, J., and Kettenmann, H. (2009). The principal neurons of the medial nucleus of the trapezoid body and NG2+ glial cells receive coordinated excitatory synaptic input. J. Gen. Physiol. *134*, 115–127. 10.1085/jgp.200910194.

Murphy-Royal, C., Dupuis, J.P., Varela, J.A., Panatier, A., Pinson, B., Baufreton, J., Groc, L., and Oliet, S.H.R. (2015). Surface diffusion of astrocytic glutamate transporters shapes synaptic transmission. Nat. Neurosci. *18*, 219–226. 10.1038/nn.3901.

Muzio, M.R., and Cascella, M. (2022). Histology, Axon (StatPearls [Internet]. Treasure Island (FL): StatPearls Publishing).

Nagy, B., Hovhannisyan, A., Barzan, R., Chen, T., and Kukley, M. (2017). Different patterns of neuronal activity trigger distinct responses of oligodendrocyte precursor cells in the corpus callosum. PLoS Biol. 1–32. 10.1371/journal.pbio.2001993.

Naruse, M., Ishizaki, Y., Ikenaka, K., Tanaka, A., and Hitoshi, S. (2017). Origin of oligodendrocytes in mammalian forebrains: a revised perspective. J. Physiol. Sci. *67*, 63–70. 10.1007/s12576-016-0479-7.

Ngugi, A.K., Bottomley, C., Kleinschmidt, I., Sander, J.W., and Newton, C.R. (2010). Estimation of the burden of active and life-time epilepsy: A meta-analytic approach. Epilepsia *51*, 883–890. 10.1111/j.1528-1167.2009.02481.x.

Nishiyama, A., Lin, X.H., Giese, N., Heldin, C.H., and Stallcup, W.B. (1996). Co-localization of NG2 proteoglycan and PDGF α-receptor on O2A progenitor cells in the developing rat brain. J. Neurosci. Res. *43*, 299–314. 10.1002/(SICI)1097-4547(19960201)43:3<299::AID-JNR5>3.0.CO;2-E.

Nishiyama, A., Komitova, M., Suzuki, R., and Zhu, X. (2009). Polydendrocytes (NG2 cells): multifunctional cells with lineage plasticity. Nat. Rev. Neurosci. *10*, 9–22. 10.1038/nrn2495.

Nosov, G., Kahms, M., and Klingauf, J. (2020). The Decade of Super-Resolution Microscopy of the Presynapse. Front. Synaptic Neurosci. *12*, 32. 10.3389/fnsyn.2020.00032.

Okabe, S. (2007). Molecular anatomy of the postsynaptic density. Mol. Cell. Neurosci. *34*, 503–518. 10.1016/j.mcn.2007.01.006.

Oliet, S.H.R., and Bonfardin, V.D.J. (2010). Morphological plasticity of the rat supraoptic nucleus - cellular consequences. Eur. J. Neurosci. *32*, 1989–1994. 10.1111/j.1460-9568.2010.07514.x.

Olsen, M.L., Khakh, B.S., Skatchkov, S.N., Zhou, M., Lee, C.J., and Rouach, N. (2015). New Insights on Astrocyte Ion Channels : Critical for Homeostasis and Neuron-Glia Signaling. J. Neurosci. *35*, 13827–13835. 10.1523/JNEUROSCI.2603-15.2015.

Ordaz, R.P., Garay, E., Limon, A., Pérez-Samartín, A., Sánchez-Gómez, M.V., Robles-Martínez, L., Cisneros-Mejorado, A., Matute, C., and Arellano, R.O. (2021). GABAA receptors expressed in oligodendrocytes cultured from the neonatal rat contain a3 and g1 subunits and present differential functional and pharmacological properties. Mol. Pharmacol. *99*, 133–146. 10.1124/MOLPHARM.120.000091.

Otis, T.S., Wu, Y.-C., and Trussell, L.O. (1996). Delayed Clearance of Transmitter and the Role of Glutamate Transporters at Synapses with Multiple Release Sites. J. Neurosci. *16*, 1634–1644.

Otsu, Y., Couchman, K., Lyons, D.G., Collot, M., Agarwal, A., Mallet, J.M., Pfrieger, F.W., Bergles, D.E., and Charpak, S. (2015). Calcium dynamics in astrocyte processes during neurovascular coupling. Nat. Neurosci. *18*, 210–218. 10.1038/nn.3906.

Paez, P.M., and Lyons, D.A. (2020). Calcium Signaling in the Oligodendrocyte Lineage: Regulators and Consequences. Annu. Rev. Neurosci. *43*, 163–186. 10.1146/annurev-neuro-100719-093305.

Pajarillo, E., Rizor, A., Lee, J., Aschner, M., and Lee, E. (2019). The role of astrocytic glutamate transporters GLT-1 and GLAST in neurological disorders: Potential targets for neurotherapeutics. Neuropharmacology *161*, 107559. 10.1016/j.neuropharm.2019.03.002.

Pan, S., Mayoral, S.R., Choi, H.S., Chan, J.R., and Kheirbek, M.A. (2020). Preservation of a remote fear memory requires new myelin formation. Nat. Neurosci. *23*, 487–499. 10.1038/s41593-019-0582-1.

Passlick, S., Trotter, J., Seifert, G., Steinhäuser, C., and Jabs, R. (2016). The NG2 Protein Is Not Required for Glutamatergic Neuron-NG2 Cell Synaptic Signaling. Cereb. Cortex *26*, 51–57. 10.1093/cercor/bhu171.

Payne, H.L. (2008). The role of transmembrane AMPA receptor regulatory proteins (TARPs) in neurotransmission and receptor trafficking (Review). Mol. Membr. Biol. *25*, 353–362. 10.1080/09687680801986480.

Pelvig, D.P., Pakkenberg, H., Stark, A.K., and Pakkenberg, B. (2008). Neocortical glial cell numbers in human brains. Neurobiol. Aging *29*, 1754–1762. 10.1016/j.neurobiolaging.2007.04.013.

Pepper, R.E., Pitman, K.A., Cullen, C.L., and Young, K.M. (2018). How Do Cells of the Oligodendrocyte Lineage Affect Neuronal Circuits to Influence Motor Function, Memory and Mood? Front. Cell. Neurosci. *12*, 50–55. 10.3389/fncel.2018.00399.

Perea, G., Navarrete, M., and Araque, A. (2009). Tripartite synapses: astrocytes process and control synaptic information. Trends Neurosci. *32*, 421–431. 10.1016/j.tins.2009.05.001.

Perez-Alvarez, A., Navarrete, M., Covelo, A., Martin, E.D., and Araque, A. (2014). Structural and functional plasticity of astrocyte processes and dendritic spine interactions. J. Neurosci. *34*, 12738–12744. 10.1523/JNEUROSCI.2401-14.2014.

Perez-Gianmarco, L., Kurt, B., and Kukley, M. (2023). Technical approaches and challenges to study AMPA receptors in oligodendrocyte lineage cells: Past, present, and future. Glia *71*, 819–847. 10.1002/glia.24305.

Peters, A., and Palay, S.L. (1996). The morphology of synapses. J. Neurocytol. *25*, 687–700. 10.1007/bf02284835.

Picken Bahrey, H.L., and Moody, W.J. (2003). Early Development of Voltage-Gated Ion Currents and Firing Properties in Neurons of the Mouse Cerebral Cortex. J. Neurophysiol. *89*, 1761–1773.

Piet, R., Vargová, L., Syková, E., Poulain, D.A., and Oliet, S.H.R. (2004). Physiological contribution of the astrocytic environment of neurons to intersynaptic crosstalk. Proc. Natl. Acad. Sci. U. S. A. *101*, 2151–2155. 10.1073/pnas.0308408100.

Pringle, N.P., and Richardson, W.D. (1993). A singularity of PDGF alpha-receptor expression in the dorsoventral axis of the neural tube may define the origin of the oligodendrocyte lineage. Development *117*, 525–533. 10.1242/dev.117.2.525.

Pringle, N.P., Mudhar, H.S., Collarini, E.J., and Richardson, W.D. (1992). PDGF receptors in the rat CNS: during late neurogenesis, PDGF alpha-receptor expression appears to be restricted to glial cells of the oligodendrocyte lineage. Development *115*, 535–551. 10.1242/dev.115.2.535.

Psachoulia, K., Jamen, F., Young, K.M., and Richardson, W.D. (2009). Cell cycle dynamics of NG2 cells in the postnatal and ageing brain. Neuron Glia Biol. *5*, 57–67. 10.1017/S1740925X09990354.

Puech, C., Hodin, S., Forest, V., He, Z., Mismetti, P., Delavenne, X., and Perek, N. (2018). Assessment of HBEC-5i endothelial cell line cultivated in astrocyte conditioned medium as a human blood-brain barrier model for ABC drug transport studies. Int. J. Pharm. *551*, 281–289. 10.1016/j.ijpharm.2018.09.040.

Raabe, F.J., Slapakova, L., Rossner, M.J., Cantuti-Castelvetri, L., Simons, M., Falkai, P.G., and Schmitt, A. (2019). Oligodendrocytes as a new therapeutic target in schizophrenia: From histopathological findings to neuron-oligodendrocyte interaction. Cells *8*. 10.3390/cells8121496.

Reich, D.S., Lucchinetti, C.F., and Calabresi, P.A. (2018). Multiple Sclerosis. N. Engl. J. Med. *378*, 169–180. 10.1056/NEJMra1401483.

Reichenbach, A., Derouiche, A., and Kirchhoff, F. (2010). Morphology and dynamics of perisynaptic glia. Brain Res. Rev. *63*, 11–25. 10.1016/j.brainresrev.2010.02.003.

Reiner, A., and Levitz, J. (2018). Glutamatergic Signaling in the Central Nervous System: Ionotropic and Metabotropic Receptors in Concert. Neuron *98*, 1080–1098. 10.1016/j.neuron.2018.05.018.

Reynolds, R., and Hardy, R. (1997). Oligodendroglial progenitors labeled with the O4 antibody persist in the adult rat cerebral cortex in vivo. J. Neurosci. Res. *47*, 455–470. 10.1002/(SICI)1097-4547(19970301)47:5<455::AID-JNR1>3.0.CO;2-G.

Richardson, W.D., Kessaris, N., and Pringle, N. (2006). Oligodendrocyte wars. Nat. Rev. Neurosci. *7*, 11–18. 10.1038/nrn1826.

Rivers, L.E., Young, K.M., Rizzi, M., Jamen, F., Psachoulia, K., Wade, A., Kessaris, N., and Richardson, W.D. (2008). PDGFRA/NG2 glia generate myelinating oligodendrocytes and piriform projection neurons in adult mice. Nat. Neurosci. *11*, 1392–1401. 10.1038/nn.2220.

Rollenhagen, A., Sätzler, K., Rodríguez, E.P., Jonas, P., Frotscher, M., and Lübke, J.H.R. (2007). Structural determinants of transmission at large hippocampal mossy fiber synapses. J. Neurosci. *27*, 10434–10444. 10.1523/JNEUROSCI.1946-07.2007.

Romanos, J., Benke, D., Saab, A.S., Zeilhofer, H.U., and Santello, M. (2019). Differences in glutamate uptake between cortical regions impact neuronal NMDA receptor activation. Commun. Biol. *2*. 10.1038/s42003-019-0367-9.

Roth, B.L. (2016). DREADDs for Neuroscientists. Neuron *89*, 683–694. 10.1016/j.neuron.2016.01.040.

Rothstein, J.D., Martin, L., Levey, A.I., Dykes-Hoberg, M., Jin, L., Wu, D., Nash, N., and Kuncl, R.W. (1994). Localization of neuronal and glial glutamate transporters. Neuron *13*, 713–725. 10.1016/0896-6273(94)90038-8.

Rowitch, D.H., and Kriegstein, A.R. (2010). Developmental genetics of vertebrate glial–cell specification. Nature *468*, 214–222. 10.1038/nature09611.

Rusakov, D.A., and Kullmann, D.M. (1998). Extrasynaptic glutamate diffusion in the hippocampus: Ultrastructural constraints, uptake, and receptor activation. J. Neurosci. *18*, 3158–3170.

Sampaio-Baptista, C., Khrapitchev, A.A., Foxley, S., Schlagheck, T., Scholz, J., Jbabdi, S., DeLuca, G.C., Miller, K.L., Taylor, A., Thomas, N., Kleim, J., Sibson, N.R., Bannerman, D., and Johansen-Berg, H. (2013). Motor skill learning induces changes in white matter microstructure and myelination. J. Neurosci. *33*, 19499–19503. 10.1523/JNEUROSCI.3048-13.2013.

Sánchez-González, R., Bribián, A., and López-Mascaraque, L. (2020). Cell Fate Potential of NG2 Progenitors. Sci. Rep. *10*, 1–12. 10.1038/s41598-020-66753-9.

Sánchez, M.M., Hearn, E.F., Do, D., Rilling, J.K., and Herndon, J.G. (1998). Differential rearing affects corpus callosum size and cognitive function of rhesus monkeys. Brain Res. *812*, 38–49. 10.1016/S0006-8993(98)00857-9.

Sando, R., Bushong, E., Zhu, Y., Huang, M., Considine, C., Phan, S., Ju, S., Uytiepo, M., Ellisman, M., and Maximov, A. (2017). Assembly of Excitatory Synapses in the Absence of Glutamatergic Neurotransmission. Neuron *94*, 312-321.e3. 10.1016/j.neuron.2017.03.047.

Santello, M., Toni, N., and Volterra, A. (2019). Astrocyte function from information processing to cognition and cognitive impairment. Nat. Neurosci. *22*, 154–166. 10.1038/s41593-018-0325-8.

Santuy, A., Tomás-Roca, L., Rodríguez, J.R., González-Soriano, J., Zhu, F., Qiu, Z., Grant, S.G.N., DeFelipe, J., and Merchan-Perez, A. (2020). Estimation of the number of synapses in the hippocampus and brain-wide by volume electron microscopy and genetic labeling. Sci. Rep. *10*, 1–15. 10.1038/s41598-020-70859-5.

Sätzler, K., Söhl, L.F., Bollmann, J.H., Borst, J.G.G., Frotscher, M., Sakmann, B., and Lübke, J.H.R. (2002). Three-dimensional reconstruction of a calyx of Held and its postsynaptic principal neuron in the medial nucleus of the trapezoid body. J. Neurosci. *22*, 10567–10579. 10.1523/jneurosci.22-24-10567.2002.

Schaeffer, S., and Iadecola, C. (2021). Revisiting the neurovascular unit. Nat. Neurosci. *24*, 1198–1209. 10.1038/s41593-021-00904-7.

Scheefhals, N., and MacGillavry, H.D. (2018). Molecular and Cellular Neuroscience Functional organization of postsynaptic glutamate receptors. Mol. Cell. Neurosci. *91*, 82–94. 10.1016/j.mcn.2018.05.002.

Scholz, J., Klein, M.C., Behrens, T.E.J., and Johansen-Berg, H. (2009). Training induces changes in white-matter architecture. Nat. Neurosci. *12*, 1370–1371. 10.1038/nn.2412.

Scimemi, A., Fine, A., Kullmann, D.M., and Rusakov, D.A. (2004). NR2B-containing receptors mediate cross talk among hippocampal synapses. J. Neurosci. *24*, 4767–4777. 10.1523/JNEUROSCI.0364-04.2004.

Scimemi, A., Tian, H., and Diamond, J.S. (2009). Neuronal Transporters Regulate Glutamate Clearance, NMDA Receptor Activation, and Synaptic Plasticity in the Hippocampus. J. Neurosci. *29*, 14581–14595. 10.1523/JNEUROSCI.4845-09.2009.

Segarra, M., Aburto, M.R., and Acker-Palmer, A. (2021). Blood–Brain Barrier Dynamics to Maintain Brain Homeostasis. Trends Neurosci. *44*, 393–405. 10.1016/j.tins.2020.12.002.

Seifert, G., and Steinhauser, C. (2004). Ion channels in astrocytes. In Glial - Neuronal Signaling, pp. 187–213.

Sherman, D.L., and Brophy, P.J. (2005). Mechanisms of axon ensheathment and myelin growth. Nat. Rev. Neurosci. *6*, 683–690. 10.1038/nrn1743.

Shuvaev, A., Belozor, O., and Shuvaev, A. (2024). Information Load from Neuromediator Diffusion to Extrasynaptic Space: The Interplay between the Injection Frequency and Clearance. Biology (Basel). *13*, 566. 10.3390/biology13080566.

Sigler, A., Oh, W.C., Imig, C., Atlas, B., Kawabe, H., Cooper, B.H., Kwon, H.-B., Rhee, J.-S., and Brose, N. (2017). Formation and Maintenance of Functional Spines in the Absence of Presynaptic Glutamate Release. Neuron *94*, 304–311. 10.1016/j.neuron.2017.03.029.

Silbereis, J.C., Pochareddy, S., Zhu, Y., Li, M., and Sestan, N. (2016). The Cellular and Molecular Landscapes of the Developing Human Central Nervous System. Neuron *89*, 248. 10.1016/j.neuron.2015.12.008.

Sim, F.J., Zhao, C., Penderis, J., and Franklin, R.J.M. (2002). The Age-Related Decrease in

CNS Remyelination Efficiency Is Attributable to an Impairment of Both Oligodendrocyte Progenitor Recruitment and Differentiation. J. Neurosci. *22*, 2451–2459. 10.1523/jneurosci.22-07-02451.2002.

Simon, C., Götz, M., and Dimou, L. (2011). Progenitors in the adult cerebral cortex: Cell cycle properties and regulation by physiological stimuli and injury. Glia *59*, 869–881. 10.1002/glia.21156.

Simons, M., and Trotter, J. (2007). Wrapping it up: the cell biology of myelination. Curr. Opin. Neurobiol. *17*, 533–540. 10.1016/j.conb.2007.08.003.

Skripuletz, T., Lindner, M., Kotsiari, A., Garde, N., Fokuhl, J., Linsmeier, F., Trebst, C., and Stangel, M. (2008). Cortical demyelination is prominent in the murine cuprizone model and is strain-dependent. Am. J. Pathol. *172*, 1053–1061. 10.2353/ajpath.2008.070850.

Söhl, G., Maxeiner, S., and Willecke, K. (2005). Expression and functions of neuronal gap junctions. Nat. Rev. Neurosci. *6*, 191–200. 10.1038/nrn1627.

Špaček, J. (1985). Three-dimensional analysis of dendritic spines - III. Glial sheath. Anat. Embryol. (Berl). *171*, 245–252. 10.1007/BF00341419.

Spassky, N., Olivier, C., Cobos, I., LeBras, B., Goujet-Zalc, C., Martínez, S., Zalc, B., and Thomas, J.L. (2001). The early steps of oligodendrogenesis: Insights from the study of the plp lineage in the brain of chicks and rodents. Dev. Neurosci. *23*, 318–326. 10.1159/000048715.

Spitzer, S.O., Sitnikov, S., Kamen, Y., Faria, O. De, Agathou, S., Spitzer, S.O., Sitnikov, S., Kamen, Y., Evans, K.A., and Kronenberg-versteeg, D. (2019). Oligodendrocyte progenitor cells become regionally diverse and heterogeneous with age. Neuron *101*, 459–471. 10.1016/j.neuron.2018.12.020.

Steadman, P.E., Xia, F., Ahmed, M., Mocle, A.J., Penning, A.R.A., Geraghty, A.C., Steenland, H.W., Monje, M., Josselyn, S.A., and Frankland, P.W. (2020). Disruption of Oligodendrogenesis Impairs Memory Consolidation in Adult Mice. Neuron *105*, 1–15. 10.1016/j.neuron.2019.10.013.

Sturrock, R.R. (1980). Myelination of the mouse corpus callosum. Neuropathol. Appl. Neurobiol. *6*, 415–420.

Südhof, T.C. (2012). The presynaptic active zone. Neuron *75*, 11–25. 10.1016/j.neuron.2012.06.012.

Südhof, T.C. (2021). The cell biology of synapse formation. J. Cell Biol. *220*, 1–18. 10.1083/jcb.202103052.

Sun, W., and Dietrich, D. (2013). Synaptic integration by NG2 cells. Front. Cell. Neurosci. *7*, 255. 10.3389/fncel.2013.00255.

Takeuchi, H., Sekiguchi, A., Taki, Y., Yokoyama, S., Yomogida, Y., Komuro, N., Yamanouchi, T., Suzuki, S., and Kawashima, R. (2010). Training of working memory impacts structural connectivity. J. Neurosci. *30*, 3297–3303. 10.1523/JNEUROSCI.4611-09.2010.

Tanaka, K., Watase, K., Manabe, T., Yamada, K., Watanabe, M., Takahashi, K., Iwama, H., Nishikawa, T., Ichihara, N., Kikuchi, T., Okuyama, S., Kawashima, N., Hori, S., Takimoto, M., and Wada, K. (1997). Epilepsy and exacerbation of brain injury in mice lacking the glutamate transporter GLT-1. Science (80-.). *276*, 1699–1702. 10.1126/science.276.5319.1699.

Taubert, M., Draganski, B., Anwander, A., Müller, K., Horstmann, A., Villringer, A., and Ragert, P. (2010). Dynamic properties of human brain structure: Learning-related changes in cortical areas and associated fiber connections. J. Neurosci. *30*, 11670–11677. 10.1523/JNEUROSCI.2567-10.2010.

Tepavčević, V., and Lubetzki, C. (2022). Oligodendrocyte progenitor cell recruitment and

remyelination in multiple sclerosis: the more, the merrier? Brain *145*, 4178–4192. 10.1093/brain/awac307.

Thomas, C.G., Tian, H., and Diamond, J.S. (2011). The relative roles of diffusion and uptake in clearing synaptically released glutamate change during early postnatal development. J. Neurosci. *31*, 4743–4754. 10.1523/JNEUROSCI.5953-10.2011.

Tognatta, R., Sun, W., Goebbels, S., Nave, K.A., Nishiyama, A., Schoch, S., Dimou, L., and Dietrich, D. (2016). Transient Cnp expression by early progenitors causes Cre-Lox-based reporter lines to map profoundly different fates. Glia *65*, 342–359. 10.1002/glia.23095.

Tomlinson, L., Huang, P.H., and Colognato, H. (2018). Prefrontal cortex NG2 glia undergo a developmental switch in their responsiveness to exercise. Dev. Neurobiol. *78*, 687–700. 10.1002/dneu.22590.

Trapp, B.D., Nishiyama, A., Cheng, D., and Macklin, W. (1997). Differentiation and Death of Premyelinating Oligodendrocytes in Developing Rodent Brain. J. Cell Biol. *137*, 459–468.

Tyzio, R., Represa, A., Jorquera, I., Ben-Ari, Y., Gozlan, H., and Aniksztejn, L. (1999). The establishment of GABAergic and glutamatergic synapses on CA1 pyramidal neurons is sequential and correlates with the development of the apical dendrite. J. Neurosci. *19*, 10372–10382.

Tzingounis, A. V., and Wadiche, J.I. (2007). Glutamate transporters: Confining runaway excitation by shaping synaptic transmission. Nat. Rev. Neurosci. *8*, 935–947. 10.1038/nrn2274.

Ullian, E.M., Sapperstein, S.K., Christopherson, K.S., and Barres, B.A. (2001). Control of Synapse Number by Glia. Science (80-.). *291*, 657–661. 10.1126/science.291.5504.657.

Valério-Gomes, B., Guimarães, D.M., Szczupak, D., and Lent, R. (2018). The absolute number of oligodendrocytes in the adult mouse brain. Front. Neuroanat. *12*, 1–19. 10.3389/fnana.2018.00090.

Vallstedt, A., Klos, J.M., and Ericson, J. (2005). Multiple dorsoventral origins of oligodendrocyte generation in the spinal cord and hindbrain. Neuron *45*, 55–67. 10.1016/j.neuron.2004.12.026.

Vana, N.S., van Loo, K.M.J., van Waardenberg, A.J., Tießen, M., Cases-Cunillera, S., Sun, W., Quatraccioni, A., Schoch, S., and Dietrich, D. (2023). Early cortical oligodendrocyte precursor cells are transcriptionally distinct and lack synaptic connections. Glia 2210–2233. 10.1002/glia.24388.

Vélez-Fort, M., Maldonado, P.P., Butt, A.M., Audinat, E., and Angulo, M.C. (2010). Postnatal switch from synaptic to extrasynaptic transmission between interneurons and NG2 cells. J. Neurosci. *30*, 6921–6929. 10.1523/JNEUROSCI.0238-10.2010.

Ventura, R., and Harris, K.M. (1999). Three-dimensional relationships between hippocampal synapses and astrocytes. J. Neurosci. *19*, 6897–6906. 10.1523/jneurosci.19-16-06897.1999.

Verhage, M., Maia, A.S., Plomp, J.J., Brussaard, A.B., Heeroma, J.H., Vermeer, H., Toonen, R.F., Hammer, R.E., Van Den Berg, T.K., Missler, M., Geuze, H.J., and Südhof, T.C. (2000). Synaptic assembly of the brain in the absence of neurotransmitter secretion. Science (80-.). *287*, 864–869. 10.1126/science.287.5454.864.

Verity, A.N., and Campagnoni, A.T. (1988). Regional expression of myelin protein genes in the developing mouse brain: In situ hybridization studies. J. Neurosci. Res. *21*, 238–248. 10.1002/jnr.490210216.

Verkhratsky, A. (2007). Calcium and Cell Death. In Calcium Signalling and Disease, (Dordrecht: Springer Netherlands), pp. 465–480. 10.1007/978-1-4020-6191-2_17.

Verkhratsky, A. (2008). Neurotransmitter Receptors in Astrocytes. In Astrocytes in (Patho)Physiology of the Nervous System, pp. 49–67. 10.1007/978-0-387-79492-1.

Verkhratsky, A., and Nedergaard, M. (2014). Astroglial cradle in the life of the synapse. Philos. Trans. R. Soc. B Biol. Sci. *369*. 10.1098/rstb.2013.0595.

Verkhratsky, A., and Pivoriūnas, A. (2023). Astroglia support, regulate and reinforce brain barriers. Neurobiol. Dis. *179*. 10.1016/j.nbd.2023.106054.

Verkhratsky, A., Nedergaard, M., and Hertz, L. (2015). Why are Astrocytes Important? Neurochem. Res. *40*, 389–401. 10.1007/s11064-014-1403-2.

Voirin, A.C., Perek, N., and Roche, F. (2020). Inflammatory stress induced by a combination of cytokines (IL-6, IL-17, TNF-α) leads to a loss of integrity on bEnd.3 endothelial cells in vitro BBB model. Brain Res. *1730*, 146647. 10.1016/j.brainres.2020.146647.

Walton, C., King, R., Rechtman, L., Kaye, W., Leray, E., Marrie, R.A., Robertson, N., La Rocca, N., Uitdehaag, B., van der Mei, I., Wallin, M., Helme, A., Angood Napier, C., Rijke, N., and Baneke, P. (2020). Rising prevalence of multiple sclerosis worldwide: Insights from the Atlas of MS, third edition. Mult. Scler. J. *26*, 1816–1821. 10.1177/1352458520970841.

El Waly, B., Macchi, M., Cayre, M., and Durbec, P. (2014). Oligodendrogenesis in the normal and pathological central nervous system. Front. Neurosci. *8*, 145. 10.3389/fnins.2014.00145.

Wang, F., Ren, S.Y., Chen, J.F., Liu, K., Li, R.X., Li, Z.F., Hu, B., Niu, J.Q., Xiao, L., Chan, J.R., and Mei, F. (2020). Myelin degeneration and diminished myelin renewal contribute to age-related deficits in memory. Nat. Neurosci. *23*, 481–486. 10.1038/s41593-020-0588-8.

Wang, Y., Fathali, H., Mishra, D., Olsson, T., Keighron, J.D., Skibicka, K.P., and Cans, A.S. (2019). Counting the Number of Glutamate Molecules in Single Synaptic Vesicles. J. Am. Chem. Soc. *141*, 17507–17511. 10.1021/jacs.9b09414.

Warf, B.C., Fok-Seang, J., and Miller, R.H. (1991). Evidence for the ventral origin of oligodendrocyte precursors in the rat spinal cord. J. Neurosci. *11*, 2477–2488. 10.1523/jneurosci.11-08-02477.1991.

Weng, Q., Wang, J., Wang, J., He, D., Cheng, Z., Zhang, F., Verma, R., Xu, L., Dong, X., Liao, Y., He, X., Potter, A., Zhang, L., Zhao, C., Xin, M., Zhou, Q., Aronow, B.J., Blackshear, P.J., Rich, J.N., et al. (2019). Single-Cell Transcriptomics Uncovers Glial Progenitor Diversity and Cell Fate Determinants during Development and Gliomagenesis. Cell Stem Cell *24*, 707-723.e8. 10.1016/j.stem.2019.03.006.

Wenzel, J., Lammert, G., Meyer, U., and Krug, M. (1991). The influence of long-term potentiation on the spatial relationship between astrocyte processes and potentiated synapses in the dentate gyrus neuropil of rat brain. Brain Res. *560*, 122–131. 10.1016/0006-8993(91)91222-M.

Wilson, H.C., Scolding, N.J., and Raine, C.S. (2006). Co-expression of PDGF α receptor and NG2 by oligodendrocyte precursors in human CNS and multiple sclerosis lesions. J. Neuroimmunol. *176*, 162–173. 10.1016/j.jneuroim.2006.04.014.

Winkler, C.C., Yabut, O.R., Fregoso, S.P., Gomez, H.G., Dwyer, B.E., Pleasure, S.J., and Franco, S.J. (2018). The dorsal wave of neocortical oligodendrogenesis begins embryonically and requires multiple sources of sonic hedgehog. J. Neurosci. *38*, 5237–5250. 10.1523/JNEUROSCI.3392-17.2018.

De Wit, J., and Ghosh, A. (2016). Specification of synaptic connectivity by cell surface interactions. Nat. Rev. Neurosci. *17*, 22–35. 10.1038/nrn.2015.3.

Witcher, M.R., Kirov, S.A., and Harris, K.M. (2007). Plasticity of perisynaptic astroglia during synaptogenesis in the mature rat hippocampus. Glia *55*, 13–23. 10.1002/glia.20415.

Wolswijk, G. (1998). Chronic stage multiple sclerosis lesions contain a relatively quiescent population of oligodendrocyte precursor cells. J. Neurosci. *18*, 601–609. 10.1523/jneurosci.18-02-00601.1998.

Wolswijk, G., and Noble, M. (1989). Identification of an adult-specific glial progenitor cell. Development *105*, 387–400. 10.1016/0922-3371(89)90618-7.

Wu, D., Chen, Q., Chen, X., Han, F., Chen, Z., and Wang, Y. (2023). The blood–brain barrier: structure, regulation, and drug delivery. Signal Transduct. Target. Ther. *8*. 10.1038/s41392-023-01481-w.

Wu, Y.W., Grebenyuk, S., McHugh, T.J., Rusakov, D.A., and Semyanov, A. (2012). Backpropagating Action Potentials Enable Detection of Extrasynaptic Glutamate by NMDA Receptors. Cell Rep. *1*, 495–505. 10.1016/j.celrep.2012.03.007.

Xiao, L., Ohayon, D., McKenzie, I.A., Sinclair-Wilson, A., Wright, J.L., Fudge, A.D., Emery, B., Li, H., and Richardson, W.D. (2016). Rapid production of new oligodendrocytes is required in the earliest stages of motor skill learning. Nat. Neurosci. *19*, 1210–1217. 10.1038/nn.4351.Rapid.

Yang, Q.-K., Xiong, J.-X., and Yao, Z.-X. (2013). Neuron-NG2 Cell Synapses: Novel Functions for Regulating NG2 Cell Proliferation and Differentiation. Biomed Res. Int. 1–14. 10.1155/2013/402843.

Yeh, H.-J., Silos-Santiago, I., Wang, Y.-X., George, R.J., Snider, W.D., and Deuel, T.F. (1993). Developmental expression of the platelet-derived growth factor a-receptor gene in mammalian central nervous system. Proc. Natl. Acad. Sci. U. S. A. *90*, 1952–1956.

Yeung, M.S.Y., Zdunek, S., Bergmann, O., Bernard, S., Salehpour, M., Alkass, K., Perl, S., Tisdale, J., Possnert, G., Brundin, L., Druid, H., and Frisén, J. (2014). Dynamics of oligodendrocyte generation and myelination in the human brain. Cell *159*, 766–774. 10.1016/j.cell.2014.10.011.

Young, K.M., Psachoulia, K., Tripathi, R.B., Dunn, S.J., Cossell, L., Attwell, D., Tohyama, K., and Richardson, W.D. (2013). Oligodendrocyte dynamics in the healthy adult CNS: Evidence for myelin remodeling. Neuron *77*, 873–885. 10.1016/j.neuron.2013.01.006.

Yu, G., Su, Y., Guo, C., Yi, C., Yu, B., Chen, H., Cui, Y., Wang, X., Wang, Y., Chen, X., Wang, S., Wang, Q., Chen, X., Hu, X., Mei, F., Verkhratsky, A., Xiao, L., and Niu, J. (2022). Pathological oligodendrocyte precursor cells revealed in human schizophrenic brains and trigger schizophrenia-like behaviors and synaptic defects in genetic animal model. Mol. Psychiatry *27*, 5154–5166. 10.1038/s41380-022-01777-3.

Yuan, X., Chittajallu, R., Belachew, S., Anderson, S., McBain, C.J., and Gallo, V. (2002). Expression of the green fluorescent protein in the oligodendrocyte lineage: A transgenic mouse for developmental and physiological studies. J. Neurosci. Res. *70*, 529–545. 10.1002/jnr.10368.

Yuzwa, S.A., Borrett, M.J., Innes, B.T., Voronova, A., Ketela, T., Kaplan, D.R., Bader, G.D., and Miller, F.D. (2017). Developmental Emergence of Adult Neural Stem Cells as Revealed by Single-Cell Transcriptional Profiling. Cell Rep. *21*, 3970–3986. 10.1016/j.celrep.2017.12.017.

Zarekiani, P., Nogueira Pinto, H., Hol, E.M., Bugiani, M., and de Vries, H.E. (2022). The neurovascular unit in leukodystrophies: towards solving the puzzle. Fluids Barriers CNS *19*, 1–19. 10.1186/s12987-022-00316-0.

Zawadzka, M., Rivers, L.E., Fancy, S.P.J., Zhao, C., Tripathi, R., Jamen, F., Young, K., Goncharevich, A., Pohl, H., Rizzi, M., Rowitch, D.H., Kessaris, N., Suter, U., Richardson, W.D., and Franklin, R.J.M. (2010). CNS-Resident Glial Progenitor/Stem Cells Produce Schwann Cells as well as Oligodendrocytes during Repair of CNS Demyelination. Cell Stem Cell *6*, 578–590. 10.1016/j.stem.2010.04.002.

Zhang, H., and Miller, R.H. (1996). Density-dependent feedback inhibition of oligodendrocyte precursor expansion. J. Neurosci. *16*, 6886–6895. 10.1523/jneurosci.16-21-06886.1996.

Zhang, X., Liu, Y., Hong, X., Li, X., Meshul, C.K., Moore, C., Yang, Y., Han, Y., Li, W.-G., Qi, X., Lou, H., Duan, S., Xu, T.-L., and Tong, X. (2021). NG2 glia-derived GABA release tunes inhibitory synapses and contributes to stress-induced anxiety. Nat. Commun. *12*, 1–18. 10.1038/s41467-021-25956-y.

Zheng, K., Scimemi, A., and Rusakov, D.A. (2008). Receptor actions of synaptically released glutamate: The role of transporters on the scale from nanometers to microns. Biophys. J. *95*, 4584–4596. 10.1529/biophysj.108.129874.

Zheng, K., Jensen, T.P., Savtchenko, L.P., Levitt, J.A., Suhling, K., and Rusakov, D.A. (2017). Nanoscale diffusion in the synaptic cleft and beyond measured with time-resolved fluorescence anisotropy imaging. Sci. Rep. *7*, 1–10. 10.1038/srep42022.

Zhu, X., Bergles, D.E., and Nishiyama, A. (2008). NG2 cells generate both oligodendrocytes and gray matter astrocytes. Development *135*, 145–157. 10.1242/dev.004895.

Zhu, X., Hill, R.A., Dietrich, D., Komitova, M., Suzuki, R., and Nishiyama, A. (2011). Age-dependent fate and lineage restriction of single NG2 cells. Development *138*, 745–753. 10.1242/dev.047951.

Ziskin, J.L., Nishiyama, A., Rubio, M., Fukaya, M., and Bergles, D.E. (2007). Vesicular release of glutamate from unmyelinated axons in white matter. Nat. Neurosci. *10*, 321–330. 10.1038/nn1854.

Zlokovic, B. V. (2008). The Blood-Brain Barrier in Health and Chronic Neurodegenerative Disorders. Neuron *57*, 178–201. 10.1016/j.neuron.2008.01.003.

Zlokovic, B. V. (2011). Neurovascular pathways to neurodegeneration in Alzheimer's disease and other disorders. Nat. Rev. Neurosci. *12*, 723–738. 10.1038/nrn3114.

Zonouzi, M., Scafidi, J., Li, P., Mcellin, B., Edwards, J., Dupree, J.L., Harvey, L., Sun, D., Hübner, C.A., Cull-candy, S.G., Farrant, M., and Gallo, V. (2015). GABAergic regulation of cerebellar NG2 cell development is altered in perinatal white matter injury. Nat. Neurosci. *18*, 674–682. 10.1038/nn.3990.

Zuber, B., Nikonenko, I., Klauser, P., Muller, D., and Dubochet, J. (2005). The mammalian central nervous synaptic cleft contains a high density of periodically organized complexes. Proc. Natl. Acad. Sci. U. S. A. *102*, 19192–19197. 10.1073/pnas.0509527102.

6 List of Abbreviations

2P	Two-photon
AMPA	α-amino-3-hydroxy-5-methyl-4-isoxazolepropionic acid
AMPAR	AMPA receptor
ABC	ATP-binding cassette
BBB	Blood-brain barrier
CAM	Cell adhesion molecule
CC	Corpus callosum
CNS	Central nervous system
CSPG4	chondroitin sulfate proteoglycan 4
E	Embryonic day
EAAT	Excitatory amino acid transporter
fEPSP	field excitatory postsynaptic potential
GABA	γ-aminobutyric acid
iGluSnFR	intensity-based glutamate-sensing fluorescent reporter
LTD	Long-term depression
LTP	Long-term potentiation
mPSC	Miniature postsynaptic current
MS	Multiple sclerosis
NG2	Neuron-glial antigen 2
NMDA	N-methyl-D-aspartate
NMDAR	NMDA receptor
OL	Oligodendrocyte
OPC	Oligodendrocyte precursor cell
PAPs	Peripheral astrocytic processes
PDGFRα	platelet-derived growth factor receptor α
PSD	Postsynaptic density
TARP	Transmembrane AMPAR regulatory protein
TMR	biocytin-tetra-methylrhodamine

7 Acknowledgements

I want to thank my supervisor Prof. Dirk Dietrich for giving me the chance to do my doctoral studies in his lab. He not only provided me the infrastructure and the funding to conduct my research experiments, but also the support and strength to push forward. I appreciate to have learned from and worked with a great mind, who always had an answer or idea at hand, usually accompanied by wisecracks. Moreover, I express my deepest gratitude to my co-supervisor Prof. Susanne Schoch. Her engaging manner and helpful advices always kept me inspired and motivated. Both of them enabled me to attend several research conferences and supported me during intern and extern presentations of my work.

I also want to sincerely thank all our collaboration partners for the trust they had placed in me and our lab, and the time of shared excitement and interests.

Of course, I also want to honor all the researchers, students, technical assistants and other people I had the pleasure to meet and walk part of the way together. I believe for many it was an influential phase of their live – thank you for sharing.

Last but not least, I am very thankful to my second supervisor Prof. Michael Pankratz, Prof. Alf Lamprecht and Prof. Irmgard Förster for agreeing and taking the time to be part of my doctoral committee.

On a personal note, I am grateful towards my family and loved ones for always cheering me on and believing in me. In my mind I send special thanks to those, who were unable to witness the completion of my work, but hopefully gaze down on me with a smile on their face.

8 Appendix

Received: 13 October 2022 | Revised: 26 April 2023 | Accepted: 8 May 2023

DOI: 10.1002/glia.24388

GLIA

WILEY

RESEARCH ARTICLE

Early cortical oligodendrocyte precursor cells are transcriptionally distinct and lack synaptic connections

Natascha S. Vana[1,2] | Karen M. J. van Loo[2] | Ashley J. van Waardenberg[3] | Monika Tießen[1] | Silvia Cases-Cunillera[2] | Wenjing Sun[1] | Anne Quatraccioni[2] | Susanne Schoch[2] | Dirk Dietrich[1]

[1]Department of Neurosurgery, University Hospital Bonn, Bonn, Germany

[2]Department of Neuropathology, University Hospital Bonn, Bonn, Germany

[3]i-Synapse, Bioinformatics, Cairns, Australia

Correspondence
Dirk Dietrich, Department of Neurosurgery, University of Bonn Medical Center, Venusberg-Campus 1, D-53127 Bonn, Germany.
Email: dirk.dietrich@uni-bonn.de

Susanne Schoch, Department of Neuropathology, University of Bonn Medical Center, Venusberg-Campus 1, D-53127 Bonn, Germany.
Email: susanne.schoch@uni-bonn.de

Present addresses
Karen M. J. van Loo, Department of Epileptology and Neurology, RWTH Aachen University, Aachen, Germany; and Wenjing Sun, Department of Neuroscience, Wexner Medical Center, The Ohio State University, Columbus, Ohio, USA.

Funding information
Deutsche Forschungsgemeinschaft, Grant/Award Numbers: DI 853/3-5 & 7, SCHO 820/4-7, SPP1757

Abstract

Oligodendrocyte precursor cells (OPCs) generate oligodendrocytes, a process that may be tuned by neuronal activity, possibly via synaptic connections to OPCs. However, a developmental role of synaptic signaling to OPCs has so far not been shown unequivocally. To address this question, we comparatively analyzed functional and molecular characteristics of highly proliferative and migratory OPCs in the embryonic brain. Embryonic OPCs in mice (E18.5) shared the expression of voltage-gated ion channels and their dendritic morphology with postnatal OPCs, but almost completely lacked functional synaptic currents. Transcriptomic profiling of PDGFRα$^+$ OPCs revealed a limited abundance of genes coding for postsynaptic signaling and synaptogenic cell adhesion molecules in the embryonic versus the postnatal period. RNA sequencing of single OPCs showed that embryonic synapse-lacking OPCs are found in clusters distinct from postnatal OPCs and with similarities to early progenitors. Furthermore, single-cell transcriptomics demonstrated that synaptic genes are transiently expressed only by postnatal OPCs until they start to differentiate. Taken together, our results indicate that embryonic OPCs represent a unique developmental stage biologically resembling postnatal OPCs but without synaptic input and a transcriptional signature in the continuum between OPCs and neural precursors.

KEYWORDS
neuron glia synapse, NG2 cells, oligodendroglial lineage, OPC proliferation, transcriptomics

1 | INTRODUCTION

Oligodendrocytes are generated from oligodendrocyte precursor cells (OPCs). Accumulating evidence suggests that the process of oligodendrogenesis and myelination is guided by the electrical activity of neurons (Foster et al., 2019; Káradóttir & Kuo, 2016). It still is a major unresolved question if and how electrical activity of neurons could guide these processes and influence the proliferation of OPCs. In contrast to other glial cell types in the CNS, a unique and remarkable functional connection exists between neurons and OPCs: OPCs receive classical synapses from neurons in gray and white matter (Bergles et al., 2000; Haberlandt et al., 2011; Kukley et al., 2007;

Susanne Schoch and Dirk Dietrich contributed equally to this work

Ziskin et al., 2007) and vesicular release from neurons activates neurotransmitter receptors to depolarize OPCs (glutamate and GABA receptors) (Biase et al., 2010; Kukley et al., 2008; Lin & Bergles, 2003). Those synaptic depolarizations are translated into intracellular calcium signals (Sun et al., 2016) and intracellular calcium levels in turn have been shown to modulate proliferation and migration of OPCs/NG2 cells (Pitman et al., 2020; Zhao et al., 2021). Therefore, activity-dependent synaptic transmitter release is viewed as one candidate to guide the generation of new OPCs (Foster et al., 2019; Káradóttir & Kuo, 2016).

However, recent evidence supporting a role of neuronal activity in controlling the proliferation of OPCs is conflicting. While some studies have reported an increased generation of OPCs in the rodent CNS in response to neuronal activity (Gibson et al., 2014; Mitew et al., 2018), others have not observed this effect (Simon et al., 2011; Xiao et al., 2016).

OPCs (PDGFRα$^+$ and NG2$^+$) begin to appear in the dorsal embryonic forebrain around embryonic day (E) 16/17 (Kessaris et al., 2006; Nishiyama et al., 1996; Tognatta et al., 2017; Winkler et al., 2018). Embryonic OPCs, studied in the spinal cord and optic nerve, show the highest proliferative activity compared to postnatal stages (Calver et al., 1998; Gao & Raff, 1997; Van Heyningen et al., 2001). Therefore, if this strong proliferative activity is dependent on synaptic connections from neurons, synaptic input to embryonic OPCs should also be pronounced. Recently, Spitzer et al. (2019) reported that embryonic OPCs in the forebrain (E18, selected based on NG2-YFP expression) indeed already express functional glutamate receptors. However, it remained open whether embryonic OPCs are contacted by synapses which could activate those receptors.

To define the developmental timing of synaptic input to OPCs and to explore changes in the presence and abundance of synaptic components in OPCs, we performed a combined electrophysiological, morphological and transcriptional analysis of PDGFRα$^+$ and NG2$^+$ OPCs in the dorsal embryonic and postnatal forebrain. Our data show that the phenotype of embryonic OPCs is very closely related to postnatal OPCs in the dorsal cortex except that embryonic OPCs lack synaptic connections from neurons. The transcriptional analysis revealed that many synaptic genes are not yet expressed in embryonic OPCs and that the general transcriptional signature of embryonic OPCs is clearly distinct from their postnatal counterparts.

2 | MATERIALS AND METHODS

2.1 | Animals

NG2DsRedBAC (Tg(Cspg4-DsRed.T1)1Akik/J, kind gift from A. Nishiyama, UConn, USA) mice expressing the red fluorescent protein DsRed.T1 under the control of the NG2 (Cspg4) promoter were used for all analyses (Zhu et al., 2008). All efforts were made to minimize pain and suffering and to reduce the number of animals used, according to the ARRIVE guidelines. Mice were housed under a 12 h light–dark-cycle (light-cycle 7 am/7 pm), in a temperature (22 ± 2°C) and humidity (55 ± 10%) controlled environment with food/water ad libitum. All procedures were planned and performed in accordance with the guidelines of the University of Bonn Medical Centre Animal-Care-Committee as well as the guidelines approved by the European Directive (2010/63/EU) on the protection of animals used for experimental purposes. Embryonic NG2DsRedBAC mice were obtained by timed breeding, whereby mice were housed together for one day. The day of separation was counted as (gestational day) embryonic day (E) 0.5. For bulk and single-cell RNA sequencing of isolated OPCs C57BL/6NCrl (Charles River) mice of three (E16.5, P4, and P12) or two different ages (E16.5 and P5) were used, respectively.

2.2 | Brain slice preparation

NG2DsRedBAC mice were anesthetized using isoflurane and sacrificed by rapid decapitation.

Embryonic (E18.5) and postnatal ("P7", P7-8 and "P12", P12-14) mice of both sexes were used in electrophysiological experiments. The brain was quickly removed from the skull and placed in ice-cold and oxygenated high-sucrose dissection buffer containing (in mM): 87 NaCl, 2.5 KCl, 1.25 NaH_2PO_4, 7 $MgCl_2$, 0.5 $CaCl_2$, 25 $NaHCO_3$, 25 glucose, 75 sucrose (pH 7.4). Acute coronal brain slices of 300 µm (for electrophysiology) or 400 µm (for immunohistochemistry) were cut using a Leica VT 1200S (Leica Microsystems) vibratome while being immersed in the ice-cold dissection solution, transferred to an incubation chamber at 35°C for 25 minutes and subsequently stored at room temperature for at least 40 minutes before recording in the bath solution containing (in mM): 124 NaCl, 3 KCl, 1.25 NaH_2PO_4, 2 $MgCl_2$, 2 $CaCl_2$, 26 $NaHCO_3$, 10 glucose (pH 7.4).

For the preparation of embryonic brain slices pregnant damns were anesthetized and decapitated. Embryos were removed, decapitated and their heads were temporally kept in the ice-cold and oxygenated dissection buffer described above. For better visual guidance the brains of embryonic mice were isolated under a Zeiss Stemi 2000-C (Carl Zeiss Microscopy) stereomicroscope while being submerged in oxygenated dissection buffer. The head was held by a forceps attached to the frontal bone while a second forceps was used to strip the skin off the skull. Once the skull was exposed, the skull was broken open with a forceps and the brain eventually was scooped out with a small spatula. For the preparation of acute brain slices the embryonic brains were embedded in 4% super low melting agarose (Roth). Little agarose cubes each containing one brain were cut out and glued next to each other on the specimen tray of the vibratome where all embryonic brains were cut simultaneously into 300 µm thick slices.

2.3 | Immunohistochemistry

Acute brain slices (400 µm) of NG2DsRedBAC mice belonging to the age groups of P7-14, 4–7 weeks and 4–5 months were fixed in 8% PFA in PBS, pH 7.4, overnight at 4°C. For embryonic brains, the

cerebellum and the very frontal part of the brain were cut off and the remaining tissue was fixed in 4% or 8% PFA in PBS, pH 7.4, overnight. After three PBS washing steps (10 minutes each), the fixed brain tissue was embedded in 3% Agar in PBS, cut into 50 μm thick coronal brain sections and subsequently stored in TBS, pH 7.4. Some of the embryonic brains were cryopreserved in cryostorage glycol solution consisting of 1% Polyvinylpyrrolidone (PVP)-40, 30% sucrose and 30% ethylene glycol in 0.2 M phosphate buffer (pH 7.4) between fixation and re-sectioning. Incubations with primary and secondary antibodies were performed as described below with washing steps (three times TBS for 10 minutes at room temperature) in between. Brain sections were incubated overnight at 4°C with the respective primary antibody (rabbit anti-SV2B (Synaptic Systems, 1:500), rabbit anti-DsRed (Takara Bio, 1:500), rat anti-AN2 (Miltenyi, 1:500), rat anti-PDGFRα (BD Pharmigen, 1:100). Primary antibodies were diluted in TBS containing Triton X-100 at a concentration of 0.3% (SV2B, AN2, PDGFRα) or 0.1% (DsRed). For SV2B detection sections were incubated with the secondary antibody, biotinylated goat anti-rabbit IgG (Vector Laboratories, 1:167), for 3 hours at 35°C and then incubated with Alexa Fluor 488-conjugated Streptavidin (Jackson ImmunoResearch, 1:167) for another 3 hours at 35°C. All other primary antibodies were followed by incubation with either goat anti-rabbit RRX (Jackson Immuno Research, 1:167) or goat anti-rat Alexa Fluor 488 (Thermo Fisher Scientific, 1:167 for AN2 or 1:100 for PDGFRα) for 3 hours at 35°C. Secondary antibodies were diluted in TBS containing 0.3% Triton X-100. Finally, sections were incubated for 20 minutes with Hoechst 33342 (0.02 mg/mL in TBS) at room temperature and mounted on glass slides using Vectashield (Vector Laboratories). For each experiment, 4–6 sections of one animal from every age group were stained in parallel. In addition, negative controls, in which the primary antibody was omitted (2–3 sections per age group), were run for each of the experiment.

2.4 | Analysis of immunohistochemical stainings

SV2B fluorescence intensity in embryonic, postnatal, young adult and adult brain sections was assessed on an inverted epifluorescence microscope (Nikon Eclipse Ti). All samples of one experiment, that is, SV2B staining and negative control for each of the four age groups, were imaged on the same day. Image acquisition settings were kept constant throughout all age groups and all experiments. Three images per hemisphere were taken for all age groups and conditions. For the postnatal to adult age groups, neighboring non-overlapping imaging spots were chosen in the middle layer of the motor cortex (bregma: −1.3 to −2.5 mm) excluding auditory fields. Embryonic images were acquired in corresponding planes along the rostral-caudal axis but in the intermediate zone, where also the electrophysiological recordings were conducted.

The mean fluorescence intensity of all images was assessed using Fiji (Schindelin et al., 2012) and the fluorescence intensity of the negative control was subtracted from the intensity of slices stained with SV2B.

To test for the co-localization between DsRed and AN2 as well as between DsRed and PDGFRα in embryonic NG2DsRedBAC mice, confocal images were acquired on a Nikon A1 confocal microscope and subsequently analyzed in Fiji.

2.5 | Slice electrophysiology

Electrophysiological recordings were performed at room temperature (18°C) on an Olympus BX51WI microscope which is part of a Prairie Technologies Ultima Multiphoton Microscopy System (Bruker) equipped with two Chameleon Vision II lasers (Coherent). OPCs were patch-clamped in whole-cell recording mode using borosilicate glass pipettes (4–6 MΩ, pulled using a Narishige PP-830 puller) filled with an intracellular solution containing (in mM): 125 K-gluconate, 2 $MgCl_2$, 3 NaCl, 20 KCl, 4 Na_2ATP, 10 Hepes, 0.5 EGTA and 0.1% Lucifer Yellow. In brain slices derived from embryonic mice (E18.5), OPCs of the intermediate zone were targeted, while in the two postnatal groups (P7 and P12) OPCs located in the cortex were recorded. mPSCs were recorded at room temperature in voltage-clamp mode in the presence of 1 μM Tetrodotoxin (TTX, for all but two E18.5 OPCs) and 100 μM Ruthenium Red, filtered at 1 kHz and sampled at 20 kHz using a HEKA EPC 10 patch-clamp amplifier (including the Humbug filter). Cells were held at −85 mV and recorded using the Patchmaster software (HEKA Elektronik). mPSCs were recorded between 5 and 12 minutes after Ruthenium Red and TTX application for a total duration of 200–300 s per cell for all age groups, except for two cells within each group which could be recorded only for 120 s and 175 s (E18.5), 95 s and 174 s (P7) and 160 s and 180 s (P14). Analysis of spontaneous vesicle release was conducted in Axograph X (Axon Instruments), which detected mPSCs semi-automatically using a sliding template with the function f(t) = exp (−t/Rise) – exp (−t/Decay) and the following parameters: Rise = 1 ms, Decay = 4 ms, 10 ms pre-event baseline plus 4 ms event duration (total duration of template 14 ms). All other electrophysiological data were analyzed using Igor Pro software (WaveMetrics).

2.6 | OPC isolation via magnetic-activated cell sorting (MACS) and RNA extraction

OPCs were isolated from whole brains of C57BL/6NCrl mice at E16.5, P4 and P12 using a Neural Tissue Dissociation Kit (Miltenyi Biotec). 5 samples per age group were used for RNA analysis, whereby the P12 group consisted of one P11 and four P12 samples. To collect sufficient cells for each of the 5 biological replicates per age group, we pooled multiple mouse brains for each of the time points: 4–6 for E16.5, 2 for P4 and 2 for P12. Brains were collected in Hank's Balanced Salt Solution (HBSS) and tissue was dissociated into cells by using the Neural Tissue Dissociation Kit (following manufacturer's instructions). Briefly, tissue was transferred to a gentleMACS C tube containing pre-heated enzyme mix 1. After an incubation period of 5 minutes at 37°C brains were roughly dissociated using a 5 mL

pipette and enzyme mix 2. Samples were further dissociated using the automated gentleMACS Octo Dissociator (Miltenyi Biotec). The dissociated tissue was filtered with a 70 µm cell strainer first, followed by a second filtration with a 40 µm cell strainer, and washed in between with DMEM. The resulting cell suspension was centrifuged at 1000*g* for 10 minutes, the pellet resuspended in DMEM containing 1% horse serum (DMEM/HS) and centrifuged again. The washed pellet was resuspended in DMEM/HS and OPCs were labeled by incubating the cell suspension with CD140a MicroBeads (Miltenyi Biotec) for 15 minutes at 4°C. The cells were washed with 20 mL DMEM/HS and centrifuged again. Subsequently, the cell pellet was resuspended in DMEM/HS at a ratio of 500 µL buffer per 1×10^7 cells. The cell suspension was then loaded on a MS column (Miltenyi Biotec) and placed in a magnetic cell separator (Miltenyi Biotec). To isolate CD140a$^+$ cells, first unbound cells were removed by 3 washing steps with 500 µL washing buffer and then the CD140a$^+$ cells were eluted with 1 mL elution buffer. All samples were frozen in liquid nitrogen and stored at −80°C before RNA extraction. To verify the specificity of this purification procedure, aliquots of eluted cells derived from a NG2DsRedBAC mouse (P7) were placed on a coverslip and checked in an inverted epifluorescence microscope (Nikon Eclipse Ti) for fluorescence labeling.

2.7 | Library preparation and sequencing using Smart-Seq2 for bulk RNA-sequencing (RNA-seq)

Total RNA was isolated using the miRNeasy mini kit (Qiagen) according to the manufacturer's instructions. RNA integrity and concentration were determined using the RNA assay on a Tapestation 4200 system (Agilent). Library preparation was based on the Smart-Seq2 protocol (Picelli et al., 2014): 5 ng total RNA (in 1 µL) was added to 4.5 µL Guanidine buffer (50 mM Guanidine Hydrochloride, 17.4 mM dNTPs, 2.2 µM SMART dT30VN primer). Smart-Seq2 libraries were generated on a Tecan Freedom EVO and Nanodrop II (BioNex) system. In short, RNA was incubated at 95°C for 3 minutes. 6 µL RT mix containing SuperScript II buffer (Invitrogen), 9.3 mM DTT, 370 mM Betaine, 15 mM $MgCl_2$, 50 U SuperScript II RT (Invitrogen), 10 U recombinant RNase Inhibitor (Takara) and 3.3 µM template-switching oligo was aliquoted to each sample using a Nanodrop II liquid handling system (BioNex) and incubated at 42°C for 90 minutes and 70°C for 15 minutes. 15 µL preamplification mix containing KAPA HiFi HotStart ReadyMix and 0.1 µM ISPCR primers was added to each sample and full-length cDNA was amplified for 12 cycles. cDNA was purified with 1X Agencourt AMPure XP beads (Beckman Coulter) and eluted in 14 µL nuclease-free water. Concentration and cDNA fragment size distribution was determined using a High Sensitivity D5000 assay for the Tapestation 4200 system (Agilent). cDNA was diluted to an average of 200 pg/µl and 100 pg cDNA from each sample was tagmented by adding 2 µL TD and 1 µL ATM from the Nextera XT DNA Library Preparation Kit (Illumina) to 1 µL diluted cDNA. The tagmentation reaction was incubated at 55°C for 8 minutes before removing the Tn5 from the DNA by adding 1 µL NT buffer. 1 µL indexing primer mix from Nextera XT Index Kit v2 Set A and 3 µL NPM was added and the tagmented cDNA was amplified for 14 cycles according to the manufacturer's specifications. PCR products were purified with 1X Agencourt AMPure XP beads (Beckman Coulter). The fragment size distribution was determined using a High Sensitivity D5000 assay for the Tapestation 4200 system (Agilent) and library concentration was determined using a Qubit dsDNA HS assay (Thermo Fischer). Libraries were clustered at 1.4 pM concentration using High Output v2 chemistry and sequenced on a NextSeq500 system (Illumina) SR 75 bp with 2*8 bp index reads.

2.8 | Bioinformatic analysis for bulk RNA-seq

Sequencing data were demultiplexed using bcl2fastq2 v2.20 and aligned to the mouse reference transcriptome mm10 from UCSC by kallisto v0.44.0 using default parameters. Raw counts were imported using tximport function from the tximport package and DESeqDataSetFromTximport function from DEseq2 and rlog transformed according to DEseq2 pipeline. DESeq2 was used to calculate normalized counts for each transcript using default parameters. All normalized transcripts with a maximum over all row mean lower than 10 were excluded resulting in 15,059 present transcripts. Group-wise comparisons of the three different times (E17.5, P4 and P12) were conducted using the Degust: Interactive RNA-seq analysis Version 3.2.0 (v.4.1.4) platform (http://degust.erc.monash.edu/) with voom/limma and adjusted for multiple testing using the Benjamini-Hochberg False Discovery Rate (FDR) method. Volcano plots were generated to visualize the differentially expressed genes of each comparison (FDR <0.05 and fold change >1.5).

2.9 | Deconvolution analysis of bulk RNA-seq with single-cell sequencing data

Deconvolution of our RNA-seq data to infer single-cell (SC) population state (or cell abundances) was performed using the CPM (Cellulation Population Mapping) algorithm (Frishberg et al., 2019) implemented in scBio v0.1.6. Inputs to the CPM function of scBio were as followed: "BulkData" (our RNA-seq data) were the normalized to counts per million (cpm) using the "cpm" function of edgeR v3.32.1 with defaults settings; "SCData" (single-cell input data) were log normalized, scaled and centered counts using the "NormalizeData" and "ScaleData" functions of Seurat v4.0.3 (Hao et al., 2021) with default arguments; "cellSpace," was the tSNE coordinates generated by Marques et al. (2018); "SCLabels," were the names of clusters identified by Marques et al.; and, "calculateCI" was set to "TRUE." Input data were limited to the genes that were present in both the RNA-seq and scRNA-seq data sets. Uniform Manifold Approximation and Projection (UMAP) dimensionality reduction (Marques et al., 2018) was performed using the RunUMAP function from Seurat, with arguments "reduction" set to "pca" and "dims" as 1:20, where the input data was the Principle Component Analysis (PCA) performed using the RunPCA function. Cell trajectory

was inferred using the predicted cell population states returned from scBio for each individual replicate to the mean of the P12 predicted cell population states. Distance was then calculated as 1-correlation, where the correlation method used was "spearman." Single-cell transcriptome counts, metadata and tSNE coordinates were downloaded from the UCSC Cell Browser on 22 July 2021: https://cells.ucsc.edu/?ds=oligo-lineage-dev. All analyses were performed using RStudio Server v1.4.1106, running R v4.0.5.

2.10 | Gene ontology annotation and enrichment analysis

General gene ontology (GO) analysis was performed with GOrilla (Eden et al., 2009) using differentially expressed genes as the target list, which contained up- and down-regulated genes, and the entire list of annotated genes as the background list. Ontology terms were selected based on Cellular Component. GO terms were considered statistically enriched when FDR q-value <0.05.

Synaptic Gene Ontologies were obtained using the SynGO software (Koopmans et al., 2019). Here, the target lists were the differentially up-regulated genes and the background lists the brain expressed genes from the SynGO database. SynGO terms were considered statistically enriched when FDR q-value <0.05. Heatmapper (Babicki et al., 2016) was used to generate heatmaps of the Log_2 median DESeq2 normalized counts of the various subgroups.

2.11 | Neuron isolation and cell sorting

For isolation of cortical pyramidal neurons, mice were in utero electroporated with plasmids expressing hrGFP at E14.5. At P33-35 cortical areas with green fluorescent cells were micro-dissected from 300 µm-thick coronal brain sections under an epifluorescence microscope (Zeiss Axio Observer A1), collected in ice-cold DPBS and dissociated using the Adult Tissue Dissociation Kit (Miltenyi Biotec). Enzymatic cell dissociation by papain was supported by mechanic dissociation using a gentleMACS Octo Dissociator (Miltenyi Biotec). The cell suspension was filtered through a 70 µm cell strainer and washed with DPBS, followed by a debris removal step. After rewashing the cells with DPBS, red blood cells were removed and the final cell pellet was resuspended in 1 mL of HBSS. Prior to fluorescence-activated cell sorting (FACS), 1 µL of 10 µg/mL DAPI was added to the cell suspensions. Cells that were positive for hrGFP and negative for DAPI were sorted using an Aria Cell sorter III (BD Biosciences) and collected in 1 mL of QIAzol. RNA isolation and sequencing was performed as described above.

2.12 | OPC isolation via MACS for single-cell RNA-seq

For scRNA-seq OPCs were isolated from E16.5 and P5 C57BL/6N mice ordered from Charles River as timed breedings. The E16.5 group consisted of the developing neocortices (neopallial cortex, intermediate zone and ventricular zone) (Chen, Chen, et al., 2017) of a total of 10 embryos (5 embryos of 2 dams each), which were dissected out from coronal brain sections using a Leica M165 FC stereomicroscope. For the P5 group isocortices of six mice (three pups of two different dams) were pooled. Brain tissue was collected in HBSS kept on ice until further processed for OPC isolation. Tissue was dissociated into cells by using the Neural Tissue Dissociation Kit (following manufacturer's instructions). Samples were further dissociated using the automated gentleMACS Octo Dissociator (Miltenyi Biotec). The dissociated tissue was filtered using a 70 µm cell strainer and DMEM was used to wash the samples. The obtained cell suspension was centrifuged at 300*g* for 10 minutes and after discarding the supernatant, the pellet was resuspended in DMEM containing 1% horse serum (DMEM/HS) and centrifuged again. The resulting pellet was resuspended in DMEM/HS containing CD140a MicroBeads (Mitenyi Biotec) and incubated for 15 minutes at 4°C. After washing with DMEM/HS, samples were centrifugated again and the pellet was resuspended in DMEM/HS before applying the solution through an MS column (Miltenyi Biotec), placed in a magnetic cell separator (Miltenyi Biotec). The column was washed three times with DMEM/HS to eliminate the unbound cells and $CD140a^+$ cells were eluted with a plunger by placing the MS column (Miltenyi Biotec) in a 15 mL falcon. The samples were finally centrifugated at 300*g* for 10 minutes and resuspended in 100 µL DMEM/HS buffer.

2.13 | Library preparation and single-cell RNA-seq

Upon quality control on the Countess Automated Cell Counter (Thermo Fisher), the resulting cell suspensions ($CD140a^+$) were loaded directly to a Chromium Single-Cell 3´GEM Instrument (Chromium Next GEM Chip G Single-Cell Kit, 10X Genomics). Corresponding libraries were generated with the Chromium Next GEM Single-Cell 3′ GEM Library & Gel Bead Kit v3.1 employing the Dual Index Kit TT Set A (10X Genomics) according to the manufacturer's instructions. Libraries were produced from 1000 cells per sample. Sequencing of the final Single-Cell RNA libraries was performed using an SP 100 flow cell (600-800 M reads) (Illumina Inc) on an Illumina NovaSeq 6000 platform, aiming at a minimum sequencing depth of 150 000 reads per cell.

2.14 | Analysis of single-cell RNA-seq data

Mapping of RAW single-cell RNA sequencing data was performed using Cell Ranger version 6.1.2 (Zheng et al., 2017). The primary DNA assembly sequences and GTF transcriptome was downloaded from Ensembl release 105 (GRCm39) for Mus musculus (http://ftp.ensembl.org/pub/release-105/). The transcriptome GTF file was filtered for protein-coding genes and a reference assembly prepared using the cellranger "mkref" subcommand. Fastq files of the raw sequencing data for each sample were input into the cellranger

"count" subcommand for alignment of RNA-seq reads and assignment of barcodes to cells. Raw feature count matrices generated by Cell Ranger were imported into R (version 4.0.5) as a SeuratObject using the "CreateSeuratObject" function (Seurat version 4.0.2) using default parameters (Hao et al., 2021). DropletUtils (version 1.10.3) (Griffiths et al., 2018; Lun et al., 2019) was used to infer which barcodes belonged to intact cells versus ambient background after reading in 10X count data using the "read10xCounts" function. emptyDroplets "by.rank" parameter was set to 1200 as an approximation of expected input cell counts and "niters," the number of permutations for determining statistical significance was set to 100,000. Cells with an FDR ≤ 0.01 were retained as intact cells for further analysis.

Single cells were then initially retained if the number of genes detected "nFeature_RNA" was ≥ 250 and ≤ 8000, percentage of reads mapped to mitochondria genes ≤ 40, percentage of reads mapped to ribosomal genes ≤ 20. Features retained were required to be detected in at least 3 cells. Mitochondrial and ribosomal read count percentages were calculated using the "PercentageFeatureSet" function of Seurat to determine the percentage of reads that mapped to "MT-*" and "RPS* or RPL*" genes, respectively. Doublet filtering was performed using DoubletFinder version 2.0.3 (McGinnis et al., 2019) on each filtered single-cell data set (E16.5, P5) to remove multiplets, with an expected doublet rate of 0.6% of 1200 cells and parameters pN = 0.25, pK = 0.09, using 30 principal components. Remaining E16.5 and P5 single cells were then merged into a single Seurat object and log-normalized (using the Seurat "NormalizeData" function). The top 2000 most variable features were obtained using the "FindVariableFeatures" function for subsequent Principal Component Analysis (PCA) dimensionality reduction ("RunPCA") on the first 30 principal components, followed by UMAP generation ("RunUMAP") using the prior PCA reductions. Nearest-neighbor graphs were constructed using "FindNeighbors" on the PCA reductions and clusters determined using "FindClusters" at a resolution of 0.6. Four small and far-scattered clusters were then removed from the analysis. Cells retained were then required to have a percentage of mapped reads to mitochondrial genes less than the upper quantile (29.86%) before removal of mitochondrial genes, filtering of features for detection in at least 3 cells and re-normalization as outlined above. For final dimensionality reduction, the top 1000 most variable features were used, 30 principle components used and the neighborhood size parameter of RunUMAP set to 100 ("n. neighbors"). 1548 cells and 13,612 features (genes) remained after the final filtering, comprised of 562 E16.5 and 986 P5 cells.

2.15 | Integration of single-cell RNA-seq data

Marques et al., 2018 single-cell count data and metadata were downloaded as described for single-cell deconvolution. Genes detected in our single-cell data or features detected in at least 3 cells were retained (a total of 1956 cells). Marques and our combined single-Cell data UMI count data (3504 cells) were then normalized together by regularized negative binomial regression to account for differences in UMI depth (implemented in the "SCTransform" method of Seurat) (Hafemeister & Satija, 2019). Integration of our data with Marques followed to approximate our cell neighborhood locations with Marques cells (Stuart et al., 2019). The top 2000 variable features ("SelectIntegrationFeatures") were input to "PrepSCTIntegration," followed by "FindIntegrationAnchors" to identify pairwise cells within each other's neighborhood, followed by "IntegrateData" using the identified anchor cells, with "normalization.method" set to "SCT." PCA ("RunPCA") on the first 30 principal components was followed by UMAP generation ("RunUMAP") using the prior PCA reduction with a neighborhood size set to 200 ("n.neighbors"). Integration with Marques identified multiple E16.5 clusters. To resolve these clusters in our E16.5/P5 data set, shared nearest-neighbor graphs were constructed using the "FindNeighbors" function on the PCA reductions exploiting the additional information in the integrated data for our E16.5/P5 cells only and then clusters determined using "FindClusters" at a resolution of 1.1, identifying a total of 10 clusters. For the analysis of the expression of synaptic proteins integrated data was assessed using 140 curated genes (Supp. Table 3). Of the 140 genes, 138 genes were detected in the integrated single-cell data. "PercentageFeatureSet" function of Seurat (with parameter assay = RNA) was used to determine the percentage of reads that mapped to these 138 genes.

2.16 | Data analysis

Data are shown as means ± standard errors of the mean (SEM) unless stated otherwise, n denotes the number of cells unless stated otherwise. Statistical analyses were performed with GraphPad Prism (GraphPad Software). For comparisons of two groups statistical significance was determined using an unpaired, two-tailed t-test. When there were more than two groups a one-way ANOVA in conjunction with a post-hoc Tukey's test was conducted. Values were considered significant if $p < .05$, indicated by asterisks in the figure.

3 | RESULTS

We and others have shown that daughter OPCs inherit synaptic contacts from the mother cell during cell division in the first postnatal week (Ge et al., 2009; Kukley et al., 2008). However, the time point when OPCs start acquiring functional synaptic contacts during development is still unresolved. In rodents, OPCs emerge within the embryonic dorsal cortical plate around E16-17 (Kessaris et al., 2006; Nishiyama et al., 1996; Tognatta et al., 2017; Winkler et al., 2018). To examine whether OPCs are surrounded by synapses during prenatal development, we first immuno-labeled coronal mouse brain slices with a marker for neuronal glutamatergic synaptic vesicles (SV2B) (Stout et al., 2019) (Figure 1a–c). In E18.5 brains we found the synaptic marker SV2B to be expressed in the intermediate cortical layer where OPCs first appear (Tognatta et al., 2017) (Figure 1a–c, E18.5: 27.9 ± 1.5 a.u. vs. P7-14: 95.4 ± 9.2 a.u. versus 4–7 weeks: 115.5 ± 9.4 a.u. vs. 4–5 months: 121.5 ± 6.1 a.u. [$n = 4$]).

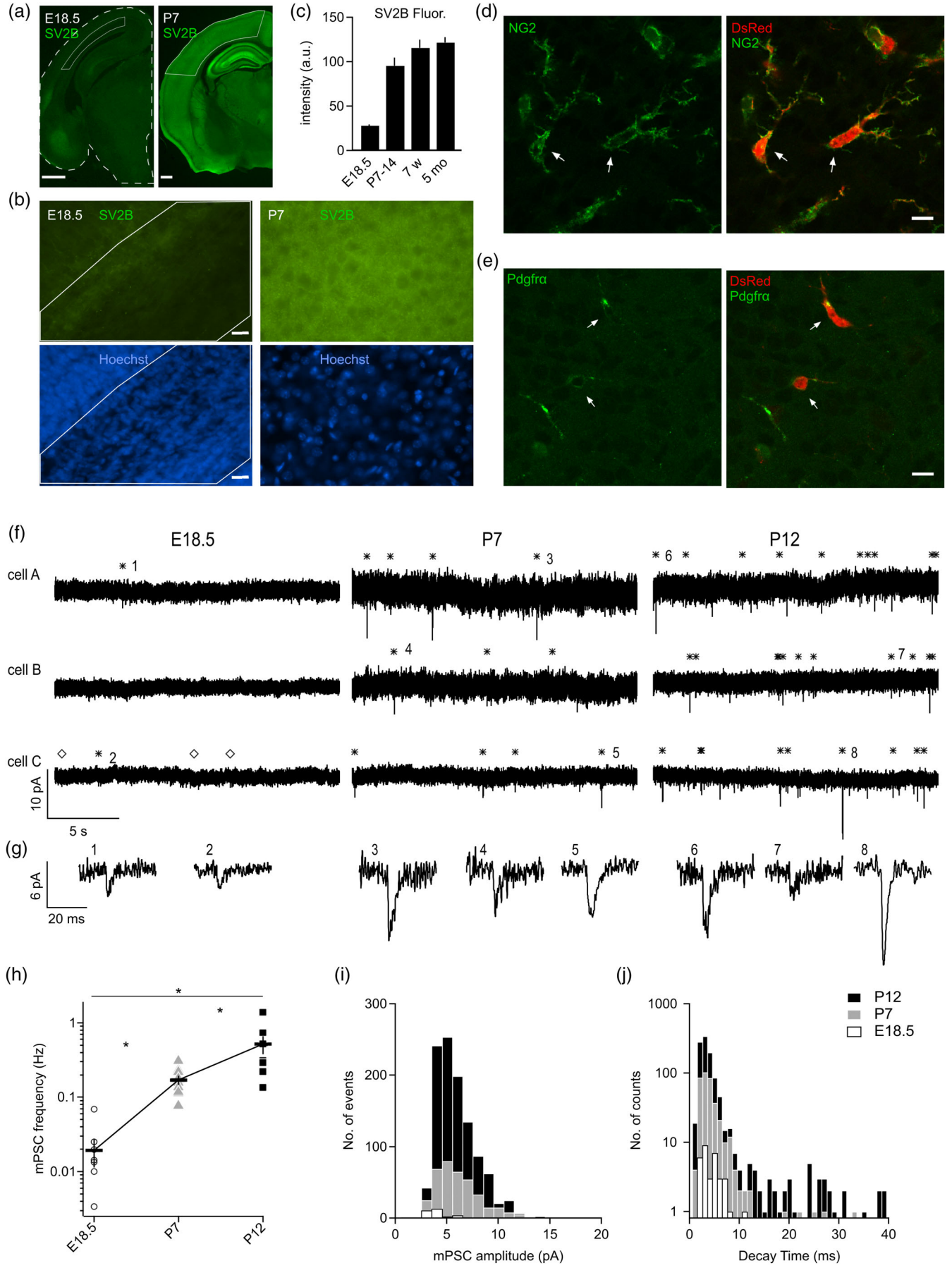

FIGURE 1 Legend on next page.

To investigate whether OPCs form functional synaptic contacts with neurons as early as E18, we patch-clamped DsRed-expressing cells in acute brain slices of NG2DsRedBAC mice which express DsRed solely in OPCs (Biase et al., 2010; Zhu et al., 2008; Ziskin et al., 2007). Co-immunolabeling of E18.5 brain slices with DsRed and NG2 or PDGFRα, the two main marker proteins for OPCs (Nishiyama et al., 1996; Pringle & Richardson, 1993), validated the specific labeling of OPC by DsRed. We found that >95% of parenchymal DsRed+ cells were also positive for NG2 (Figure 1d) and PDGFRα (Figure 1e) and >93% of NG2 cells were marked by the DsRed transgene indicating that E18.5 NG2DsRedBAC mice were well suited to identify embryonic OPCs. Patched cells were held at −85 mV and perfused with 1 μM TTX and 100 μM Ruthenium Red (see methods) to block action potentials and to enhance spontaneous vesicle release downstream of calcium entry (Trudeau et al., 1996), respectively. Using this protocol, we previously measured spontaneously occurring synaptic currents in almost all OPCs tested (Kukley et al., 2007, 2008, 2010). In contrast, OPCs in the intermediate cortical layer at E18.5 appeared virtually silent and no synaptic currents could be detected by eye (Figure 1f, left). Under the same conditions spontaneous synaptic currents were readily observed at postnatal stages, P7-8 (P7) and P12-14 (P12) (Figure 1f, middle and right). With the help of a template-based detection algorithm a low frequency of small miniature postsynaptic currents (mPSCs) could be identified in 9 of 10 cells in the embryonic group (Figure 1f–i, E18.5: 0.02 ± 0.01 Hz [$n = 8$]). The same algorithm detected an order of magnitude more frequent synaptic currents in OPCs of the neocortex of postnatal mice at both P7 and P12 (Figure 1f–i, P7: 0.17 ± 0.02 Hz ($n = 9$); P12: 0.52 ± 0.14 Hz ($n = 8$); E18.5 vs. P7 $p < .05$, E18.5 vs. P12 $p < .05$, P7 vs. P12 $p < .05$, one-way ANOVA with post-hoc Tukey's test). mPSCs in embryonic OPCs were not only very rare but also substantially smaller than in OPCs of both postnatal groups and rarely exceeded 5 pA (Figures 1i and 3.6 ± 0.3 pA for E18, 5.9 ± 0.2 pA and 5.3 ± 0.1 pA at P7 and P12, respectively). In contrast, the decay of mPSCs was comparable in all groups: the largest fraction of currents decayed fast with time constants <10 ms (Figure 1j, E18.5: 3.6 ± 0.3 ms vs. P7: 3.3 ± 0.1 ms and P12: 2.9 ± 0.1 ms). In the P7 and P12 groups smaller fractions of 2%–3% showed decay times longer than 10 ms (P7: 18.8 ± 2.7 ms and P12: 22.6 ± 2.7 ms). In the E18.5 group only one slowly decaying event was recorded (Figure 1j). The fast and slowly decaying currents likely represent glutamatergic and GABA-ergic currents, respectively (Bergles et al., 2000; Kukley et al., 2008; Zonouzi et al., 2015), implying that the depolarizing synaptic input to embryonic and postnatal OPCs arises largely from glutamatergic neurons.

We next asked whether the mPSC frequency correlates with the complexity of the dendritic architecture of OPCs. To compare the morphology of OPCs in the intermediate zone of E18.5 mice and the neocortex of P7-14 mice, we included a tracer in the pipette solution and scanned patched OPCs using two-photon microscopy in acute slices after recording (Figure 2a–f). The dendritic tree of OPCs recorded from E18.5 mice occupied a substantially smaller area than that of postnatal OPCs (Figure 2g, E18.5: 1654 ± 133.66 μm^2 [$n = 10$] vs. P7: 4155 ± 533 μm^2 [$n = 8$] $p < .05$; E18.5 vs. P12: 4829 ± 677 μm^2 [$n = 10$] $p < .05$; P7 vs. P12 $p > .05$, one-way ANOVA with post-hoc Tukey's test). Tracing of individual dendrites in 3D two-photon image stacks showed that in embryonic OPCs also the total dendritic length was profoundly shorter (Figure 2h, E18.5: 527 ± 46 μm vs. P7: 1944 ± 126 μm $p < .05$ and E18.5 vs. P12: 2214 ± 278 μm $p < .05$; P7 vs. P12 $p > .05$, one-way ANOVA with post-hoc Tukey's test) and the branching pattern more simplified (Figure 2i) when compared to postnatal stages. While the mPSC frequency does positively correlate with the size of the dendritic tree (Figure 2j, E18.5 [$n = 8$], P7 [$n = 6$], P12 [$n = 8$], $r = 0.6232$, $r^2 = 0.3884$, $p < .05$, Pearson correlation coefficient), the shorter total dendritic length alone cannot explain the very low frequency of synaptic currents observed in embryonic OPCs as the event rate per mm of dendrite length was also significantly smaller in the embryonic group (Figure 2k, E18.5: 0.04 ± 0.01 events/[s*mm] [$n = 8$] vs. P7: 0.09 ± 0.01 events/[s*mm] [$n = 9$] $p < .05$, E18.5 vs. P12: 0.23 ± 0.06 events/[s*mm] [$n = 8$] $p < .05$, P7 vs. P12 $p < .05$, one-way ANOVA

FIGURE 1 OPCs in the embryonic mouse brain almost lack synaptic input. (a) Representative epifluorescence images of immunohistochemical staining against the synaptic vesicle marker SV2B in coronal brain sections of NG2DsRedBAC mice at E16.5 and P7-14. Regions of interest (outlined by light gray traces) were used for fluorescence intensity measurement, that is, intermediate zone for brain slices from embryonic mice and neocortex for postnatal age groups. Scale bars = 500 μm. (b) Dual channel fluorescence images (SV2B and Hoechst) acquired with a higher power objective illustrating the region (left, white line, right entire image) defined for quantitative analysis. Scale bar = 20 μm. (c) Quantification of the mean SV2B fluorescence intensity of different age groups. $n = 4$ mice for each age group. Error bars represent SEM. (d and e) Colocalization of DsRed and the OPC marker proteins NG2 or PDGFRα in coronal E18.5 NG2DsRedBAC mouse brain slices. DsRed immunoreactive cells (red) in the intermediate zone at E18.5 also expressed the NG2 protein (green). Furthermore, DsRed positive cells (red) were also co-labeled with PDGFRα (green), validating that DsRed marks embryonic OPCs in the NG2DsRedBAC transgenic line. White arrows in each panel indicate OPCs. Scale bars = 10 μm. (f and g) Representative voltage-clamp recordings of OPCs in the mouse cortex from different developmental ages in the presence of 1 μM TTX and 100 μM Ruthenium Red. Asterisks indicate synaptic events; numbers label corresponding events shown in detail in (g). Note that synaptic currents at E18.5 were extremely rare. White diamonds denote positions at which single data points were deleted to remove high-frequency noise in low-frequency recordings. (h) The frequency of spontaneous mPSCs in E18.5 (white circle, $n = 10$) and P7 OPCs (gray triangle, $n = 10$) is lower than in P12 OPCs (black squares, $n = 8$, E18.5 vs. P7 $p < .05$, E18.5 vs. P12 $p < .05$, P7 vs. P12 $p < .05$, one-way ANOVA with post-hoc Tukey's test). (i) Histogram of the mPSC amplitudes recorded in E18.5 (white), P7 (gray) and P12 (black) OPCs. Overall mPSCs from E18.5 OPCs showed much smaller amplitudes than currents recorded postnatally. (j) The histogram of the decay times illustrates a similar distribution between OPCs of embryonic and postnatal mice indicating that the shape of the events is comparable between the three age groups.

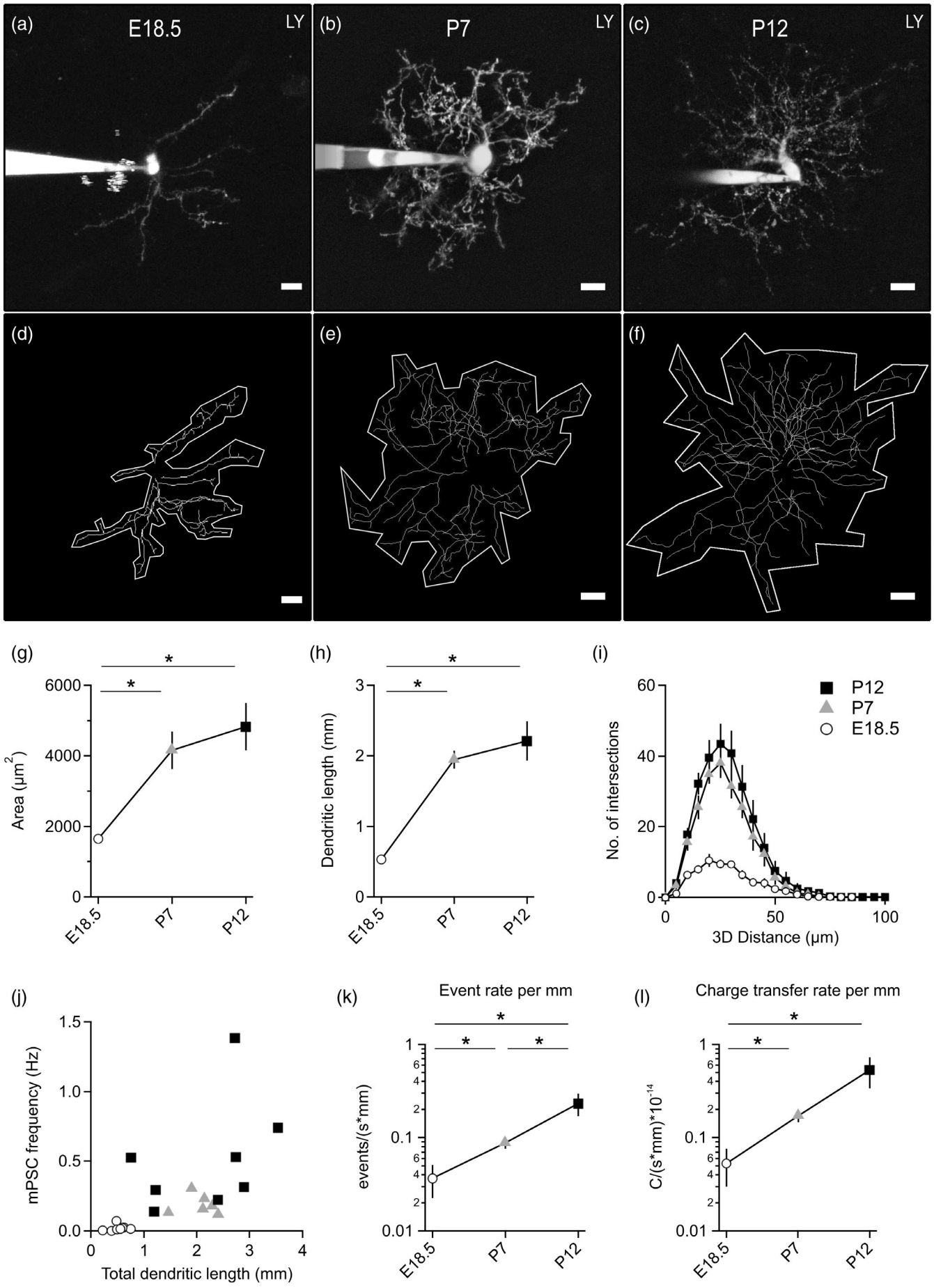

FIGURE 2 Legend on next page.

with post-hoc Tukey's test). This low level of functional synaptic input onto embryonic OPCs becomes most apparent when also taking into account the lower amplitude and the predominantly fast decay of their synaptic currents showing that also the charge transfer rate per mm of dendrite length is significantly smaller (Figure 2l, E18.5: 0.06 ± 0.02 $*10^{-14}$ C/(s*mm) ($n = 8$) vs. P7: 0.17 ± 0.02 $*10^{-14}$ C/(s*mm) ($n = 9$) $p < .05$, E18.5 vs. P12: 0.53 ± 0.19 $*10^{-14}$ C/(s*mm) ($n = 8$) $p < .05$, P7 vs. P12 $p > .05$, one-way ANOVA with post-hoc Tukey's test).

We previously reported that electrical properties of postnatal OPCs play an important role for synaptic signal integration (Sun et al., 2016). Therefore, we next asked what the passive electrical properties of E18.5 OPCs are and whether they might be equipped with a similar set of voltage-gated ion channels or even a more excitable one to compensate for the weak synaptic innervation described above. The resting membrane potential (RMP) in OPCs was measured ~10 mV more depolarized at E18.5 than at P7 implying that the ion permeability ratio at resting potential is shifted toward depolarizing forces in embryonic OPCs (Figure 3a, E18.5: −65.7 ± 4.2 mV [n = 10] vs. P7: −81.5 ± 2.3 mV [$n = 10$] $p > .05$, Student's t-test, P12: −85.4 ± 1.6 mV [$n = 7$]). If passive electrical properties per unit of OPC membrane were similar across age groups, cell capacitance (Cm) and membrane resistance (Rm) would be expected to scale with the size of the dendritic tree and the cell's surface area. This was clearly observed for the Cm where the value of the P7 group similarly exceeded the E18.5 value, as did the total dendritic length (Figure 3b, E18.5: 12 ± 2.6 pF ($n = 10$) vs. P7: 40 ± 3.3 pF ($n = 11$) $p < .05$, Student's t-test, P12: 44.6 ± 3.7 pF ($n = 10$); total dendritic length is roughly proportional to the cell's surface area). In contrast, the Rm was very similar between age groups (Figure 3c, E18.5: 1.40 ± 0.23 GΩ ($n = 10$) vs. P7: 1.23 ± 0.41 GΩ ($n = 11$) $p > .05$, Student's t-test, P12: 49.2 ± 5.3 MΩ ($n = 10$)), indicating that E18.5 OPCs express substantially more un-gated potassium channels per surface area than postnatal ones in order to display the same Rm with a smaller surface area.

Voltage steps applied during voltage clamp recordings activated large transient and persistent outward currents in all age groups (Figure 3d,e), which were previously shown to represent A- and DR-type of potassium channels (Maldonado et al., 2013; Sun et al., 2016; Yuan et al., 2002). At the beginning of the depolarization, we identified a small transient inward current which resembled a TTX-sensitive current as previously described (Figure 3d,e) (Biase et al., 2010; Xie et al., 2007), which usually is too small to generate action potentials (Berret et al., 2017; Biase et al., 2010; Chittajallu et al., 2004; but see Káradóttir et al., 2008; Xie et al., 2007). A-type potassium currents (Figure 3f, at 40 mV E18.5: 1.10 ± 0.13 nA ($n = 8$) vs. P7: 1.79 ± 0.15 nA ($n = 5$) $p < .05$, Student's t-test) appeared reduced in E18.5 OPCs compared to postnatal OPCs, while DR-type potassium channels (Figure 3g, at 40 mV E18.5: 684 ± 63 pA ($n = 8$) vs. P7: 936 ± 146 pA ($n = 5$) $p > .05$, Student's t-test) and voltage-activated sodium currents (Figure 3h, at 0 mV E18.5: −103 ± 17 pA (n = 8) vs. P7: −204 ± 55 pA ($n = 5$) $p > .05$, Student's t-test) were found at similar levels. Whether or not an EPSP or IPSP would be enhanced by activating sodium channels also depends on the strength of rapidly activating potassium currents. To compare the excitability of OPCs across age groups, we calculated a ratio of the amplitudes of sodium and A-type currents recorded between −40 and 0 mV, a potential beyond the threshold for sodium channel activation. E18.5 cells showed a similar excitability index when compared to P7 (Figure 3i, mean I_{Na}/mean Peak I_K between −40 and 0 mV, E18.5: 0.23 ± 0.05 ($n = 8$) vs. P7: 0.24 ± 0.09 ($n = 5$) $p > .05$, Student's t-test).

Our findings so far show that embryonic OPCs display a substantially reduced synaptic input drive although synapses seem to be present in their neighborhood. To assess the possibility that embryonic OPCs may be too immature to receive and establish synaptic connections, we compared the molecular signatures between embryonic and postnatal OPCs. OPCs were immuno-isolated from the whole mouse brain at E16.5, P4, and P12 by anti-PDGFRα-mediated magnetic activated cell sorting (MACS, yielding at least 90% purity of $NG2^+$ cells, see methods) and subjected to bulk RNA sequencing (RNA-seq) (Figure 4). The principal component analysis (PCA) of the data set showed that the biological replicates of the different time points clustered together and that the molecular signatures of all time points were clearly different from each other, indicating pronounced developmental changes (Figure 4a). The expression at P4 of a panel of representative marker genes for different brain cell types was consistent

FIGURE 2 Embryonic OPCs have a reduced morphological size and complexity compared to OPCs in the postnatal mouse brain. (a–c) Representative scans obtained via two-photon imaging of dye-filled OPCs recorded in NG2DsRedBAC mice at E18.5 (a), P7 (b) or P12 (c) respectively. (a: Note that this OPC was dividing at the time of acquisition. Scale bar = 10 µm.) (d–f) The maximum projection of the traced dendrites for the cell shown in (a–c) are displayed in (d–f). Scale bars = 10 µm. The maximum projection of the z-stack of a given OPC was outlined to determine the area the cell is occupying. (g–h) For each cell the outlined territory (g, area) and the summed length of all dendrites traced (h, dendritic length) as indicated in (d–f) was measured. The mean value for the area and the dendritic length of each age group ($n = 10$ [E18.5], $n = 8$ [P7], $n = 10$ [P12]), is shown in (g) (E18.5 vs. P7 $p < .05$ and E18.5 vs. P12 $p < .05$; P7 vs. P12 $p > .05$, one-way ANOVA with post-hoc Tukey's test) and (h) (E18.5 vs. P7 $p < .05$ and E18.5 vs. P12 $p < .05$; P7 vs. P12 $p > .05$, one-way ANOVA with post-hoc Tukey's test) respectively. (i) The 3D-traced dendrites (as shown in [d–f]) were used for a 3D Sholl analysis. OPCs in the embryonic brain only show a third of the number of intersections found in postnatal OPCs. The most distant intersections identified were 85 µm and 100 µm remote from the soma in embryonic and postnatal OPCs, respectively. (j) The summed length of all dendritic paths positively correlated with the mPSC frequency in OPCs, ($r = 0.6232$, $r^2 = 0.3884$, $p < .05$, Pearson correlation coefficient). (k) To account for the reduced size of the embryonic OPCs the frequency of mPSCs was normalized to the mean total length of the OPC dendrites at the respective age (E18.5 vs. P7 $p < .05$, E18.5 vs. P12 $p < .05$, P7 vs. P12 $p < .05$, one-way ANOVA with post-hoc Tukey's test). (l) Charge transfer also takes amplitudes and decay time into account for comparing synaptic drive of OPCs (E18.5 vs. P7 $p < .05$, E18.5 vs. P12 $p < .05$, P7 vs. P12 $p > .05$, one-way ANOVA with post-hoc Tukey's test).

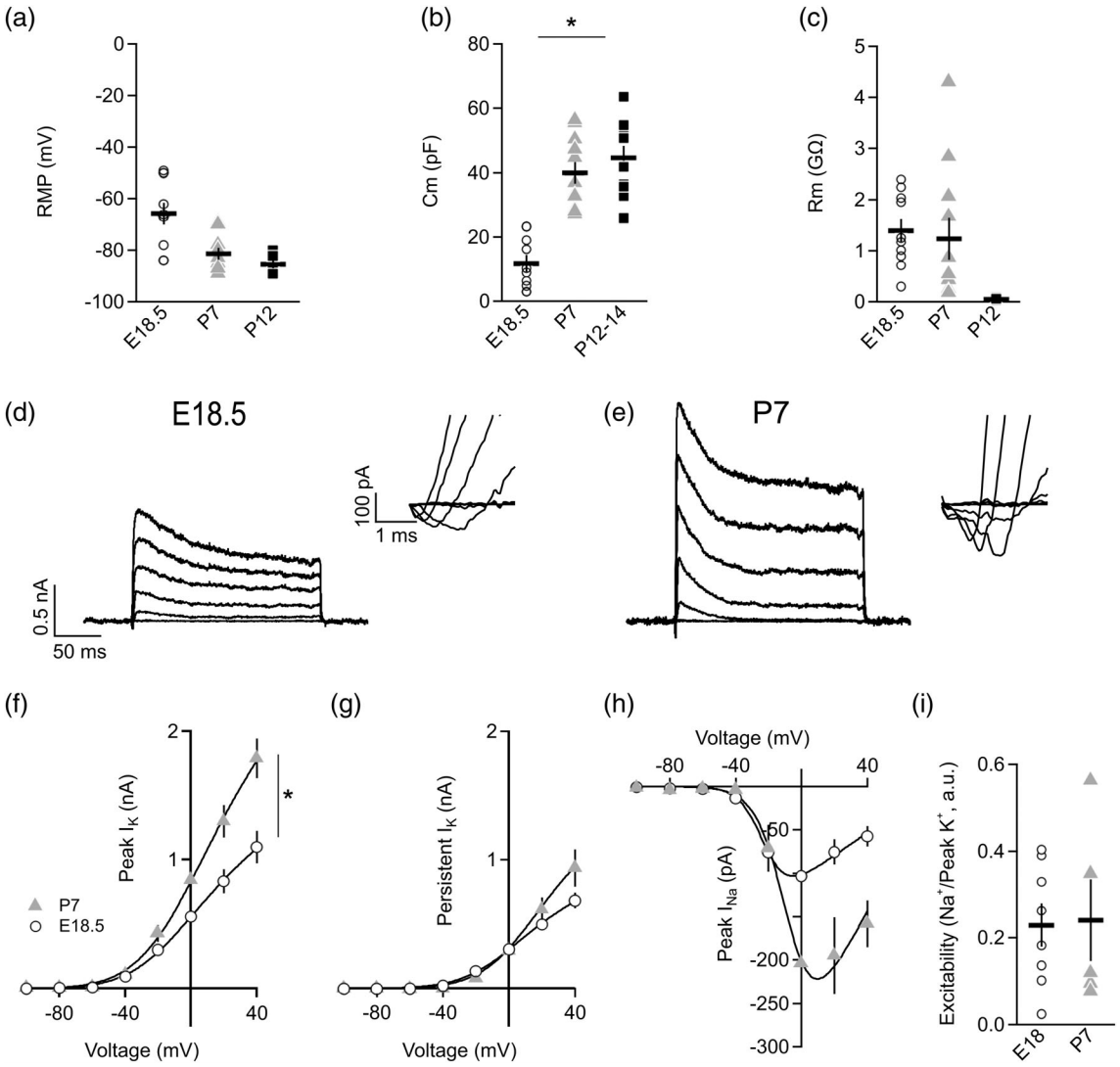

FIGURE 3 Ion channels of OPCs in the embryonic and the postnatal brain. (a and b) OPCs in the embryonic brain tended to show a more depolarized resting membrane potential but the statistical comparison to the postnatal group did not reach the level of significance (RMP; E18.5 [$n = 12$ cells] vs. P7 [$n = 13$ cells] $p > .05$, Unpaired t test). Embryonic OPCs displayed a smaller membrane capacitance (Cm; E18.5 [$n = 12$ cells] vs. P7 [$n = 14$ cells], $p < .05$, Student's t-test) compared to OPCs in postnatal mice. (c) The membrane resistance (Rm) of OPCs at E18.5 was comparable to P7 OPCs (E18.5 ($n = 12$ cells) vs. P7 ($n = 14$ cells) $p > .05$, Student's t-test). Note the significant drop of membrane resistance in the P12 group ($p < .05$, 1-way ANOVA). (d and e) Representative membrane current patterns of OPCs. Membrane currents were obtained by subjecting the cells to hyper- and depolarizing voltage steps ranging between −100 and +40 mV. Original membrane currents were leak current-subtracted to reveal the Na^+ currents at more depolarizing membrane potentials, which are indicated by the rectangular boxes and depicted on a smaller time scale next to each membrane current recording. (f–h) IV curves for the peak K^+ current (f) (peak K^+ current at +40 mV of E18.5 [$n = 9$ cells] vs. P7 [$n = 8$ cells] $p < .05$, Student's t-test), the persistent K^+ current (g) (persistent K^+ current at +40 mV of E18.5 [$n = 9$ cells] vs. P7 [$n = 8$ cells] $p > .05$, Student's t-test) and the peak Na^+ current (h) (peak Na^+ current at 0 mV of E18.5 [$n = 9$ cells] vs. P7 [n = 8 cells] $p > .05$, Student's t-test) were obtained from the leak current-subtracted IV curves shown in e and f. (i) The excitability of OPCs at E18.5 (d) calculated by dividing the Na^+ current by the peak K^+ current recorded between −40 and 0 mV was comparable to P7 OPCs (E18.5 [$n = 9$ cells] vs. P7 [$n = 8$ cells] $p > .05$, Student's t-test).

with the OPC identity of isolated cells (Figure 4b and Supplementary Figure 1a–c).

Our RNA-seq analysis revealed 3265 genes to be differentially expressed between E16.5 and P4 (1922 up- and 1343 down-regulated genes, Supplementary Figure 1d), while 2288 genes were differentially expressed between P4 and P12 (1733 up- and 555 down-regulated genes, Supplementary Figure 1e). All differentially expressed genes (DEGs) of our samples, up- and down-regulated, were further analyzed using the gene ontology enrichment analysis and visualization tool (GOrilla) to determine their potential functions, localizations and pathways. When comparing the DEGs between E16.5 and P4, GO-terms related to the synapse, the plasma membrane, the extracellular region and cell junctions were highly enriched (Supplementary Figure 1f and Supplementary Table 1 for the

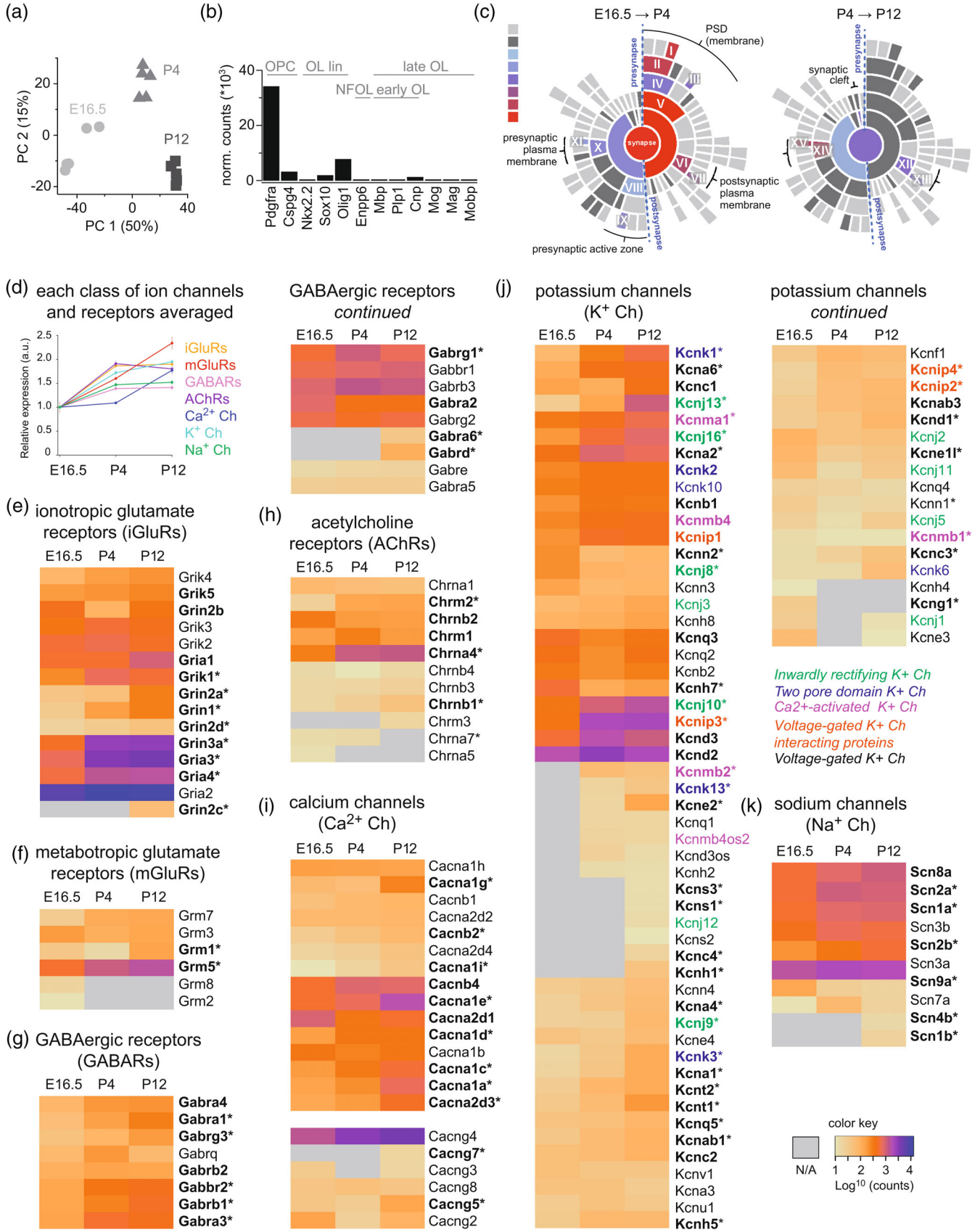

FIGURE 4 Legend on next page.

individual DEGs per GO-term; only GO-terms with a FDR $<10^{-11}$ are listed). Strikingly, when comparing differentially expressed genes between P4 and P12 we found a high association with the same GO-terms (FDR $<10^{-11}$), but the GO-terms synapse and cell junction were not enriched anymore (Supplementary Figure 1g, and Supplementary Table 2 for the individual DEGs per GO-term), indicating, in accordance with our electrophysiological recordings, that the synaptic drive of OPCs by neurons is largely established only early postnatally and then maintained from P4 on at a high level.

To investigate the developmental regulation of synaptic genes in OPCs in more detail, we analyzed genes that exhibited an increase in expression from E16.5 to P4 or from P4 to P12 using a database of curated annotations of synaptic genes, SynGO (Koopmans et al., 2019). As seen with GOrilla, the increase in the expression of synaptic genes was most pronounced between E16.5 and P4 (Figure 4c left) and only few up-regulated genes were found between P4 and P12 (Figure 4c right). Up-regulated synaptic genes found at P4 to the largest extent encoded postsynaptic proteins, but not presynaptic proteins, consistent with the physiological observation that OPCs are postsynaptic partners and not known to synapse onto other cells (Figure 4c).

We performed a single gene-based analysis for proteins important for postsynaptic electrical signal integration, neurotransmitter receptors and ion channels. Overall, mRNA expression levels of those genes were up-regulated during development for all channel and receptor subclasses. Except for metabotropic glutamate receptors and calcium channels, the most pronounced changes were seen between E16.5 and P4 (Figure 4d). This was also evident for a small group of highly abundant genes which exhibited very substantial mRNA levels from P4 onwards: *Gria3* (GluR-3), *Gria4* (GluR-4) and *Grin3a* (GluN3A) (ionotropic glutamate receptor subunits), *Grm5* (mGluR5, metabotropic glutamate receptor), *Gabra3* (GABA(A) receptor subunit beta-3), *Gabbr2* (GABA(B) receptor subunit 2), *Chrna4* (neuronal acetylcholine receptor subunit alpha-4), voltage-gated calcium channel *Cacna1e* ($Ca_V2.3$, Shal-related), *Kcnd2* (Kv4.2, A-type potassium channel), *Kcnd3* (Kv4.3, A-type potassium channel), *Kcnj10* (Kir4.1, background potassium channel), *Kcna2* (Kv1.2, delayed rectifier) and sodium voltage-gated channel alpha subunits (*Scn1a*, *Scn2a*, *Scn3a* and *Scn8a*) (Figure 4e–k). *Gria2*, the subunit limiting the calcium permeability of AMPA receptors, stands out as it is already highly expressed at E16.5 (Figure 4e) and is the most abundant of all receptor genes listed in Figure 4 at all time points.

Recruitment of R−/T-type voltage-gated calcium channels plays an important role for the integration of synaptic input by postnatal OPCs (Sun et al., 2016). This is supported by our transcriptional analyses showing that *Cacna1e* (R-type) and *Cacna1a* (P/Q-type) are the most highly expressed voltage-gated calcium channel alpha subunits in P12 OPCs (Figure 4l).

Even though Acetylcholine (Ach) signaling has been implicated in the regulation of myelination decades ago (Toran-Allerand, 1974), only recently has its direct effect on OPC proliferation and differentiation been investigated (Fields et al., 2017). Strikingly, we find a very strong increase in the levels of *Chrna4* (Neuronal acetylcholine receptor subunit alpha-4) and *Chrm2* (Cholinergic receptor muscarinic 2) from embryonic to postnatal OPCs (Figure 4h).

We next compared the abundance of genes coding for receptors and ion channels in OPCs (P12) and layer 2/3 cortical neurons (P33-35), which had been isolated by FACS and subjected to bulk RNA-seq. To this end, we ranked genes according to their abundance in each cell type and then comparatively analyzed the ranked lists

FIGURE 4 Genes coding for components of the postsynapse are strongly up-regulated in OPCs from E16.5 to P4. (a) Principal component analysis (PCA) of bulk RNA seq data of cells MACS-sorted from the brain of PDGFRα$^+$ (CD140a+) mice showed clustering of the transcriptional patterns of the samples in the three age groups ($n = 5$ for each group). (b) Mean expression levels of genes coding for cell type-specific markers for OPCs, oligodendrocytes lineage cells (OL lin), newly formed oligodendrocytes (NFOL), oligodendrocyte-specific myelinating markers up-regulated early (early OL) and oligodendrocyte-specific myelinating markers up-regulated later (late OL) in the RNA data set at P4 demonstrate a high grade of purity achieved via MACS isolation of OPCs. Further genes specific for other cell types detected in P4 samples as well as corresponding graphs for E16.5 and P12 can be found in Supplementary Figure 1a–c. (c) SynGO annotations for synaptic genes that are up-regulated in OPCs from E16.5 to P4 (left) and from P4 to P12 (right). Color scale indicates- -log10 Q-value ranging from light blue (2) to bright red (≥7) color. Sectors colored in gray represent SynGO terms holding too few genes (light gray) or being not significantly enriched (dark gray). Note that more synaptic GO-terms, especially postsynaptic GO-terms, are significantly enriched between E16.5 and P4 than between P4 and P12. I (integral component of postsynaptic density membrane), II (postsynaptic density membrane), III (integral component of postsynaptic specialization membrane), IV (postsynaptic density), V (postsynaptic specialization), VI (postsynaptic membrane), VII (integral component of postsynaptic membrane, VIII (presynaptic active zone), IX (integral component of presynaptic active zone membrane), X (presynaptic membrane), XI (integral component of presynaptic membrane), XII (postsynaptic membrane), XIII (integral component of postsynaptic membrane), XIV (presynaptic membrane), XV (integral component of presynaptic membrane). (d–k) Heatmaps plotting the DEseq2 normalized counts for genes encoding different channels and receptors found in OPCs of mice at E18, P4, and P12. Gene expression is color-coded from light yellow (low expression) to dark purple (high expression), apart from genes with count rates below 10, which are depicted In gray (N/A). Genes significantly up- or down-regulated between E16.5 and P12 are shown in bold letters, while asterisks mark genes with a more than 2-fold increase or decrease. (d) Mean expression level of the different channel and receptor families (b–h) per age group normalized to E16.5 levels. (e) ionotropic glutamate receptors. (f) metabotropic glutamate receptors. (g) GABA-ergic receptors. (h) acetylcholine receptors. (i) calcium channels. Genes encoding the calcium channel γ subunit (Cacng) family are plotted separately as Cacng2, 3, 4, 5, 7, and 8 have been identified as auxiliary proteins to AMPARs (Transmembrane AMPAR regulatory proteins, TARPs). (j) potassium channels, including inwardly rectifying potassium channels (green), two pore domain potassium channels (blue), potassium calcium-activated channels (purple), potassium voltage-gated channel interacting proteins (red), voltage-gated potassium channels (black). (k) sodium channels.

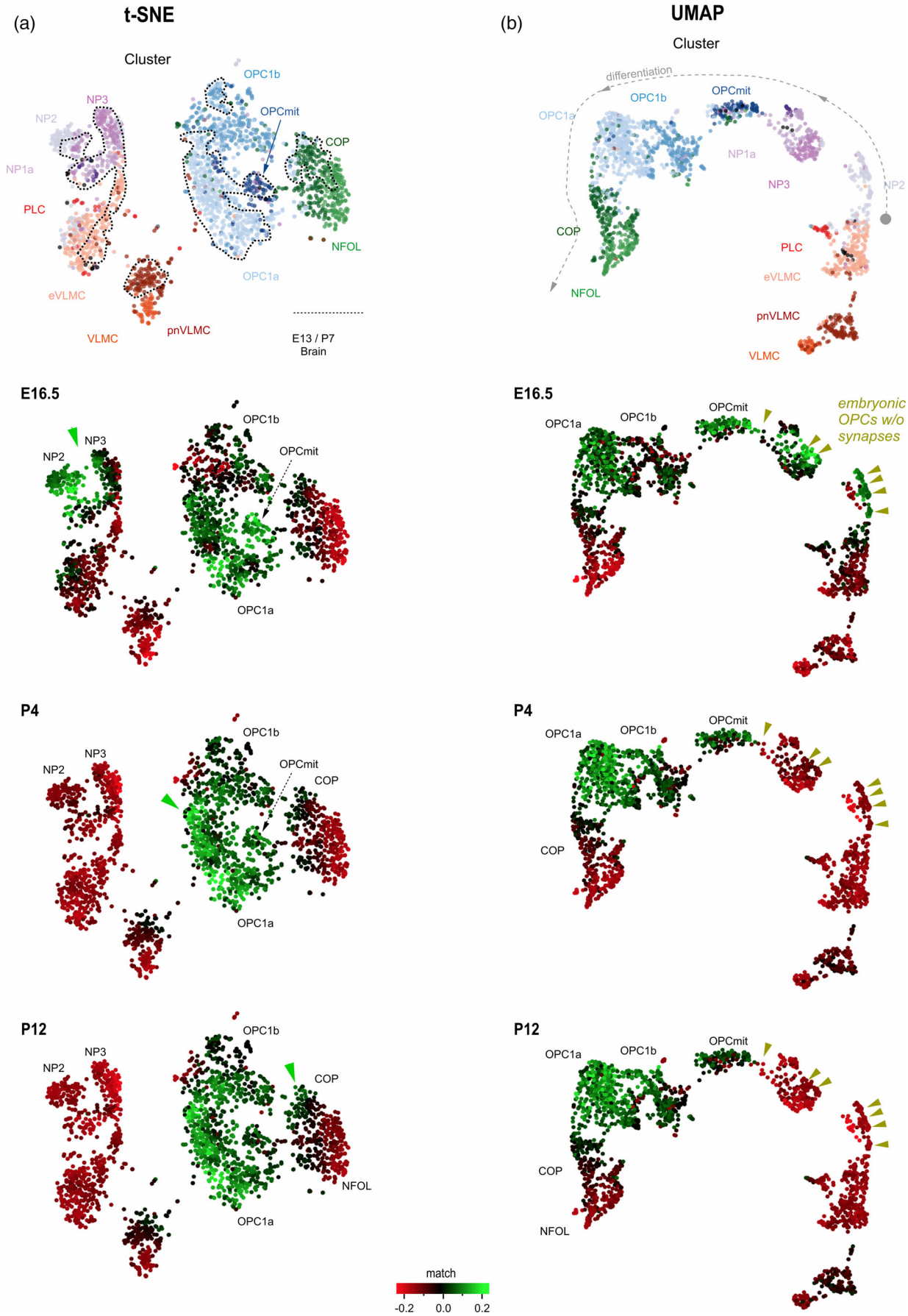

FIGURE 5 Legend on next page.

(Supplementary Figure 2a,b). Approximately half of the top 15 most highly expressed receptor genes were shared by OPCs and neurons whereas the other genes partly showed striking differences in expression. In particular, *Gria3*, *Gria1*, *Grik1*, *Chrna4*, *Gabrb3*, and *Gabrb2* were highly expressed in OPCs but only found in the lower half of all genes expressed in neurons. Conversely, *Grin2c*, *Grm3*, *Grm7*, and *Gabra4* were highly expressed in neurons but only found at lower levels in OPCs. For ion channels the most striking differences were observed for a number of calcium- and voltage-gated potassium channels and *Cacna2d4*, all highly expressed in neurons but not in OPCs whereas *Kcnj13*, *Cacna1a*, and *Kcnd3* were highly ranked in OPCs but not among the 50% most abundant genes in neurons.

The low frequency of synaptic currents in embryonic OPCs might be caused by an inability of those cells to connect to the presynaptic neurons. To investigate this hypothesis, we analyzed the expression of cell-adhesion molecules (CAMs), a broad class of molecules known to be important for synaptogenesis (Südhof, 2018), in our RNA-seq data (Supplementary Figure 3). This analysis revealed 162 DEGs out of 315 genes classified as CAMs, when comparing embryonic to P4 OPCs, levels of 104 genes increased and of 58 went down. We next classified the CAMs according to their localization at the synapse into postsynaptic, presynaptic, pre- and postsynaptic, and secreted and Supplementary Figure 3 shows the expression levels of all 315 genes. Supplementary Figure 4a depicts the regulation at the level of the four classes and demonstrates that all classes apart from presynaptic CAMs exhibited a strong increase in expression from E16.5 to P4 but only a mild or no up-regulation from P4 to P12 indicating that OPCs form functional postsynapses between E16.5 and P4. Panels c-f in Supplementary Figure 4 show the normalized expression for selected genes of each of the four classes. Among the 10 differentially expressed CAM genes showing the strongest developmental increase in abundance were the Glypican 5 (*Gpc5*, Supplementary Figures 3c and 4c), Contactin 6 and 4 (*Cntn6*, *Cntn4*, Supplementary Figures 3b and 4d), four Protocadherins (e.g., *Pcdha12*, *Pcdh20*, *Pcdhb5*, *Pcdh15*, Supplementary Figures 3b and 4d) as well as secreted CAMs, like two members of the Complement C1q Like family (*C1ql1*, *C1ql3*, Supplementary Figures 3a and 4e). In contrast, presynaptically localized CAMs showed little regulation during development (Supplementary Figures 3d and 4f).

We next also compared the abundance of genes coding for CAMs in OPCs (P12) to layer 2/3 cortical neurons (P33-35, Supplementary Figure 4b). In contrast to the receptors and ion channels analyzed above, the 15 most strongly expressed genes coding for CAMs belonged for both OPCs and neurons to the globally most abundant genes (above 95 percentile) and there were only few of the top 15 genes which were only weakly expressed in the other group. *Pcdh15* was the only top 15 OPC gene which showed low levels in neurons and *Sema4d*, *Fgf3*, and *Igsf8* were strongly expressed in neurons but not in OPCs.

Essential components of the postsynaptic signaling complex in neurons are the proteins that form the postsynaptic density (PSD). Throughout the three age groups we detected in OPCs most of the major scaffold and signaling proteins of CNS excitatory PSDs like membrane-associated guanylate kinases MAGUKs (*SAP97/Dlg1*, *PSD-93/Dlg2*, *SAP102/Dlg3*, *Dlg5*), guanylate kinase-associated protein (*GKAP/Dlgap1*), *SH3* and multiple ankyrin repeat domain proteins 1–3 (*Shank1-3*), *Homer1-3*, the Ca^{2+}-regulated serine–threonine Protein kinase *CaMKII*, *SynGAP*, *Anks1b/AIDA-1* and *IRSp53/BAIAP2* (Supplementary Figure 5a,b). The by far two most abundant PSD genes in P12 OPCs were the glycogen synthase kinase 3 beta (*Gsk3b*) and catenin beta (*Ctnnb1*), two proteins with roles in postsynaptic plasticity (Draffin et al., 2021) and transsynaptic signaling (Chen, Morrison, et al., 2017), respectively (Supplementary Figure 5a,b). Surprisingly, PSD95/Dlg4 was not found in OPCs although it represents the major scaffold protein in neuronal glutamatergic postsynapses. A comparison of P12 OPCs to cortical neurons (Supplementary Figure 5b) revealed that all top 15 PSD genes of OPCs were strongly expressed in neurons (above global 80 percentile). On the other hand, *Camk2a*, *Dnm2*, *Akap5*, *Abr*, and *Pak1* seemed to be quite specific for neurons and were found only at low levels in OPCs.

We took advantage of a published Single-Cell RNA sequencing (scRNA-seq) analysis of oligodendroglial and other cells from the brain and spinal cord (re-plotted on the left of Figure 5a, cf. Marques et al., 2018) to explore the likely cellular composition of our

FIGURE 5 Bulk transcriptomics of E16.5 OPCs matches SC clusters previously identified as NPs. Deconvolution of our bulk RNA-seq data using the Marques et al. (2018) scRNA-seq data. In the first row (a and b), each point indicates an individual cell analyzed by Marques et al. (2018) and is colored according to the cell cluster it was assigned to. Clusters are labeled as in Marques et al. (2018): NP (neural progenitor), PLC (pericyte lineage cell), e/pnVLMC (embryonic/postnatal vascular and leptomeningeal cell, OPC (oligodendrocyte precursor cell), OPCmit (mitotic OPC, previously called OPCcyc), COP (committed oligodendrocyte precursor cell) and NFOL (newly formed oligodendrocyte). Black cells labeled "Cycling cells" and intermingled with cells of several clusters in the original plot were omitted due to their small number. (a) tSNE coordinate space is reproduced from Marques et al. (2018) (see methods). Dotted lines demarcate regions containing cells derived from brain (E13/P7) versus spinal cord cells or cells from the juvenile to adult brain (outside dotted line). (b) Same as (a), however here the feature space plot of cells from the Marques et al. (2018) scRNA-seq data was determined using UMAP instead of tSNE. A gray dotted line with arrowheads indicates the starting point and direction of the putative OPC differentiation. Rows two, three and four in (a) and (b) color code for each cell in the Marques data set how well it is aligned to our bulk RNA samples obtained at E16.5, P4, and P12, respectively. The color of each point indicates the inferred abundance of individual cells from the Marques data set in our bulk RNA-seq samples, ranging from negative (red) to positive (green). Abundance levels are scaled and comparable across samples. The alignment of our E16.5 bulk RNA-seq data not only with OPC but also NP populations suggests that groups previously classified as NP might represent embryonic OPCs, which do not yet bear synapses. This putative group of cells is indicated by the dark-yellow arrowheads (arrowheads do not point at individual cells).

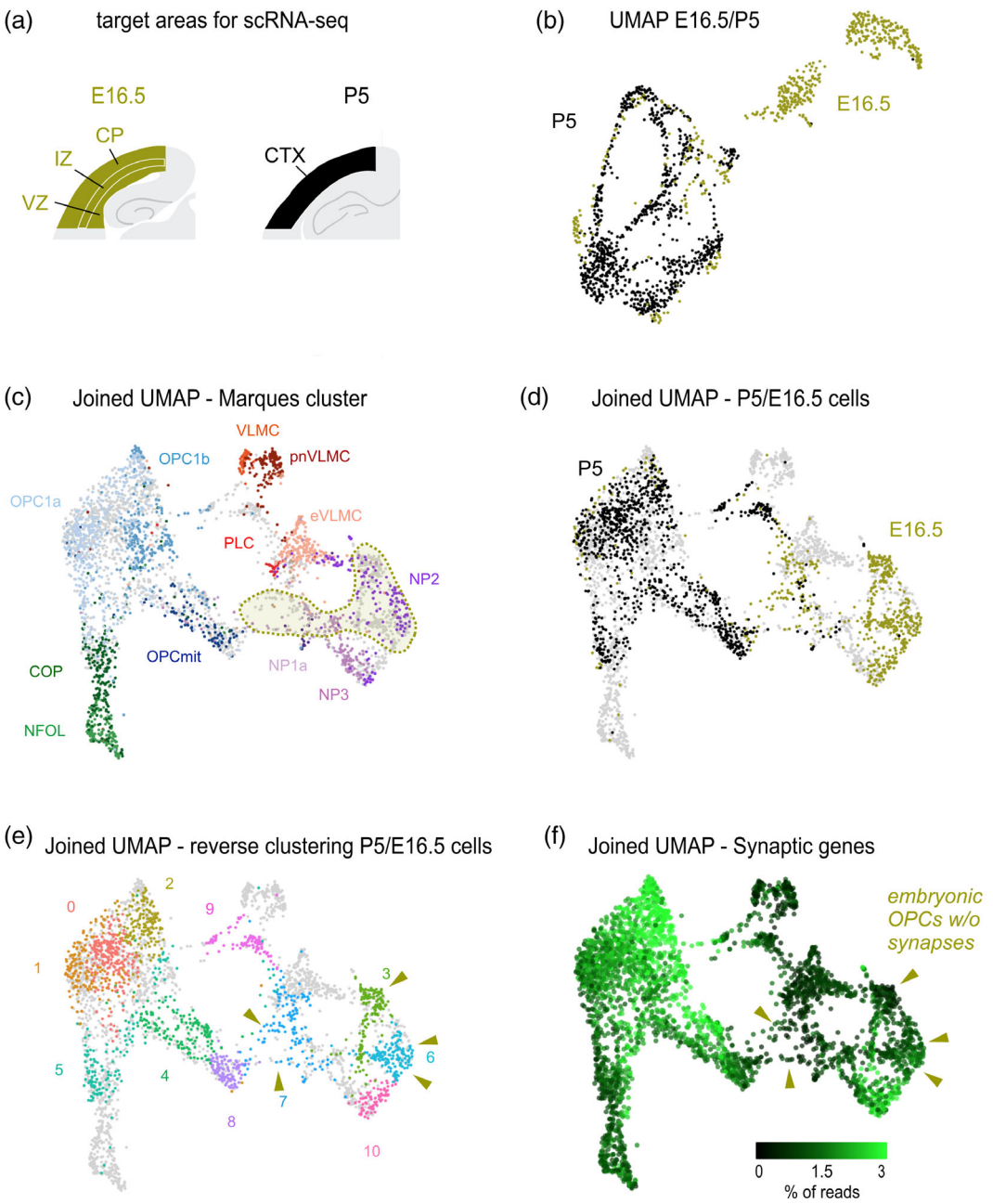

FIGURE 6 Single-cell transcriptomic analysis reveals that embryonic OPCs represent a unique developmental state with similarities to neuronal progenitors. (a) Schemes illustrating the brain areas dissected for collecting OPCs that underwent scRNA-seq. In both age groups OPCs were isolated from the isocortex (CTX), which at E16.5 consists of the cortical plate (CP), intermediate zone (IZ) and ventricular zone (VZ). (b) UMAP plot for the E16.5 (yellow) and P5 (black) PDGFRα^{+} cells harvested from regions shown in a. (c) Joint UMAP plot integrating our E16.5/P5 cells (in gray) and the E14, P7, P20-30, and P60 cells from Marques et al. (2018). Cells analyzed in our study are gray and in the background. Note that the overall architecture of the feature space plot is maintained compared to Figure 5b. (d) Same as in c but illustrating the distribution of our cells in the foreground according to age (E16.5 in yellow, P5 in black, cells from Marques et al. (2018) in gray and in the background). (e) Clusters of our cells reversely defined using E16.5/P5 cellular reductions of the joint UMAP. Note that these clusters demonstrate clear separation on our E16.5/P5 UMAP (d). Yellow arrowheads denote the group of cells likely representing embryonic OPCs without synapses (arrowhead do not point at individual cells). (f) The expression levels of 140 genes coding for synaptic proteins (CAMs, PSD, receptors, channels) ranging from low (black) to high (green) for each cell on the integrated UMAP graph are shown as the percentage of reads mapping to all 140 genes (Supplementary Table 3).

developmental data set. To this end, we deconvolved our bulk RNA-seq data with the previously published scRNA-seq data set (Marques et al., 2018) and labeled those cells green when their gene expression was aligned well with our average bulk sequencing data from E16.5, P4, and P12 (Figure 5a). This analysis confirmed that our cell population was not contaminated by non-oligodendroglial cells (vascular and

leptomeningeal cell ("VLMC"), pericyte lineage cell ("PLC") or newly formed oligodendrocytes ("NFOL") and showed a good alignment of our samples with OPCs harvested from the embryonic and postnatal brain but to a lesser extent with cells isolated from spinal cord (Figure 5a, dashed lines encircle cells of brain origin). Furthermore, this analysis revealed a clear developmental progression (denoted by the green arrowheads): the match of our samples progressed from the left of the tSNE-based feature space plot (E16.5), toward the right for P4 and P12. E16.5 samples shared few features with late OPCs (committed OPCs, "COP") for which an overlap was only seen in P12 samples (Figure 5a). "NFOL" did not show a match with any of our samples. Importantly, we observed for the E16.5 but not for the P4 or P12 samples a pronounced inferred abundance of cells within clusters previously called neural progenitors ("NP1-3") (Figure 5a green arrowhead at E16.5). This inspired us to re-explore cluster relationships by calculating a UMAP-based similarity matrix from the published data. UMAP has been demonstrated to be more reproducible and to better preserve the global structure of scRNA-seq data, making the inference of distances between cells and clusters more meaningful (Becht et al., 2019). When plotting using a UMAP-based feature space, the cell clusters previously defined were well maintained, but the "NP" clusters now were located close to the "OPC" clusters (Figure 5b). In addition, a linear path of putative OPC differentiation starting near the NP2 cluster became apparent and the non-oligodendroglial clusters ("VLMC", "PLC") were better separated from oligodendroglial clusters (Figure 5b, left panel, gray dashed line). The existence of this path was supported by a gradual transition and emergence of well-aligned, "green" cells from right to left in our deconvolved RNA-seq samples from E16.5, P4, and P12, respectively (Figure 5b, right panels). This developmental progression was also observed within the E16.5 group (likely due to some unavoidable variability in the time between conception and sample preparation). Reorganization of these individual samples according to their similarity to the P12 group revealed a gradual conversion toward P4 (Supplementary Figure 6a) and a decreasing enrichment of cells belonging to the NP clusters. Supplementary Figure 6b shows how the large variability in the E16.5 samples converges onto the P4 samples and that the variability within the P4 and the P12 group was much lower, indicating a more homogenous transcriptional profile of cells of the postnatal samples.

This suggested that cells belonging to the "NP" clusters may not be "neural progenitors" but instead represent early OPCs and potentially the starting point for early oligodendroglial development. The finding that cells of "NP" clusters selectively aligned well to our E16.5 samples and that our physiological analysis showed that OPCs without synaptic input also only occurred in the E16.5 group suggested that those "NP" cell clusters corresponded to embryonic OPCs lacking synaptic input (Figure 5b). The cluster "OPC1a, OPC1b" and "OPCmit" were also well aligned with our E16.5 data set and we assumed that those cells represented OPCs from brain regions which at E16.5 contain OPCs which already had developed further and established synapses. For example, in cerebellum and spinal cord, regions at least partially contained in our samples, OPCs start to differentiate around birth whereas differentiation only occurs approximately 1 week later in the rodent cortex (Cristobal & Lee, 2022; Reynolds & Wilkin, 1988; Trapp et al., 1997).

Apart from the regional heterogeneity of the OPCs in our bulk samples, a weakness of the deconvolution approach is that while it shows how a bulk sample can potentially be explained by a certain combination of cells from a SC data set, it cannot prove that the bulk sample indeed contained individual cells which express the set of genes from a given cell of the scRNA-seq data set.

To avoid the regional heterogeneity and overcome the limitations of the deconvolution approach we micro-dissected similar regions used for our electrophysiological analysis (cortical plate/intermediate layer at E16.5 and cortex at P5; Figure 6a, cf Figure 1a), isolated OPCs and subjected them to scRNA-seq (see methods for details). After initial processing, we obtained 562 (E16.5) and 986 (P5) cells, which predominantly separated on a UMAP plot by developmental time (Figure 6b) confirming the transcriptional differences between developmental states reported above.

We next directly integrated our scRNA-seq data with that of Marques et al. (2018) and calculated a UMAP-based cellular feature space to determine the joint cellular neighborhoods of our cells with Marques cells (Figure 6c,d). Although the precise arrangement of cells was expected to deviate from the original Marques UMAP with inclusion of two additional time points (E16.5 and P5), the overall preservation of global cellular locations, and in particular the direction of differentiation from right to left and to the bottom, indicated a high consistency of the two data sets. The vast majority of our E16.5 OPCs were grouped with the NP annotated clusters (Figure 6c,d), previously identified as neural progenitor cells (Marques et al., 2018) and supporting our view derived from the bulk RNA-seq data analysis that many cells of the NP clusters in fact represent early embryonic OPCs. In contrast, OPCs from P5 tissue were solely found within the OPC1a/b, OPCmit and COP clusters. Based on this UMAP (Figure 6d) we performed a reverse clustering of our data (Figure 6e). These clusters superimposed well onto many of the clusters defined by Marques et al. (2018) (Figure 6c,e). To explore which cells might be or have the potential to be engaged in synaptic signaling we quantified the expression levels of synaptic genes across all cells. We curated a list of 140 genes based on the most abundantly expressed synaptic CAMs (50), PSD proteins (40) and receptors/ion channels (50) in the P4 group of our bulk RNA-seq data from above (Figure 4d–k, Supplementary Figures 3–5, see methods for details). The integrated cell space in Figure 6f shows that in cells from both data sets, Marques et al. (2018) and ours, synaptic genes at high levels are predominantly found in the OPC clusters (OPC1a/b, OPCmit largely corresponding to 0, 1, 2, 4, 8). In contrast, clusters from our E16.5 group in proximity to the NP clusters (cluster 3, 6 and 7; Figure 6c–e) demonstrated lower levels of synaptic gene expression. Our E16.5 cluster 10, which partially overlaps with NP2 and NP3, represented a notable exception and displayed high levels of synaptic gene expression. Overall, considering that embryonic OPCs did not, or only very rarely, show functional synaptic currents and that these cells did not cluster with postnatal OPCs but rather group with NP cells, supports a view that they represent a distinct developmental stage of embryonic OPCs without synapses. The

location of cells coding for expression levels of synaptic genes (Figure 6f) not only showed a gradient of increased expression from embryonic to mature OPCs but also a decline in expression when OPCs further differentiate into COPs and NFOL. The latter is in agreement with previous electrophysiological observations showing that differentiating oligodendroglial cells loose synaptic input from neurons (Biase et al., 2010; Kukley et al., 2010).

We did not observe OPCs without synapses in the postnatal period (Kukley et al., 2008, 2010) opening the question whether embryonic OPCs without synapses mostly die before the postnatal period, possibly because synaptic innervation is needed for their survival. Indeed, it was reported that many of the OPCs which were generated in the embryonic brain disappear from the cortex during the first postnatal week (Kessaris et al., 2006). OPCs rapidly disappearing in the early postnatal period are derived from NKx2.1-expressing precursors, whereas surviving OPCs stem from precursors expressing Gsh2 or Emx1 (Kessaris et al., 2006). Emx1 is present in cells of the E16-18 intermediate zone (Briata et al., 1996; Gulisano et al., 1996) and these progenitors generate a large proportion (Kessaris et al., 2006) if not most (Winkler et al., 2018) of the postnatal and embryonic oligodendroglial cells. To check whether our embryonic OPCs may belong to the surviving or disappearing fraction we analyzed the Emx1, Gsh2 and NKx2.1 expression in our embryonic and postnatal OPCs. While none of the markers were expressed in P5 OPCs, expression of Emx1 but not Gsh2 or NKx2.1 was found within clusters 3 and 6 (Supplementary Figure 7) suggesting that embryonic OPCs lacking synapses derive from the NP clusters 3, 6, and 7 or even overlap (cluster 3 and 6) with Emx1 expressing precursors and very likely survive into the postnatal period thereby contributing to the cortical oligodendroglial progeny by further expansion and differentiation.

4 | DISCUSSION

In this study, we found that the synaptic input to embryonic (E18.5) OPCs is at least ~3–10 times weaker compared to P7-14 OPCs. At the molecular level our RNA-seq analyses revealed that the overall abundance of genes coding for the postsynaptic signaling complex/apparatus is much lower at E16.5 than at P4 and P12 (also see Marques et al., 2018). The comparison of our bulk- and scRNA-seq to a previously published scRNA-seq data (Marques et al., 2018) suggests that embryonic OPCs without synaptic input form a transcriptionally distinct group of precursor cells at the beginning of the developmental trajectory of the oligodendroglial lineage. We propose that these cells represent a unique developmental stage that is not yet receptive for synapses from neurons because the required transcriptional programs are not yet activated to the full extent. The data also show that pronounced proliferation and migration of OPCs occur in the absence of synaptic input.

Synaptic input has been reported in almost all hippocampal OPCs examined so far (Biase et al., 2010; Kukley et al., 2008, 2010). However, these measurements were performed only in postnatal OPCs, ranging from P4-5 (Biase et al., 2010; Kukley et al., 2008) up to old age (Passlick et al., 2016; Ziskin et al., 2007). Here, we show for the first time that embryonic OPCs almost completely lack synaptic input. Considering the relatively small size of E18.5 OPCs the question arises whether their smaller surface area could explain the reduced frequency of synaptic currents. However, when correcting for the smaller dendritic arbor as well as the frequency, amplitude and charge of synaptic currents, the synaptic drive of OPCs remains negligible and dramatically smaller than at postnatal stages.

What causes the lower frequency of synaptic currents in embryonic versus postnatal OPCs? One reason for the low frequency of mPSCs detected in embryonic OPCs could be that at this stage of brain development synaptic transmission in general is not sufficiently mature. However, this is not the case as it has been shown that cortical neurons already at E16 receive functional glutamatergic and GABA-ergic synaptic contacts (Kilb et al., 2011). This is consistent with our immunohistochemical analysis of the synaptic vesicle marker protein (SV2B) which we found widely distributed throughout the embryonic brain. Therefore, it appears that there is not a general inability to establish synapses in the embryonic period but that embryonic OPCs do not have the capacity to receive synaptic connections or that embryonic OPCs are not suitable synaptic targets for neurons. Because the mPSCs, which we quantified in the presence of TTX, reflect synaptic vesicle release independent of presynaptic action potentials, the reduced frequency of mPSCs can be considered an indicator of the number of functional synapses (assuming a uniform spontaneous vesicle release rate in Ruthenium Red). Thereby, our functional data indicate that embryonic OPCs have fewer functional synaptic contacts compared to postnatal ones (also when correcting for shorter dendrites).

The mPSCs in embryonic OPCs were not only extremely rare but also showed substantially smaller amplitudes. A potential reason for smaller amplitudes may be a much lower density of postsynaptic glutamate and GABA receptors at this early developmental stage compared to postnatal time points. On the other hand, our transcriptomics analysis showed that several glutamate and GABA receptor subunits are already expressed at E16.5. Furthermore, Spitzer et al. (2019 pharmacologically activated glutamate receptors on E18 OPCs and reported current densities (amplitudes divided by cell capacitance) comparable to a group of postnatal OPCs (P6-P16). This suggests that not the total number of glutamate receptors is the factor limiting the amplitude of synaptic currents but their distribution. If receptors are spread over the entire surface of OPCs they will be activated when applying agonists to the whole membrane but they may not be sufficiently concentrated at those synaptic contact sites where neurons locally release neurotransmitter-filled vesicles. Such apparent lack of clustering of neurotransmitter receptors around synaptic release sites may be a consequence of the immature expression pattern of genes coding for postsynaptic cell adhesion molecules in embryonic OPCs (Supplementary Figure 4, also see Marques et al., 2018). In summary, together with Spritzer et al. (2019) and Marques et al. (2018) our findings indicate an almost complete absence of synaptic connections between neurons and OPCs in the embryonic

brain and suggest that the existing very rare synaptic connections contain very few receptors only.

Could there be a functional relevance of the electrophysiological phenotype of embryonic OPCs which is characterized by a different set of ion channels and almost absent synaptic input? Postnatal OPCs express a large number of voltage-gated ion channels, including Na^+, K^+, and Ca^{2+} channels (Figures 3 and 4; Biase et al., 2010; Haberlandt et al., 2011; Maldonado et al., 2013; Spitzer et al., 2019), and these ion channels could actively participate in the synaptic integration of OPCs (Sun & Dietrich, 2013). It was previously shown that A-type K^+ currents strictly gate synaptic integration and the following Ca^{2+} signaling through the rapid suppression of post-synaptic depolarization (Sun et al., 2016). Here, we showed that embryonic OPCs are resting at a more depolarized potential and this depolarization will partially inactivate A-type K^{+-}currents, which are already found at significantly lower levels in embryonic compared to postnatal OPCs (but see Spitzer et al., 2019). Therefore, an A-type K^+-current-induced gating effect will be largely absent in embryonic OPCs and their dendrites could more readily generate calcium signals in response to synaptic input. In fact, we found substantial levels of mRNA encoding the alpha subunits of T-, R- and N-type calcium channels (*Cacna1h*, *b*, *e*) in embryonic OPCs (also see Marques et al., 2018), which mediate synaptically-induced calcium signaling in postnatal OPCs (Sun et al., 2016). However, as synaptic input to embryonic OPCs is so small, it is quite unlikely that those calcium responses will be triggered at E18.5. But once these cells further develop and establish their first synaptic connections, they are set for dendritic calcium signaling.

Dendritic complexity of OPCs strongly increased from E18.5 to P7 as did the area covered by individual OPCs. During this phase of intense dendritic growth OPCs need to map out their space with regard to other OPCs and to neurons, a process that requires the expression of cell adhesion molecules and guidance receptors. Fittingly, our and previous analyses of bulk RNA-seq data comparing embryonic to postnatal OPCs showed an up-regulation of GO terms related to cell adhesion, cell communication as well as synapse and a down-regulation of terms linked to brain development and neuron migration at the postnatal stage (Marques et al., 2018; Spitzer et al., 2019). Our comprehensive analysis of the developmental transcriptional profile of cell adhesion molecules supports the involvement of several proteins which have been reported to play a role in dendritic outgrowth and pathfinding of OPCs, like ephrins and EphA/B receptors (Harboe et al., 2018; Linneberg et al., 2015), NCAM (Harboe et al., 2018; Oumesmar et al., 1995), L1-CAM (Laursen et al., 2009), Cadm/SynCAM/IGSF (Elazar et al., 2019; Hughes & Appel, 2019), FGFR2 (Furusho et al., 2012), Teneurin-4 (Hayashi et al., 2020), plexin-A4/−A3 (Okada et al., 2007; Xiang et al., 2012), contactin-1 (Lamprianou et al., 2011), and Nrg2/3 (Vartanian et al., 1999) as their expression levels strongly differ between embryonic and postnatal OPCs. Our data however goes a step further by identifying differentially expressed genes coding for cell adhesion molecules that have so far not been linked to OPC development, for example Cadherin EGF LAG seven-pass G-type receptor (*Celsr*) and complement C1q Like (*C1ql*), as well as novel isoforms of the above listed protein families (e.g. Ephrins, contactins, protocadherins, plexins). In particular, we for the first time identify cell adhesion molecules whose expression level is strongly up-regulated during the period of neuron—OPC synaptogenesis, suggesting a role in this process, which previously have only been studied in neurons, like *LRRTM3*, *GRID1*/2, and *Cntnap5* (Südhof, 2021). Interestingly, also Neuroligin 3 which has been reported to be up-regulated during brain tumor growth (Venkatesh et al., 2015, 2017) increases in expression during the phase of synaptogenesis supporting its role in normal neuron—OPC function but also indicating that its abundance needs to be tightly controlled. Overall, our systematic analysis provides a resource for further studies into the molecular mechanisms underlying dendritic outgrowth and synapse formation of OPCs.

Our comparative analysis of our bulk RNA-seq and the Marques et al. (2018) scRNA-seq data sets lead us to suggest that some clusters previously classified as neural precursors (part of NP2 and NP1a) represent an early stage of OPC development, a stage of OPCs lacking synapses (cluster 3, 6, 7). This suggestion was based on the following observations: (1) Our E16.5 bulk RNA-seq sample obtained from the whole brain using anti-PDGFRα-based cell isolation showed a pronounced alignment with the NP clusters. (2) Replotting the previously published data set as a UMAP removed the gap previously seen between NP and OPC clusters and brought the NP clusters closer to the OPCmit cluster and this neighborhood indicates transcriptional similarity. (3) PDGFRα-expressing cells in the cortical plate and intermediate zone at E18.5 also express NG2 (Figure 1) and $NG2^+$ cells in that region do not express neural precursors markers (Tognatta et al., 2017) which indicate that those cells represent OPCs. These cells were used for our scRNA-seq sample and they almost exclusively mapped onto the NP clusters. (4) Our patch-clamp analysis of NG2-DsRed+, $NG2^+$ and $PDGFR\alpha^+$ cells in the intermediate zone at E18.5 demonstrated that those cells are morphologically very related to postnatal OPCs (Figure 2) and show a very similar pattern of ion channel expression (Figure 3) which further supports the view that the E16.5 isolated embryonic OPCs which overlap with NP clusters indeed represent early OPCs. On the other hand, it appears likely that not all cells contained in the NP clusters defined by Marques et al. (2018) represent early OPCs. This can best be seen in the NP3 cluster which only showed minimal overlap with our E16.5 cells. Also, our E16.5 data set seems to contain a small number of cells not compatible with embryonic OPCs lacking synapses: cluster 10, overlapping with parts of NP2 and parts of NP3 (Figure 6) showed a strong expression of synaptic genes not expected from OPCs without synapses. Therefore, the composition of the NP clusters likely is heterogeneous and may include both neural precursor cells and early OPCs. Their proximity in all feature space plots (UMAP and t-SNE) strongly indicates that neural precursors and early OPCs exhibit a similar transcriptional profile at least for certain prominent subsets of genes. Further, considering that the early neural and oligodendroglial developments are tightly linked (Bergles & Richardson, 2016), it may well be that either NP cells and early OPCs derive from the same

progenitor or that early OPCs (Emx1^{+}) even directly arise from cells of the NP clusters. The close transcriptional relationship of OPCs, early OPCs and neural or intermediate progenitors has been well documented (Hochgerner et al., 2018; Manno et al., 2021; Weng et al., 2019; Yuzwa et al., 2017).

There are important differences in the approaches taken by the previous and this study to isolate cells for RNA-seq analysis: While we used antibodies fused to magnetic beads to isolate PDGFRα-expressing cells from the dorsal cortical area of E16.5 brains, Marques et al. (2018) relied on the expression of fluorescent marker proteins in two different transgenic mouse lines to isolate cells five days earlier from E13.5 brains. A Pdgfra promoter drove either Cre-Recombinase (Cre) or nuclear GFP-expression and Cre activity was induced at E12. Kessaris et al. (2006), Nishiyama et al. (1996), Winkler et al. (2018) reported that the first PDGFRα-immunoreactive cells in the dorsal forebrain are not found before E16 but neural stem cells express Pdgfra earlier in development (Funa & Sasahara, 2014; Pringle & Richardson, 1993). This may explain a preference for isolating those cells in the NP clusters representing true neural precursor cells versus embryonic OPCs in the Marques and the present study, respectively.

Our electrophysiological recordings were obtained from mice at E18.5, 2 days later than the time of isolation of our cells for the transcriptional analysis (E16.5) opening the question how representative our transcriptomics data is for the stage of the cells when physiologically analyzed. It was previously shown that the transcriptional signatures of glial precursors only slightly changed from E16 to E18 (Manno et al., 2021) and more specifically that OPCs harvested at E17.5 still mapped well to OPC and NP clusters of cells harvested much earlier at E13.5 (Marques et al., 2018). We therefore argue that the results of our transcriptomic analysis can be reasonably well compared to our physiological OPC data recorded 2 days later. Nevertheless, we admit that we do not have direct evidence showing how representative our transcriptomic data is for the time point at which we patch-clamped embryonic OPCs and this represents a weakness of our study.

In summary, our data reveals that the earliest embryonic OPCs are physiologically and morphologically similar to postnatal OPCs but lack the typical synaptic input from neurons. Embryonic OPCs do not sufficiently express genes for postsynaptic signal reception and processing and are therefore not yet receptive for connections from neurons. Furthermore, the data demonstrates that embryonic OPCs do not need synapses to proliferate or migrate in the embryonic brain.

During early development of zebrafish two subgroups of OPCs were identified (Marisca et al., 2020), which share features with postnatal and embryonic OPCs observed in this study. One group defined by their position being in the neuronal somata-rich area displayed a complex dendritic tree, proliferated slowly, expressed synaptic genes and generated stronger calcium signals in response to neural activity and can be viewed to correspond to our postnatal cortical OPCs. Another group being placed in the neurite and dendrite-rich areas showed a simple morphology, enriched genes for mitosis and migration, rapidly divided and only weakly responded to neuronal activity and thus seems to be more comparable to embryonic OPCs lacking synapses. These similarities may be taken to suggest an analogy between the two types of OPCs across species. However, there are a number of important differences. While the two subgroups of OPCs coexist in the larval brain of zebrafish, our embryonic OPCs and classical OPCs in the mouse were almost exclusively observed embryonically and postnatally, respectively. Further, while OPCs in the neurite/dendrite-rich area generated most oligodendrocytes in zebrafish, this is not the case for embryonic OPCs in the mouse because the first oligodendrocytes in rodent cortex and corpus callosum only appear after the first postnatal week (Trapp et al., 1997). Finally, both subgroups of OPCs in zebrafish showed a clear, classical OPC transcriptional signature whereas that was clearly not the case for our group of embryonic OPCs. Future studies are needed to explore to which extent the different subgroups of OPCs correspond across species and whether they have similar roots or functions in the brain.

It should be noted that the lack of synapses does not rule out that ambient neurotransmitters influence the development of embryonic OPCs in a non-synaptic manner nor that synaptic input may guide these processes during later developmental stages. Nevertheless, in our eyes the present data support the view that these synaptic one-to-one connections tune the early and local interaction between processes of OPCs and unmyelinated axons (Call et al., 2020; Paez & Lyons, 2020).

AUTHOR CONTRIBUTIONS

All authors contributed to writing this manuscript.

ACKNOWLEDGMENTS

Our work was supported by the Deutsche Forschungsgemeinschaft (DFG) (SS: SFB1089, SCHO 820/4-7, SPP1757; DD: SFB1089, SPP1757, INST1172 15, DI853/3-5&7, INST 217/785-1) and the BONFOR program of the Faculty of Medicine of Bonn University (SS, DD). We acknowledge the support of PRECISE—Platform for Single-Cell Genomics and Epigenomics (University of Bonn and the German Center for Neurodegenerative Diseases (DZNE) and of the Next Generation Sequencing Core Facility (Medical Faculty at the University of Bonn). Special thanks to Shane McGee McMahon for providing practical support on two-photon microscopy. We would like to thank Jessica Klemmer, Sabine Opitz and Julia Kaspari for their excellent technical assistance. Open Access funding enabled and organized by Projekt DEAL.

CONFLICT OF INTEREST STATEMENT

The authors declare no conflict of interests.

DATA AVAILABILITY STATEMENT

The data that support the findings of this study are available from the corresponding authors upon reasonable request.

ORCID

Wenjing Sun https://orcid.org/0000-0002-0905-7420
Susanne Schoch https://orcid.org/0000-0002-2046-2670

REFERENCES

Babicki, S., Arndt, D., Marcu, A., Liang, Y., Grant, J. R., Maciejewski, A., & Wishart, D. S. (2016). Heatmapper: Web-enabled heat mapping for all. *Nucleic Acids Research*, *44*(W1), W147–W153. https://doi.org/10.1093/nar/gkw419

Becht, E., McInnes, L., Healy, J., Dutertre, C.-A., Kwok, I. W. H., Ng, L. G., Ginhoux, F., & Newell, E. W. (2019). Dimensionality reduction for visualizing single-cell data using UMAP. *Nature Biotechnology*, *37*(1), 38–44. https://doi.org/10.1038/nbt.4314

Bergles, D. E., & Richardson, W. D. (2016). Oligodendrocyte development and plasticity. *Cold Spring Harbor Perspectives in Biology*, *8*(2), a020453. https://doi.org/10.1101/cshperspect.a020453

Bergles, D. E., Roberts, J. D., Somogyi, P., & Jahr, C. E. (2000). Glutamatergic synapses on oligodendrocyte precursor cells in the hippocampus. *Nature*, *405*(6783), 187–191. https://doi.org/10.1038/35012083

Berret, E., Barron, T., Xu, J., Debner, E., Kim, E. J., & Kim, J. H. (2017). Oligodendroglial excitability mediated by glutamatergic inputs and Nav1.2 activation. *Nature Communications*, *8*(1), 557. https://doi.org/10.1038/s41467-017-00688-0

Biase, L. M. D., Biase, L. M. D., Nishiyama, A., Nishiyama, A., Bergles, D. E., & Bergles, D. E. (2010). Excitability and synaptic communication within the oligodendrocyte lineage. *Journal of Neuroscience*, *30*(10), 3600–3611. https://doi.org/10.1523/jneurosci.6000-09.2010

Briata, P., Blas, E. D., Gulisano, M., Mallamaci, A., Iannone, R., Boncinelli, E., & Corte, G. (1996). EMX1 homeoprotein is expressed in cell nuclei of the developing cerebral cortex and in the axons of the olfactory sensory neurons. *Mechanisms of Development*, *57*(2), 169–180. https://doi.org/10.1016/0925-4773(96)00544-8

Call, C. L., Biase, L. M. D., & Bergles, D. E. (2020). Patterning and cell type specification in the developing CNS and PNS. *Comprehensive Developmental Neuroscience*, 891–918. https://doi.org/10.1016/b978-0-12-814405-3.00036-9

Calver, A. R., Hall, A. C., Yu, W.-P., Walsh, F. S., Heath, J. K., Betsholtz, C., & Richardson, W. D. (1998). Oligodendrocyte population dynamics and the role of PDGF In vivo. *Neuron*, *20*(5), 869–882. https://doi.org/10.1016/s0896-6273(00)80469-9

Chen, C., Chen, Y., Wang, J., Huang, Y., & Tai, C. (2017). Postsynaptic Y654 dephosphorylation of β-catenin modulates presynaptic vesicle turnover through increased n-cadherin-mediated transsynaptic signaling. *Developmental Neurobiology*, *77*(1), 61–74. https://doi.org/10.1002/dneu.22411

Chen, V. S., Morrison, J. P., Southwell, M. F., Foley, J. F., Bolon, B., & Elmore, S. A. (2017). Histology atlas of the developing prenatal and postnatal mouse central nervous system, with emphasis on prenatal days E7.5 to E18.5. *Toxicologic Pathology*, *45*(6), 705–744. https://doi.org/10.1177/0192623317728134

Chittajallu, R., Aguirre, A., & Gallo, V. (2004). NG2-positive cells in the mouse white and grey matter display distinct physiological properties. *The Journal of Physiology*, *561*(1), 109–122. https://doi.org/10.1113/jphysiol.2004.074252

Cristobal, C. D., & Lee, H. K. (2022). Development of myelinating glia: An overview. *Glia*, *70*(12), 2237–2259. https://doi.org/10.1002/glia.24238

Draffin, J. E., Sánchez-Castillo, C., Fernández-Rodrigo, A., Sánchez-Sáez, X., Ávila, J., Wagner, F. F., & Esteban, J. A. (2021). GSK3α, not GSK3β, drives hippocampal NMDAR-dependent LTD via tau-mediated spine anchoring. *The EMBO Journal*, *40*(2), e105513. https://doi.org/10.15252/embj.2020105513

Eden, E., Navon, R., Steinfeld, I., Lipson, D., & Yakhini, Z. (2009). GOrilla: A tool for discovery and visualization of enriched GO terms in ranked gene lists. *BMC Bioinformatics*, *10*(1), 48. https://doi.org/10.1186/1471-2105-10-48

Elazar, N., Vainshtein, A., Golan, N., Vijayaragavan, B., Schaeren-Wiemers, N., Eshed-Eisenbach, Y., & Peles, E. (2019). Axoglial adhesion by Cadm4 regulates CNS myelination. *Neuron*, *101*(2), 224–231.e5. https://doi.org/10.1016/j.neuron.2018.11.032

Fields, R. D., Dutta, D. J., Belgrad, J., & Robnett, M. (2017). Cholinergic signaling in myelination. *Glia*, *65*(5), 687–698. https://doi.org/10.1002/glia.23101

Foster, A. Y., Bujalka, H., & Emery, B. (2019). Axoglial interactions in myelin plasticity: Evaluating the relationship between neuronal activity and oligodendrocyte dynamics. *Glia*, *67*(11), 2038–2049. https://doi.org/10.1002/glia.23629

Frishberg, A., Peshes-Yaloz, N., Cohn, O., Rosentul, D., Steuerman, Y., Valadarsky, L., Yankovitz, G., Mandelboim, M., Iraqi, F. A., Amit, I., Mayo, L., Bacharach, E., & Gat-Viks, I. (2019). Cell composition analysis of bulk genomics using single-cell data. *Nature Methods*, *16*(4), 327–332. https://doi.org/10.1038/s41592-019-0355-5

Funa, K., & Sasahara, M. (2014). The roles of PDGF in development and during neurogenesis in the Normal and diseased nervous system. *Journal of Neuroimmune Pharmacology*, *9*(2), 168–181. https://doi.org/10.1007/s11481-013-9479-z

Furusho, M., Dupree, J. L., Nave, K.-A., & Bansal, R. (2012). Fibroblast growth factor receptor signaling in oligodendrocytes regulates myelin sheath thickness. *The Journal of Neuroscience*, *32*(19), 6631–6641. https://doi.org/10.1523/jneurosci.6005-11.2012

Gao, F.-B., & Raff, M. (1997). Cell size control and a cell-intrinsic maturation program in proliferating oligodendrocyte precursor cells. *The Journal of Cell Biology*, *138*(6), 1367–1377. https://doi.org/10.1083/jcb.138.6.1367

Ge, W.-P., Zhou, W., Luo, Q., Jan, L. Y., & Jan, Y. N. (2009). Dividing glial cells maintain differentiated properties including complex morphology and functional synapses. *Proceedings of the National Academy of Sciences*, *106*(1), 328–333. https://doi.org/10.1073/pnas.0811353106

Gibson, E. M., Purger, D., Mount, C. W., Goldstein, A. K., Lin, G. L., Wood, L. S., Inema, I., Miller, S. E., Bieri, G., Zuchero, J. B., Barres, B. A., Woo, P. J., Vogel, H., & Monje, M. (2014). Neuronal activity promotes oligodendrogenesis and adaptive myelination in the mammalian brain. *Science*, *344*(6183), 1252304. https://doi.org/10.1126/science.1252304

Griffiths, J. A., Richard, A. C., Bach, K., Lun, A. T. L., & Marioni, J. C. (2018). Detection and removal of barcode swapping in single-cell RNA-seq data. *Nature Communications*, *9*(1), 2667. https://doi.org/10.1038/s41467-018-05083-x

Gulisano, M., Broccoli, V., Pardini, C., & Boncinelli, E. (1996). Emx1 and Emx2 show different patterns of expression during proliferation and differentiation of the developing cerebral cortex in the mouse. *European Journal of Neuroscience*, *8*(5), 1037–1050. https://doi.org/10.1111/j.1460-9568.1996.tb01590.x

Haberlandt, C., Derouiche, A., Wyczynski, A., Haseleu, J., Pohle, J., Karram, K., Trotter, J., Seifert, G., Frotscher, M., Steinhäuser, C., & Jabs, R. (2011). Gray matter NG2 cells display multiple Ca2+-signaling pathways and highly motile processes. *PLoS One*, *6*(3), e17575. https://doi.org/10.1371/journal.pone.0017575.s006

Hafemeister, C., & Satija, R. (2019). Normalization and variance stabilization of single-cell RNA-seq data using regularized negative binomial regression. *Genome Biology*, *20*(1), 296. https://doi.org/10.1186/s13059-019-1874-1

Hao, Y., Hao, S., Andersen-Nissen, E., Mauck, W. M., Zheng, S., Butler, A., Lee, M. J., Wilk, A. J., Darby, C., Zager, M., Hoffman, P., Stoeckius, M., Papalexi, E., Mimitou, E. P., Jain, J., Srivastava, A., Stuart, T., Fleming, L. M., Yeung, B., … Satija, R. (2021). Integrated analysis of multimodal single-cell data. *Cell*, *184*(13), 3573–3587.e29. https://doi.org/10.1016/j.cell.2021.04.048

Harboe, M., Torvund-Jensen, J., Kjaer-Sorensen, K., & Laursen, L. S. (2018). Ephrin-A1-EphA4 signaling negatively regulates myelination in the central nervous system. *Glia*, *66*(5), 934–950. https://doi.org/10.1002/glia.23293

Hayashi, C., Suzuki, N., Mabuchi, Y., Kikura, N., Hosoda, Y., Vega, S. d., & Akazawa, C. (2020). The extracellular domain of teneurin-4 promotes cell adhesion for oligodendrocyte differentiation. *Biochemical and Biophysical Research Communications*, *523*(1), 171–176. https://doi.org/10.1016/j.bbrc.2019.12.002

Hochgerner, H., Zeisel, A., Lönnerberg, P., & Linnarsson, S. (2018). Conserved properties of dentate gyrus neurogenesis across postnatal development revealed by single-cell RNA sequencing. *Nature Neuroscience*, *21*(2), 290–299. https://doi.org/10.1038/s41593-017-0056-2

Hughes, A. N., & Appel, B. (2019). Oligodendrocytes express synaptic proteins that modulate myelin sheath formation. *Nature Communications*, *10*(1), 4125. https://doi.org/10.1038/s41467-019-12059-y

Káradóttir, R., Hamilton, N. B., Bakiri, Y., & Attwell, D. (2008). Spiking and nonspiking classes of oligodendrocyte precursor glia in CNS white matter. *Nature Neuroscience*, *11*(4), 450–456. https://doi.org/10.1038/nn2060

Káradóttir, R. T., & Kuo, C. T. (2016). Neuronal activity-dependent control of postnatal neurogenesis and gliogenesis. *Annual Review of Neuroscience*, *41*(1), 1–23. https://doi.org/10.1146/annurev-neuro-072116-031054

Kessaris, N., Fogarty, M., Iannarelli, P., Grist, M., Wegner, M., & Richardson, W. D. (2006). Competing waves of oligodendrocytes in the forebrain and postnatal elimination of an embryonic lineage. *Nature Neuroscience*, *9*(2), 173–179. https://doi.org/10.1038/nn1620

Kilb, W., Kirischuk, S., & Luhmann, H. J. (2011). Electrical activity patterns and the functional maturation of the neocortex. *European Journal of Neuroscience*, *34*(10), 1677–1686. https://doi.org/10.1111/j.1460-9568.2011.07878.x

Koopmans, F., Van Nierop, P., Andres-Alonso, M., Byrnes, A., Cijsouw, T., Coba, M. P., Cornelisse, L. N., Farrell, R. J., Goldschmidt, H. L., Howrigan, D. P., Hussain, N. K., Imig, C., de Jong, A. P. H., Jung, H., Kohansalnodehi, M., Kramarz, B., Lipstein, N., Lovering, R. C., MacGillavry, H., … Verhage, M. (2019). SynGO: An evidence-based, expert-curated Knowledge Base for the synapse. *Neuron*, *103*(2), 217–234.e4. https://doi.org/10.1016/j.neuron.2019.05.002

Kukley, M., Capetillo-Zarate, E., & Dietrich, D. (2007). Vesicular glutamate release from axons in white matter. *Nature Neuroscience*, *10*(3), 311–320. https://doi.org/10.1038/nn1850

Kukley, M., Kiladze, M., Tognatta, R., Hans, M., Swandulla, D., Schramm, J., & Dietrich, D. (2008). Glial cells are born with synapses. *The FASEB Journal*, *22*(8), 2957–2969. https://doi.org/10.1096/fj.07-090985

Kukley, M., Nishiyama, A., & Dietrich, D. (2010). The fate of synaptic input to NG2 glial cells: Neurons specifically downregulate transmitter release onto differentiating oligodendroglial cells. *Journal of Neuroscience*, *30*(24), 8320–8331. https://doi.org/10.1523/jneurosci.0854-10.2010

Lamprianou, S., Chatzopoulou, E., Thomas, J.-L., Bouyain, S., & Harroch, S. (2011). A complex between contactin-1 and the protein tyrosine phosphatase PTPRZ controls the development of oligodendrocyte precursor cells. *Proceedings of the National Academy of Sciences*, *108*(42), 17498–17503. https://doi.org/10.1073/pnas.1108774108

Laursen, L. S., Chan, C. W., & French-Constant, C. (2009). An integrin–contactin complex regulates CNS myelination by differential Fyn phosphorylation. *The Journal of Neuroscience*, *29*(29), 9174–9185. https://doi.org/10.1523/jneurosci.5942-08.2009

Lin, S., & Bergles, D. E. (2003). Synaptic signaling between GABAergic interneurons and oligodendrocyte precursor cells in the hippocampus. *Nature Neuroscience*, *7*(1), 24–32. https://doi.org/10.1038/nn1162

Linneberg, C., Harboe, M., & Laursen, L. S. (2015). Axo-glia interaction preceding CNS myelination is regulated by bidirectional Eph-ephrin signaling. *ASN Neuro*, *7*(5), 175909141560285. https://doi.org/10.1177/1759091415602859

Lun, A. T. L., Riesenfeld, S., Andrews, T., Dao, T. P., Gomes, T., & Marioni, J. C. (2019). EmptyDrops: Distinguishing cells from empty droplets in droplet-based single-cell RNA sequencing data. *Genome Biology*, *20*(1), 63. https://doi.org/10.1186/s13059-019-1662-y

Maldonado, P. P., Velez-Fort, M., Levavasseur, F., & Angulo, M. C. (2013). Oligodendrocyte precursor cells are accurate sensors of local K+ in mature gray matter. *Journal of Neuroscience*, *33*(6), 2432–2442. https://doi.org/10.1523/jneurosci.1961-12.2013

Manno, G. L., Siletti, K., Furlan, A., Gyllborg, D., Vinsland, E., Albiach, A. M., Langseth, C. M., Khven, I., Lederer, A. R., Dratva, L. M., Johnsson, A., Nilsson, M., Lönnerberg, P., & Linnarsson, S. (2021). Molecular architecture of the developing mouse brain. *Nature*, *596*(7870), 92–96. https://doi.org/10.1038/s41586-021-03775-x

Marisca, R., Hoche, T., Agirre, E., Hoodless, L. J., Barkey, W., Auer, F., Castelo-Branco, G., & Czopka, T. (2020). Functionally distinct subgroups of oligodendrocyte precursor cells integrate neural activity and execute myelin formation. *Nature Neuroscience*, *23*(3), 363–374. https://doi.org/10.1038/s41593-019-0581-2

Marques, S., van Bruggen, D., Vanichkina, D. P., Floriddia, E. M., Munguba, H., Väremo, L., Giacomello, S., Falcão, A. M., Meijer, M., Björklund, Å. K., Hjerling-Leffler, J., Taft, R. J., & Castelo-Branco, G. (2018). Transcriptional convergence of oligodendrocyte lineage progenitors during development. *Developmental Cell*, *46*(4), 504–517.e7. https://doi.org/10.1016/j.devcel.2018.07.005

McGinnis, C. S., Murrow, L. M., & Gartner, Z. J. (2019). DoubletFinder: Doublet detection in single-cell RNA sequencing data using artificial nearest neighbors. *Cell Systems*, *8*(4), 329–337.e4. https://doi.org/10.1016/j.cels.2019.03.003

Mitew, S., Gobius, I., Fenlon, L. R., McDougall, S. J., Hawkes, D., Xing, Y. L., Bujalka, H., Gundlach, A. L., Richards, L. J., Kilpatrick, T. J., Merson, T. D., & Emery, B. (2018). Pharmacogenetic stimulation of neuronal activity increases myelination in an axon-specific manner. *Nature Communications*, *9*(1), 1–16. https://doi.org/10.1038/s41467-017-02719-2

Nishiyama, A., Lin, X. H., Giese, N., Heldin, C. H., & Stallcup, W. B. (1996). Co-localization of NG2 proteoglycan and PDGF alpha-receptor on O2A progenitor cells in the developing rat brain. *Journal of Neuroscience Research*, *43*(3), 299–314.

Okada, A., Tominaga, M., Horiuchi, M., & Tomooka, Y. (2007). Plexin-A4 is expressed in oligodendrocyte precursor cells and acts as a mediator of semaphorin signals. *Biochemical and Biophysical Research Communications*, *352*(1), 158–163. https://doi.org/10.1016/j.bbrc.2006.10.176

Oumesmar, B. N., Vignais, L., Duhamel-Clerin, E., Avellana-Adalid, V., Rougon, G., & Evercooren, A. B. (1995). Expression of the highly Polysialylated neural cell adhesion molecule during postnatal myelination and following chemically induced demyelination of the adult mouse spinal cord. *European Journal of Neuroscience*, *7*(3), 480–491. https://doi.org/10.1111/j.1460-9568.1995.tb00344.x

Paez, P. M., & Lyons, D. A. (2020). Calcium signaling in the oligodendrocyte lineage: Regulators and consequences. *Annual Review of Neuroscience*, *43*(1), 1–24. https://doi.org/10.1146/annurev-neuro-100719-093305

Passlick, S., Trotter, J., Seifert, G., Steinhäuser, C., & Jabs, R. (2016). The NG2 protein is not required for glutamatergic neuron–NG2 cell synaptic signaling. *Cerebral Cortex*, *26*(1), 51–57. https://doi.org/10.1093/cercor/bhu171

Picelli, S., Faridani, O.R., Björklund, Å.K., Winberg, G., Sagasser, S., and Sandberg, R. (2014). Full-length RNA-seq from single cells using Smart-seq2. *Nature Protoc. 9*, 171–181. https://doi.org/10.1038/nprot.2014.006.

Pitman, K. A., Ricci, R., Gasperini, R., Beasley, S., Pavez, M., Charlesworth, J., Foa, L., & Young, K. M. (2020). The voltage-gated calcium channel CaV1.2 promotes adult oligodendrocyte progenitor cell survival in the mouse corpus callosum but not motor cortex. *Glia*, *68*(2), 376–392. https://doi.org/10.1002/glia.23723

Pringle, N. P., & Richardson, W. D. (1993). A singularity of PDGF alpha-receptor expression in the dorsoventral axis of the neural tube may

define the origin of the oligodendrocyte lineage. *Development*, *117*(2), 525–533. https://doi.org/10.1242/dev.117.2.525

Reynolds, R., & Wilkin, G. P. (1988). Development of macroglial cells in rat cerebellum II. An in situ immunohistochemical study of oligodendroglial lineage from precursor to mature myelinating cell. *Development*, *102*(2), 409–425. https://doi.org/10.1242/dev.102.2.409

Schindelin, J., Arganda-Carreras, I., Frise, E., Kaynig, V., Longair, M., Pietzsch, T., Preibisch, S., Rueden, C., Saalfeld, S., Schmid, B., Tinevez, J.-Y., White, D. J., Hartenstein, V., Eliceiri, K., Tomancak, P., & Cardona, A. (2012). Fiji: An open-source platform for biological-image analysis. *Nature Methods*, *9*(7), 676–682. https://doi.org/10.1038/nmeth.2019

Simon, C., Götz, M., & Dimou, L. (2011). Progenitors in the adult cerebral cortex: Cell cycle properties and regulation by physiological stimuli and injury. *Glia*, *59*(6), 869–881. https://doi.org/10.1002/glia.21156

Spitzer, S. O., Sitnikov, S., Kamen, Y., Evans, K. A., Kronenberg-Versteeg, D., Dietmann, S., de Faria, O., Agathou, S., & Káradóttir, R. T. (2019). Oligodendrocyte progenitor cells become regionally diverse and heterogeneous with age. *Neuron*, *101*(3), 459–471.e5. https://doi.org/10.1016/j.neuron.2018.12.020

Stout, K. A., Dunn, A. R., Hoffman, C., & Miller, G. W. (2019). The synaptic vesicle glycoprotein 2: Structure, function, and disease relevance. *ACS Chemical Neuroscience*, *10*(9), 3927–3938. https://doi.org/10.1021/acschemneuro.9b00351

Stuart, T., Butler, A., Hoffman, P., Hafemeister, C., Papalexi, E., Mauck, W. M., Hao, Y., Stoeckius, M., Smibert, P., & Satija, R. (2019). Comprehensive integration of single-cell data. *Cell*, *177*(7), 1888–1902.e21. https://doi.org/10.1016/j.cell.2019.05.031

Südhof, T. C. (2018). Towards an understanding of synapse formation. *Neuron*, *100*(2), 276–293. https://doi.org/10.1016/j.neuron.2018.09.040

Südhof, T. C. (2021). The cell biology of synapse formation. *Journal of Cell Biology*, *220*(7), e202103052. https://doi.org/10.1083/jcb.202103052

Sun, W., & Dietrich, D. (2013). Synaptic integration by NG2 cells. *Frontiers in Cellular Neuroscience*, *7*, 255. https://doi.org/10.3389/fncel.2013.00255

Sun, W., Matthews, E. A., Nicolas, V., Schoch, S., & Dietrich, D. (2016). NG2 glial cells integrate synaptic input in global and dendritic calcium signals. *eLife*, *5*, 1812. https://doi.org/10.7554/elife.16262

Tognatta, R., Sun, W., Goebbels, S., Nave, K., Nishiyama, A., Schoch, S., Dimou, L., & Dietrich, D. (2017). Transient Cnp expression by early progenitors causes Cre-lox-based reporter lines to map profoundly different fates. *Glia*, *65*(2), 342–359. https://doi.org/10.1002/glia.23095

Toran-Allerand, C. D. (1974). Acetylcholinesterase inhibition and myelinogenesis in vitro. *Experimental Neurology*, *43*(1), 216–226. https://doi.org/10.1016/0014-4886(74)90142-3

Trapp, B. D., Nishiyama, A., Cheng, D., & Macklin, W. (1997). Differentiation and death of Premyelinating oligodendrocytes in developing rodent brain. *The Journal of Cell Biology*, *137*(2), 459–468. https://doi.org/10.1083/jcb.137.2.459

Trudeau, L. E., Doyle, R. T., Emery, D. G., & Haydon, P. G. (1996). Calcium-independent activation of the secretory apparatus by ruthenium red in hippocampal neurons: A new tool to assess modulation of presynaptic function. *The Journal of Neuroscience: The Official Journal of the Society for Neuroscience*, *16*(1), 46–54.

Van Heyningen, P., Calver, A. R., & Richardson, W. D. (2001). Control of progenitor cell number by mitogen supply and demand. *Current Biology*, *11*(4), 232–241. https://doi.org/10.1016/s0960-9822(01)00075-6

Vartanian, T., Fischbach, G., & Miller, R. (1999). Failure of spinal cord oligodendrocyte development in mice lacking neuregulin. *Proceedings of the National Academy of Sciences*, *96*(2), 731–735. https://doi.org/10.1073/pnas.96.2.731

Venkatesh, H. S., Johung, T. B., Caretti, V., Noll, A., Tang, Y., Nagaraja, S., Gibson, E. M., Mount, C. W., Polepalli, J., Mitra, S. S., Woo, P. J., Malenka, R. C., Vogel, H., Bredel, M., Mallick, P., & Monje, M. (2015). Neuronal activity promotes glioma growth through neuroligin-3 secretion. *Cell*, *161*(4), 803–816. https://doi.org/10.1016/j.cell.2015.04.012

Venkatesh, H. S., Tam, L. T., Woo, P. J., Lennon, J., Nagaraja, S., Gillespie, S. M., Ni, J., Duveau, D. Y., Morris, P. J., Zhao, J. J., Thomas, C. J., & Monje, M. (2017). Targeting neuronal activity-regulated neuroligin-3 dependency in high-grade glioma. *Nature*, *549*(7673), 533–537. https://doi.org/10.1038/nature24014

Weng, Q., Wang, J., Wang, J., He, D., Cheng, Z., Zhang, F., Verma, R., Xu, L., Dong, X., Liao, Y., He, X., Potter, A., Zhang, L., Zhao, C., Xin, M., Zhou, Q., Aronow, B. J., Blackshear, P. J., Rich, J. N., … Lu, Q. R. (2019). Single-cell transcriptomics uncovers glial progenitor diversity and cell fate determinants during development and Gliomagenesis. *Cell Stem Cell*, *24*(5), 707–723.e8. https://doi.org/10.1016/j.stem.2019.03.006

Winkler, C. C., Yabut, O. R., Fregoso, S. P., Gomez, H. G., Dwyer, B. E., Pleasure, S. J., & Franco, S. J. (2018). The dorsal wave of neocortical Oligodendrogenesis begins embryonically and requires multiple sources of sonic hedgehog. *The Journal of Neuroscience*, *38*(23), 5237–5250. https://doi.org/10.1523/jneurosci.3392-17.2018

Xiang, X., Zhang, X., & Huang, Q.-L. (2012). Plexin A3 is involved in semaphorin 3F-mediated oligodendrocyte precursor cell migration. *Neuroscience Letters*, *530*(2), 127–132. https://doi.org/10.1016/j.neulet.2012.09.058

Xiao, L., Ohayon, D., McKenzie, I. A., Sinclair-Wilson, A., Wright, J. L., Fudge, A. D., Emery, B., Li, H., & Richardson, W. D. (2016). Rapid production of new oligodendrocytes is required in the earliest stages of motor skill learning. *Nature Neuroscience*, *19*(9), 1210–1217. https://doi.org/10.1038/nn.4351

Xie, M., Lynch, D. T., Schools, G. P., Feustel, P. J., Kimelberg, H. K., & Zhou, M. (2007). Sodium channel currents in rat hippocampal NG2 glia: Characterization and contribution to resting membrane potential. *Neuroscience*, *150*(4), 853–862. https://doi.org/10.1016/j.neuroscience.2007.09.057

Yuan, X., Chittajallu, R., Belachew, S., Anderson, S., McBain, C. J., & Gallo, V. (2002). Expression of the green fluorescent protein in the oligodendrocyte lineage: A transgenic mouse for developmental and physiological studies. *Journal of Neuroscience Research*, *70*(4), 529–545. https://doi.org/10.1002/jnr.10368

Yuzwa, S. A., Borrett, M. J., Innes, B. T., Voronova, A., Ketela, T., Kaplan, D. R., Bader, G. D., & Miller, F. D. (2017). Developmental emergence of adult neural stem cells as revealed by single-cell transcriptional profiling. *Cell Reports*, *21*(13), 3970–3986. https://doi.org/10.1016/j.celrep.2017.12.017

Zhao, N., Huang, W., Cātālin, B., Scheller, A., & Kirchhoff, F. (2021). L-type Ca2+ channels of NG2 glia determine proliferation and NMDA receptor-dependent plasticity. *Frontiers in Cell and Developmental Biology*, *9*, 759477. https://doi.org/10.3389/fcell.2021.759477

Zheng, G. X. Y., Terry, J. M., Belgrader, P., Ryvkin, P., Bent, Z. W., Wilson, R., Ziraldo, S. B., Wheeler, T. D., McDermott, G. P., Zhu, J., Gregory, M. T., Shuga, J., Montesclaros, L., Underwood, J. G., Masquelier, D. A., Nishimura, S. Y., Schnall-Levin, M., Wyatt, P. W., Hindson, C. M., … Bielas, J. H. (2017). Massively parallel digital transcriptional profiling of single cells. *Nature Communications*, *8*(1), 14049. https://doi.org/10.1038/ncomms14049

Zhu, X., Bergles, D. E., & Nishiyama, A. (2008). NG2 cells generate both oligodendrocytes and gray matter astrocytes. *Development*, *135*(1), 145–157. https://doi.org/10.1242/dev.004895

Ziskin, J. L., Nishiyama, A., Rubio, M., Fukaya, M., & Bergles, D. E. (2007). Vesicular release of glutamate from unmyelinated axons in white matter. *Nature Neuroscience*, *10*(3), 321–330. https://doi.org/10.1038/nn1854

Zonouzi, M., Scafidi, J., Li, P., McEllin, B., Edwards, J., Dupree, J. L., Harvey, L., Sun, D., Hübner, C. A., Cull-Candy, S. G., Farrant, M., &

Gallo, V. (2015). GABAergic regulation of cerebellar NG2 cell development is altered in perinatal white matter injury. *Nature Neuroscience*, *18*(5), 674–682. https://doi.org/10.1038/nn.3990

SUPPORTING INFORMATION

Additional supporting information can be found online in the Supporting Information section at the end of this article.

How to cite this article: Vana, N. S., van Loo, K. M. J., van Waardenberg, A. J., Tießen, M., Cases-Cunillera, S., Sun, W., Quatraccioni, A., Schoch, S., & Dietrich, D. (2023). Early cortical oligodendrocyte precursor cells are transcriptionally distinct and lack synaptic connections. *Glia*, *71*(9), 2210–2233. https://doi.org/10.1002/glia.24388

Cell Reports

Article

Local Efficacy of Glutamate Uptake Decreases with Synapse Size

Graphical Abstract

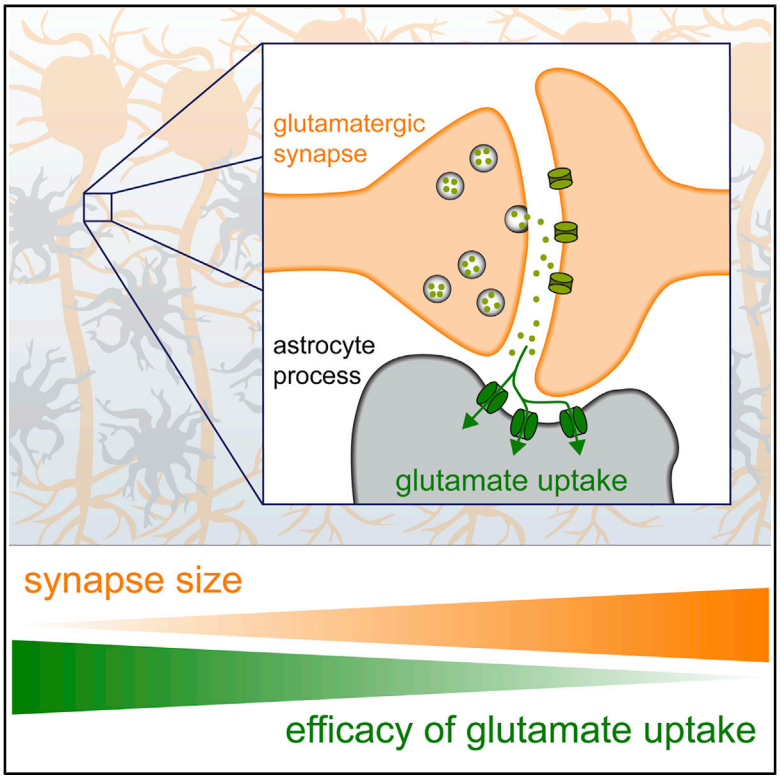

Authors

Michel K. Herde, Kirsten Bohmbach, Cátia Domingos, ..., Dirk Dietrich, Martin K. Schwarz, Christian Henneberger

Correspondence

christian.henneberger@uni-bonn.de

In Brief

Herde et al. demonstrate a dependence of the local efficacy of glutamate uptake at glutamatergic synapses on spine size. As predicted by the relative astrocytic coverage of spines, extracellular glutamate transients and Ca^{2+} entry through glutamate receptors are less strongly controlled by glutamate uptake at large than at small spines.

Highlights

- Relative astrocytic coverage of glutamatergic spines decreases with spine size
- Control of perisynaptic glutamate transients by uptake decreases with spine size
- Control of receptor-mediated Ca^{2+} entry by uptake decreases with spine size
- Accordingly, small spines are better shielded from invading glutamate

Herde et al., 2020, Cell Reports *32*, 108182
September 22, 2020
https://doi.org/10.1016/j.celrep.2020.108182

CellPress

Cell Reports

CellPress
OPEN ACCESS

Article

Local Efficacy of Glutamate Uptake Decreases with Synapse Size

Michel K. Herde,[1] Kirsten Bohmbach,[1] Cátia Domingos,[1] Natascha Vana,[2] Joanna A. Komorowska-Müller,[1] Stefan Passlick,[1] Inna Schwarz,[4] Colin J. Jackson,[3] Dirk Dietrich,[2] Martin K. Schwarz,[4] and Christian Henneberger[1,5,6,7,*]

[1]Institute of Cellular Neurosciences, Medical Faculty, University of Bonn, Bonn, Germany
[2]Department for Neurosurgery, University Hospital Bonn, Bonn, Germany
[3]Research School of Chemistry, Australian National University, Canberra, Australia
[4]Institute of Epileptology, Medical Faculty, University of Bonn, Bonn, Germany
[5]Institute of Neurology, University College London, London, UK
[6]German Centre for Neurodegenerative Diseases (DZNE), Bonn, Germany
[7]Lead Contact
*Correspondence: christian.henneberger@uni-bonn.de
https://doi.org/10.1016/j.celrep.2020.108182

SUMMARY

Synaptically released glutamate is largely cleared by glutamate transporters localized on perisynaptic astrocyte processes. Therefore, the substantial variability of astrocyte coverage of individual hippocampal synapses implies that the efficacy of local glutamate uptake and thus the spatial fidelity of synaptic transmission is synapse dependent. By visualization of sub-diffraction-limit perisynaptic astrocytic processes and adjacent postsynaptic spines, we show that, relative to their size, small spines display a stronger coverage by astroglial transporters than bigger neighboring spines. Similarly, glutamate transients evoked by synaptic stimulation are more sensitive to pharmacological inhibition of glutamate uptake at smaller spines, whose high-affinity N-methyl-D-aspartate receptors (NMDARs) are better shielded from remotely released glutamate. At small spines, glutamate-induced and NMDAR-dependent Ca^{2+} entry is also more strongly increased by uptake inhibition. These findings indicate that spine size inversely correlates with the efficacy of local glutamate uptake and thereby likely determines the probability of synaptic crosstalk.

INTRODUCTION

The uptake of released neurotransmitters is an essential mechanism in synaptic transmission and prevents excitotoxic effects of the neurotransmitter glutamate. Its clearance is largely performed by astrocytic glutamate transporters (Danbolt, 2001; Rose et al., 2018). Therefore, the spatial proximity between astrocytic transporters and synaptic glutamate release sites determines how far glutamate can diffuse before it is taken up. For example, the physiological reduction of the coverage of neurons by astrocytes in the supraoptic nucleus during lactation is accompanied by a decreased uptake of synaptically released glutamate, which can increase the recruitment of presynaptic glutamate receptors (Oliet et al., 2001). Therefore, the degree of coverage of synapses by transporter-enriched astrocytic processes can represent an important parameter of synapse function.

In the rodent hippocampus, a key model for studying synaptic transmission and plasticity, electron microscopy studies of the CA1 *stratum radiatum* revealed that only ~40%–60% of synapses have astrocyte processes, which can be as thin as 100–200 nm, directly apposed (Ventura and Harris, 1999; Witcher et al., 2007). Numerous further studies have successfully established fundamental correlations between, for instance, the size and morphological class of an individual spine, how much of its surface and boundary are directly contacted by astrocytic processes, and how much astrocytic process volume is nearby (Gavrilov et al., 2018; Genoud et al., 2006; Lushnikova et al., 2009; Medvedev et al., 2014; Patrushev et al., 2013; Ventura and Harris, 1999; Witcher et al., 2007, 2010). For example, we have previously demonstrated that the distance from postsynaptic densities to neighboring astrocyte processes differs between large mushroom spines and thin spines (Medvedev et al., 2014). However, the functional correlate of a difference in astrocytic coverage between postsynaptic spine types has remained largely unclear. Therefore, it also remains to be established which morphological aspects of astrocytic coverage are functionally relevant and for which biological processes.

Theory and numerical modeling predict that the geometry of synapses and adjacent astrocytes determine the spread and clearance of glutamate, activation of extrasynaptic receptors, and glutamate escape to neighboring synapses (Gavrilov et al., 2018; Medvedev et al., 2014; Rose et al., 2018; Zheng et al., 2008). Some of the predictions from these studies have more recently become testable by experimental means. We reasoned that if spine type and size determine the degree by which individual spines are covered by astroglial processes and thus by astrocytic glutamate transporters, then spine size would set the local

strength of glutamate uptake. As a consequence, spine size is expected to determine how well spines are also protected from a "spill-in" of glutamate from neighboring synapses and also how likely synaptically released glutamate escapes into perisynaptic space. In the present study, we explored these scenarios by taking advantage of super-resolution microscopy, glutamate imaging, and other techniques. We found that the local efficacy of glutamate uptake is low at large compared to small spines and correlates best with the amount of GLT-1 and astrocytic volume relative to the spine volume.

RESULTS

Superresolved Visualization of Perisynaptic Astroglial Glutamate Transporters

A quantitative assessment of the spatial relationship between glutamate transporters localized on perisynaptic astrocyte processes and synaptic spines requires high-resolution visualization of the spines and the leaf-like perisynaptic astrocyte processes, which can be as thin as 100–200 nm (Heller and Rusakov, 2015; Medvedev et al., 2014; Ventura and Harris, 1999). Here, we took advantage of expansion microscopy (ExM) (Asano et al., 2018; Chen et al., 2015; Chozinski et al., 2016), which provides the required resolution using well-characterized antibodies for standard confocal microscopy to label target proteins and structures. Indeed, ExM of astrocytes expressing cytosolic EGFP reveals the fine structural details of hippocampal astrocytes in the CA1 *stratum radiatum* at a drastically improved level (Figure 1A). Because of the improved resolution in all three dimensions, single focal sections display more clearly defined and much sparser astrocytic processes, more reminiscent of electron microscopy. Registration analysis revealed that the error introduced by either repetitive mounting for imaging and/or ExM is small and amounts to about 10% at the relevant sub-micrometer level (Figures S1A–S1C). We estimated the resolution achieved by ExM by using an immunolabeling of the synaptic protein Homer1 and could resolve objects as small as 40 nm in the x-y plane (Figures S1D–S1G), which provides an upper limit of the resolving power of ExM. Next, we combined ExM visualization of EGFP-expressing astrocytes with immunolabeling of the glutamate transporters GLT-1 and GLAST (Figures 1B and S2). In line with the notion that astroglial glutamate transporters mediate most of hippocampal glutamate uptake (Danbolt, 2001; Rose et al., 2018), GLT-1 labeling outlined EGFP-positive astrocyte processes. In addition, virtually all GLT-1-positive structures were EGFP positive (Figures 1B and S2A–S2D) and GLT-1 and GLAST colocalized (Figures S2E and S2F). We therefore used GLT-1 labeling to localize and characterize perisynaptic astrocyte processes carrying glutamate transporters around individual synaptic spines of CA1 pyramidal cells expressing yellow fluorescent protein (YFP) using ExM (Figure 1C).

The amount of GLT-1 immediately adjacent to individual spines on dendritic segments was quantified by determining the number of pixels positive for GLT-1 and YFP in spherical volumes of interest centered on spines (radius, r = 0.50 μm; Figure 1D; also see STAR Methods). For each dendritic segment, the analyzed spines were then categorized as "small" or "large" if their volume (see STAR Methods) was below or above the median spine volume of that dendritic segment. We used the spine volume as a single measure of spine size throughout, instead of, for instance, threshold-based volume or surface renderings, because it can be readily obtained from ExM and two-photon excitation (2PE) microscopy data (see below), it is relatively insensitive to the optical resolution, and it does not require setting a threshold. We found that for volumes of interest with r = 0.50 μm, on average, the amount of GLT-1 was lower at small than at large spines on individual dendritic segments (Figure 1E). However, large spines have a higher surface area and a larger perimeter. A similar amount of GLT-1 could thus translate into a reduced density of glutamate uptake at the spine surface. We therefore also calculated the relative GLT-1 coverage by normalizing the number of pixels positive for GLT-1 and YFP to the spine size, i.e., spine volume. Indeed, GLT-1 was relatively less abundant at large spines (Figure 1F). We then asked if these findings change if the volume of interest is reduced by 40% (r = 0.42 μm) and made qualitatively similar observations (Figures 1G and 1H). Next, we wondered if the dependence of GLT-1 coverage on spine volume would also hold for larger volumes of interest and set the radius of volumes of interest to 0.65 μm, the average inter-synapse distance (Ventura and Harris, 1999). Here, we found that the raw abundance of pixels positive for GLT-1 and YFP, i.e., the amount of spine surface covered by GLT-1, was independent of spine volume. A likely explanation is that increasing the radius of analysis includes neighboring spines and dendritic shafts and thereby obscures spine size dependencies (Figures 1G and 1H).

Overall, these observations demonstrate that within a short distance the amount of GLT-1 is higher at large spines. However, when calculated relative to the spine volume, the GLT-1 coverage was smaller at big spines at all radii (Figure 1H). Similarly, we found a highly significant negative correlation between spine volume and the relative GLT-1 coverage at all analyzed radii (Figures S2G and S2H).

These results reveal that the size of an individual dendritic spine is a strong predictor of its coverage by astroglial GLT-1: the total surface of a large spine covered by GLT-1 is larger than that of a small spine. However, relative to their size, larger spines are generally less well covered by GLT-1. This raised two questions. First, does the efficacy of local glutamate uptake correlate with the absolute or relative abundance of GLT-1 at a spine? Second, does the volume of perisynaptic astrocyte processes display the same dependency on spine size?

Spine Size Dependence of Local Distribution of Astrocytic Volume

We have previously shown that the fluorescence of dye distributed in the astrocytic cytosol can be used as a measure of astrocytic process volume (Medvedev et al., 2014). Therefore, we used transgenic mice expressing EGFP under a GFAP promoter (Nolte et al., 2001) to visualize astrocyte processes using ExM. For the identification of excitatory synapses, we also labeled the presynaptic protein bassoon and the postsynaptic protein shank2, which is a component of the postsynaptic density

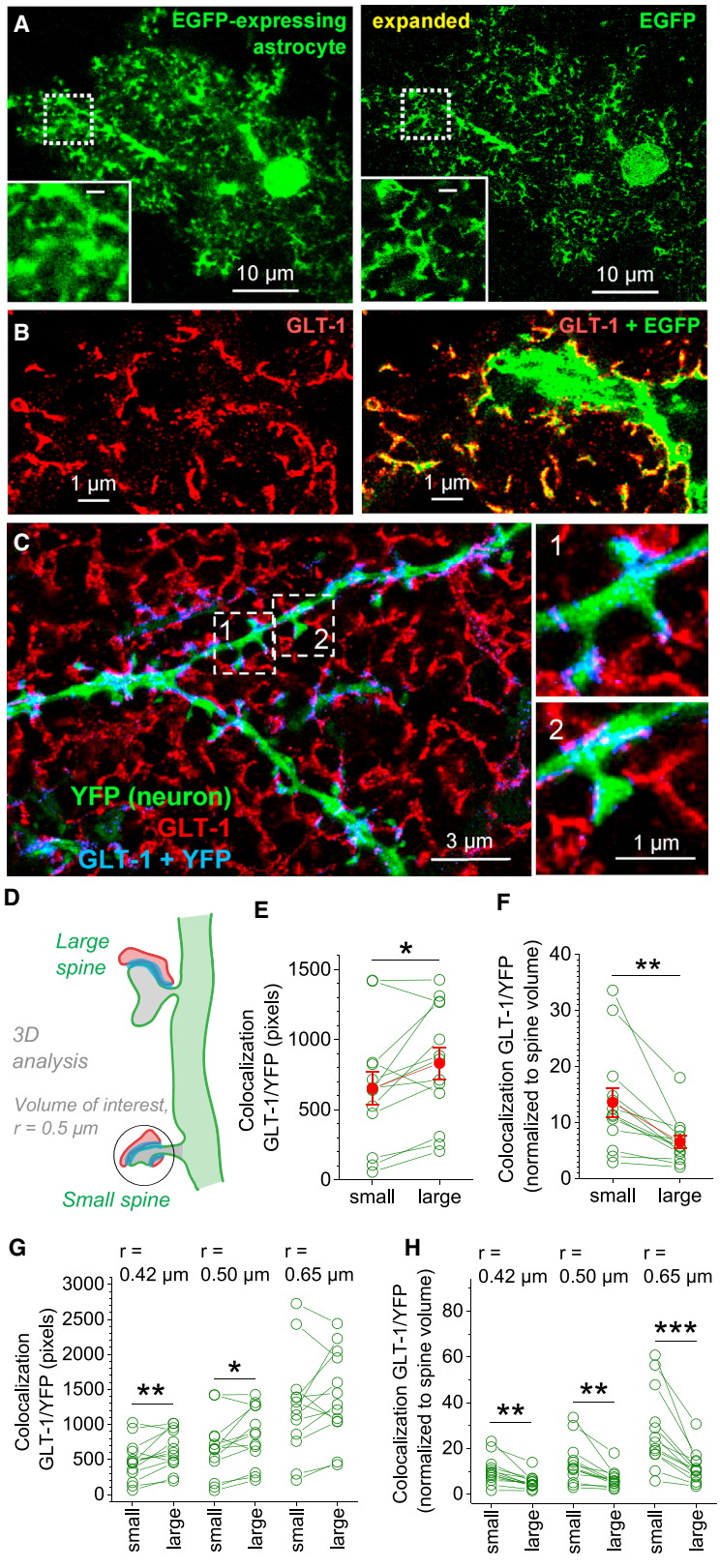

Figure 1. Expansion Microscopy (ExM) of Perisynaptic Astroglial Processes Reveals a Size-Dependent Coverage of Spines by the Astroglial Glutamate Transporter GLT-1 in Mouse CA1 *Stratum Radiatum*

(A) Example of a confocal image of the same astrocyte expressing EGFP before (left) and after (right panel) expansion (Chen et al., 2015; Chozinski et al., 2016). Scale bars correspond to pre-expansion dimensions (i.e., actual size/expansion factor for the right panel). See insets for higher magnification (scale bar, 1 µm). Note the more clearly defined astrocyte branches in ExM and the disappearance of out-of-focus structures. See Figure S1 for a more detailed characterization of ExM. Note that only a subset of hippocampal astrocytes in these animals express EGFP (Nolte et al., 2001).

(B) ExM example of the glutamate transporter GLT-1 (left panel) and in combination with the visualization of an EGFP-expressing astrocyte (right panel). Note that virtually all GLT-1-positive structures colocalized with EGFP-positive astrocyte branches (yellow). Large branches are outlined by GLT-1 label. See Figure S2 for further examples of colocalization of glutamate transporters (GLT-1 and GLAST) and astrocyte branches.

(C) ExM of spines on a radial oblique dendrite of a CA1 pyramidal neuron (green, YFP) and the surrounding GLT-1 positive (red) astrocyte processes (left panel, see also Figure S2). Regions of immediate juxtaposition, i.e., appearing colocalized, are shown in blue. Numbered regions of interest (ROIs; dashed boxes): magnifications of sample ROIs (right panels).

(D) Illustration of the 3D analysis of GLT-1 coverage of individual spines. The total number of pixels positive for GLT-1 and YFP (blue, colocalization GLT-1/YFP in (E) was determined in spherical volumes of interest centered on the spine head (r = 0.50 µm). Spines were categorized as "small" or "large" if their volume (see STAR Methods) was lower or higher, respectively, than the median spine volume on the analyzed dendritic branch. In total, 347 spines from 13 dendritic segments obtained from 4 separate experiments were analyzed.

(E) The total number of pixels positive for GLT-1 and YFP was significantly lower at small spines than at large spines (r = 0.50 µm). Connected circles represent the average number of pixels at small and large spines of a single dendrite (paired data). Red data points represent averages and SEM across all analyzed dendrites. Paired Student's t test on 13 individual dendrites, p = 0.0220; n = 13 dendrites.

(F) Relative to the individual spine volume, smaller spines are more strongly covered by GLT-1 (r = 0.50 µm). For all spines across all experiments, the GLT-1/YFP colocalization in pixels was normalized to the spine volume to obtain the relative abundance of GLT-1 at small and large spines. Data presentation as in (E). Relative GLT-1 coverage is higher at small spines than at large spines (paired Student's t test, p = 0.00223; n = 13 dendrites).

(G) Comparison of GLT-1/YFP colocalization between small and large spines with differently sized volumes of interest (r = 0.42 µm, 0.50 µm and 0.65 µm from left to right). Data for r = 0.50 µm is replotted from (E). Paired Student's t tests, p = 0.00942, 0.0220, and 0.237 from left to right; n = 13 dendrites.

(H) Analysis of colocalization relative to spine volume with differently sized volumes of interest, as in (G). Paired Student's t tests, p = 0.00108, 0.00223, and 0.000359 from left to right; n = 13 dendrites.

(PSD) of glutamatergic synapses (Sheng and Hoogenraad, 2007). This ExM triple labeling allowed us to localize glutamatergic synaptic contacts within the territory of single astrocytes (Figure 2A). For 3D analysis, we pseudo-randomly chose volumes of interest containing single putative synaptic contacts (see STAR Methods) with directly apposed pre- and postsynaptic label (without inspection of the local EGFP fluorescence to avoid a selection bias). We then analyzed the fluorescence intensity of EGFP, i.e., the astroglial volume distribution in spherical shells with increasing diameter centered on the PSD (Figure 2A, bottom right panel; STAR Methods). The center of the PSD was chosen because we were interested in how abundant astrocyte processes are close to the postsynaptic receptors. In total, we analyzed 151 volumes of interest covered by 8 different astrocytes from 3 independent experiments. As above, we categorized the PSDs as small or large depending on whether their volume (see STAR Methods) was lower or higher, respectively, than the median PSD volume for the studied astrocyte territory. We found that the sum of EGFP fluorescence within shells continuously increased with distance, whereas the density within the spherical shells reached a plateau at about 300–400 nm, which is similar to results of a previous study using electron microscopy (Patrushev et al., 2013). No difference between the profiles at small and large PSDs was observed (Figures 2B and 2C). As expected from this observation, the cumulative EGFP fluorescence within a radius of 1 μm was not significantly different when we compared small and large PSDs within the territory of single astrocytes (Figure 2D). Therefore, the absolute volume of perisynaptic astroglial processes in the immediate vicinity of a glutamatergic synapse does not depend on the size of its PSD and, because PSD size and spine volume are strongly correlated (Harris and Stevens, 1989; Lushnikova et al., 2009), not on spine size. Because absolute GLT-1 surface coverage displayed a spine size dependence at a short distance, this finding suggests that the surface-to-volume ratio of astrocytic processes differs between small and large spines.

Larger spines could also have bigger presynaptic terminals with larger active zones and a higher release probability (Holderith et al., 2012; Murthy et al., 2001; Schikorski and Stevens, 1997). This could lead to stronger astrocytic sodium accumulation during uptake and thereby to an impairment of glutamate uptake, for review (Rose et al., 2018), if the increase of release probability at large spines is not matched by an increase of perisynaptic astrocyte volume. To quantify the relative abundance of perisynaptic astrocyte volume, we normalized the cumulative EGFP fluorescence to the PSD volume. We found that this relative measure of astrocyte volume around a PSD is significantly lower at large PSDs (Figure 2E). Although we have analyzed EGFP fluorescence in Figures 2E and 2F for a radius of 1 μm, which may include undetected neighboring spines, this finding will apply to shorter distances because the profiles in Figures 2B and 2C are virtually identical (also see legend).

This again raised the question if the relative scarceness of astrocyte processes leads to less effective glutamate uptake at glutamatergic synapses with large postsynaptic spines or PSDs. To address this question, we next performed experiments that directly assess the efficacy of glutamate clearance at individual spines.

The Efficacy of Local Glutamate Clearance is Lower at Large Spines

To investigate the functional role of the dependency between the amount of perisynaptic astroglia and the spine/PSD size, we visualized glutamate transients at individual spines triggered by synaptic glutamate release. This was achieved by viral expression of the optical glutamate sensor iGluSnFR (Marvin et al., 2013) on the surface of astrocytes and observation of its fluorescence using 2PE microscopy in the CA1 *stratum radiatum* of acute hippocampal slices (Figure 3). Individual spines of CA1 pyramidal cells were imaged simultaneously after loading a single cell with Alexa Fluor 594 (by a whole-cell patch pipette, pipette withdrawal after 10 min). Extracellular glutamate transients were induced by electrical stimulation of CA3-CA1 axons with brief bursts (10 pulses at 100 Hz) with glutamate receptors blocked. Responses were readily detectable at sets of simultaneously monitored individual spines (Figures 3A–3C). Using this experimental paradigm, we then quantified the local strength of glutamate uptake by the sensitivity of the recorded glutamate transients to pharmacological partial blockade of glutamate transporters using 200 nM TFB-TBOA (bath application). Although TFB-TBOA does not inhibit a specific transporter at this concentration and bath application is not cell-type specific, we used this approach because the astroglial transporters GLT-1 and GLAST far outnumber other glutamate transporters in this brain region and are mostly localized on astrocytes (Holmseth et al., 2012; also see Figure S2).

We first analyzed the global effect of TBOA and found that the area under the curve (AUC, $\Delta F/F_0 \times$ ms), which we chose in order to capture changes of amplitude and decay, increased after application of TBOA but not in control experiments (Figure S3). To investigate the effect of TBOA on the level of single spines, we then calculated the difference between the AUC during baseline and after TBOA application (TBOA effect, $\Delta AUC = AUC_{TBOA} - AUC_{baseline}$) at individual spines (for example, see Figure 3D). Again, spine volumes were analyzed and expressed relative to the median volume of 10 spines on the same dendritic segment. The overall magnitude of the TBOA effect varied between recordings (three examples in Figure 3E), but a negative correlation between the TBOA effect and spine volume appeared to be a consistent finding. A potential explanation is that TBOA could increase the resting glutamate levels, thereby increasing F_0 and thus downscaling AUC_{TBOA} across spines. To analyze the pooled data, we therefore aligned data by subtracting the mean TBOA effect at a dendrite from each data point of that dendrite (see filled orange circles representing a single experiment in Figures 3D–3F). Performing this analysis across 65 spines (from 12 dendrites in independent experiments), we revealed a statistically significant negative correlation between the glutamate transient sensitivity to TBOA and the spine volume (Figure 3F).

Our findings indicate that the perisynaptic concentration of synaptically released glutamate is more strongly affected by transporter blockade at small than at large postsynaptic spines. In other words, glutamate transients at small spines are more tightly controlled by glutamate transporters than at large spines. Comparing these findings to the morphological data obtained by ExM, this shows that the local uptake efficacy changes in parallel

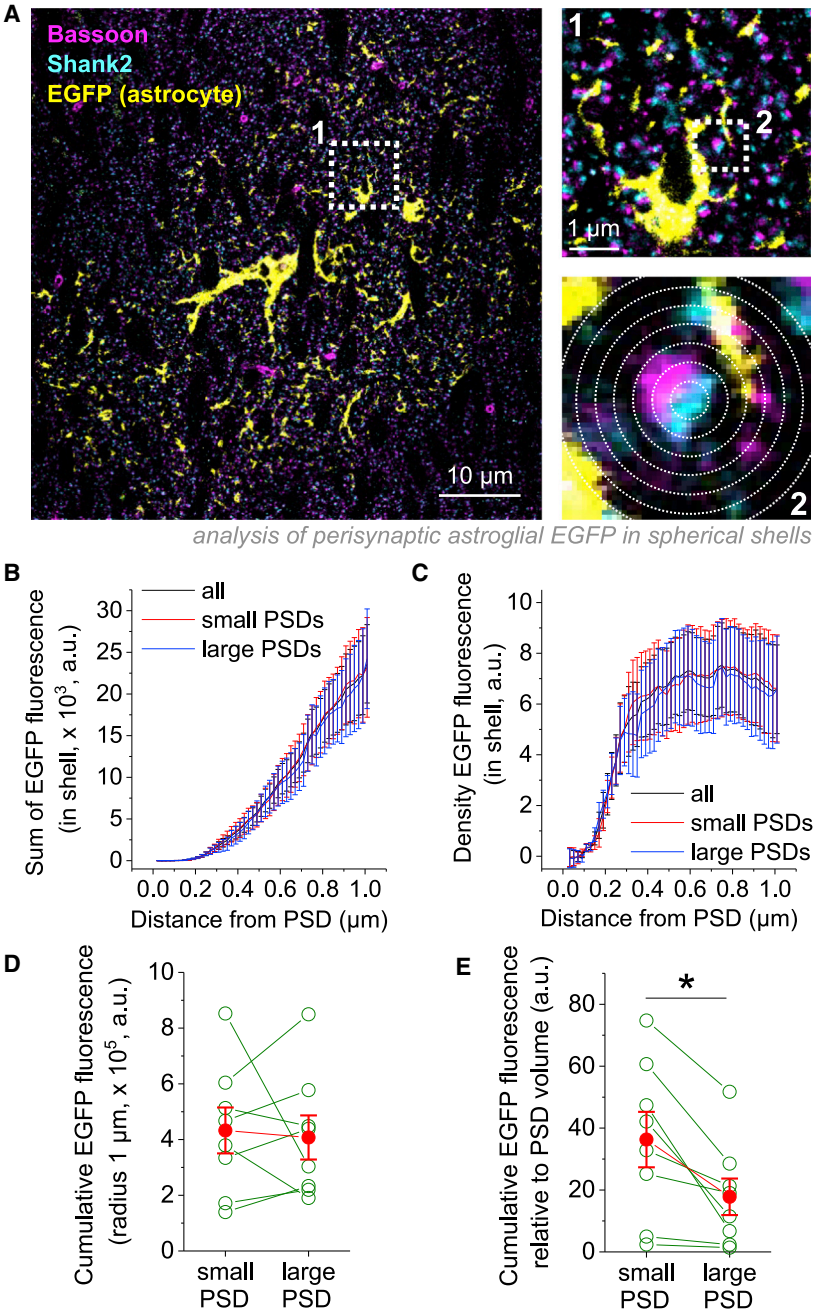

Figure 2. Dependence of the Volume of Perisynaptic Astrocytic Processes on the Size of the Postsynaptic Density (PSD)

(A) ExM of EGFP-expressing astrocytes and pre- and postsynaptic sites (example of a single focal plane). Left panel: low-magnification examples of a triple-label ExM experiment (astrocyte: cytosolic EGFP, yellow; presynaptic label: bassoon, magenta; PSD label: shank2, cyan). The empty elongated regions most likely represent cross sections of pyramidal cell dendrites. Top right panel: enlarged section from boxed region (white, 1) in left panel. Bottom right panel: further magnified view from top right panel (white box, 2). Size, 1.25 × 1.25 µm^2. Analysis was performed in 3D by quantifying astroglial EGFP fluorescence in spherical shells centered on the shank2 label (3 independent experiments, 8 astrocytes, 151 putative synapses). See Results and STAR Methods for further details.

(B) The summed up EGFP fluorescence intensities in spherical shells with increasing radius were calculated (all spines: black). For each analyzed astrocyte, PSDs were categorized as small or large if their volume was below or above the median PSD volume within that astrocyte, respectively (see STAR Methods). The EGFP fluorescence profiles were averaged and displayed for both categories (mean ± SEM, in all panels). The profiles for small and large PSDs were not different (repeated-measures two-way ANOVA, $p < 0.0001$ for distance, $p = 0.908$ for PSD size).

(C) The volume density of EGFP fluorescence intensity was calculated similarly to (B). Again, the EGFP density distribution was not different between small and large PSDs (repeated-measures two-way ANOVA, $p < 0.0001$ for distance, $p = 0.916$ for PSD size).

(D) The cumulative intensity of astroglial EGFP fluorescence within a radius of 1 µm around the PSD was calculated for small and large PSDs covered by individual astrocytes and compared. No statistically significant difference was found (paired Student's t test, $p = 0.783$, $n = 8$ astrocytes).

(E) The cumulative intensity of astroglial EGFP fluorescence was normalized to the PSD size and then compared between small and large PSDs for each astrocyte as in (D). Relative to their size, large PSDs were surrounded by less astrocyte volume (paired Student's t test, $p = 0.0106$, $n = 8$ astrocytes).

with the relative and not the absolute amount of local GLT-1 and astroglial volume at spines. These observations also imply that the stronger local glutamate uptake shields small spines particularly well from glutamate released nearby, for instance at neighboring synapses.

Invasion of Glutamate Depends on Spine Size

We directly tested this hypothesis by combing 2PE fluorescence imaging and glutamate uncaging with whole-cell patch clamp recordings (Matsuzaki et al., 2001; Smith et al., 2003; Sun et al., 2016) of excitatory postsynaptic currents (EPSCs) mediated by N-methyl-D-aspartate receptors (NMDARs). NMDAR EPSCs were chosen in these experiments because of their relatively high affinity to glutamate. Dendrites and spines of individual CA1 pyramidal cells were visualized using 2PE fluorescence microscopy, and glutamate was first uncaged directly at the head of a pseudo-randomly chosen spine (Figure 4A, #1). The NMDAR-mediated component of the uncaging-evoked EPSCs (uEPSCs) was isolated pharmacologically and by recording at a holding potential of +40 mV. The recorded uEPSCs were

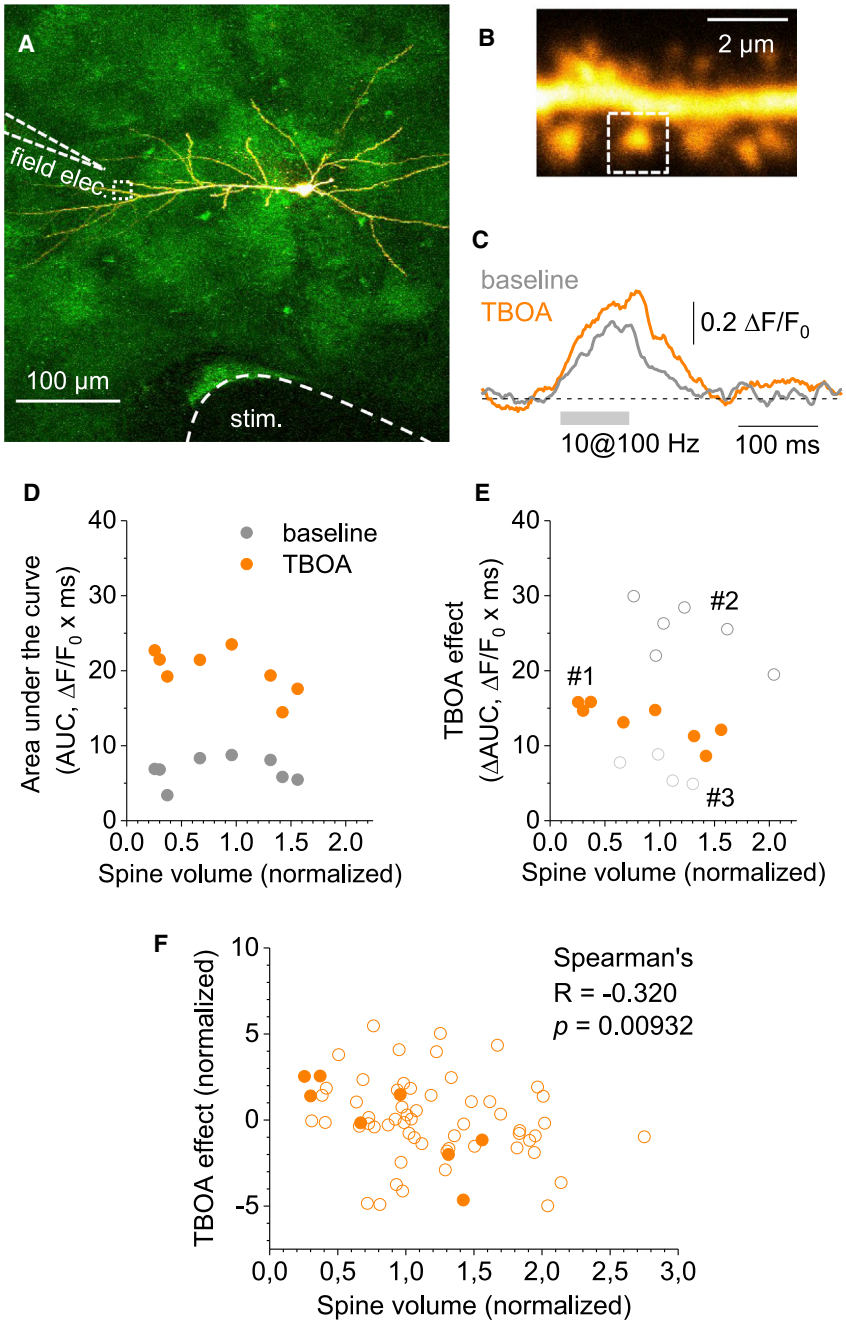

Figure 3. Perisynaptic Glutamate Transients Are More Tightly Controlled by Glutamate Transporters at Small Postsynaptic Spines Than Larger Neighbors

(A) Astrocytic expression of the glutamate sensor iGluSnFR (green; Marvin et al., 2013) visualized in acute hippocampal slices by two-photon excitation fluorescence microscopy. Note that the majority of astrocytes express iGluSnFR. A CA1 pyramidal neuron (yellow) was filled with Alexa Fluor 594 to localize and investigate its spines (dashed box, region of interest [ROI], see B). A field electrode (field elec.) was placed near its dendritic arbor in the *stratum radiatum* and CA3-CA1 axons, i.e., Schaffer collaterals were electrically stimulated (stim.; field responses not shown). Experiments were done in the presence of 50 µM D-APV, 10 µM NBQX, and 100 µM LY341495.

(B) Sample dendritic segment with spines of different sizes (magnified from A; only Alexa Fluor 594 shown) with a ROI positioned on an individual spine.

(C) iGluSnFR fluorescence transients around dendritic spines (B) in response to axonal stimulation (50 sweeps of 10 pulses at 100 Hz every 20 s) were recorded (baseline, dark gray trace) and the effect of the glutamate transporter inhibitor TFB-TBOA (200 nM) was analyzed (orange).

(D) The area under the curve (AUC, $\Delta F/F_0$ × ms) of iGluSnFR fluorescence transients during a baseline recording and after TBOA application were analyzed. Example of a simultaneous recording from eight dendritic spines. For each spine, the volume was measured and normalized to the median spine volume on that dendritic segment. Vertically aligned baseline/TBOA data points represent the same spine during baseline and TBOA.

(E) The TBOA effect was quantified by calculating the AUC difference between TBOA and baseline. #1 corresponds to (D). #2 and #3 represent two other examples.

(F) Summary data from 65 spines (open circles, 12 independent experiments, data obtained from spines in B–D as solid circles). For each set of recorded spines, the average TBOA effect (ΔAUC) was subtracted before pooling all data (see Results). The TBOA effect displayed a negative correlation with the normalized spine volume, suggesting a higher uptake capacity at small spines (Spearman's rank correlation, p = 0.00932, R = −0.320).

mediated almost exclusively by NMDARs because addition of the NMDAR inhibitor APV (50 µM) to the extracellular solution reduced the uEPSC amplitude by >95% (control: 14.7 ± 4.60 pA, n = 5 cells [156 spines in total], APV: 0.489 ± 0.105 pA, n = 5 cells [264 spines in total], not illustrated).

Next, we recorded NMDAR uEPSCs at two different distances from the spine, immediately adjacent and at a distance of 500 nm (Figure 4A, #1 and #2). First, we analyzed if the amplitude or the decay time constant of NMDAR-mediated uEPSCs evoked by uncaging immediately at the spine (#1) correlated with spine size, which was not the case (Figure S4). Second, if the NMDARs mediating the uEPSCs are shielded well from invading glutamate, then moving the site of glutamate uncaging away from the spine should reduce the uEPSC amplitude. The increased average distance that uncaged glutamate needs to travel to the recorded NMDARs could, for instance, increase the probability of glutamate binding to glutamate transporters before reaching recorded NMDARs. This attenuation of the NMDAR-mediated response was calculated as $I_{Glu,\ 0\ nm}/I_{Glu,\ 500\ nm}$ for recordings at 21 spines (Figures 4B and 4C for example). Given the

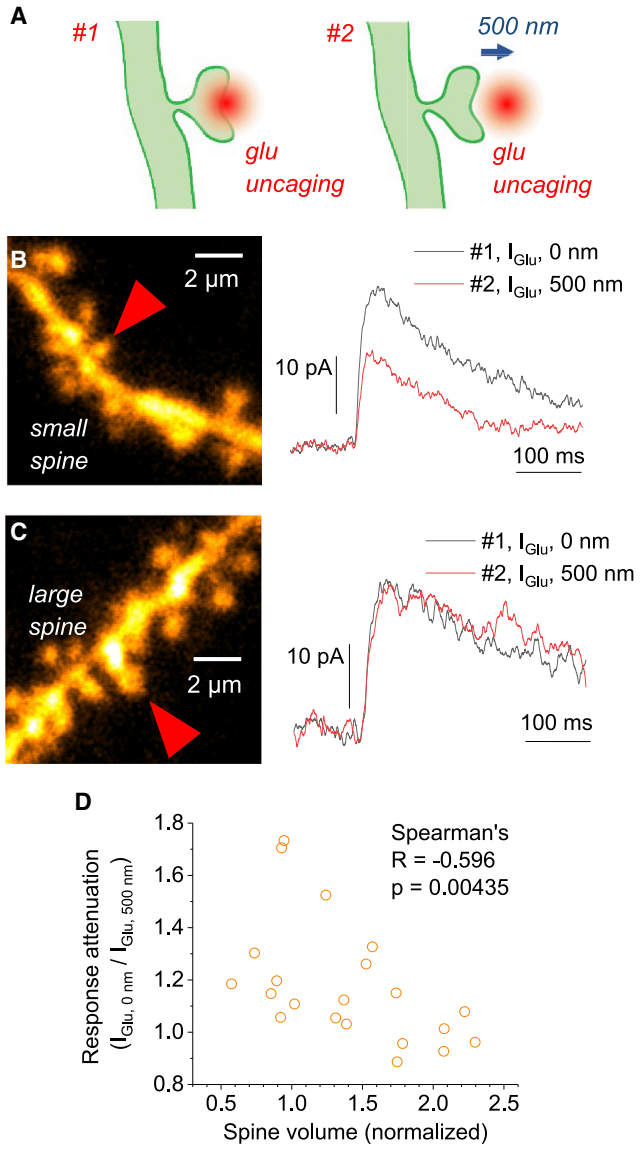

Figure 4. NMDA Receptors (NMDARs) at Small Spines Are More Strongly Protected from Invading Glutamate Than Larger Spines

(A) Schematic illustration of the experimental approach. NMDAR-mediated excitatory postsynaptic currents (EPSCs) were recorded from CA1 pyramidal cells and evoked by two-photon uncaging of glutamate (uEPSC). uEPSC recordings at two different distances from the spine head were obtained by sequential uncaging at 0 nm (#1) and 500 nm (#2). Three of such recordings were recorded for a given spine and averaged for analysis. The uncaging response recorded at 500 nm (#2) is expected to be smaller if, for instance, NMDARs are efficiently shielded by local glutamate transporters.

(B) Example of an uncaging experiment at a relatively small spine. Left panel: dendritic segment; red arrow indicates investigated spine. Right panel: NMDAR-mediated EPSCs at distance #1 (black trace) and #2 (red trace). Note the amplitude reduction after moving the uncaging spot 500 nm away from the spine.

(C) As in (B) for a larger spine from another cell. Note the absence of an amplitude reduction in this example.

(D) For each spine, the uEPSC attenuation ($I_{Glu,\ 0\ nm}$ / $I_{Glu,\ 500\ nm}$) and the spine volume relative to the median spine volume of the corresponding dendritic segment were calculated. Overall, a statistically significant negative correlation was observed (Spearman's rank correlation, R = −0.596, p = 0.00435; n = 21 spines, from 21 different dendrites, 7 pyramidal cells, 5 animals). Note that there was a tendency to pick spines for uncaging experiments that turned out to be relatively large during analysis (normalized volume > 1.0 for 15 out of 21 spines). The strength of the true correlation could, therefore, be underestimated.

high relative amount of GLT-1 (ExM) and the high efficacy of glutamate uptake (iGluSnFR imaging) at small spines, we expected better shielding of NMDARs and thus a higher attenuation of the uEPSC amplitude at small dendritic spines. This was tested by correlating the spine volume (normalized to the median spine volume of the corresponding dendrite) to the attenuation of the NMDAR-mediated EPSCs (average attenuation of 1.18 ± 0.051, n = 21). Indeed, a statistically significant negative correlation was observed (Figure 4D). On its own, this finding may also be explained by different properties of the extracellular space (ECS), into which glutamate is uncaged, and NMDAR properties or distributions at spines of different sizes. However, consistent differences of NMDAR density and subunit composition between large and small spines would also be expected to affect the absolute uEPSC amplitudes and decay time constants (Cull-Candy and Leszkiewicz, 2004). Because neither was observed (Figures S4B and S4C), the stronger attenuation of uEPSCs at small spines likely reflects the spine size dependence of the local efficacy of glutamate uptake and of the relative amount of local GLT-1 and astrocyte process volume, as described above.

Control of NMDAR-Mediated Ca^{2+} Entry by Glutamate Uptake Depends on Spine Size

In the next set of experiments, we further explored how the local control of NMDAR function by glutamate uptake depends on spine size. Because of the importance of NMDAR-mediated Ca^{2+} entry for synaptic plasticity, we focused on NMDAR-mediated Ca^{2+} transients. In these experiments, release of glutamate into the neuropil was emulated by iontophoretic application of glutamate while monitoring Ca^{2+} entry in nearby spines by using established techniques (Minge et al., 2017). CA1 pyramidal cells were filled with Alexa Fluor 594 and the Ca^{2+} indicator Fluo-4 and held in the whole-cell voltage clamp configuration (Figure 5A). We then identified a set of spines on a dendritic segment of that cell, placed an iontophoresis pipette nearby, and used Ca^{2+} influx through the high-affinity NMDARs as a detector of glutamate invasion of the synaptic environment (holding voltage at −20 mV). The ratio (R) of the fluorescence intensities of the Ca^{2+}-indicator Fluo-4 and Alexa Fluor 594 was used as a measure of intracellular Ca^{2+}. Glutamate iontophoresis induced clearly defined Ca^{2+} responses in spines, which were largely inhibited by the NMDAR antagonist APV (Figures 5A and 5B).

The local efficacy of glutamate uptake in shielding synapses from invading glutamate was then tested by pharmacological inhibition of glutamate uptake (200 nM TFB-TBOA) and compared to control recordings, in which no TBOA was added. In both sets of experiments, a baseline recording was obtained first and then a second control recording (green data pairs and bars) or a recording in TBOA (orange data pairs and bars) was acquired. Spine volumes were determined as before and normalized to

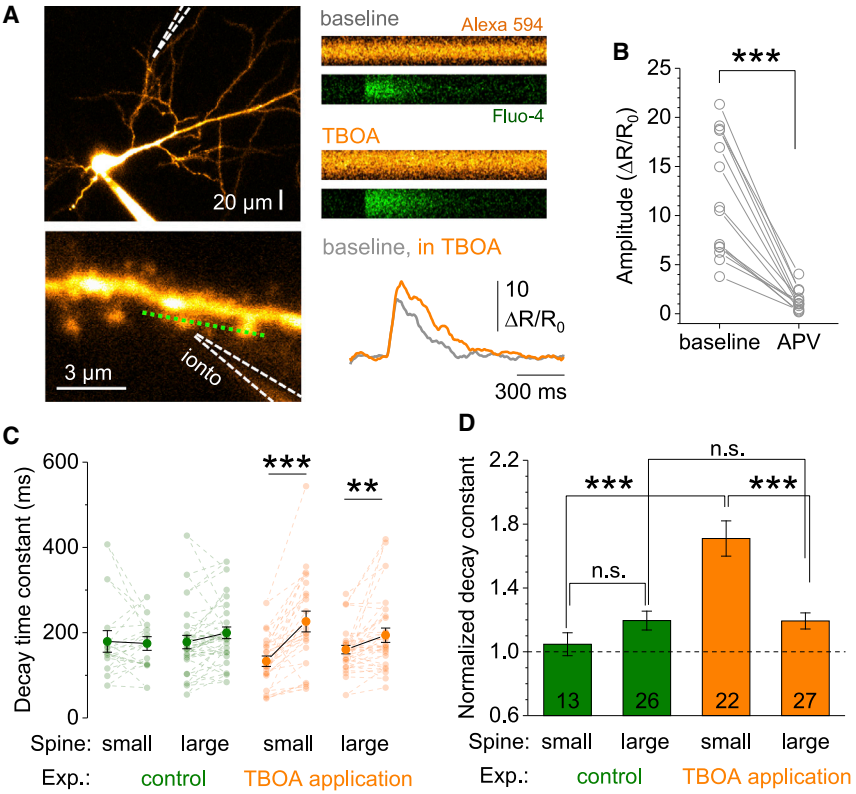

Figure 5. Glutamate Uptake Controls NMDAR-Mediated Ca^{2+} Entry More Effectively at Small Spines Than at Large Ones

(A) Example of a CA1 pyramidal neuron patched and filled with Alexa Fluor 594 (orange) and the Ca^{2+} indicator Fluo-4 (top left panel). Glutamate application by iontophoresis near spines (bottom left panel, dashed lines; average distance to closest spine, 3.9 ± 0.2 µm; n = 12) was combined with postsynaptic depolarization in order to use NMDAR-dependent Ca^{2+} entry as an indicator of glutamate invasion. Simultaneous line scans (bottom left panel, dotted green line) of Fluo-4 and Alexa Fluor 594 fluorescence across multiple spines (sample line scans, top right panels; total duration, 1,350 ms). The ratio (R) of Ca^{2+}-indicator (Fluo-4) and Alexa Fluor 594 fluorescence intensities was used as a measure of intracellular Ca^{2+} (STAR Methods). Note the prominent Ca^{2+} entry representing glutamate entering extracellular space around spines and the effect of inhibiting glutamate transporters with TFB-TBOA (200 nM). All experiments were performed in the presence of 1 µM TTX, 20 µM nifedipine, 10 µM NBQX, 10 µM MPEP, and 50 µM LY341495.

(B) Ca^{2+} transients were highly sensitive to NMDAR inhibition by APV (50 µM). Amplitudes were quantified in this experiment as the ratio of the peak ΔR and R_0, the pretransient baseline. Residual amplitudes in APV were 12.4% ± 1.86% of the pre-APV values ($p < 0.0001$, Student's paired t test; n = 12).

(C) Spine Ca^{2+} transients were recorded a first time to obtain a baseline measurement. In control recordings (green data points), a second recording was performed 8 min later under the same conditions. In experiments probing the strength of glutamate uptake (orange data points), TBOA was applied by the extracellular bath solution and a second recording was obtained. Spines were categorized as small or large if their volume (STAR Methods) was below or above, respectively, the median spine volume of the corresponding dendritic segment. The effects on the decay of Ca^{2+} transients were analyzed (see Figure S5 for further details). Each pair of data points connected by a dashed line represents a single spine during baseline and after a control period or TBOA application. Averages with SEM connected by solid lines. Paired Student's t tests ($p = 0.796$, $p = 0.0501$, $p < 0.0001$, and $p = 0.00129$ from left to right).

(D) The relative change of the decay time constant in control and TBOA experiments was calculated by normalizing the decay time constant of the second measurement to that of the baseline period for each spine. Two-way ANOVA analysis identified significant effects of spine size (small versus large, $p = 0.0216$), treatment (control versus TBOA, $p < 0.0001$), and a significant interaction between both ($p < 0.0001$). Post hoc analysis using the Tukey test revealed that the effect of TBOA was significantly higher in small than in large spines ($p < 0.0001$), whereas spine volume played no statistically relevant role in control recordings ($p = 0.608$, n.s.). Similarly, a statistically significant difference between control and TBOA recordings was observed for small spines ($p < 0.0001$) but not for large spines ($p = 1.00$).

Control experiments: n = 13 small and 26 large spines, recorded from 11 dendritic segments of 11 cells; TBOA experiments: n = 22 small and 27 large spines, recorded from 15 dendritic segments of 15 cells). See Figure S5 for further analyses. Averages with SEM.

the median spine volume on the dendritic segment. Statistical analyses of the recordings are shown in Figures 5C, 5D, and S5. It is noteworthy that similar to glutamate uncaging experiments, we observed no correlation between spine volume and the properties of Ca^{2+} transients obtained during baseline recordings (Figures S5A–S5C). After TBOA application, we detected increases in the resting Ca^{2+} levels (Figure S5D), which is likely the consequence of the previously documented TBOA-induced increase of tonic NMDAR currents (Cavelier and Attwell, 2005; Le Meur et al., 2007), and an unspecific rundown of Ca^{2+} transient amplitudes in most experimental conditions (Figure S5E), which is probably due to strong Ca^{2+} influx after repetitive holding potential increases and glutamate applications at relatively distal dendrites (Rosenmund and Westbrook, 1993). In contrast, the decay time constant was stable in control recordings, and changes of the decay time constant of NMDAR-mediated currents have previously been shown to follow changes of glutamate uptake (Armbruster et al., 2016; Romanos et al., 2019). The decay time constant was therefore used as a readout of a spine-size-specific effect of TBOA (Figures 5C and 5D).

We found that TBOA selectively increased the decay time constant of Ca^{2+} transients at small but not at large spines (Figure 5D). This finding is further supported by a statistically highly significant negative correlation between the normalized spine volume and the effect of TBOA on the Ca^{2+} signal decay time constant (Spearman's rank correlation, $R = -0.589$, $p < 0.0001$, n = 49 spines), which was not observed in control experiments ($R = 0.011$, $p = 0.947$, n = 39 spines). Importantly, experimentally measured changes of the decay time constant were statistically independent of unspecific rundown (Spearman's rank correlation, $R = -0.0268$, $p = 0.856$, n = 88 spines spines) and changes of Ca^{2+} resting levels (Spearman's rank correlation,

R = 0.0939, p = 0.521, n = 88 spines). Together, these observations indicate that the dwell time of iontophoretically applied glutamate in the perisynaptic environment is more tightly controlled by glutamate uptake at small spines than at large spines. They also provide a third line of evidence for a higher local glutamate uptake efficacy at small than at large spines. Probing glutamate handling at single spines of various sizes thus revealed an inverse relationship between postsynaptic spine size and the local efficacy of glutamate uptake, which matches the negative correlation between the relative amount of local GLT-1 and astrocytic process volume and spine size.

DISCUSSION

A variable coverage of glutamatergic synaptic terminals by astrocytic processes and a large percentage of synapses without immediately apposed astrocytic processes are consistent findings in the literature (Gavrilov et al., 2018; Korogod et al., 2015; Lushnikova et al., 2009; Medvedev et al., 2014; Patrushev et al., 2013; Ventura and Harris, 1999; Witcher et al., 2007, 2010). This raised unanswered questions about the functional relevance of differential astrocytic synaptic coverage, for instance for glutamate uptake, and the mechanisms that determine it. Here, we took advantage of more recently developed techniques like ExM to visualize glutamate transporters (GLT-1) and astrocyte volume in the vicinity of synapses and spines (Chen et al., 2015; Chozinski et al., 2016). We then correlated our findings with optical probing of glutamate dynamics with single-spine resolution to establish the functional correlate of differential astrocytic coverage of spines with different sizes.

Investigating the abundance of GLT-1 at the spine surface by using ExM, we found that the total amount of GLT-1 immediately at the spine surface is higher at big spines than at small ones when analyzed close to the spine. Because the strong GLT-1 label in ExM reliably outlined the astrocyte cytosol (Figures 1 and S2), this relationship is likely to also apply to the absolute amount of astrocyte membrane in direct apposition with the spine, which would be in line with a previous report using electron microscopy (Lushnikova et al., 2009). A similar dependency between spine size and the volume of perisynaptic astrocyte processes was not found, which is overall in line with previous studies using electron microscopy (Gavrilov et al., 2018; Patrushev et al., 2013). In addition to the absolute GLT-1/spine colocalization and perisynaptic astroglial volume, we also determined each parameter relative to the spine size for two reasons. First, the amount of GLT-1 relative to the spine size, i.e., the GLT-1 density could determine how well the postsynaptic receptors are covered and protected by glutamate uptake and how likely glutamate can escape from the active synapse. Second, the number of docked vesicles, the active zone size, the release probability, and the size of spines and PSDs are positively correlated (Bartol et al., 2015; Harris and Stevens, 1989; Holderith et al., 2012; Murthy et al., 2001; Schikorski and Stevens, 1997), and glutamate uptake leads to astrocytic sodium entry (Danbolt, 2001; Rose et al., 2018). Therefore, the relative abundance of perisynaptic astrocyte cytosol could determine how easily sodium accumulates in astrocytes and whether that leads to a reduction of the sodium driving force of glutamate uptake. We consistently found that both the amount of GLT-1 at the spine surface and astrocytic process volume relative to the spine size were lower at large than at small spines.

It is important to note that in these experiments and other work using similar tissue fixation protocols, for instance for electron microscopy, ECS is often collapsed. The ECS normally accounts for ~20% of living tissue volume in CA1 *stratum radiatum* (Syková and Nicholson, 2008) and amounts to about double the fraction of tissue volume taken up by astrocytes (Korogod et al., 2015; Medvedev et al., 2014). Chemical fixation can thereby lead to morphological alterations of perisynaptic astrocyte processes and more increased direct apposition of neuronal and astrocytic membranes (Korogod et al., 2015). Indeed, a recent study using STED superresolution microscopy in live organotypic slices discovered new morphological features of astrocytes, such as nodes, shafts, and loops (Arizono et al., 2020). Given the many possible measures of astrocytic coverage of spines and the potential drawbacks of preparations and methods, it is important to establish a functional correlate of astrocytic coverage of synapses. We therefore probed the local efficacy of glutamate uptake and extracellular glutamate spread.

Using glutamate uncaging, we could demonstrate that small spines are better shielded from the invasion of glutamate than larger spines. This individual finding could also be explained by a different ECS configuration (e.g., tortuosity) at small and large spines. New optical methods that visualize the ECS on the nanometer scale in living tissue using STED microscopy (Tønnesen et al., 2018) or imaging of carbon nanotubes (Godin et al., 2017) and mapping the proximity of neuronal and astrocytic surfaces using FRET probes (Octeau et al., 2018) could be useful for testing if the ECS indeed displays spine-size-dependent configurations. Such information would also be useful for modeling glutamate diffusion at spines with different sizes. To estimate the local efficacy of glutamate uptake more directly, we measured the effect of pharmacological glutamate uptake inhibition on glutamate transients evoked by synaptic stimulation and NMDAR-mediated Ca^{2+} entry in response to iontophoretic glutamate application at single spines of various sizes. We consistently found that uptake inhibition had a larger effect at small spines, which indicates that glutamate uptake is more effective at these spines. This result can directly explain why these spines were better shielded in uncaging experiments. Under baseline/control conditions, NMDAR-mediated currents or Ca^{2+} entry did not show a clear spine size dependence (Figures S4 and S5A–S5C), which is likely due to the variations of the uncaging spot position relative to the PSD, amount of uncaged glutamate, and of the placement of the iontophoretic pipette between experiments. Instead, the spine size dependence of the uptake efficiency was robustly unmasked by inhibition of glutamate uptake and moving the glutamate uncaging spot. It is also noteworthy that the size of this effect is not expected to be quantitatively identical between experimental approaches because iGluSnFR fluorescence, NMDAR currents, and especially Ca^{2+} transients, which could also be affected by endogenous buffers and extrusion mechanisms, are non-linear readouts of the extracellular glutamate concentration.

On a qualitative level, all functional experiments pointed toward a higher efficacy of glutamate uptake at small spines.

Because the spine volume of CA1 pyramidal cell dendrites is tightly correlated with the PSD size and the number of presynaptic vesicles (Bartol et al., 2015; Harris and Stevens, 1989; Murthy et al., 2001), our observations imply that, in general, astrocytic glutamate uptake at synapses with a small vesicle pool, small PSD, and low spine volume is particularly effective in constraining extracellular glutamate diffusion. The magnitude of this effect is likely to be underestimated in the present experiments using diffraction-limited 2PE microscopy (Figures 3, 4, and 5) because the volume density of synapses in the CA1 *stratum radiatum* is $\sim$2 μm^{-3} (Rusakov and Kullmann, 1998). Therefore, probing perisynaptic glutamate handling at a small spine will, to some degree, cosample the perisynaptic environment of a nearby, unlabeled synapse, which for statistical reasons is likely larger, and vice versa for probing of a large spine. Thus, the spine size dependence of glutamate uptake is likely to be stronger than that detected here. It correlated best with the relative abundance of glutamate transporters or astrocyte volume at small and large spines in ExM experiments (Figures 1 and 2). It is straightforward to imagine that the higher amount of surface GLT-1 relative to spine size (i.e., local GLT-1 density) at small spines (Figure 1) shields them better from distant glutamate sources (Figure 4) and leads to stronger increases of local glutamate transients (Figure 3) and NMDAR-mediated Ca^{2+} transients (Figure 5) at these spines after inhibition of glutamate uptake. But, although differences of the relative abundance of astrocytic GLT-1 are an intuitive explanation of the size dependence of glutamate uptake, a causal relationship remains to be established. Future work could, for instance, test if an experimentally induced rapid reduction or displacement of GLT-1 has a stronger effect on glutamate dynamics at smaller spines.

Our observation of a spine size dependence of glutamate uptake also adds to the recently emerging notion that glutamate uptake and glutamate transporter localization are regulated on more levels and in a more complex manner than previously appreciated. The deletion of the gap junction protein connexin 30, for instance, resulted in the invasion of the synaptic cleft by astrocyte processes, increased glutamate uptake, and decreased excitatory synaptic transmission (Pannasch et al., 2014). In addition, the mobility of the glutamate transporter GLT-1 on the astrocyte surface has recently been shown to be particularly high and activity and location dependent (Murphy-Royal et al., 2015), which adds another layer of complexity to astrocyte glutamate uptake. Similarly, glutamate uptake is modulated rapidly by burst-like neuronal activity in the cortex (Armbruster et al., 2016) and, more subtle, on a longer timescale of half an hour by pharmacological PAR1 activation in the hippocampus (Sweeney et al., 2017). Furthermore, the activity-dependence of glutamate uptake differs between brain regions (Romanos et al., 2019). We demonstrate that such variability and local adaptation of glutamate uptake can also be found at the level of single synapses.

Functional Significance of Spine-Size-Dependent Glutamate Uptake

At Schaffer collateral synapses, a reduction of glutamate uptake has been shown to increase synaptic crosstalk by GluN2B-containing NMDARs (Scimemi et al., 2004), i.e., it increases the probability of synaptically released glutamate to act on NMDARs at inactive synapses. Similarly, Monte Carlo simulations of synaptic glutamate signaling indicate that removing perisynaptic glutamate uptake increases the activation of perisynaptic NMDARs by synaptically released glutamate (Zheng et al., 2008). Thus, our results suggest that at large postsynaptic spines, released glutamate is more likely to activate perisynaptic NMDARs and to invade the extrasynaptic ECS. Because activation of GluN2B-containing, extrasynaptic NMDARs has been associated with the induction of long-term depression (LTD) (Liu et al., 2004; Papouin et al., 2012), our results also suggest that synaptic plasticity at large spines could be biased toward LTD. At thin spines, the relatively stronger local glutamate uptake is instead likely to confine glutamate signaling more strongly to synaptic GluN2A-containing NMDARs, thus favoring long-term potentiation (LTP) (Papouin et al., 2012). However, there has been a considerable debate about the association between NMDAR subunit composition and the direction of long-term plasticity (Morishita et al., 2007; Shipton and Paulsen, 2013). Exploring if the localization of NMDARs influences the direction and magnitude of synaptic plasticity independently of subtype composition could provide further insights. It is interesting in that regard that increasing GLT-1 expression by ceftriaxone was indeed reported to impair LTD at hippocampal mossy fiber synapses (Omrani et al., 2009).

A stronger glutamate uptake around small spines shields them and their high-affinity NMDARs better from glutamate spilling in from neighboring synapses (Figures 4 and 5). This may prevent activation of their NMDARs and induction of synaptic plasticity when nearby synapses are active. From the perspective of a small spine, its neighbors are likely to be large and, because of the positive correlation of spine size, presynaptic bouton volume, active zone area, and release probability (Holderith et al., 2012; Matz et al., 2010; Murthy et al., 2001; Schikorski and Stevens, 1997), their presynaptic terminals are more likely to release glutamate during presynaptic action potential firing. In this scenario, small spines would be preferentially shielded from their larger and more active neighboring synapses, provided that presynaptic action potential firing is similar and not compensating for the difference of release probability. Independent of these local variations in glutamate uptake and spread between synapses, the synaptically released glutamate is eventually mostly taken up by astrocytes. Therefore, the basic relationship between the amount of released glutamate across the many thousands of synapses within the territory of a single astrocyte and the transporter current recorded at the astrocyte cell body (Diamond et al., 1998; Lüscher et al., 1998) is unaffected by our observations.

The decrease of local glutamate uptake with increasing spine size also indicates that spine growth/shrinkage could be accompanied by changes of local glutamate uptake. Interestingly, induction of LTP is a potent trigger for both acute spine growth (Matsuzaki et al., 2004) and also for changes of perisynaptic astrocyte process motility and structure (Bernardinelli et al., 2014; Perez-Alvarez et al., 2014; Wenzel et al., 1991). Such plasticity-associated structural changes of perisynaptic astrocyte branches are, therefore, expected to modify local glutamate uptake.

The strength of local glutamate uptake could also determine the probability of released glutamate to activate presynaptic

glutamate receptor either at the same or a neighboring synapse. Experiments in the supraoptic nucleus revealed, for instance, that a low coverage of neurons by astrocytes in lactating animals is associated with reduced glutamate uptake and stronger tonic activation of presynaptic metabotropic glutamate receptors (mGluRs) (Oliet et al., 2001). Accordingly, recruitment of presynaptic mGluRs at Schaffer collateral synapses could be more prominent near large postsynaptic spines. Thus, the gradual decrease of perisynaptic glutamate uptake efficiency with increasing postsynaptic spine size represents a rule that could also govern other aspects of synaptic neuron-astrocyte interactions.

Whether the present observations at hippocampal CA3-CA1 synapses also apply to other synapse populations and brain regions remains to be established. Future studies could also explore the functional relevance of different astrocytic coverage of distinct synaptic pathways, as documented, for example, in the cerebellum (Xu-Friedman et al., 2001).

STAR★METHODS

Detailed methods are provided in the online version of this paper and include the following:

- KEY RESOURCES TABLE
- RESOURCE AVAILABILITY
  - Lead Contact
  - Materials Availability
  - Data and Code Availability
- EXPERIMENTAL MODEL AND SUBJECT DETAILS
- METHOD DETAILS
  - Expansion microscopy of spine coverage by GLT-1
  - ExM analysis of the perisynaptic astrocytic volume
  - Stereotactic injections
  - Preparation of acute brain slices
  - Glutamate imaging using iGluSnFR
  - Glutamate uncaging on CA1 pyramidal cell spines
  - Glutamate iontophoresis and Ca^{2+} imaging
- QUANTIFICATION AND STATISTICAL ANALYSIS

SUPPLEMENTAL INFORMATION

Supplemental Information can be found online at https://doi.org/10.1016/j.celrep.2020.108182.

ACKNOWLEDGMENTS

The glutamate sensor iGluSnFR was kindly provided by Loren L. Looger (Janelia Farm Research Campus, Howard Hughes Medical Institute). We thank Dmitri A. Rusakov (London) for helpful comments on a previous version of the manuscript. Research was supported by the Human Frontiers Science Program (HFSP; RGY0084/2012 to C.H. and C.J.J.), the German Academic Exchange Service (DAAD-Go8) Travel Fellowship (to C.H. and C.J.J.), the NRW-Rückkehrerprogramm (C.H.), and German Research Foundation (DFG; SFB1089 B03, SPP1757 HE6949/1, FOR2795, and HE6949/3 to C.H.; SPP1757 young investigator grant to M.K.H.; SFB1089 P03 to M.K.S.; and SFB1089 B03, SPP1757 DI853/5, DI853/3, DI853/4, and DI853/7 to D.D.).

AUTHOR CONTRIBUTIONS

M.K.H. and S.P. performed glutamate imaging experiments. K.B. did all Ca^{2+} imaging. M.K.S., M.K.H., C.D., and J.A.K.-M. established and performed expansion microscopy. N.V. and D.D. performed and analyzed glutamate uncaging experiments. C.H. designed the study, analyzed data, and together with M.K.H. wrote the initial manuscript, to which then all authors contributed.

DECLARATION OF INTERESTS

The authors declare no competing interests.

Received: April 28, 2017
Revised: August 12, 2020
Accepted: September 1, 2020
Published: September 22, 2020

REFERENCES

Anders, S., Minge, D., Griemsmann, S., Herde, M.K., Steinhäuser, C., and Henneberger, C. (2014). Spatial properties of astrocyte gap junction coupling in the rat hippocampus. Philos. Trans. R. Soc. Lond. B Biol. Sci. *369*, 20130600.

Arizono, M., Inavalli, V.V.G.K., Panatier, A., Pfeiffer, T., Angibaud, J., Levet, F., Veer, M.J.T.T., Stobart, J., Bellocchio, L., Mikoshiba, K., et al. (2020). Structural basis of astrocytic Ca 2+ signals at tripartite synapses. Nat. Commun. *11*, 1–15.

Armbruster, M., Hanson, E., and Dulla, C.G. (2016). Glutamate Clearance Is Locally Modulated by Presynaptic Neuronal Activity in the Cerebral Cortex. J. Neurosci. *36*, 10404–10415.

Asano, S.M., Gao, R., Wassie, A.T., Tillberg, P.W., Chen, F., and Boyden, E.S. (2018). Expansion Microscopy: Protocols for Imaging Proteins and RNA in Cells and Tissues. Curr. Protoc. Cell Biol. *80*, e56.

Bartol, T.M., Jr., Bromer, C., Kinney, J., Chirillo, M.A., Bourne, J.N., Harris, K.M., and Sejnowski, T.J. (2015). Nanoconnectomic upper bound on the variability of synaptic plasticity. eLife *4*, e10778.

Bernardinelli, Y., Randall, J., Janett, E., Nikonenko, I., König, S., Jones, E.V., Flores, C.E., Murai, K.K., Bochet, C.G., Holtmaat, A., and Muller, D. (2014). Activity-dependent structural plasticity of perisynaptic astrocytic domains promotes excitatory synapse stability. Curr. Biol. *24*, 1679–1688.

Cavelier, P., and Attwell, D. (2005). Tonic release of glutamate by a DIDS-sensitive mechanism in rat hippocampal slices. J. Physiol. *564*, 397–410.

Chen, F., Tillberg, P.W., and Boyden, E.S. (2015). Optical imaging. Expansion microscopy. Science *347*, 543–548.

Chozinski, T.J., Halpern, A.R., Okawa, H., Kim, H.-J., Tremel, G.J., Wong, R.O.L., and Vaughan, J.C. (2016). Expansion microscopy with conventional antibodies and fluorescent proteins. Nat. Methods *13*, 485–488.

Cull-Candy, S.G., and Leszkiewicz, D.N. (2004). Role of distinct NMDA receptor subtypes at central synapses. Sci. STKE *2004*, re16.

Danbolt, N.C. (2001). Glutamate uptake. Prog. Neurobiol. *65*, 1–105.

Diamond, J.S., Bergles, D.E., and Jahr, C.E. (1998). Glutamate release monitored with astrocyte transporter currents during LTP. Neuron *21*, 425–433.

Feng, G., Mellor, R.H., Bernstein, M., Keller-Peck, C., Nguyen, Q.T., Wallace, M., Nerbonne, J.M., Lichtman, J.W., and Sanes, J.R. (2000). Imaging neuronal subsets in transgenic mice expressing multiple spectral variants of GFP. Neuron *28*, 41–51.

Gavrilov, N., Golyagina, I., Brazhe, A., Scimemi, A., Turlapov, V., and Semyanov, A. (2018). Astrocytic Coverage of Dendritic Spines, Dendritic Shafts, and Axonal Boutons in Hippocampal Neuropil. Front. Cell. Neurosci. *12*, 248.

Genoud, C., Quairiaux, C., Steiner, P., Hirling, H., Welker, E., and Knott, G.W. (2006). Plasticity of astrocytic coverage and glutamate transporter expression in adult mouse cortex. PLoS Biol. *4*, e343.

Godin, A.G., Varela, J.A., Gao, Z., Danné, N., Dupuis, J.P., Lounis, B., Groc, L., and Cognet, L. (2017). Single-nanotube tracking reveals the nanoscale organization of the extracellular space in the live brain. Nat. Nanotechnol. *12*, 238–243.

Harris, K.M., and Stevens, J.K. (1989). Dendritic spines of CA 1 pyramidal cells in the rat hippocampus: serial electron microscopy with reference to their biophysical characteristics. J. Neurosci. *9*, 2982–2997.

Heller, J.P., and Rusakov, D.A. (2015). Morphological plasticity of astroglia: Understanding synaptic microenvironment. Glia *63*, 2133–2151.

Helmchen, F., and Denk, W. (2005). Deep tissue two-photon microscopy. Nat. Methods *2*, 932–940.

Holderith, N., Lorincz, A., Katona, G., Rózsa, B., Kulik, A., Watanabe, M., and Nusser, Z. (2012). Release probability of hippocampal glutamatergic terminals scales with the size of the active zone. Nat. Neurosci. *15*, 988–997.

Holmseth, S., Dehnes, Y., Huang, Y.H., Follin-Arbelet, V.V., Grutle, N.J., Mylonakou, M.N., Plachez, C., Zhou, Y., Furness, D.N., Bergles, D.E., et al. (2012). The density of EAAC1 (EAAT3) glutamate transporters expressed by neurons in the mammalian CNS. J. Neurosci. *32*, 6000–6013.

Korogod, N., Petersen, C.C., and Knott, G.W. (2015). Ultrastructural analysis of adult mouse neocortex comparing aldehyde perfusion with cryo fixation. eLife *4*, e05793.

Le Meur, K., Galante, M., Angulo, M.C., and Audinat, E. (2007). Tonic activation of NMDA receptors by ambient glutamate of non-synaptic origin in the rat hippocampus. J. Physiol. *580*, 373–383.

Liu, L., Wong, T.P., Pozza, M.F., Lingenhoehl, K., Wang, Y., Sheng, M., Auberson, Y.P., and Wang, Y.T. (2004). Role of NMDA receptor subtypes in governing the direction of hippocampal synaptic plasticity. Science *304*, 1021–1024.

Lüscher, C., Malenka, R.C., and Nicoll, R.A. (1998). Monitoring glutamate release during LTP with glial transporter currents. Neuron *21*, 435–441.

Lushnikova, I., Skibo, G., Muller, D., and Nikonenko, I. (2009). Synaptic potentiation induces increased glial coverage of excitatory synapses in CA1 hippocampus. Hippocampus *19*, 753–762.

Marvin, J.S., Borghuis, B.G., Tian, L., Cichon, J., Harnett, M.T., Akerboom, J., Gordus, A., Renninger, S.L., Chen, T.-W., Bargmann, C.I., et al. (2013). An optimized fluorescent probe for visualizing glutamate neurotransmission. Nat. Methods *10*, 162–170.

Matsuzaki, M., Ellis-Davies, G.C., Nemoto, T., Miyashita, Y., Iino, M., and Kasai, H. (2001). Dendritic spine geometry is critical for AMPA receptor expression in hippocampal CA1 pyramidal neurons. Nat. Neurosci. *4*, 1086–1092.

Matsuzaki, M., Honkura, N., Ellis-Davies, G.C.R., and Kasai, H. (2004). Structural basis of long-term potentiation in single dendritic spines. Nature *429*, 761–766.

Matz, J., Gilyan, A., Kolar, A., McCarvill, T., and Krueger, S.R. (2010). Rapid structural alterations of the active zone lead to sustained changes in neurotransmitter release. Proc. Natl. Acad. Sci. USA *107*, 8836–8841.

Medvedev, N., Popov, V., Henneberger, C., Kraev, I., Rusakov, D.A., and Stewart, M.G. (2014). Glia selectively approach synapses on thin dendritic spines. Philos. Trans. R. Soc. Lond. B Biol. Sci. *369*, 20140047.

Minge, D., Senkov, O., Kaushik, R., Herde, M.K., Tikhobrazova, O., Wulff, A.B., Mironov, A., van Kuppevelt, T.H., Oosterhof, A., Kochlamazashvili, G., et al. (2017). Heparan Sulfates Support Pyramidal Cell Excitability, Synaptic Plasticity, and Context Discrimination. Cereb. Cortex *27*, 903–918.

Morishita, W., Lu, W., Smith, G.B., Nicoll, R.A., Bear, M.F., and Malenka, R.C. (2007). Activation of NR2B-containing NMDA receptors is not required for NMDA receptor-dependent long-term depression. Neuropharmacology *52*, 71–76.

Murphy-Royal, C., Dupuis, J.P., Varela, J.A., Panatier, A., Pinson, B., Baufreton, J., Groc, L., and Oliet, S.H.R. (2015). Surface diffusion of astrocytic glutamate transporters shapes synaptic transmission. Nat. Neurosci. *18*, 219–226.

Murthy, V.N., Schikorski, T., Stevens, C.F., and Zhu, Y. (2001). Inactivity produces increases in neurotransmitter release and synapse size. Neuron *32*, 673–682.

Nolte, C., Matyash, M., Pivneva, T., Schipke, C.G., Ohlemeyer, C., Hanisch, U.K., Kirchhoff, F., and Kettenmann, H. (2001). GFAP promoter-controlled EGFP-expressing transgenic mice: a tool to visualize astrocytes and astrogliosis in living brain tissue. Glia *33*, 72–86.

Octeau, J.C., Chai, H., Jiang, R., Bonanno, S.L., Martin, K.C., and Khakh, B.S. (2018). An Optical Neuron-Astrocyte Proximity Assay at Synaptic Distance Scales. Neuron *98*, 49–66.e9.

Oliet, S.H., Piet, R., and Poulain, D.A. (2001). Control of glutamate clearance and synaptic efficacy by glial coverage of neurons. Science *292*, 923–926.

Omrani, A., Melone, M., Bellesi, M., Safiulina, V., Aida, T., Tanaka, K., Cherubini, E., and Conti, F. (2009). Up-regulation of GLT-1 severely impairs LTD at mossy fibre–CA3 synapses. J. Physiol. *587*, 4575–4588.

Pannasch, U., Freche, D., Dallérac, G., Ghézali, G., Escartin, C., Ezan, P., Cohen-Salmon, M., Benchenane, K., Abudara, V., Dufour, A., et al. (2014). Connexin 30 sets synaptic strength by controlling astroglial synapse invasion. Nat. Neurosci. *17*, 549–558.

Papouin, T., Ladépêche, L., Ruel, J., Sacchi, S., Labasque, M., Hanini, M., Groc, L., Pollegioni, L., Mothet, J.-P., and Oliet, S.H.R. (2012). Synaptic and extrasynaptic NMDA receptors are gated by different endogenous coagonists. Cell *150*, 633–646.

Patrushev, I., Gavrilov, N., Turlapov, V., and Semyanov, A. (2013). Subcellular location of astrocytic calcium stores favors extrasynaptic neuron-astrocyte communication. Cell Calcium *54*, 343–349.

Perez-Alvarez, A., Navarrete, M., Covelo, A., Martin, E.D., and Araque, A. (2014). Structural and functional plasticity of astrocyte processes and dendritic spine interactions. J. Neurosci. *34*, 12738–12744.

Protopapas, A.D., Vanier, M., and Bower, J.M. (1998). Simulating large networks of neurons. Methods in Neuronal Modeling: From Ions to Networks (MIT Press), p. 461.

Romanos, J., Benke, D., Saab, A.S., Zeilhofer, H.U., and Santello, M. (2019). Differences in glutamate uptake between cortical regions impact neuronal NMDA receptor activation. Commun. Biol. *2*, 127.

Rose, C.R., Felix, L., Zeug, A., Dietrich, D., Reiner, A., and Henneberger, C. (2018). Astroglial Glutamate Signaling and Uptake in the Hippocampus. Front. Mol. Neurosci. *10*, 451.

Rosenmund, C., and Westbrook, G.L. (1993). Rundown of N-methyl-D-aspartate channels during whole-cell recording in rat hippocampal neurons: role of Ca2+ and ATP. J. Physiol. *470*, 705–729.

Rusakov, D.A., and Kullmann, D.M. (1998). Extrasynaptic glutamate diffusion in the hippocampus: ultrastructural constraints, uptake, and receptor activation. J. Neurosci. *18*, 3158–3170.

Schikorski, T., and Stevens, C.F. (1997). Quantitative ultrastructural analysis of hippocampal excitatory synapses. J. Neurosci. *17*, 5858–5867.

Scimemi, A., Fine, A., Kullmann, D.M., and Rusakov, D.A. (2004). NR2B-containing receptors mediate cross talk among hippocampal synapses. J. Neurosci. *24*, 4767–4777.

Sheng, M., and Hoogenraad, C.C. (2007). The postsynaptic architecture of excitatory synapses: a more quantitative view. Annu. Rev. Biochem. *76*, 823–847.

Shipton, O.A., and Paulsen, O. (2013). GluN2A and GluN2B subunit-containing NMDA receptors in hippocampal plasticity. Philos. Trans. R. Soc. Lond. B Biol. Sci. *369*, 20130163.

Smith, M.A., Ellis-Davies, G.C., and Magee, J.C. (2003). Mechanism of the distance-dependent scaling of Schaffer collateral synapses in rat CA1 pyramidal neurons. J. Physiol. *548*, 245–258.

Sun, W., Matthews, E.A., Nicolas, V., Schoch, S., and Dietrich, D. (2016). NG2 glial cells integrate synaptic input in global and dendritic calcium signals. eLife *5*, e16262.

Sweeney, A.M., Fleming, K.E., McCauley, J.P., Rodriguez, M.F., Martin, E.T., Sousa, A.A., Leapman, R.D., and Scimemi, A. (2017). PAR1 activation induces rapid changes in glutamate uptake and astrocyte morphology. Sci. Rep. *7*, 43606.

Syková, E., and Nicholson, C. (2008). Diffusion in brain extracellular space. Physiol. Rev. *88*, 1277–1340.

Tønnesen, J., Inavalli, V.V.G.K., and Nägerl, U.V. (2018). Super-Resolution Imaging of the Extracellular Space in Living Brain Tissue. Cell *172*, 1108–1121.e15.

Ventura, R., and Harris, K.M. (1999). Three-dimensional relationships between hippocampal synapses and astrocytes. J. Neurosci. *19*, 6897–6906.

Wenzel, J., Lammert, G., Meyer, U., and Krug, M. (1991). The influence of long-term potentiation on the spatial relationship between astrocyte processes and potentiated synapses in the dentate gyrus neuropil of rat brain. Brain Res. *560*, 122–131.

Witcher, M.R., Kirov, S.A., and Harris, K.M. (2007). Plasticity of perisynaptic astroglia during synaptogenesis in the mature rat hippocampus. Glia *55*, 13–23.

Witcher, M.R., Park, Y.D., Lee, M.R., Sharma, S., Harris, K.M., and Kirov, S.A. (2010). Three-dimensional relationships between perisynaptic astroglia and human hippocampal synapses. Glia *58*, 572–587.

Xu-Friedman, M.A., Harris, K.M., and Regehr, W.G. (2001). Three-dimensional comparison of ultrastructural characteristics at depressing and facilitating synapses onto cerebellar Purkinje cells. J. Neurosci. *21*, 6666–6672.

Zhang, W.H., Herde, M.K., Mitchell, J.A., Whitfield, J.H., Wulff, A.B., Vongsouthi, V., Sanchez-Romero, I., Gulakova, P.E., Minge, D., Breithausen, B., et al. (2018). Monitoring hippocampal glycine with the computationally designed optical sensor GlyFS. Nat. Chem. Biol. *14*, 861–869.

Zheng, K., Scimemi, A., and Rusakov, D.A. (2008). Receptor actions of synaptically released glutamate: the role of transporters on the scale from nanometers to microns. Biophys. J. *95*, 4584–4596.

STAR★METHODS

KEY RESOURCES TABLE

REAGENT or RESOURCE	SOURCE	IDENTIFIER
Antibodies		
chicken anti GFP	Abcam	ab13970; RRID:AB_300798
guinea-pig anti GLT-1	Millipore	AB1783; RRID:AB_90949
rabbit anti GLAST	Abcam	ab416; RRID:AB_304334
goat anti chicken Alexa Fluor 488	ThermoFisher	A11039; RRID:AB_2534096
goat anti guinea-pig Alexa Fluor 568 or 594	ThermoFisher	A11075; RRID:AB_2534119 or A11076; RRID:AB_2534120
goat anti rabbit biotin	Jackson ImmunoResearch	111-066-144; RRID:AB_2337970
guinea-pig anti-Shank2	Synaptic Systems	162 204; RRID:AB_2619861
mouse anti Bassoon	Enzo	SAP7F407; RRID:AB_10618753
goat anti mouse biotin	Jackson ImmunoResearch	115-067-003; RRID:AB_2338586
Bacterial and Virus Strains		
AAV GFAP-iGluSnFR	PennCore	AAV1.GFAP.iGluSnFr.WPRE.SV40
Chemicals, Peptides, and Recombinant Proteins		
Tetrodotoxin	Tocris	Cat. #1069
Nifedipine	Sigma-Aldrich	Cat. #N7634
LY341495	Tocris	Cat. #4062
MPEP	Abcam	Cat. ab120008
TFB-TBOA	Tocris	Cat. #2532
D-APV	Abcam	Cat. ab120003
Alexa Fluor 594 Hydrazide	ThermoFisher	Cat. A10438
Fluo-4, pentapotassium salt	ThermoFisher	Cat. F14200
NBQX	Abcam	Cat. ab120046
MNI-caged-L-glutamate	Tocris	Cat. #1490
Experimental Models: Organisms/Strains		
C57BL6/N mice	Charles River	Strain Code 027
Wistar rats	Charles River	Strain Code 003
Thy1-YFP mice	Feng et al., 2000	N/A
GFAP-EGFP mice	Nolte et al., 2001	N/A
Software and Algorithms		
Custom imaging data analysis scripts	This manuscript	N/A

RESOURCE AVAILABILITY

Lead Contact

Further information and requests for resources and reagents should be directed to and will be fulfilled by the Lead Contact, Christian Henneberger (christian.henneberger@uni-bonn.de).

Materials Availability

This study did not generate new unique reagents.

Data and Code Availability

The data supporting the current study and custom code have not yet been deposited in a public repository because of their highly diverse nature and formats but are available from the lead contact on request. Original/source data for figures in the paper are also available on request.

EXPERIMENTAL MODEL AND SUBJECT DETAILS

All animal procedures were conducted in accordance with the regulations of the European Commission and all relevant national and institutional guidelines and requirements. Procedures have been approved by the Landesamt für Natur, Umwelt und Verbraucherschutz Nordrhein-Westfalen (LANUV, Germany) where required.

All animals used in this study were housed under 12 h light/dark conditions and were allowed *ad libitum* access to food and water. For expansion microscopy, male and female Thy1-YFP mice (Feng et al., 2000) or male and female GFAP-EGFP mice (Nolte et al., 2001), in which a subset of hippocampal astrocytes express EGFP, were sacrificed at an age of 7 to 10 weeks. iGluSnFR experiments were performed on 7 to 10-week-old male C57BL6/N mice (see below for virus injection procedure). Glutamate iontophoresis experiments were performed on 3-5 week-old male Wistar rats. For glutamate uncaging experiments, male C57BL/6J mice between 26 and 44 days of age were used. All experiments were performed in the *stratum radiatum* of the CA1 region of the hippocampus.

METHOD DETAILS

Expansion microscopy of spine coverage by GLT-1

The expansion microscopy (ExM) technique was adopted from the literature (Asano et al., 2018; Chen et al., 2015; Chozinski et al., 2016). Thy1-YFP mice were deeply anesthetized and transcardially perfused with 4% paraformaldehyde in phosphate buffered saline (PBS, pH 7.4). Brains were removed from the skull, postfixed for 1-2 h at 4°C before being stored in PBS. Coronal sections of 70 μm thickness were cut on a vibratome and blocked for 6 h at room temperature (RT) in blocking buffer (5% normal goat serum, 0.1% Triton X-100 in PBS). Primary antibodies were incubated in blocking buffer for 48 h at 4°C. Antibodies used were: chicken anti GFP (1:5000; Abcam ab13970, lot GR89472-16), guinea-pig anti GLT-1 (1:500; Millipore AB1783, lot 2572967), rabbit anti GLAST (1:200; Abcam ab416, lot GR266539-1). After 3x20 min washing in blocking buffer, samples were incubated with secondary antibodies at 4°C for 12 h. Secondary antibodies used were: goat anti chicken Alexa Fluor 488 (1:200; ThermoFisher A11039), goat anti guinea-pig Alexa Fluor 568 or 594 (1:200; ThermoFisher A11075 or A11076), goat anti rabbit biotin (1:400; Jackson ImmunoResearch 111-066-144). After washing in blocking buffer, slices were pre-expansion imaged in PBS containing 0.05% p-phenyldiamine. Further treatment was adopted from Chen et al. (2015) and Chozinski et al. (2016). Briefly, slices were incubated in 1 mM methylacrylic acid-NHS (Sigma Aldrich #730300) at RT for 1 h. After washing, slices were incubated for 45 min in monomer solution (in g/100 mL PBS: 8.6 sodium acrylate, 2.5 acrylamide, 0.15 N,N′-methylenebisacrylamide, 11.7 NaCl) at 4°C. Then, slices were incubated with gelling solution (monomer solution supplemented with %(w/v): 0.01 4-hydroxy-TEMPO, 0.2 TEMED, 0.2 APS) at 4°C for 5 min before transferring them to a chamber sandwiched between coverslips at 37°C for 2 h. Coverslips were removed and proteins were digested in digestion buffer (50 mM Tris pH 8, 1 mM EDTA, 0.5% Triton X-100, 0.8 M guanidine, 16 U/ml proteinase K) at 37°C for 12-14 h. For a triple label (Figure S2), slices were incubated with streptavidin Alexa Fluor 647 (1:1000; Jackson ImmunoResearch 016-600-084) in PBS with 3% bovine serum albumine at RT for 1 h. For expansion, slices were then incubated for 2.5 h in distilled water and water was exchanged repeatedly every 15-20 min. Finally, slices were transferred to a custom mounting chamber filled with distilled water, mounted by superglueing its edges to the chamber's bottom and sealed with a coverslip on the top. Image stacks were acquired on a Leica SP8 confocal microscope using a 40x/1.1NA water immersion objective and hybrid detectors (pixel dimension x-y plane 90 × 90 nm^2, z-steps 426 nm, typical stack size x-y-z of 1000 × 1000 × 70 voxels). The expansion factor was determined by measuring gel sizes before and after expansion. On average, we measured an expansion factor of 4.55 ± 0.05 (n = 9). An upper limit of the spatial resolution obtainable by expansion microscopy was established using a punctate staining against Homer1 (see Figure S1). Using expansion microscopy, we could resolve Homer1 puncta as small as ~40 nm (x-y plane) and ~270 nm (z-plane). This is in line with previous reports (Chen et al., 2015; Chozinski et al., 2016). Images were deconvolved using Huygens Essential and analyzed in 3D with FIJI, Elastix and custom-written software (Chozinski et al., 2016).

GLT-1 coverage of dendritic spines of hippocampal CA1 pyramidal cells was analyzed by using the RG2B colocalization tool of ImageJ. Coverage was determined by counting voxels positive for GLT-1 and YFP in spherical volumes of interest with varying radii. The volume of interest was centered on the spine's center of mass of YFP fluorescence. A measure of relative GLT-1 coverage was obtained by normalizing this pixel count to the spine volume. This analysis was performed in spheres of interest with three diameters (0.42 μm, 0.50 μm, 0.65 μm, see Figure 1 and Results). Also see Quantification and Statistical Analysis below for further details.

The *spine volume* was obtained from Z axis profiles of spine YFP fluorescence. Z-profiles of the average intensity in square regions of interest (~1 × 1 μm^2 real size, ~4 × 4 μm^2 post-expansion) centered on the spine were plotted for each individual spine. The area under the curve of each profile was fitted by a Gaussian function and used as a measure of spine volume. This measure of spine volume was used instead of, for instance, threshold-based volume or surface renderings because it can be readily obtained from both ExM and two-photon excitation microscopy data (see below), it is relatively insensitive to the optical resolution and it does not require setting a threshold. To account for varying YFP expression levels between cells and varying imaging conditions between experiments, individual spine volumes were normalized to the median volume of neighboring spines on the same dendritic segment. We used the median because spine volumes were often not normally distributed in these experiments. Individual spines were categorized as 'small' or 'large' if their volume was below or above, respectively, this median spine volume.

ExM analysis of the perisynaptic astrocytic volume

Brain perfusion and fixation of GFAP-EGFP mice were performed as described above, with an overnight post-fixation period. Coronal hippocampal slices (70 μm thickness) were cut on a vibratome and blocked overnight (ON) at 4°C in permeabilization buffer (0.5% Triton X-100 in PBS pH 7.4). Antibodies were incubated individually for 24 h at 4°C in permeabilization buffer (0.5% Triton X-100 in PBS) if not otherwise stated. In between antibody incubations, slices were washed in PBS 3x20 min at RT. Primary antibodies: chicken anti GFP (1:5000; Abcam ab13970, lot GR236651-g), guinea-pig anti-Shank2 (1:100; Synaptic Systems 162 204), mouse anti Bassoon (1:100; Enzo SAP7F407, lot 06231712). Secondary antibodies: goat anti chicken Alexa Fluor 488 (1:200; ThermoFisher A11039, lot 1899519), goat anti guinea pig Alexa Fluor 568 (1:200; ThermoFisher A11075, lot 1692965), goat anti mouse biotin (1:200; Jackson ImmunoResearch 115-067-003, lot 130148). After washing in PBS, slices were incubated with Hoechst 33342 (1:2000, Invitrogen H3570, lot 1874027) in distilled water for 10 min at RT. After washing again, slices were imaged in PBS before expansion with a 20x/0.75 NA objective in a Leica SP8 confocal microscope. ExM was performed as described above (see also Asano et al., 2018, section Basic ProExM protocol for intact tissues), with the following modifications. Incubation with the linker methylacrylic acid-NHS, gelling and digestion steps were performed as described above, except digestion occurred at 25°C for 12-14 h. After digestion, slices were incubated with streptavidin Alexa Fluor 647 (1:200; Jackson ImmunoResearch 016-600-084, lot 124695) in PBS at RT for 2 h. For expansion, slices were then incubated in distilled water (adjusted pH 7.4 with NaOH) for 2.5 h at RT and water exchanged repeatedly every 15-20 min. Finally, slices were mounted on poly-lysine coated μ-Slide 2 well Ibidi-chambers and sealed with a poly-lysine coated coverslip on top, adding a drop of water to prevent the gel from drying. μ-Slide 2 Ibidi chambers and coverslips were poly-lysine coated by incubation with poly-l-lysine solution (0.01% w/v in water (P8920, Sigma-Aldrich, lot: 050M4339) for at least 45 min at RT shaking and dried with pressured air.

Fluorescence microscopy was performed on a Leica SP8 inverted confocal microscope using a 40x/1.1NA objective and hybrid detectors. For each sample, the expansion factor was determined by identifying the same cells labeled with Hoechst 33342 in the dentate gyrus before and after expansion and then measuring their sizes pre- and post-expansion. The expansion factor of an individual sample was then calculated as the average ratio of post- and pre-expansion sizes of ~10 measures from the same sample. On average, we obtained an expansion factor of 4.61 ± 0.18 (n = 4) in these experiments. For analysis, image stacks of astrocytes (EGFP) and covered pre- and postsynaptic structures (Bassoon and Shank2) were acquired (x-y-z, typically ~2500 × 2500 × 15 voxels, voxel dimensions ~0.1 μm x 0.1 μm x 0.4 μm, corresponding to pre-expansion dimensions of ~0.02 μm x 0.02 μm x 0.09 μm). Image stacks were then deconvolved in Leica Systems software and further processed with FIJI and MATLAB.

Individual putative single synaptic contacts were identified by direct apposition of pre- and post-synaptic labeling (bassoon and shank2, respectively) within the astrocyte territory (without inspection of their astrocytic 3D coverage to avoid a selection bias). 3D volumes of interest of putative single synaptic contacts were obtained by cropping a volume of 1.5 × 1.5 × 1.5 μm^3 centered on the center of mass of post-synaptic shank2 fluorescence, i.e., the post-synaptic density (PSD). The PSD volume was then calculated as the cumulative fluorescence intensity of shank2, measured in a rectangular volume of interest centered and exclusively containing the post-synaptic domain. For each analyzed astrocyte, PSDs were categorized as 'small' or 'large' if their volume was below or above, respectively, the median PSD volume for that astrocyte. For each synaptic contact, the distribution of astrocytic EGFP fluorescence was quantified in 3D after background subtraction. This analysis was performed by determining the astroglial EGFP fluorescence in spherical shells with a thickness of 20 nm and increasing diameter (see Figure 2 for an illustration) centered on the shank2 label (PSD center of mass as above). For each shell, the sum and average of EGFP fluorescence intensity was determined. For each astrocyte, profiles of EGFP intensity over distance at small and large PSDs were averaged, both for the sum and for the average of EGFP fluorescence. From these, the population averages and SEM across all astrocytes were calculated (Figures 2B and 2C). For other analyses (Figures 2D and 2E), the cumulative EGFP fluorescence across all shells was obtained, averaged for small and large PSDs in each astrocyte (paired data) and then compared across individual astrocytes.

Stereotactic injections

For the expression of the glutamate sensor iGluSnFR (Marvin et al., 2013) in astrocytes, an AAV virus expressing iGluSnFR under a GFAP promoter (AAV1.GFAP.iGluSnFr.WPRE.SV40, PennCore) was injected bilaterally into the ventral hippocampus. C57BL6/N mice (4 weeks old, Charles Rivers Laboratories) were injected intra-peritoneally (i.p.) with a ketamin/medotomidine anesthesia (100 and 0.25 mg per kg body weight in NaCl, injection volume 0.1 mL per 10 g body weight, ketamin 10%, betapharm; Cepotir 1 mg/ml, CPPharma). First, the head fur was removed and the underlying skin disinfected. After ensuring that the animal was under deep anesthesia, the head was fixed in a stereotactic frame (Model 901, David Kopf Instruments). After making an incision, bregma was localized. Next, the coordinates for the ventral hippocampus (relative to bregma: anterior −3.5 mm, lateral ± 3 mm, ventral −2.5 mm) were determined and the skull was locally opened with a dental drill. Under control of a micro injection pump (100 nl/min, WPI) 1 μl viral particles were injected with a beveled needle nanosyringe (nanofil 34G BVLD, WPI). After retraction of the syringe, the incision was sutured using absorbable thread (Ethicon). Finally, the anesthesia was stopped by i.p. injection of atipamezol (2.5 mg per kg body weight in NaCl, injection volume 0.1 mL per 10 g body weight, antisedan 5 mg/ml, Ventoquinol). To ensure analgesia, carprofen (5 mg/kg in NaCl, injection volume 0.1 ml/20 g body weight, Rimadyl 50 mg/ml, Zoetis) was injected subcutaneously directly, 24 h and 48 h after the surgery.

Preparation of acute brain slices

Preparation of acute hippocampal slices was performed as described previously (Anders et al., 2014; Minge et al., 2017; Zhang et al., 2018). Briefly, animals were deeply anesthetized with isoflurane, decapitated and 300 μm thick horizontal hippocampal slices were prepared in an ice-cold solution containing (in mM): NaCl 60, sucrose 105, KCl 2.5, $MgCl_2$ 7, NaH_2PO_4 1.25, ascorbic acid 1.3, sodium pyruvate 3, $NaHCO_3$ 26, $CaCl_2$ 0.5 and glucose 10 (osmolarity 305–310 mOsm). Slices were kept in slicing solution at 34°C for 15 min and then transferred to an artificial cerebrospinal fluid (ACSF) solution containing (in mM): NaCl 131, KCl 2.5, $MgSO_4$ 1.3, NaH_2PO_4 1.25, $NaHCO_3$ 21, $CaCl_2$ 2 and glucose 10 (pH 7.35–7.45; osmolarity adjusted to 297–303 mOsm) at RT. Slices were allowed to rest for at least 45 min at RT before experiments were started.

Glutamate imaging using iGluSnFR

Slices were transferred to a submersion-type recording chamber mounted on an Olympus FV10MP two-photon excitation (2PE) fluorescence microscope with a 25x/1.05NA objective and superfused with ACSF at 34°C. For the spine imaging experiments shown, a CA1 pyramidal neuron was briefly patched (5-10 min, using a Multiclamp 700B amplifier) with an intracellular solution containing (in mM): KCH_3O_3S 135, HEPES 10, di-Tris-Phosphocreatine 10, $MgCl_2$ 4, Na_2-ATP 4, Na-GTP 0.4 Alexa Fluor hydrazide 0.2 (pH adjusted to 7.2 using KOH, osmolarity 290-295 mOsm). A dendritic segment with a variety of different apparent spine sizes and an iGluSnFR-expressing astrocyte (identified by their typical ramified morphology with fine processes) nearby was selected and an extracellular field electrode pulled from borosilicate glass (2-4 MΩ resistance) was placed nearby. Then, a concentric bipolar stimulation electrode (FHC, CBARC75) was placed in the Schaffer collateral pathway ~200 μm from the imaging site. iGluSnFR fluorescence responses to 100 Hz stimulation (for 100 ms, 70 μA intensity, 50 sweeps) were imaged at an 2PE wavelength of 910 nm using a femtosecond pulsed laser (Vision S, Coherent) and a photomultiplier tube connected to a single photon counting board (Picoharp with Symphotime software, Picoquant). Throughout the study, the laser power was adjusted so that the fluorescence intensity at the region of interest was equivalent to that obtained with imaging at 3 mW at the slice surface. The analysis of iGluSnFR transients in 1 μm^2 ROIs around individual spines was performed offline using custom written MATLAB (Mathworks) scripts and Clampfit (Molecular Devices). The iGluSnFR fluorescence intensity over time was extracted from single photon counting data and corrected for excitation-independent photons, i.e., by subtracting for each time window the photon count that corresponds to the photon count rate measured with the laser shutter closed. Fluorescence intensity changes (ΔF) were normalized to the baseline fluorescence intensity (F_0). Experiments were excluded from analysis if the amplitudes of iGluSnFR fluorescence transients were < 1.5% $\Delta F/F_0$. Spine volumes were determined from stack images (z step 0.5 μm) through the dendritic segment and were analyzed as described for ExM (see above). Relative spine volumes were calculated normalizing to the median of 10 neighboring spines.

Glutamate uncaging on CA1 pyramidal cell spines

CA1 pyramidal cells in acute hippocampal slices (300 μm thick, see above for further details) were recorded from at RT. We used a combination of whole-cell recordings and two-photon uncaging of MNI-glutamate (Tocris) to elicit glutamatergic responses at single synapses of hippocampal CA1 pyramidal neurons (Matsuzaki et al., 2001; Smith et al., 2003; Sun et al., 2016). Cells were patched using borosilicate glass pipettes (3-6 MΩ) filled with an intracellular solution containing (in mM): 100 Cs-gluconate, 4 $MgCl_2$, 4 ATP disodium salt, 0.5 EGTA, 10 HEPES, 30 CsCl, 5 QX-314 Bromide and 0.025 Alexa Fluor 594 (Thermo Fisher). To avoid evoking action potential-induced currents and to isolate NMDAR currents, the recording solution was supplemented with 1 μM TTX (Biotrend) and 10 μM CNQX (Tocris). Once a whole-cell configuration was established the perfusion was stopped and MNI-glutamate and D-serine (Sigma) were added directly to the recording chamber to achieve a final concentration of 5 mM and 100 μM respectively. D-serine was added to avoid a potential contribution of variable NMDAR co-agonist site occupancy to the results. MNI-glutamate uncaging-induced currents were recorded only between 10 and 25 minutes after drug application to ensure an equal concentration of the substances in the chamber, while maintaining cell viability. NMDAR-mediated currents were recorded at +40 mV holding potential upon photolysis of MNI-glutamate using a Prairie Technologies Ultima Multiphoton Microscopy System (Bruker) in combination with the Prairieview software controlling two Ti:sapphire lasers and two scan heads. The uncaging laser pulse (duration 0.6 ms, wavelength 730 nm) was delivered at a laser power of 20 mW as measured at the objective. To keep the laser power at the spine comparable over all experiments, only spines between 20 and 30 μm below the surface were considered. The glutamate-induced current at every spine was tested three times at each distance (Figure 4 and legend) and averaged to obtain an optimal signal-to-noise ratio. Igor Pro 7 (WaveMetrics) was used for all offline analyzes including the fitting of the uEPSCs obtained at 0 nm and 500 nm from the spine. Most uEPSCs were approximated with the custom-written fit function (adopted from Protopapas et al., 1998)

$$y(t) = y_0 + a \times \left(e^{-(t - onset)/decay} - e^{-(t - onset)/rise}\right)$$

for $t \geq onset$ and $y(t) = y_0$ otherwise, with uEPSCs starting at $t = onset$ and *decay* and *rise* referring to the decay and rise time constants, respectively. The amplitude was determined by evaluating $y(t)$ at its maximum $t_{peak} = onset + ln(decay/rise) \times (decay \times rise)/(decay - rise)$. See Figure S4A for an example. In a few cases the decay of the uEPSC had to be fit with a mono-exponential curve to obtain the decay time. An image stack (z steps of 1 μm) encompassing the recorded spine, the dendrite and nearby spines was obtained to analyze the spine volumes, as above (ExM).

It should be noted that the spatial resolution of both diffraction-limited two-photon excitation imaging and uncaging is insufficient to precisely mimic glutamate release from a presynaptic vesicle into the synaptic cleft. The initial spatial distribution of uncaged glutamate is determined by the uncaging point spread function (PSF), which is typically a few hundred nm wide in x-y and a multiple of that in z (Helmchen and Denk, 2005; Matsuzaki et al., 2001; Smith et al., 2003). When aiming at a spine surface, the PSF inevitably covers adjacent structures, visible or not, like spines and presynaptic boutons and the surrounding extracellular space, and the exact configuration changes from synapse to synapse. Therefore, the amount and extracellular distribution of glutamate uncaged into the extracellular space and the exact relative positions of spines, sampled NMDARs and uncaged glutamate will vary considerably from synapse to synapse, which could contribute to the variability of absolute uEPSC amplitudes (Figure S4). This also increases the variability of the attenuation of NMDAR-mediated currents. Therefore, the statistical relevance of the correlation between spine size and attenuation (Figure 4D) is an underestimate.

Glutamate iontophoresis and Ca^{2+} imaging

Ca^{2+} imaging was performed as previously documented (Minge et al., 2017). Acute slices were transferred to a submersion-type recording chamber mounted on a Scientifica 2PE fluorescence microscope with a 40x/0.8 NA objective (Olympus), or a Olympus FV10MP 2PE fluorescence microscope with a 25x/1.05 NA objective, and superfused with ACSF at 34°C containing 10 μM NBQX, 1 μM TTX, 20 μM nifedipine, 50 μM LY341495, 10 μM MPEP. A CA1 pyramidal neuron was patched with a borosilicate glass pipette (3-4 MΩ resistance, using a Multiclamp 700B amplifier) with an intracellular solution containing (in mM): KCH_3O_3S 135, HEPES 10, di-Tris-Phosphocreatine 10, $MgCl_2$ 4, Na_2-ATP 4, Na-GTP 0.4, Alexa Fluor 594 hydrazide 0.04 (to visualize the patched cell including its dendritic spines) and the Ca^{2+}-sensitive fluorescent dye Fluo-4 0.2 (pH adjusted to 7.2 using KOH, 290-295 mOsm). Iontophoretic glutamate application was used to locally stimulate NMDARs at dendritic spines (MVCS-C-01C-150, NPI). The microiontophoretic pipette (60-80 MΩ resistance) was filled with 150 mM glutamic acid (pH adjusted to 7.0 with NaOH) and 50 μM Alexa Fluor 594 hydrazide or Alexa Fluor 633 to localize the pipette. Patched cells with their dendritic spines and the microiontophoretic pipettes were visualized by 2PE imaging (wavelength 800 nm) and the microiontophoretic pipettes were brought in close proximity (~4 μm) to a dendritic segment. To avoid leakage of glutamic acid a small positive retain current (< 8 nA) was constantly applied. Neurons were held in the voltage clamp configuration at −70 mV. Recordings were discarded if the initial access resistance exceeded 16 MΩ or changed by more than 20% during the recording. The holding voltage was increased to −20 mV 30 s before iontophoretic glutamate application, to release the Mg^{2+} block of NMDARs, and decreased back to −70 mV after four stimulation trials. The iontophoretic stimulation intensity (pulse duration < 0.7 ms, pulse intensity −0.5 to −0.9 μA) was adjusted to obtain stable Fluo-4 fluorescence intensity transients using line scanning across multiple spines (~400 Hz, see Figure 5 for an illustration). Four baseline recordings were performed before 200 nM TFB-TBOA was bath-applied for at least eight minutes and another four recordings were obtained. In otherwise identical control experiments, TBOA was not added to the superfusion solution. In a subset of experiments 50 μM D-APV was washed in to confirm the NMDAR-dependence of the Fluo-4 response. For analysis, averages of the four baseline and four test trials were calculated and background-corrected. The Fluo-4 signal (F) was then normalized to the corresponding Alexa Fluor 594 signal (A) to obtain the ratio R = F/A. Responses to ionotophoretic glutamate application were further quantified by calculating the response's peak ratio (R_{MAX}), the resting ratio before the stimulus (R_0) and the response amplitude ($\Delta R/R_0 = (R_{MAX}-R_0)/R_0$). The decay of responses was approximated by a monoexponentially decaying function. Spine volumes were determined from Alexa Fluor 594 image stacks (z-step 0.25 - 0.5 μm) as described above (ExM).

QUANTIFICATION AND STATISTICAL ANALYSIS

Image analysis was performed in FIJI/ImageJ (NIH), Huygens Essential (Scientific Volume Imaging), Elastix (https://doi.org/10.1109/TMI.2009.2035616) and MATLAB (Mathworks). Numerical and statistical analysis was performed in Excel (Microsoft), Origin Pro (OriginLab Corporation) and MATLAB (Mathworks). In the text, results are given as mean ± standard error of the mean (SEM) unless stated otherwise. n denotes the number of experiments. In graphs, statistical significance is indicated by asterisks. * for $p < 0.05$, ** for $p < 0.01$ and *** for $p < 0.001$. Paired and unpaired Student's t test and other analyses were used as appropriate and as indicated in the text and figure legends. All statistical tests were two-tailed. In some experiments, measurements at small and large spines on the same dendritic segment were compared (e.g., Figures 1 and 2). A paired statistical test was used in these cases, because measurements at small and large spines were obtained from the same sample. In other experiments, Spearman's rank correlation was used to analyze pooled data (Figures 3 and 4), because the number of spines per individual experiment/dendrite was sometimes low (Figure 3) or one (Figure 4). In these analyses, the volume of each spine was normalized to the median spine volume of the corresponding dendritic segment before pooling all data for statistical analysis using Spearman's rank correlation.

OXFORD

Cerebral Cortex, 2022, **00**, 1–21
https://doi.org/10.1093/cercor/bhab440
Original Article

Optical Analysis of Glutamate Spread in the Neuropil

E. A. Matthews[1,2,11,†], W. Sun[1,12,†], S. M. McMahon[1,13,†], M. Doengi[3], L. Halka[3], S. Anders[4], J. A. Müller[2], P. Steinlein[1,5], N. S. Vana[1], G. van Dyk[1], J. Pitsch[2,6], A. J. Becker[2,6], A. Pfeifer[7], E. T. Kavalali[8], A. Lamprecht[5], C. Henneberger[4,9,10], V. Stein[3], S. Schoch[2,6] and D. Dietrich[1]

[1]Department of Neurosurgery, University Hospital Bonn, 53127 Bonn, Germany
[2]Section for Translational Epilepsy Research, Department of Neuropathology, University Hospital Bonn, 53127 Bonn, Germany
[3]Institute of Physiology, Medical Faculty, University of Bonn, 53115 Bonn, Germany
[4]Institute of Cellular Neurosciences, Medical Faculty, University of Bonn, 53127 Bonn, Germany
[5]Department of Pharmaceutics, Institute of Pharmacy, University of Bonn, Bonn, Germany
[6]Department of Epileptology, University Hospital Bonn, 53127 Bonn, Germany
[7]Institute of Pharmacology and Toxicology, University Hospital, University of Bonn, 53127 Bonn, Germany
[8]Department of Pharmacology, The Vanderbilt Brain Institute, Vanderbilt University, Nashville, TN 37240-7933, USA
[9]German Center for Neurodegenerative Diseases (DZNE), 53127 Bonn, Germany
[10]Institute of Neurology, University College London, London, WC1N 3BG, UK
[11]Current address: Department of Neurosurgery, Duke University, Durham, NC, USA
[12]Current address: Department of Neuroscience, The Ohio State University, Columbus, OH, USA
[13]Current address: Department of Neuroscience, University of Wisconsin, Madison, WI, USA
Address correspondence to Prof. Dr Dirk Dietrich, Department of Neurosurgery, University Hospital Bonn, Venusberg Campus 1, Bonn 53127, Germany. Email: dirk.dietrich@uni-bonn.de; and Prof. Dr Susanne Schoch, Institute of Neuropathology, University Hospital Bonn, Venusberg Campus 1, Bonn 53127, Germany. Email: susanne.schoch@uni-bonn.de
[†]E. A. Matthews, W. Sun, and S. M. McMahon have contributed equally to this work

Abstract

Fast synaptic communication uses diffusible transmitters whose spread is limited by uptake mechanisms. However, on the submicron-scale, the distance between two synapses, the extent of glutamate spread has so far remained difficult to measure. Here, we show that quantal glutamate release from individual hippocampal synapses activates extracellular iGluSnFr molecules at a distance of >1.5 μm. 2P-glutamate uncaging near spines further showed that alpha-amino-3-hydroxy-5-methyl-4-isoxazolepropionic acid (AMPA)-Rs and N-methyl-D-aspartate (NMDA)-Rs respond to distant uncaging spots at approximately 800 and 2000 nm, respectively, when releasing the amount of glutamate contained in approximately five synaptic vesicles. The uncaging-induced remote activation of AMPA-Rs was facilitated by blocking glutamate transporters but only modestly decreased by elevating the recording temperature. When mimicking release from neighboring synapses by three simultaneous uncaging spots in the microenvironment of a spine, AMPA-R-mediated responses increased supra-additively. Interfering with extracellular glutamate diffusion through a glutamate scavenger system weakly reduced field synaptic responses but not the quantal amplitude. Together, our data suggest that the neuropil is more permissive to short-range spread of transmitter than suggested by theory, that multivesicular release could regularly coactivate nearest neighbor synapses and that on this scale glutamate buffering by transporters primarily limits the spread of transmitter and allows for cooperative glutamate signaling in extracellular microdomains.

Keywords: glutamate signaling, iGluSnFr, multivesicular release, neurotransmitter diffusion, synaptic crosstalk

Introduction

The billions of neurons in the brain are wired to networks and form functional ensembles that are essential to generate distinct behaviors (Yuste 2015). Neurons are connected structurally and functionally through submicrometer-sized synapses at which signaling to the downstream neurons happens by the release of diffusible neurotransmitters from presynaptic vesicles. The function of synapses goes beyond simple relay stations and they represent a major element for memory formation and storage of information in the brain by virtue of their adjustable synaptic strength (Abbott and Regehr 2004; Varshney et al. 2006; Benna and Fusi 2016). The storage capacity of the brain scales with the number of synapses that operate independently (Varshney et al. 2006; Benna and Fusi 2016). To ensure synaptic independence and avoid diffusible neurotransmitters activating the neighboring neurons, synaptic junctions are surrounded by astrocytes that take up and clear released neurotransmitters (Murphy-Royal et al. 2017).

Mammalian brains are tightly packed with synapses (~2/μm^3) with an average nearest neighbor distance of only ~450 nm and those closely spaced synapses mostly originate from different presynaptic neurons (Rusakov and Kullmann 1998; Mishchenko et al. 2010; Bourne 2013; Uppal et al. 2015). Therefore, the question arises whether

Received: August 8, 2021. **Revised:** November 3, 2021. **Accepted:** November 9, 2021

receptor activation beyond 0.5 μm by diffusing transmitters can completely be avoided by glutamate clearance mechanisms. The physical distance at which synaptically released glutamate can activate glutamate receptors is difficult to address experimentally and was only amenable to theoretical analysis. For such theoretical analyses, the neuropil was modeled as a porous medium and glutamate diffusion out of the synaptic cleft and into the porous medium as well as its binding to remote glutamate receptors was numerically simulated. These studies collectively concluded that synaptic cross-talk only leads to a negligible activation of alpha-amino-3-hydroxy-5-methyl-4-isoxazolepropionic acid (AMPA)-Rs at neighboring synapses (at ~500 nm, less than ~3% of the synaptic response) while a low level of cross-talk activation of NMDA receptors of ~10% was considered likely (Rusakov and Kullmann 1998; Barbour 2001; Rusakov 2001; Zheng et al. 2008; Zheng and Rusakov 2015).

In agreement with this theoretical viewpoint, several functional studies of cortical synaptic terminals identified cross-talk mediated by NMDA-Rs under certain conditions (Asztely et al. 1997; Lozovaya et al. 1999; Diamond 2001; Pankratov and Krishtal 2003; Scimemi et al. 2004; Arnth-Jensen et al. 2002; Savtchenko and Rusakov 2005). AMPA-Rs display a much lower affinity to glutamate, so AMPA-R mediated cross-talk would be smaller when compared to that mediated by NMDA-Rs and AMPA-Rs would also respond only to activity from a more restricted neighborhood. Therefore, cross-talk mediated by this type of receptor will require a high spatial density of activated synapses, which may be difficult to achieve experimentally. Accordingly, in some studies, synaptic cross-talk at AMPA-Rs remained undetectable while cross-talk at NMDA-Rs was observed under the same conditions (Lozovaya et al. 1999; Pankratov and Krishtal 2003). Other studies in the cerebellum successfully demonstrated synaptic cross-talk to AMPA-Rs situated on neighboring synapses or release sites (Barbour et al. 1994; Rossi et al. 1995; Silver et al. 1996; Kinney et al. 1997; Overstreet et al. 1999; Carter and Regehr 2000; DiGregorio et al. 2002; Szapiro and Barbour 2007).

However, to the best of our knowledge, in these studies, the maximum distance at which cross-talk can occur at NMDA-Rs or AMPA-Rs remained unknown because neither the glutamate-releasing synapses nor the site of receptor activation could directly be localized with the electrophysiological methods used.

Having an experimental estimate of the action range of glutamate at AMPA and NMDA receptors would not only help to validate theoretical studies but would also allow to evaluate, based on regional densities of synapses, how many neighbors might be coactivated and how strongly after the release of single or multiple vesicles of glutamate.

Here, we aimed at deriving experimental estimates of the spatial action of glutamate by directly visualizing individual active synapses and the spatial distribution of activated optical glutamate reporter proteins. We further created defined point-like sources of glutamate with 2P-photon uncaging and determined at what distance AMPA-Rs and NMDA-Rs responded to photorelease of glutamate to probe the action of glutamate on the submicron scale. Our results suggest that the hippocampal neuropil permits a wider spread of glutamate than predicted by theoretical studies and an increase in glutamate receptor activation of 4–5 folds in the neighborhood: In the case of multivesicular release or coincident activity of multiple synapses in an extracellular microdomain, we estimate that cross-talk responses of up to several pA may occur at AMPA-Rs in the nearest neighbor synapse (~50% of the quantal amplitude at 500 nm) and at NMDA-Rs of approximately 20 synapses in the proximity of up to 2 μm, if their Mg-block is removed concomitantly.

Materials and Methods

Animals

All procedures were planned and performed in accordance with the guidelines of the University of Bonn Medical Centre Animal-Care-Committee as well as the guidelines approved by the European Directive (2010/63/EU) on the protection of animals used for experimental purposes. According to the ARRIVE guidelines, all efforts were made to minimize pain and suffering and to reduce the number of animals used. Mice were housed in a temperature (22 ± 2 °C) and humidity ($55 \pm 10\%$)-controlled environment with food/water *ad libitum* and nesting materials (nestlets, Ancare, USA) under a 12 h light–dark-cycle (light-cycle 7 am/7 pm). Animals were given at least 1 week to acclimatize to the animal facility before surgery and were alone housed after surgery. Male and female C57Bl6/N mice (Charles River, Sulzfeld, Germany) were used between the ages of P15 and P20, except where other ages are noted in the results.

Slice Preparation

Animals were anesthetized with isofluorane gas, decapitated, and the brain was removed and submerged into ice-cold dissection solution (in mM): 87 NaCl, 2.5 KCl, 1.25 NaH_2PO_4, 7 $MgCl_2$, 0.5 $CaCl_2$, 25 $NaHCO_3$, 25 glucose, and 75 sucrose (gassed with 95%O_2/5% CO_2). Frontal or ventral horizontal slices (300 μm thick) were made on a vibratome (Leica VT 1200 or Thermo Scientific HM650V) and incubated at 35 °C for 30 min in a submerged chamber filled with the dissection solution. Slices were then transferred to a holding chamber filled with oxygenated artificial cerebral spinal fluid (ACSF) until the experiments began. The ACSF contained (in mM): 124 NaCl, 3 KCl, 1.25 NaH_2PO_4, 2 $MgCl_2$, 2 $CaCl_2$, 26 $NAHCO_3$, and 10 glucose, pH 7.4 (Sigma-Aldrich), and was continuously bubbled with 95%O_2/5% CO_2. This solution was used for perfusion during the subsequent electrophysiology recording and imaging experiments.

Electrophysiological Recordings

Slices were positioned in a recording chamber on the stage of a microscope and perfused with the recording solution which routinely contained 25 μM APV and 10 μM TTX or other blocker cocktails as stated in the text. Patch pipettes were pulled on a vertical puller (Narashige PP-830) with a resistance of 4.5–6 MΩ. Pipette solution for the voltage clamp experiments contained (in mM): 125 K-gluconate, 4 Na_2-ATP, 2 $MgCl_2$, 10 HEPES, 20 KCl, 3 NaCl, 0.5 EGTA (pH = 7.3, 280–290 mOsm), and 25 μM Alexa 594 or 100 μM tetramethyl-rhodamine (TMR, for experiments in Fig. 3, we used 400 μM TMR) to visualize spines. For experiments to determine the spatial range for NMDA receptors, Cs-based pipette solution was used. It contained (in mM) 130 CsOH, 15 CsCl, 130 D-gluconic acid, 2 $MgCl_2$, 10 HEPES, 0.5 EGTA, 5 QX314 (pH = 7.3, 280–290 mOsm), and 25 μM Alexa 594. Holding potential was set at −65 mV, except for experiments using Cs-based pipette solution, which was set at +40 mV to unblock NMDA receptors from Mg^{2+}. Electrophysiological data combined with glutamate uncaging were acquired on a 2-photon rig equipped with an Ultima multiphoton microscope (Bruker) with two independent pairs of scanning mirrors coupled to two Chameleon vision II lasers (Coherent). The amplifier was an EPC-10 (HEKA), and it was controlled by PatchMaster software (HEKA), which was triggered by the PrairieView software (Bruker) to coordinate the uncaging and imaging lasers, as well as the recording software. The electrophysiological data were sampled at 20 kHz and filtered at 3 kHz. Imaging data for the optical reporter of synaptically released glutamate (iGluSnFr) were acquired on a Nikon A1R MP 2-photon scanning microscope (Nikon) equipped with a BVC-700 (Dagan) amplifier and using the WinWCP software (Strathclyde) for current clamp recording. The miniature EPSC (mEPSC) response to enzymatic scavengers of glutamate was recorded on a conventional electrophysiology rig equipped with an EPC-7 amplifier (HEKA) using pCLAMP 9 software (Molecular Devices).

The following procedures were used to collect fEPSP data: Isoflurane (Baxter) was used to sedate the animals before they were decapitated. The brain was removed from the skull and chilled for 1 min in cooled (4 °C) artificial cerebrospinal fluid (ACSF) containing in mM: 125 NaCl; 2.6 KCl; 1.4 $MgSO_4$; 2.5 $CaCl_2$; 1.1 NaH_2PO_4; 27.5 $NaHCO_3$ and 11.1 D-glucose; pH 7.3, 310 mosm/kg. The hippocampus was cut transversally into 400 μm slices (VT1200S, Leica). Slices were equilibrated in a custom-made submerged chamber in ACSF continuously gassed with carbogen (95% O_2; 5% CO_2) for 30 min at 32 °C, and subsequently kept at RT. fEPSP recordings were obtained from P15 to P25 animals. During experiments, slices were continuously superfused with ACSF supplemented with 10 mM HEPES and 2 mM sodium pyruvate. Glutamate-pyruvate transaminase was applied in a concentration of 5 U/mL. Paired fEPSPs with an interstimulus interval of 40 ms were evoked by stimulating Schaffer collaterals at 0.033 Hz with a pulse duration of 0.2 ms. fEPSPs were recorded in the stratum radiatum of the CA1 region using glass microelectrodes (Science Products, Hofheim, Germany) filled with ACSF. Data were acquired using a Multiclamp 700B amplifier (Axon Instruments), digitized on a Digidata 1322A (Axon Instruments) and stored on a PC. All experiments were carried out at room temperature (22–24 °C). fEPSP slopes were used as a measure of dendritic activity and determined between 20 and 80% of the maximum field amplitude.

Glutamate Uncaging

To ensure accurate and repeatable results, the following alignment and calibration steps were performed every day. After the lasers were turned on and warmed up, the beam alignment for the imaging and uncaging lasers was checked at the objective using a fluorescent target. The laser power was controlled by a Conoptics EOM and was measured at the objective with a slide power meter (Thorlabs) to generate an uncaging power calibration curve for the day. The correspondence between the *x* and *y* pointings for both sets of scan mirrors was calibrated using a fluorescent plastic slide, and any required adjustments were entered in the PrairieView control software. Uncaging laser wavelength was 720 nm; imaging wavelength was determined by the experiment requirements as stated in the main text. MNI-Glu (Tocris) was prepared by dissolution into ACSF at 30 mM, then aliquoted in 100 μL portions and frozen. Aliquots were thawed immediately before addition to the recording chamber, and were never recycled/reused after thawing.

Cells were voltage clamped in the whole cell mode for 10 min to allow filling of dendritic spines. Only spines and dendritic shaft segments at a depth of 20–30 μm from the tissue surface were targeted to ensure that the uncaging power was not attenuated differently by scattering and other effects between experiments. Once a dendrite at the correct depth and orientation was found, perfusion of the recording solution was halted, and 300 μL of ACSF containing 30 mM 4-methoxy-7-nitroindolinyl-caged-L-glutamate (MNI-caged glutamate, caged glutamate) was carefully pipetted into the recording chamber. The bath volume before application of caged-glutamate was kept at 1.5 mL, such that after addition of caged-glutamate the final concentration of MNI-Glu in the recording chamber was 5 mM. The recording experiment resumed after the caged compound had been in the bath for 10 min to allow complete diffusion into the slice. A high-resolution z-stack of the targeted spine was taken to ensure that there were no dendrites or spines above or below the targeted spine from the same cell. Uncaging points were positioned orthogonally to the broadest part of the spine head and parent dendrite using the imaging laser, and the position was rechecked automatically following each uncaging protocol to eliminate any experiments where movement artifacts may have influenced the relative distance between the uncaging point and the spine head.

Typical experiments used 10 uncaging points at 1 Hz, spaced 100 nm apart, and beginning uncaging at the furthest point from the spine head. The uncaging pulses were 0.6 ms in duration, with the power was set so as to elicit an uncaging EPSC (uEPSC) at the spine head of nominally 12 pA (accepting 10–14pA due to trial-to-trial fluctuations). This amplitude matches the size of mEPSCs commonly reported and observed in the lab (data not shown). The laser power value required for this amounted to ∼23 mW and was used throughout the study.

Fitting uEPSCs

To optimally measure the amplitude of even small uEPSCs, the recorded currents were fitted with a difference of two exponential functions being defined by two-time constants describing rise (2.3 ± 0.3 ms) and decay times (9.1 ± 0.6 ms, $n = 27$) and a scaling factor describing the amplitude.

Induction of SE by Suprahippocampal Kainic Acid Application

Surgery, and the induction of SE and postoperative care were all previously described in detail (Pitsch et al. 2019). Briefly, 70 nL kainic acid (20 mM, Tocris) was injected above the left hippocampal CA1 region (-2AP -1.4ML -1.1DV, {Paxinos, 2012 #2224}) of 15 anesthetized [16 mg/kg xylazine (Xylariem, ecuphar) and 100 mg/kg ketamine, i.p. (Ketamin 10%, WDT)] adult male C57Bl6/N mice. Control injections were performed with the same volume of 0.9% NaCl. Animals were used 5–9 days following the injection.

Determination of the Optical Resolution/Width of the Point-Spread-Function of the Uncaging Laser Spot

A common test to estimate the width of a point-spread-function (PSF) is to image/scan a subresolution-sized fluorescent bead so that the apparent size of the bead in the image reflects the dimension of the underlying PSF. The full width at half-maximum fluorescent intensity can be extracted and calculated by fitting a Gaussian function to the diameter of the scanned bead (full width at half maximum – FWHM). Here, we aimed to determine the resolution of our optical system in situ, near a spine in the slice, and used a dye-filled spine itself to probe the shape of the PSF. The level of laser-induced bleaching of the spine was used to calculate the overlap of the PSF of the uncaging laser with the spine. The level of bleaching will rise the closer we bring the uncaging/bleaching spot to the spine and will reach a maximum (spine > PSF) when the PSF is fully contained in the spine (in *xy* plane, see Fig. 6F). Therefore, if a Gaussian is taken to estimate the shape of the PSF, the increase in level of bleaching when bringing the PSF/laser spot closer to the spine will follow the integral of that part of the Gaussian, which overlaps and bleaches the spine. The level of bleaching ("norm. Bleaching," Fig. 1) was fitted with a cumulative distribution function (CDF) of a Gaussian yielding the FWHM of the underlying Gaussian describing the PSF:

$$1 - 0.5\left(1 + \mathrm{erf}\left(\frac{x - x_0}{\left(\frac{\mathrm{FWHM}}{2.3548}\right) - \sqrt{2}}\right)\right)$$

Fluorescence Correlation Spectroscopy to Determine the Excitation Volume of the Optical Uncaging System

We used two-photon fluorescence correlation spectroscopy recordings acquired with the Ultima multiphoton microscope (Bruker Corporation, Billerica, USA) as employed for uncaging experiments (720 nm, 60× Nikon NIR Apo water objective NA 1.0) to estimate the uncaging excitation volume. The laser power at the sample was measured and kept between ∼5 and 7 mW. Emitted fluorescence was filtered by an IR-blocker and a band-pass filter 550/100 (AHF analysentechnik AG, Tübingen, Germany) before being detected by a cooled PMT (bh HPM-100-40 Hybrid Detector, Becker & Hickl GmbH, Berlin Germany). Three recordings (each 120 s) were performed in 1.5 mL of a 50 nM tetramethylrhodamine-dextran (D3307, Thermo Scientific, Waltham, USA) dissolved into ddH_2O at 18 °C while parking the laser beam in the center of the scan field. Time-correlated single photon counting was performed using the bh SPC-150 module and bh SPCM software (version 9.66, Becker & Hickl GmbH, Berlin, Germany). Autocorrelograms were calculated from photon arrivals times and fitted using the FFS data processor 2.7 (SSTC, Minsk, Belarusian state university) using the standard 3D-diffusion model:

$$G(t) = \frac{1}{N'} \frac{1}{\left(1 + \frac{t}{\tau}\right)\sqrt{1 + \frac{t}{a^2\tau}}} + 1$$

in which N' is the apparent average number of molecules, τ is the translational diffusion time, t is the lag time, and $a = \frac{\omega_z}{\omega_{xy}}$, ω_{xy} and ω_z being the lateral and axial $\frac{1}{e^2}$ -widths of the 2P PSF, respectively (a was set to 3.43). Residuals of the fit as shown in Figure 6 were calculated by dividing the difference between the autocorrelogram and it's fit by the standard deviation of the autocorrelogram. The standard deviation was computed based on dividing the fluorescent intensity trace in appropriate subsets according to Wohland et al. 2001. N' provides an estimate on the number of fluorophores in the effective detection volume. As this effective detection volume is an open volume without physical walls, fluorophores are moving across this boundary and contribute to the number of collected photons even when they have left the actual geometrically defined volume of the PSF (Nagy et al. 2005). Therefore $V_{eff} > V_{psf}$ and also for the number of fluorophores in V_{psf}, $N{:}N' > N$. N can be calculated from N' by multiplying with the γ-factor, $\gamma = 1/\sqrt{8}$, a geometric factor that depends on the spatial shape of the detection profile (Nagy et al. 2005; Lakowicz 2009). In our

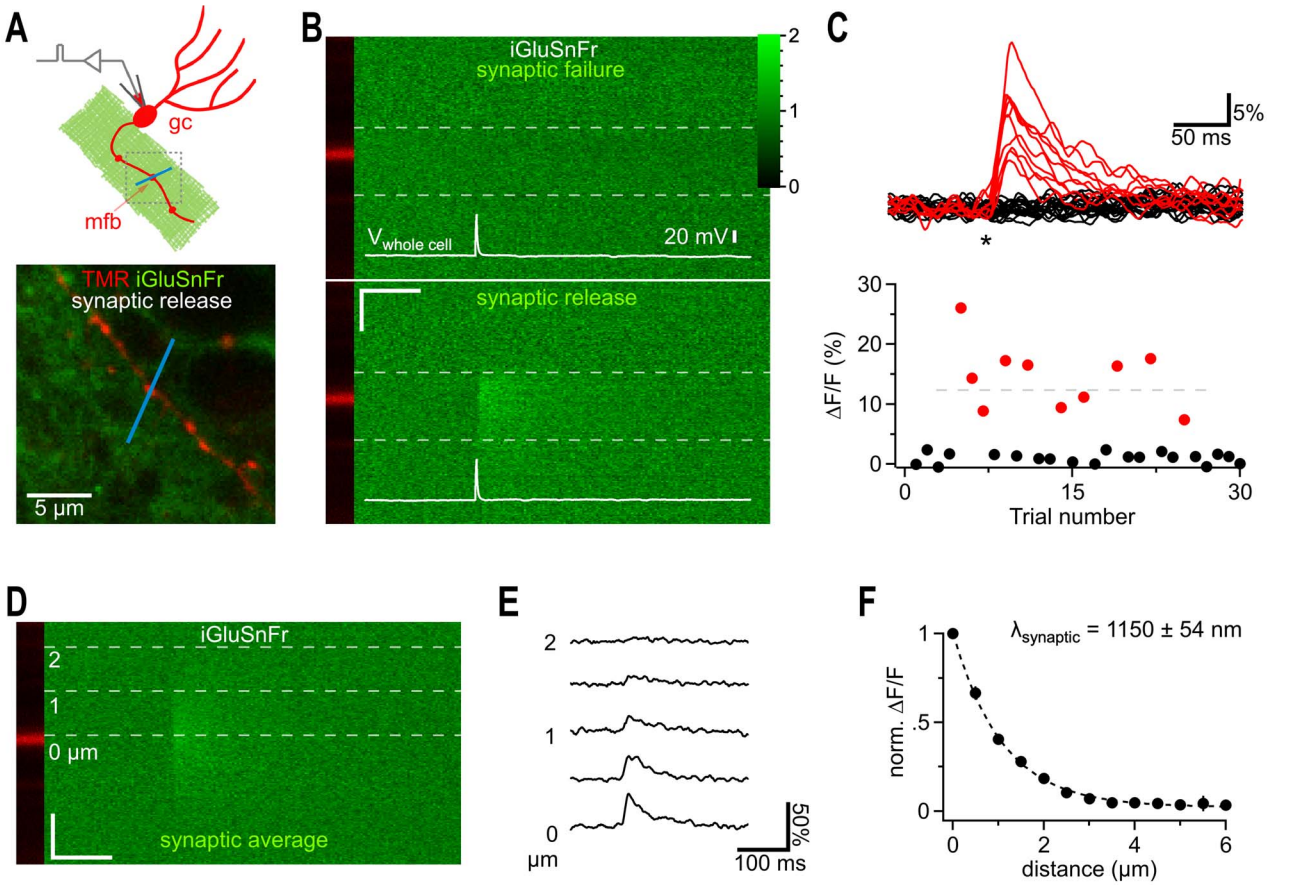

Figure 1. iGluSnFr responses far away from synaptic release sites. (*A*) Cartoon illustrating the recording condition to quantify the spatial spread of synaptically released glutamate. A granule cell (gc) was patch clamped and dye-filled (red) to identify a synaptic bouton (mossy fiber bouton, mfb) surrounded by neuronal iGluSnFr expression (green). To visualize synaptic glutamate release, a 2P line scan was drawn through the bouton (blue line). The boxed region represents a typical frame scan (as illustrated in lower panel) obtained to identify boutons and adjust the line scan. Lower panel, example dual channel two photon frame scan of a dye-filled (TMR 400 μM, red, iGluSnFr, green) mfb used for stimulation and recording of synaptic glutamate release (as shown in I-L). The bath solution contained CNQX (10 μM) to eliminate network activity and 4-AP (100 μM) and DPCPX (1 μM) to elevate release probability and thereby shorten the required recording time (release probability normally below 10%). (*B*) Dual channel 2P line scan through the bouton shown in *A*). Top panel shows a failed glutamate release, while the, bottom panel depicts a successful glutamate release. White lines illustrate the corresponding whole cell current clamp recordings of the stimulated action potentials. The bouton is in the red channel displayed on the left and does not show changes in fluorescence (tracer dye). In each line scan image, the region between the two dashed gray lines was used to calculate the fluorescence over time traces shown in (*C*). Color scale expresses fluorescence with respect to baseline and also applies to (*C*) and (*D*). Note the rapidly rising signal only occurring at the position of the bouton and at the time of the action potential. Scale bar: 50 ms, 1 μm. (*C*) Top panel, 30 example traces of line scan fluorescence over time (as indicated in *B*) demonstrate the well-known typical fluctuation of responses (red) and failures (black) known from synaptic vesicle release. Asterisk, time of action potential. Fluorescence normalized to prestimulus levels. Bottom panel, peak amplitudes of the fluorescence traces for the 30 sequential stimulations obtained from this bouton. Red markers below the dashed horizontal line represent events putatively classified as single vesicle release responses. (*D*) Line scans of synaptic responses only (excluding release failures) were averaged per bouton to improve the signal-to-noise ratio for quantification of the spread of synaptically released glutamate. Gray dashed lines indicate distances from the center of release. (*E*) Fluorescence over time extracted from (*D*) at the indicated distances. Note that the decay is slowed with distance and that weak signals can still be detected at 2 μm. The peak of these signals was quantified and plotted in *F*. (*F*) Synaptically released glutamate activated iGluSnFr at distances of more than 1.5 μm ($n = 6$). In each experiment the peak amplitudes of fluorescent transients were normalized to the largest amplitude measured at the dye-filled bouton.

case ($N \sim 16$, 50 nM TMR-Dx3kD) $V_{psf} = V_{eff} * \gamma = 0.5$ fl $*$ $0.354 \sim 0.2$ fl.

iGluSnFr Detection of Glutamate Diffusion

The optical glutamate sensor iGluSnFr was expressed by using a mix of AAV1 and AAV5 viral vectors under control of the synapsin promoter (hSyn.iGluSnFr.WPRE.SV40; Penn State Viral Vector Core). Anesthetized [16 mg/kg xylazine (Xylariem, ecuphar) and 100 mg/kg ketamine, i.p. (Ketamin 10%, WDT)] juvenile male C57Bl6/N (Charles River Laboratories) mice (5–7 weeks old) were stereotaxically injected bilaterally into both ventral CA3 hippocampal regions (stereotaxic coordinates relative to Bregma: −2.5 AP, ±3.0 ML, −3.0 AP; 1 μL of undiluted virus; appr. Titer: $8–10 \times 10^{12}$) as described previously by using a beveled needle nanosyringe (nanofil 34G BVLD, WPI) under the control of a micro injection pump (100 nL/min, WPI; van Loo et al. 2015).

Brain slices with strong expression in the Str. radiatum of CA3 and the hilus were selected for the experiment. To measure the spatial range of glutamate diffusion, a scan line (940 nm) was placed in the Str. radiatum either parallel or perpendicular to the primary dendrites of CA3 cells, with a length of 10–15 μm. A single uncaging spot

(wavelength 720 nm) was placed in the middle of the scan line and the uncaging laser pulse was triggered after a baseline of 200 lines was captured (~1 ms per line). For these experiments, the uncaging power was set to 20–25 mW at the objective. The affinity of iGluSnFr is reported to be 4.9 μM, which is similar to that of NMDAR.

For measuring the spread of synaptically released glutamate from mossy fiber boutons, slices were similarly prepared and selected. These experiments were conducted on the Nikon A1 R two-photon system with only a single imaging laser, imaging wavelength was 920 nm to excite both the red morphological dye and the iGluSnFr. Dentate granule cells were patch clamped in the current clamp configuration with internal solution containing 400 μM TMR. After holding the cell for 10–15 min, the axon would begin to fill with red dye, and complete, uncut axons were traced into the hilus region where iGluSnFr expression was the strongest. The bath solution contained CNQX (10 μM), 4-AP (100 μM), and DCPCPX (1 μM). A line scan was positioned crossing a clearly labeled presynaptic bouton, and somatic current injections of 1 nA, 0.5 ms were used to elicit action potentials.

Estimation of the Spatial Range with PSD95-GCaMP6f

The plasmid for the genetically encoded optical Ca^{2+} sensor GCaMP6f fused to PSD95, pLenti-PSD95-GCaMP6f, was used to prepare lentiviral particles. Viral injections were performed as described above by using stereotaxic coordinates −1.9 AP, ±1.5 ML, −1.5 DV to target the dorsal hippocampal CA1 region. Imaging experiments were performed 2 weeks following virus injection.

Brain slices with strong expression in the CA1 Str. radiatum were selected for the experiment. Frame scans (excitation wavelength 950 nm) of the Ca^{2+} sensitive PSD95-GCaMP6f fluorescence was acquired at ~40 ms, 110 nm spatiotemporal resolution. Glutamate uncaging was performed as previously described in the presence of 15 μM glycine to allow activation of NMDA receptors at negative potentials. Regions of interest were selected at a depth of ~25 μm below the surface. After a 600 ms baseline acquisition, a single uncaging pulse was delivered in the center of the field of view. Responding spines could be detected as an increase in the local $\Delta F/F_{max}$. Fluorescence intensity, spatially averaged over manually selected spines ($n = 50$ spines, 10 ROIs), increased rapidly in response to an uncaging event (maximal response at 80–120 ms after uncaging) and returned slowly to baseline. For many spines, resting fluorescence is undetectable above background. This precludes counting the total number of spines and calculating the fraction of activated spines in a field of view. Therefore, we conducted a pixel-based analysis to quantify the distance from uncaging site-dependence increase of GCaMP6f fluorescence: The ratio of activated pixels (ΔF greater than 4 SD in response to glutamate uncaging) at a certain distance over the total number of pixels at that distance (in the scan) was plotted versus distance from the uncaging site and used as an alternate metric for measuring the action range of uncaged glutamate at NMDA receptors.

Isotropic Spread of Iontophoretically Injected Glutamate in the Neuropil of CA1 Stratum Radiatum

The glutamate sensor iGluSnFr was virally expressed in astrocytes (AAV1.GFAP.iGluSnFr.WPRE.SV40, Penn State Viral Vector Core). Anesthetized [100 mg/kg ketamine (Ketamin 10%, betapharm) + 0.25 mg/kg medotomidine (Cepetor, CPPharma) i.p.] C57Bl6/N (Charles River Laboratories) mice (4 weeks old) were stereotaxically injected bilaterally into both ventral hippocampi (stereotaxic coordinates relative to Bregma: −3.5 AP, ±3.0 ML, −2.5 AP; 1 μL of undiluted virus) as described above. Finally, anesthesia was stopped by i.p. injection of 2.5 mg/kg atipamezol (Antisedan, Ventoquinol). To ensure analgesia, 5 mg/kg carprofen s.c. (Rimadyl, Zoetis) was injected for three consecutive days. Acute hippocampal slices (300 μm thick) were prepared after 2 to 4 weeks after virus injection. Experiments were performed in the presence of the glutamate receptor inhibitors NBQX (20 μM), D-APV (50 μM) and LY341495 (100 μM) and the sodium channel blocker TTX (1 μM) at a temperature of 34 °C.

As described previously, 2P excitation fluorescence microscopy was performed (Anders et al. 2014). An iGluSnFr-expressing astrocyte in the CA1 *Stratum radiatum* and a region of interest for line scanning in the periphery of the cell were pseudorandomly chosen. Line scanning of iGluSnFr fluorescence was performed as illustrated in Supplementary Figure 2 at a frequency of 300–500 Hz and glutamate was applied iontophoretically (npi, Germany) close to the middle of the scanned line (~1 μm) for 250 ms. In each experiment, line scans were performed both in parallel and perpendicular to the CA1 pyramidal cell layer. The iontophoretic current was 10 nA. We verified in each experiment that much larger iontophoretic glutamate injections (~100 nA) were needed to saturate iGluSnFr. The background fluorescence was subtracted from line scan data. The latter was processed and analyzed as illustrated and described in Supplementary Figure 2 and its legend.

Results

The optical glutamate reporter protein iGluSnFr, when expressed on neuronal membranes, provides a unique way to visualize synaptic glutamate signals (Marvin et al. 2013) and we and others have recently shown that it can also be used to detect quantal glutamate release events (Helassa et al. 2018; Marvin et al. 2018; Dürst et al. 2019; Jensen et al. 2019; Kopach et al. 2020). Here, we used iGluSnFr to visualize the action range of glutamate following glutamate liberation by presynaptic exocytosis in brain tissue. We virally expressed iGluSnFr (pAAV1/5-hSyn-iGluSnFr) throughout neurons in the CA3 region of the hippocampus (Fig. 1A) to visualize the

spread of glutamate. We chose to examine transmitter release from granule cells as some of their synapses, the mossy fiber synapses can easily be identified in the hilus by 2P microscopy (Fig. 1A). To unequivocally stimulate only a single mossy fiber synapse in the hilus, we patch-clamped granule cells and evoked action potentials by intracellular current injection in the presence of the glutamate receptor antagonists CNQX and APV. By loading granule cells with a tracer dye, the stimulated axon and its synaptic en-passant boutons embedded in iGluSnFr-expressing neuropil could clearly be identified (Fig. 1A). This allowed us to place line scans across activated boutons with a 2P-scanning microscope. We selected small en-passant mossy fiber synapses for recording and did not include giant mossy fiber boutons, which are typically found in the CA3 stratum lucidum. The synapses reported here displayed an average diameter of 0.86 ± 0.14 μm. Triggering single action potentials in granule cells produced either a rapid onset fluorescent response occurring immediately after the action potential and at the position of the dye-filled bouton or a failure as would be expected from the stochastic nature of synaptic vesicle release (Fig. 1B,C). These signals peaked at $27.0 \pm 3.4\%$ and quickly decayed back to baseline ($\tau = 69 \pm 9$ ms) but showed a very fast and extended spatial spread. The spatial width of the iGluSnFr signals exceeded the dimension of the bouton by several-fold (Fig. 1B–D). When averaging the line scans acquired during "response"-trials from an individual bouton (Fig. 1D,E), the resulting image displayed an excellent signal-to-noise ratio and the spatial spread of the iGluSnFr fluorescence could be directly quantified as a gradual decrease in fluorescent peak amplitude with distance from the stimulated synapse (Fig. 1D–F). Even at a distance of $\geq$1.5 μm from the bouton a "peak-shaped" fluorescent response could clearly be observed following an action potential (Fig. 1E) which, at that distance, is not expected based on the established models of glutamate diffusion in the neuropil (e.g., Rusakov and Kullmann 1998; Barbour 2001; see Discussion). The peak amplitude of these synaptically evoked responses exponentially decayed with distance from the bouton and could be described by λ_{sniff_syn} being 1.2 ± 0.05 μm (Fig. 1F). Note that λ_{sniff_syn} does not provide a direct read-out of the fractional activation of iGluSnFr compared to that in the synapse because the optical resolution limit lets us underestimate the true peak of fluorescence in the synaptic cleft. We therefore use λ to quantitively describe the apparent extent of the optical signal and to compare the distance-dependence of glutamate-induced responses across experiments in this study.

Even relatively small synaptic boutons such as those analyzed here may release multiple vesicles in response to single action potentials (Oertner et al. 2002; Christie and Jahr 2006; Jensen et al. 2019; Kusick et al. 2020; Maschi and Klyachko 2020) consistent with the large variation in iGluSnFr response amplitudes (Fig. 1C). A larger amount of glutamate released, for example, by multiple vesicles, may not only increase the responses but also favor spread into the extracellular space (Rusakov and Kullmann 1998; Barbour 2001). To address how much the apparent spread of iGluSnFr signals depends on the amount of glutamate released, we selected only the smallest responses obtained by stimulation (e.g., the smallest four red dots below the dashed line of the experiment in Fig. 1C) for averaging and analysis (Fig. 2A,B). Despite their lower amplitude ($12.7 \pm 1.4\%$, $\tau = 71.3 \pm 17.5$ ms) this subset of responses still showed clear fluorescent responses at a distances of $\geq$1.5 μm ($n = 15$, Fig. 2A) and the apparent λ_{sniff_syn} remained in the same range (1.4 ± 0.07 μm, $n = 15$, Fig. 2A).

During optical iGluSnFr recordings of stimulated small en-passant mossy fiber synapses, we also observed spontaneous fluorescent transients, which occurred in the neighborhood to the stimulated synapse and were not correlated to the action potential (Fig. 2C, $n = 26$). As excitatory transmission was blocked, firing of hippocampal neurons is rare and these events are likely to represent the optical correlate of spontaneous, action potential-independent, single vesicle release. These miniature iGluSnFr transients displayed an amplitude ($17.4 \pm 2.5\%$) comparable to that of the subset of small, stimulated responses, and decayed with a very similar time constant (Fig. 2C, $\tau = 52.1 \pm 6.1$ ms). Further, spontaneous transients also displayed clear peaks at distances $\geq$1.5 μm (Fig. 2D) and a comparable apparent λ_{sniff_syn}.

Taken together, these results strongly suggest that synaptically released glutamate can leave the synaptic cleft and spreads sufficiently far into the extracellular space to activate iGluSnFr molecules expressed on membranes of neighboring cells at >1.5 μm. While the spatial extent of this spread only weakly depended on the amount of glutamate released, the amplitude of the transients did so at all distances, consistent with the view that on average more glutamate was released during evoked signals compared to spontaneous signals (Fig. 2E).

2-Photon (2P)-based glutamate uncaging (MNI-caged-glutamate) can be used to generate a small and transient source of glutamate in brain tissue (Matsuzaki et al. 2001). While such an uncaging-based point-like source of glutamate is clearly of larger size than a synaptic cleft, it holds the advantage that its position and distance to a synapse can systematically be varied. To compare this approach to synaptic release of glutamate, we combined virus-based iGluSnFr expression in CA1 with 2P glutamate uncaging. All the following experiments were performed in CA1 to have a more uniform population of postsynaptic neurons to record uncaging-induced glutamate receptor currents from—as opposed to the hilus. Uncaging conditions including MNI-caged glutamate concentration and laser pulse, were fixed for the whole study and set such that when a laser pulse was applied to a spine head on a proximal secondary dendrite it on average produced an uncaging response (uEPSC) of ~12 pA (V_h −65 mV, APV, TTX, see below; for

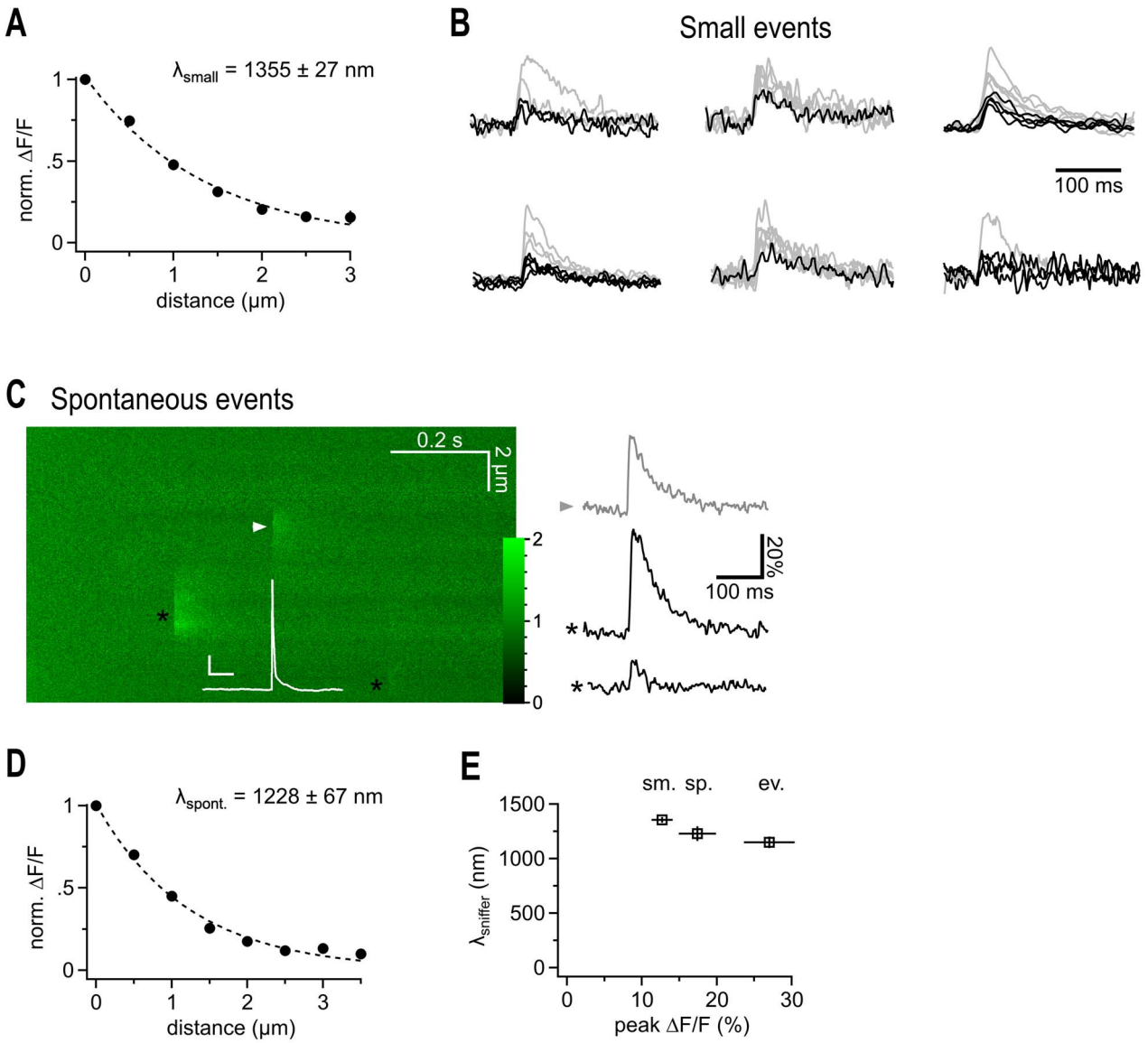

Figure 2. Putative quantal iGluSnFr signals show a similarly extended spatial decay. (*A*) Spatial extent of small synaptic iGluSnFr transients. For each recording the smallest events were selected to exclude potential multiquantal events. Note that the lambda value is in the same range as the one derived from data obtained by averaging small and large transients (cf. Fig. 1). (*B*) iGluSnFr fluorescent traces, the selected fraction of traces used for (*A*) is shown in black. Traces of peak-scaled for comparison are not shown at the same vertical scaling. Events for the cell at the right top are shown in Figure 1. (*C*) Example 2P line scan across a dye filled bouton showing the action potential-elicited iGluSnFr response (arrowhead), and two spontaneous, off-bouton events (black asterisks) used for the analysis shown in *D*. The white trace represents the simultaneous current clamp recording of the cell stimulated to fire an action potential, which released transmitter at the arrow head position (scale bars: 20 mV, 50 ms, color scale expresses fluorescence with respect to baseline). Right panel illustrates fluorescent example traces calculated at the positions indicated by the symbols. (*D*) Spatial extent of spontaneous likely miniature glutamate transients. Analysis of events that occurred independently of the timing of the action potential induced in the patch-clamped granule cell. All of them must have been released from neighboring synapses because they did not occur at the dye-filled bouton. As spontaneous action potential firing of granule cells in slices is very rare and slices are also bathed in CNQX and APV, these events are likely due to miniature, action potential-independent, single vesicle glutamate release. (*E*) $\lambda_{sniffer}$ only weakly depends on the magnitude of the signals and tends to be larger if more glutamate is released. From left to right: selected small, spontaneous, and evoked events.

details, see Methods and Supplementary Fig. 3). Under these conditions, a single uncaging pulse in the dendritic neuropil-generated spot-like iGluSnFr responses (Fig. 3A, CNQX, APV and TTX were included in the bath) showing larger peak amplitudes (0.81 ± 0.04 DF/F, $n = 22$) when compared to synaptic signals, but rise and decay kinetics were maintained (cf. pink trace). Uncaging-induced iGluSnFr fluorescence profiles yielded an only slightly larger λ_{sniff_unc} than the synaptic counterpart (~1.5 μm, Fig. 3B). The uncaging technique allowed us to test isotropy of glutamate diffusion on the micron scale. The many parallel, large diameter dendrites of CA1 pyramidal cells could cause a preferred direction of diffusion like the preferred diffusion along axons in white matter. For this, lines were scanned through the uncaging spot either perpendicular or in parallel to axons to test for a potential microanisotropy of glutamate diffusion in the extracellular space. However, the peak of the fluorescent signals decayed with a very similar length constant when probed parallel or perpendicular to axons (Fig. 3B). Lack

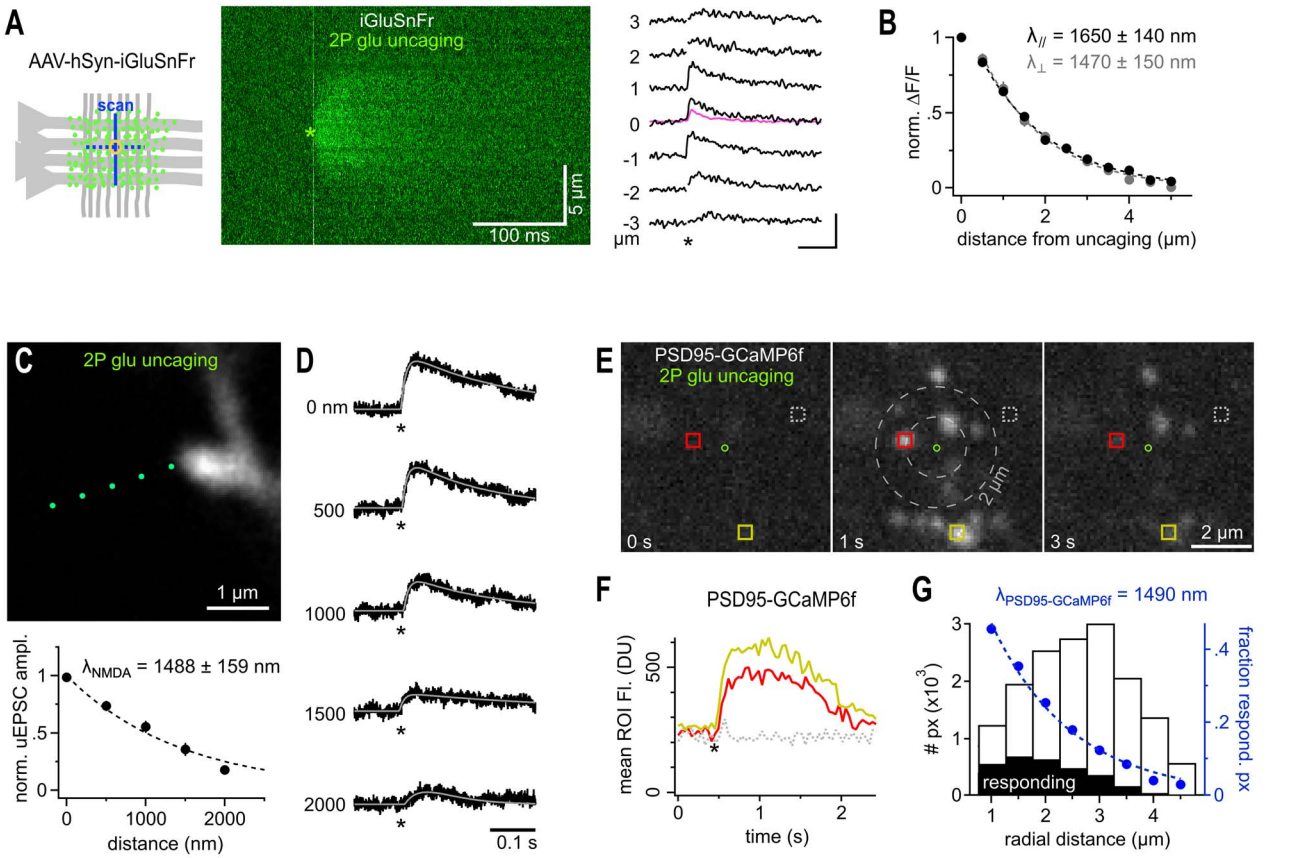

Figure 3. Extended spatial decay of NMDA-Rs mediated signals. (*A*) iGluSnFr reports a similar spread of extracellular glutamate following 2P-glutamate uncaging. Cartoon: yellow circle indicates glutamate uncaging site in the dendritic region of CA1 (Str. radiatum) where iGluSnFr reporter proteins are expressed on the neuronal membrane (green dots). 2P line scans perpendicular or parallel to axons (blue lines) were used to quantify the spatial spread of the fluorescent signal. Middle panel: Example line scans through the glutamate uncaging site (green asterisk, indicating time and position, average of three repeated uncaging spots at 3 s intervals). Note the rapid and substantial spread of the fluorescence. Line scans were normalized on the preuncaging fluorescence to account for spatial variability of initial iGluSnFr brightness (owing to varying spatial densities of membrane expression levels). Right panel: example fluorescent traces calculated from the line scan image shown in the middle. Numbers indicate distance from uncaging site; asterisk, time of uncaging. Note the visible and delayed signal at ±3 μm. Kinetics and amplitude are similar to synaptically evoked iGluSnFr responses as illustrated by the pink trace, average response from the experiment shown in Figure 1. Scale bar: 100 ms, 100%. (*B*) λ_{sniff_unc} measured from iGluSnFr signals is isotropic ($n = 10$ for each direction, black and gray markers represent scans parallel and perpendicular to axons, respectively) and only slightly exceeds λ_{sniff_syn} obtained following synaptic glutamate release. (*C*) 2P scan of a dye-filled spine incubated in 20 μM CNQX and 1 μM TTX to isolate NMDA receptors. Uncaging spots (green) were separated by 500 nm and applied at 5 s intervals to account for the substantially slower kinetics of NMDA-R mediated uEPSCs. Lower panel: λ_{NMDA} after glutamate uncaging ($n = 12$). (*D*) Example traces of NMDA receptor-mediated uEPSCs (asterisk, time of uncaging, cell voltage clamped at +40 mV). uEPSCs are still clearly seen at a distance of 2 μm and their kinetics are substantially slower. To reliably quantify peak amplitudes of even the smallest responses uEPSCs were fitted with a two-exponential function (gray line, see Methods). Note that even remotely evoked uEPSCs (>1500 nm) evoke clear currents demonstrating pronounced diffusional propagation of released glutamate. (*E*) Widespread activation of PSD95-GCaMP6f following a single uncaging pulse confirms large action range of glutamate at NMDA receptors. Three two-photon scans (taken from the 20 Hz time series quantified in *F*) in the dendritic region of CA1 before and after the uncaging pulse (green circle indicates uncaging site, 15 μM glycine to allow NMDA-R activation at resting potential, 20 μM CNQX, 1 μM TTX). Note the appearance of bright spine head-shaped structures following glutamate uncaging which occur even outside a 2 μm range (gray dashed circles). Colored squares indicate example ROIs used to calculate the fluorescence over time traces displayed in *F*. (*F*) Average ROI fluorescence over time illustrating the pronounced calcium increases induced in spine heads by activation of NMDA receptors following glutamate uncaging (asterisk, colors of traces correspond to the ROIs shown in *E*. (*G*) Estimation of λ_{NMDA} from the spatial distribution of calcium responses (PSD95-GCaMP6f) around the uncaging point. The histogram plots the frequency of responding pixels (for threshold details, see Methods) along the radial distance from the uncaging site (black bars, "responding," aggregated results over 66 uncaging events). The white bars show the number of pixels in the acquired image along the radial distance. The ratio of the black over the white bars represents the experimental probability of observing a calcium response at a given distance (blue markers, fraction of responding pixels). This probability drops with distance and follows a λ_{NMDA_GCaMP}. Notably, λ_{NMDA_GCaMP} as assessed here (blue dashed line) matches the one extracted from uncaging iGluSnFr responses (*B*) well.

of anisotropy of glutamate diffusion was confirmed by using long (250 ms) iontophoretic applications of glutamate, which produced similar near steady-state spatial gradients of glutamate in both orientations (Supplementary Fig. 1).

Such remote action of uncaged glutamate in the extracellular space should also cause physiologically relevant activation of remote glutamate receptors (Marvin et al. 2013; Reiner and Levitz 2018), our results predict NMDA receptor activation following uncaging at distances >1.5 μm (if their Mg-block is removed and cofactors are present). As spines are known sites of postsynaptic glutamate receptor clusters (Kasai et al. 2003), we identified spines on proximal secondary dendrites by

patch clamping and dye-filling CA1 pyramidal neurons in hippocampal slices (Fig. 3C). We applied the above-described glutamate uncaging protocol and recorded the distance-dependent decay of NMDA receptor-mediated uEPSCs (Fig. 3D). To isolate NMDA receptor currents ($uEPSC_{NMDA}$), we voltage-clamped cells at +40 mV (Cs-based intracellular solution) and blocked AMPA receptors and added the cofactor glycine. We selected those spines for uncaging that lacked neighboring spines within a sphere of at least approximately 2 μm diameter to minimize the possibility that other spines contribute to the electrical response by binding diffusing glutamate. When we moved the uncaging laser spot away from the spine head, $uEPSCs_{NMDA}$ clearly, but slowly, declined and were still detectable at a substantial distance of at least 2 μm (Fig. 3C,D). The decay could also be well described by an exponential function with a length constant of 1488 ± 159 nm ($n = 12$, Fig. 3C) and we refer to this apparent length constant as λ_{NMDA}. It is worth noting that this length constant does not directly report the fraction of receptors activated at a distance with respect to the synaptic cleft: we underestimate the response at the spine head (0 nm) because the spatial extend over which glutamate is released by uncaging is larger than the cleft and therefore uncaging responses close to the spine must be interpreted with care (see Discussion). The large action range (responses at a distance of 2 μm) together with the high density of synapses (~2 μm^{-3}) implies that photo-released glutamate reaches NMDA receptors on a multitude of neighboring spines around the uncaging spot and activates them. To directly visualize this prediction and show that this activation translates into a physiologically relevant down-stream signal, we virally expressed the genetically encoded calcium indicator GCaMP6f in CA1 pyramidal cells. GCaMP6f was fused to PSD95, which selectively targeted it to dendritic spines (Fig. 3E). Before stimulation, fluorescence of the calcium indicator was quite dim, and spines were almost invisible. However, a single uncaging pulse of glutamate in the center of the scan field (green circle) resulted in significant increase in fluorescence in many spines of transduced neurons around the uncaging spot (Fig. 3E,F). Importantly, not only spines very close to the uncaging site but also those at a distance of >2 μm were activated, consistent with the λ_{NMDA} estimated by $uEPSCs_{NMDA}$ recorded at increasing distances from an individual spine. In fact, when accounting for the geometric, random occurrence of PSD95-GCaMP6f expressing spines within the scan field the probability of finding a responding spine drops with the distance from the uncaging spot following a length constant, l_{NMDA_GCaMP}, of ~1.5 μm (Fig. 3G, note that not all neurons were transduced by the virus). Thus, in the 3D environment, a single uncaging pulse of glutamate concurrently activates NMDA receptors on a large number of spines from at least tens of nearby neurons, resulting in strong postsynaptic Ca^{2+} signals.

Most excitatory activity of the brain is transmitted from neuron to neuron by AMPA-Rs. AMPA-Rs show a substantially lower affinity for glutamate than NMDA-Rs and iGluSnFr. For this reason, AMPA-Rs should have lower responses to remote glutamate sources. We also used 2P glutamate uncaging to test at which distance synaptic AMPA receptors still respond to glutamate. As mentioned above, delivery of glutamate by brief laser pulses at the spine head produced an uEPSC of 12.4 ± 1.0 pA (Fig. 4A, in the presence of TTX, APV, and gabazine, for details on uncaging conditions, see Methods), which was comparable to the amplitude of mEPSCs (11.5 ± 0.6 pA, $n = 8$). uEPSCs were mediated by AMPA receptors as they were completely blocked by CNQX (Supplementary Fig. 2). When we moved the uncaging laser spot away from the spine head, responses declined much faster than for NMDA receptors but were still clearly detectable at a distance of >600 nm (Fig. 4B). We found apparent λ_{AMPA} to be 450 ± 34 nm ($n = 27$, Fig. 4C). λ_{AMPA} was similar when probed at different angles to the Schaffer collaterals (not shown) or at shaft synapses (Supplementary Fig. 2) implying that average diffusion and uptake on the submicrometer scale are isotropic and a function of the random shape of the extracellular space immediately surrounding synapses (at ~0.5 μm). This is consistent with the above-described results obtained with iGluSnFr, a macroscopic diffusion analysis in this brain region (Hrabětová 2005), and the finding that the structure of the neuropil surrounding synapses appears random and chaotic (Rusakov and Kullmann 1998).

Previous work demonstrated that largely astroglial glutamate uptake plays a role in limiting the spread of glutamate in the extracellular space but how uptake affects the physical distance at which glutamate can still activate receptors remained not exactly known (Asztely et al. 1997; Lozovaya et al. 1999; Diamond 2001; Arnth-Jensen et al. 2002; Scimemi et al. 2004; Zheng et al. 2008; Danbolt et al. 2016). We found that the λ_{AMPA} was clearly increased approximately 1.8-fold by strongly and competitively blocking transporters with tfb-TBOA (Shimamoto et al. 1998; Bridges and Esslinger 2005; Fig. 4D, 789 ± 51 nm, $n = 21$), a milder block of transporters by DL-TBOA (~3000-fold lower affinity at EAAT1) increased λ_{AMPA} to a weaker extent, Supplementary Fig. 2). The glutamate turnover rate (number of glutamate molecules translocated intracellularly per time) is known to strongly increase with temperature (Bergles and Jahr 1998). However, λ_{AMPA} probed by uncaging at near-body temperature (32 °C) only modestly decreased by ~15% to 413 ± 21 nm ($n = 32$, Fig. 4E, compared to 450 nm at RT). These results suggest that rapid binding of glutamate to transporters, which precedes translocation of glutamate and is antagonized by TBOA, is an important factor in reducing the spread of glutamate on this short temporal and spatial scale. TBOA may further facilitate glutamate spread by acting on the mobility and/or recycling of glutamate transporters

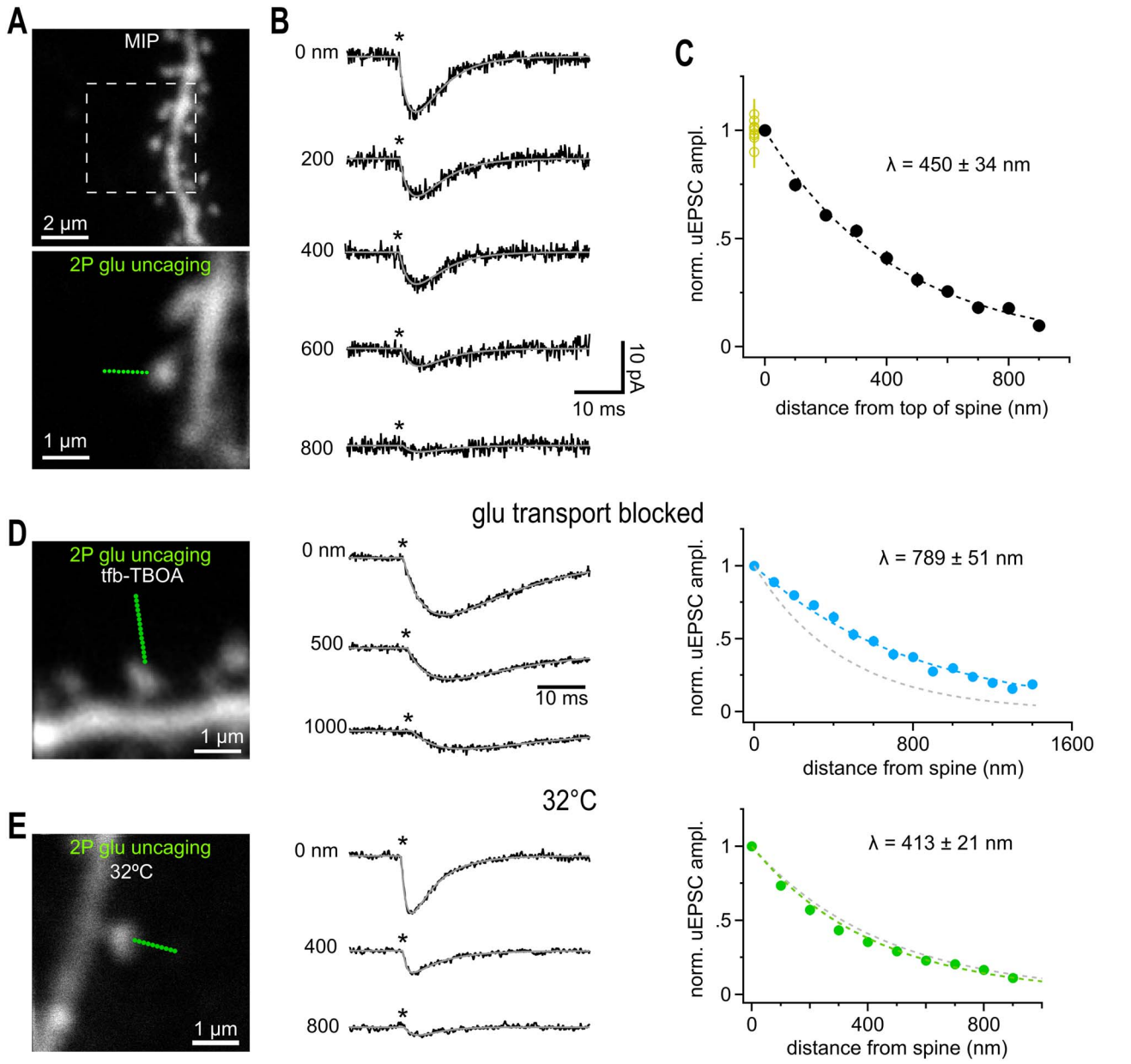

Figure 4. Glutamate uncaging beyond the nearest synaptic neighbor distance activated also activates synaptic AMPA receptors. (A) Maximum intensity projection (MIP) of CA1 pyramidal cell dendrite dialyzed with 25 μM AlexaFluor 594 scanned with a two-photon microscope. Solitary spines were selected to avoid coactivation of neighboring structures. Lower image illustrates positioning of a sequence of glutamate uncaging points (green dots, step size 100 nm) to probe the spatial dependence of uEPSC amplitudes. Single image scanned at higher resolution. (*B*) Example current traces recorded in whole-cell voltage clamp mode showing the gradual decline of the response magnitude with distance. Light pulses (0.6 ms, asterisks) were applied at 1 Hz. Gray lines show fitted with a two-exponential function used to determine the peak amplitude. Note that even uEPSCs evoked at >400 nm peak within approximately 3–4 ms reflecting the rapid diffusional propagation of glutamate. Throughout the study we used the following conditions for isolating AMPA-Rs: 720 nm, 0.6 ms, 23 mW, 5 mM MNI-caged glutamate in presence of 1 μM TTX, 50 μM APV, 10 μM Gabazine. (C) Summary graph of the distance-dependent decay of the amplitude of uEPSCs ($n = 27$ spines), which could be well approximated by an exponential function with a length constant λ (dashed black line). Fitting of the individual amplitudes over distance revealed the indicated average value of λ. Applying 10 identical glutamate uncaging pulses at 1 Hz at the spine head yielded stable responses (yellow circles at 0 nm, $n = 8$) indicating that desensitization or run-down of receptors is negligible. (*D*) Left: 2P-photon scan of a spine incubated in 1 μM tfb-TBOA, 100 μM APV, 40 μM MK801, 10 μM gabazine, and 1 μM TTX. Uncaging responses were probed over an extended distance by additional uncaging spots (green dots, step size 100 nm). Middle: Example uEPSCs (averages) taken from the three distances indicated. Note the prominent residual current at 1000 nm (compare to *B*). Asterisk, time of uncaging pulse; gray line, uEPSC fit. Right: Extended action range of uncaged glutamate in the presence of tfb-TBOA. Blue markers represent the average decay of uEPSCs measured from 21 spines yielding an average λ as indicated. Dashed gray line shows the control λ (450 nm) as determined in *C*. (*E*) as in (*A–C*) but slices were kept at 32 °C. Compared to results obtained at room temperature the action range of uncaged glutamate at AMPA-Rs is only slightly shortened at 32 °C suggesting that transmembraneous transport of glutamate (highly temperature dependent) is too slow to modify extracellular glutamate signaling on this short spatial scale. Around 32 spines yielded the average λ as indicated. Gray dashed line shows the control λ (450 nm) at room temperature (cf *C*).

(Murphy-Royal et al. 2015; Michaluk et al. 2021). In contrast, even at near-body temperature, the turnover rate seems to be too low to translocate a significant number of glutamate molecules during their diffusion time (~1 ms) on this submicrometer distance (see Discussion) like what has been observed for synaptic glutamate transients reaching Bergmann glia membranes (Dzubay and Jahr 1999).

During development (Thomas et al. 2011) and in disease (Hubbard et al. 2016), glutamate transporter activity or expression levels substantially change. These observations prompted us to test for alterations of λ_{AMPA} as an indicator of altered extracellular glutamate handling. The unchanged time course of synaptically evoked glutamate transporter currents in astrocytes of older mice has been taken as evidence that net extracellular glutamate handling is preserved during development when analyzing bulk synaptic signals (Thomas et al. 2011). We found λ_{AMPA} to be significantly reduced in adult hippocampal tissue (5–7 weeks) by ~25% when compared to the juvenile value (Fig. 5A, 345 ± 20 mn, $n = 39$ vs. 450 ± 34 nm at P17). This suggests that on the submicron scale glutamate spread in the extracellular space is more restricted in older mice and that this alteration may not be detectable when sampling transporter currents from the entire astrocytes.

Glutamate transporters were shown to be down regulated in the early phase of a mouse epilepsy model (Hubbard et al. 2016). Using the same epilepsy model (suprahippocampal kainic acid injections to induce status epilepticus, see Methods) in adult mice (6 weeks) we found λ_{AMPA} tested on spines of CA1 pyramidal cells prepared 5 days post injection from contralateral hemispheres to be significantly increased by ~20% (418 ± 26 nm, $n = 25$) compared to the adult control group (Fig. 5B). Thus, λ_{AMPA} is not a biological constant and correlates with changes in the levels of glutamate transporters.

If the spread of glutamate in the extracellular space is limited by the levels of glutamate transporters, as also suggested by the effect of TBOA (cf Fig. 4, see Discussion), then coincident glutamate release from nearby sources may cooperate to consume free transporter binding sites and show an enhanced spatial spread. We therefore tested the capabilities of AMPA receptors on spine heads to integrate inputs from remote sources in the presence of the NMDA receptor antagonist APV (and TTX). We first recorded uEPSCs as responses to three independent, consecutive (1 s interval) uncaging stimuli at three distances from the spine head (Fig. 5C, at 0, 420, 720 nm) and observed a decline with distance consistent with λ_{AMPA} determined above (Fig. 5C, top row). We then reapplied the three uncaging pulses at the same positions but this time almost simultaneously (Fig. 5, "triple spot," see Methods). Since we released more glutamate overall, the final compound response was clearly bigger than each individual uncaging response, as expected. Unexpectedly, the amplitude of this compound uEPSC ("triple spot") also significantly exceeded the arithmetic sum of the amplitudes of the three consecutively acquired uEPSCs ("Σ (1, 2, 3)"). Here, the amount of glutamate uncaged is identical and the increase in amplitude suggested an enhanced spread of coincident glutamate release activity. An alternative explanation for this supra-additivity is that the larger electrical signal in response to the triple uncaging stimulation triggers stronger electrical signaling within the spine which may boost the recorded current response (e.g., by recruiting voltage-gated channels). To address this possibilty, we redesigned the experiment and positioned all three spots at the spine head, avoiding glutamate diffusion and directly probing the responsiveness of spines (Fig. 5D). The laser power for the second and third uncaging spots was reduced so that the resulting uEPSCs mimicked the size of the responses to uncaging at 420 and 720 nm, respectively and we achieved an equivalent electrical signal. Thus, in this redesigned experiment, the degree of glutamate receptor opening in the spine was maintained compared to the original experiment but no diffusion to the spine head is involved. The three laser pulses were administered sequentially (top row) and then simultaneously ("triple spot"), as described above. In this case, supra-additivity was absent and the amplitude of the simultaneously applied uncaging spots almost exactly equaled the arithmetic sum of the amplitudes of the three single uEPSC traces ("Σ (1, 2, 3)", Fig. 5D,E). This showed that triggering of postsynaptic electrical signaling does not explain the supra-additive summation. Therefore, the supra-additive summation happened in the extracellular space and likely involved facilitated spread of glutamate from the remote uncaging spots to the spine head.

This result opens the question of how dependent λ_{AMPA} is on the amount of glutamate being released. Uncaging might release many more glutamate molecules than synaptic release, prompting us to check whether shorter estimates of λ_{AMPA} result if we reduce the amount of glutamate released. We tested the dependence of λ_{AMPA} on the amount of glutamate being released by systematically measuring λ_{AMPA} at individual spines with low, normal, and high uncaging laser power changing the free glutamate concentration to approximately 64%, 100%, and approximately 144%, respectively (by altering laser power to 80% and 120%). The amplitudes of the resulting uEPSCs clearly varied with the amount of glutamate released (Fig. 6A). In contrast, λ_{AMPA} did not become significantly shorter when we released less glutamate, indicating that λ_{AMPA} is not steeply dependent on the amount of glutamate released (Fig. 6B,C). On the other hand, the λ_{AMPA} was slightly and significantly enlarged when we released more glutamate suggesting that our standard conditions generate a glutamate load at the upper end of the extracellular glutamate handling capacity (Fig. 6B,C). This is consistent with the view that when a critical extracellular glutamate concentration has exceeded locally, increased saturation

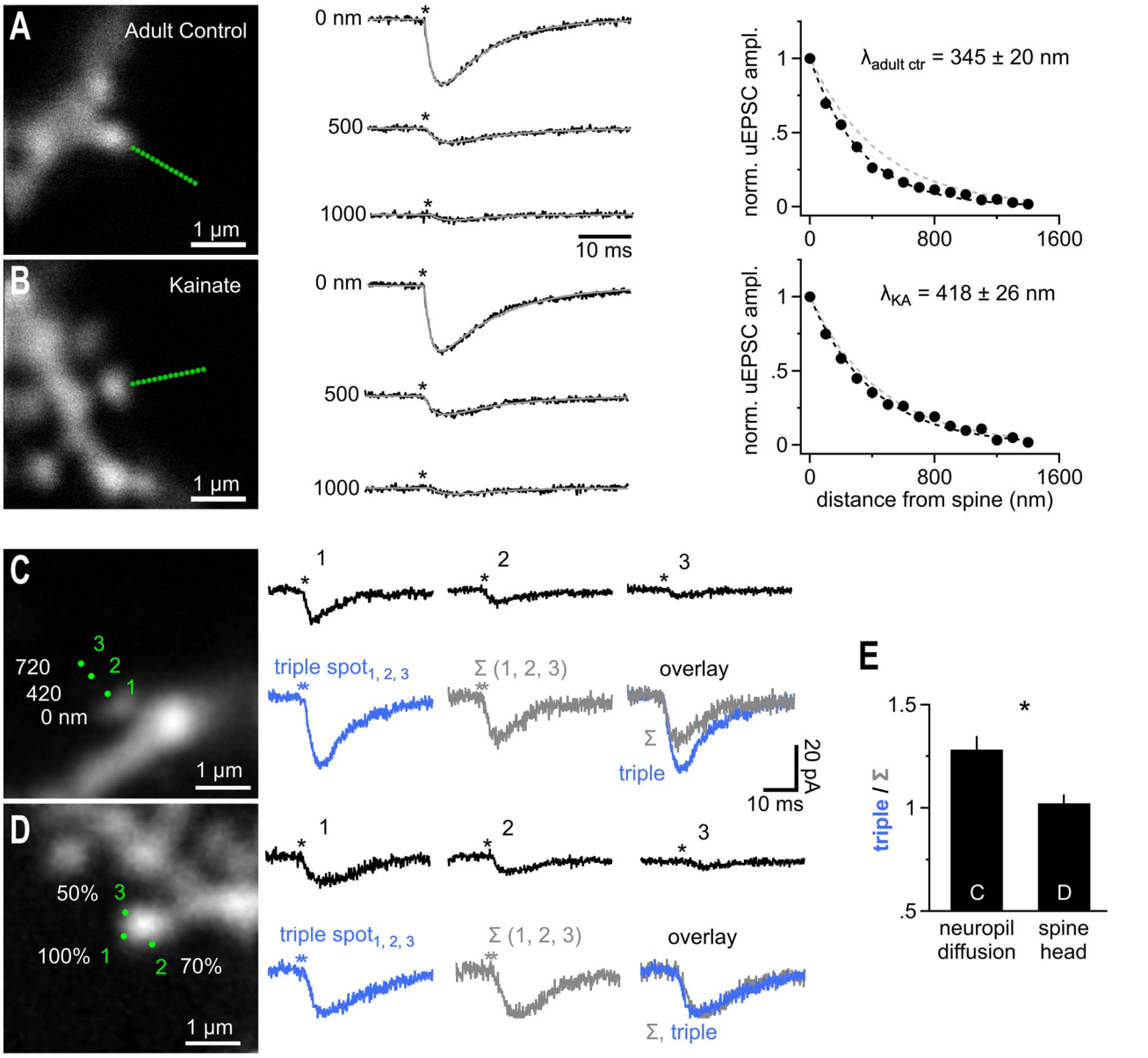

Figure 5. Extracellular temporal integration of glutamatergic released in submicron perisynaptic neighborhood. (*A*) Adult mice (6 weeks) show a reduced glutamate action range at AMPA receptors ($n = 39$). Conditions as in Figure 4A–C. Traces represent the averages of $n = 39$ recordings. For comparison the right panel also shows the λ determined for adolescent mice (gray dashed line). (*B*) In an animal model of chronic temporal lobe epilepsy (suprahippocampal kainic acid, injection-induced status epilepticus, $n = 15$) there is a significant extension of the action range of uncaged glutamate at AMPA receptors back to levels seen in adolescent mice ($n = 25$, $P = 0.024$, studentized bootstrap test for difference in means). Note that the two fits (black and gray; 450 nm control group, Fig. 4A–C dashed lines) are almost indistinguishable. (*C*) Left panel, dye-filled spine used to probe the summation of coincident activity in the spine-surrounding extracellular space. Three uncaging spots (1, 2, 3) were applied at the three distances indicated. The responses when the three uncaging spots were applied sequentially are shown in the right panel, top row (asterisks, time of uncaging pulse). Bottom row shows the response to synchronous uncaging at the three spots (left, blue, "triple spot") in comparison to an arithmetic sum (middle, **Σ** (1, 2, 3)) of the three responses shown in the top row. The overlay on the right shows that the triple response clearly exceeds the arithmetic sum. (*D*) As in *C* but the three spots were all placed right at the spine head. To mimic the weaker response obtained by uncaging spots 2 and 3 in *C* the uncaging laser power per spot was reduced to 70% and 50%. Scaling as in (*C*). The responses when the three uncaging spots were applied sequentially are shown in the right panel, top row. Bottom row shows the response to synchronous uncaging at the three spots ("triple spot", 100%, 70%, and 50% of laser power as in top row) in comparison to an arithmetic sum (**Σ** (1, 2, 3)). The overlay on the right clearly shows equal response amplitude indicating that the supra-additive summation is not a function of the spine or dendrite. (*E*) Summary of $n = 11$ (panel *C*) and $n = 34$ (panel *D*) experiments demonstrating a significantly larger response when uncaging spots were distributed in the neuropil and involved diffusion in the extracellular space.

levels of glutamate-binding sites can facilitate the spread of glutamate.

To define this critical level of glutamate and relate it to the density of synapses and their activity, the amount of glutamate released during uncaging and its spatial distribution must be determined. For this reason, we calculated estimations of the dimensions of the uncaging 2P point spread function and the number of uncaged glutamate molecules. We assessed the PSF of our 2P-uncaging system in situ by monitoring the degree of bleaching

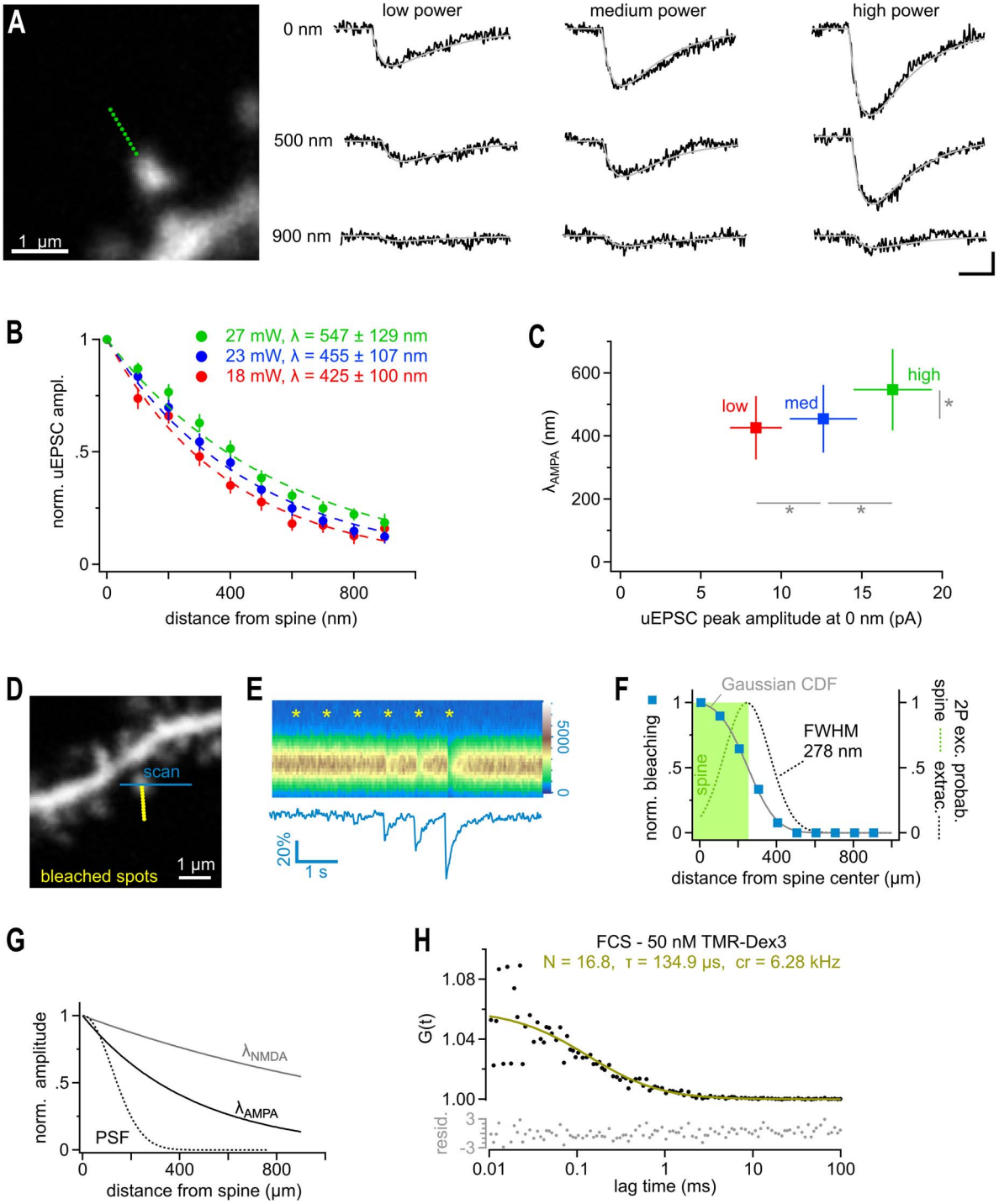

Figure 6. 2P-glutamate uncaging does not overwhelm transporters and mimics multivesicular release. (*A*) In order to test the dependence of λ on the amount of glutamate released by uncaging, 10 points were placed from 0 to 900 nm from the edge of the spine head (left panel, green dots). The uncaging power at the objective was set at 18, 23, or 27 mW (changing the free glutamate concentration to ~61%, 100%, and ~137%, respectively, due to the two-photon immanent nonlinear, quadratic, dependence of the uncaging rate on the laser power). All three power levels were tested at each of the 19 spines in a randomized order. Single responses from representative spines are shown in black, with their double exponential fits in gray (right panel). (*B*) λ at AMPA-Rs at low (red), medium (blue), and high laser power (green) extracted from all spines recorded as in A. (*C*) λ values plotted against the peak amplitude of the uncaging currents recording when uncaging at 0 nm. Note that while the amplitude of the uEPSCs significantly varied with laser power (horizontal gray bars and asterisks, repeated measures ANOVA, Tukey posthoc), λ did not decrease when releasing fewer molecules of glutamate despite a significant reduction in uEPSC amplitude suggesting that transporters are not overwhelmed and AMPA-Rs are operating in a near linear range (repeated measures ANOVA, Tukey posthoc). In contrast, releasing more glutamate did lead to a significant increase in the length constant λ (vertical gray bar and asterisk, Repeated measures ANOVA, Tukey HSD posthoc) indicating that at higher glutamate concentrations further signs of transporter saturation can be observed. Also note that the amplitude varies linearly with the estimated amount of uncaged glutamate, also suggesting that AMPA-Rs are operating in a near linear range. (*D*) Dye-filled dendrite with spines used to probe the optical resolution of our uncaging system in brain slices. The imaging scanner was used to monitor the fluorescent emission from a single spine (blue line, 820 nm). The uncaging laser (720 nm) produced a series of light spots similar to uncaging (Δx 100 nm) but the closest spot was placed directly onto the spine head (yellow dots) to measure the maximal bleaching amplitude of the spine with the line scans of the imaging laser. (*E*) Bleaching amplitude steeply

of dye-filled spines when we moved the uncaging laser progressively closer to the spine. We selected spines with a slice depth of approximately 30 μm, which we also used for uncaging experiments. This allowed us to estimate that the PSF of our uncaging laser beam shows a FWHM of approximately 278 nm (Fig. 6*D*–*F* and see Methods). Thus, receptors on a spine head in the focus of our 2P uncaging laser are initially exposed to a Gaussian-shaped spatial profile of glutamate concentrations with a FWHM of approximately 280 nm, and the optical resolution of uncaging compared well against the apparent λs (Fig. 6*G*).

The amount of glutamate molecules released by uncaging depends on the focal excitation volume of our system, the volume in which caged glutamate is converted. We experimentally determined the excitation volume of our system with fluorescent correlation spectroscopy (FCS, for details, see Methods) to be approximately 0.2 fl (Fig. 6*H*), which is in good agreement with theoretical predictions (Zipfel et al. 2003). During the experiment, the neurons in the slice are immersed in 5 mM MNI-glutamate. The number n of glutamate molecules released by our uncaging pulse can then be estimated as follows: $n = 0.2\ \text{fl} * 5\ \text{mM} * \varepsilon *$ ExVF $* N_{Av} \sim 36\,000$, with ExVF being the extracellular volume fraction (0.2) and ε represents the estimated fraction of glutamate uncaged (0.3, see Discussion). Assuming recent estimates for the number of glutamate molecules per synaptic vesicle, approximately 7000–8000 (Budisantoso et al. 2012; Wang et al. 2019), this calculation shows that our uncaging releases approximately the same number of glutamate molecules as contained in approximately five synaptic vesicles.

The mean distance to the nearest neighbor synapse in the CA1 region has been reported to be approximately 450 nm (Rusakov and Kullmann 1998). Our uncaging of approximately 36 000 molecules of glutamate or the equivalent to approximately five synaptic vesicles at this distance produced approximately 38% of the mEPSC AMPA-R-mediated amplitude (~4.6 pA vs. 12 pA quantal amplitude, cf. Fig. 3). Multivesicular release of 2–5 vesicles is a common scenario at hippocampal synapses (Oertner et al. 2002; Christie and Jahr 2006; Jensen et al. 2019; Kusick et al. 2020; Maschi and Klyachko 2020). Thus, if our glutamate uncaging responses at this distance of approximately 500 nm mimicked multivesicular synaptic release (see Discussion), there should be a small but consistent degree of cross-talk between neighboring synapses. To discern and eliminate such potential cross-talk components we applied a high concentration of glutamate-pyruvate transaminase (GPT) and pyruvate as a biochemical glutamate scavenger system (cf Min et al. 1998, see Methods) to inactivate synaptically released glutamate before it reaches a neighboring synapse. If there is cross-talk, then GPT application should reduce fEPSPs, and this reduction should be even stronger for the second, paired-pulse (40 ms) fEPSP, as this recruits a higher spatial density of active synapses due to presynaptic facilitation. Indeed, as shown in Figure 7*A*, GPT slightly reduced the first and the second fEPSPs to 92 ± 5% and 88 ± 4% ($n = 9$), respectively. A similar reduction of synaptic transmission by this scavenger system was observed by Min et al. 1998. However, the authors attributed it to an effect of GPT on glutamate still in the synaptic cleft, during diffusion to postsynaptic receptors. To test this assumption, GPT can capture glutamate while still in the synaptic cleft, we recorded mEPSCs in dissociated neuronal cultures and quantified the mEPSC amplitude, which is the response to release of a single vesicle (Fig. 7*B*). If GPT acts in the synaptic cleft it should reduce the mEPSC amplitude.

However, GPT did not reduce the amplitudes of mEPSCs, indicating that the scavenger system as applied here is not potent enough to compete for glutamate receptor activation within the synaptic cleft (Fig. 7*B*). Thus, it appears likely that the scavenger indeed reduced fEPSPs by interfering with synaptic cross-talk. In other words, GPT in the condition applied here is too slow to capture glutamate molecules on the short path across the synaptic cleft but successfully binds glutamate diffusing over longer distances to neighboring synapses. Cultures were chosen here as they grow at lower densities than neurons in brain tissue and the nearest neighbor distance of synapses typically exceeds 1 μm—a distance at which cross-talk of quantal responses should be minimal

drops off with distance from the spine. Top panel: Repetitive line scans through the spine head (color legend on the right edge). Asterisks indicate the times when bleaching spots were applied. Bleaching spots were sequentially moved towards the spine. Note that bleaching is clearly seen only with the third from last spot (200 nm) due to the small size of the bleaching spot generated by the uncaging laser. Bottom panel: average fluorescence of the scanned lines used to quantify the bleaching amplitudes. (*F*) Summary graph of six experiments as illustrated in *D* and *E* to extract an estimate of the FWHM of the diffraction limited spot of the uncaging laser. Normalized bleaching amplitudes extracted from line scans (as in *E*) are shown as blue squares. As the dimension of our detector of bleaching, the spine volume, is much larger than the bleaching spots (as opposed to the typically used sub-resolution-sized beads typically used in in vitro measurements) the blue squares do not directly yield the spatial resolution or PSF. To illustrate this relationship, the green area shows the volume occupied by a spine and the obtained bleaching is half maximal then, when the PSF is centered on the edge of the spine (dashed line). The PSF then bleaches only the left half of the spine (green dash), whereas the right half hits the extracellular space (gray dash). Maximum bleaching occurs only when the PSF is fully contained within the spine volume. Therefore, the distance-dependent bleaching amplitudes (blue squares) provide the integral of the PSF (green area under the PSF curve) and must be fitted by a Gaussian CDF ("integral of Gaussian", gray line) to extract the approximated shape of uncaging system's PSF (dashed line) and the FWHM. This analysis suggests that the optical resolution of our uncaging system was close to the theoretical optimum, FWHM = 278 nm (dashed line). (*G*) Comparison of the estimated PSF (as in *F*) to the λ values at AMPA-Rs and NMDA-Rs, respectively. Note that the latter two clearly exceed the optical resolution of our uncaging system. (*H*) Fluorescence correlation spectroscopy approach to estimate the 2P-uncaging volume. Fluctuations in emission of a 50 nM TMR-dextran3kD solution during exposure to the stationary uncaging laser beam (720 nm, NA 1) was recorded for 120 s and used to calculate the autocorrelogram (black dots). Fitting the autocorrelogram with an autocorrelation function assuming a 3D Gaussian volume (yellow) yielded 16.8 diffusing dye molecules in the effective detection volume. Together with the known dye concentration this estimates the excitation volume to be approximately 0.2 fl (including γ-factor correction, for details, see Methods). Lower panel shows the residuals of the fit (for details of residuals, see Methods).

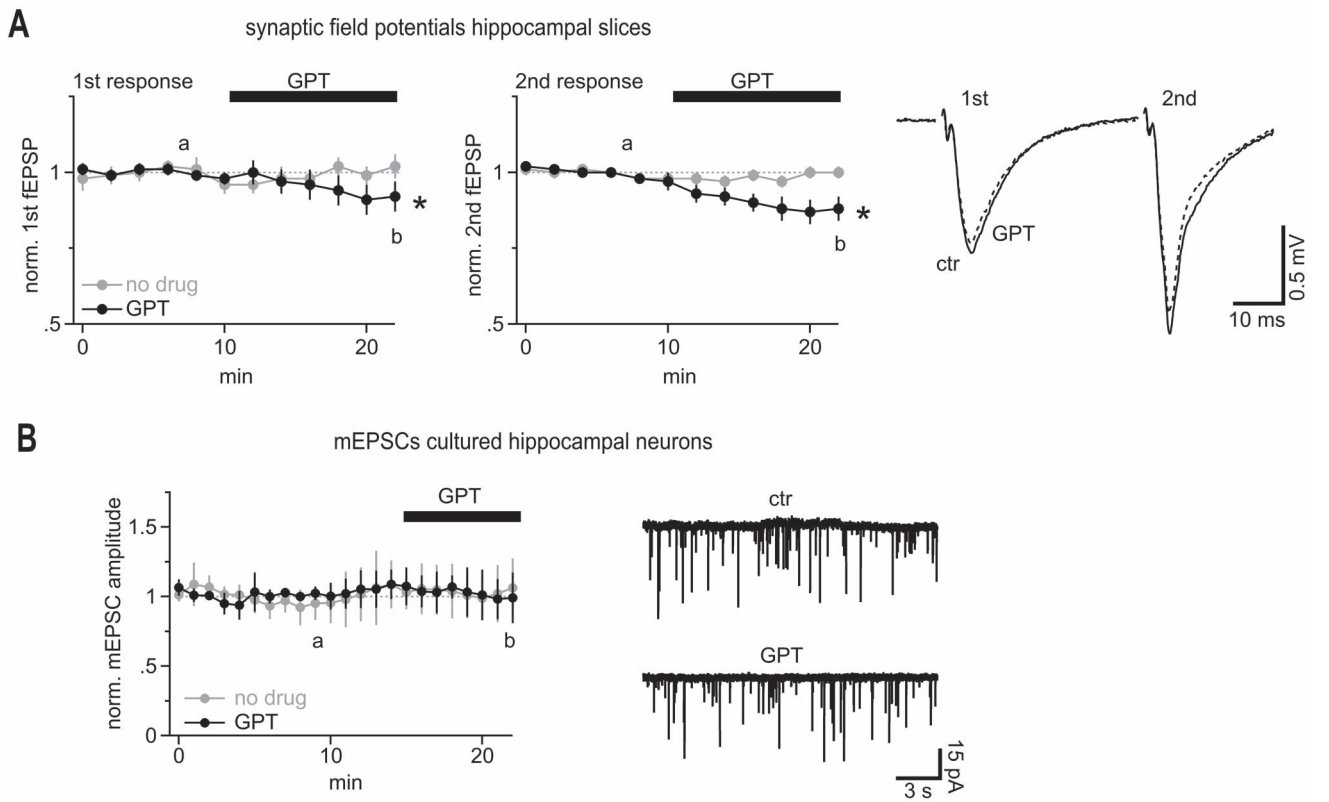

Figure 7. Synaptically released glutamate regularly coactivates neighboring synapses to a small extend. (*A*) AMPA receptor-mediated population synaptic responses in hippocampal slices are enhanced by glutamate acting on neighboring synapses. Left panel, summary of the first slopes of fEPSPs recorded in CA1 Str. rad. Note the slight, but statistically a significant decrease in fEPSPs upon application of the glutamate scavenger system (GPT, $n = 9$; "no drug" control experiment with placebo solution exchange, $n = 11$). Middle panel, the inhibitory effect of GPT is more pronounced on the second, facilitated fEPSPs, which is associated with a higher spatial density of releasing synapses. The letters "a" and "b" denote the times of the example traces illustrated in the right panel. Right panel, example traces illustrating the effect of GPT on population synaptic responses. (*B*) The glutamate scavenger system GPT is too slow to inactivate glutamate immediately after release in the synaptic cleft; the amplitude of miniature EPSCs remains unaffected. Miniature EPSCs were recorded in dissociated cultured neurons. As the nearest neighbor distance of synapses in cultured neurons is too large ($\geq 1\ \mu$m) to allow for cross-talk, the amplitude of these currents is a measure of intrasynaptic AMPA receptor activation only. The letters "a" and "b" denote the times of the example traces illustrated in the right panel.

and undetectable (Boyer et al. 1998; Kavalali et al. 1999). Therefore, mEPSCs in culture allowed us to record direct synaptic activation only.

Discussion

Our study provides experimental estimates of the distance from an individual synapse at which glutamate can activate a glutamate-binding protein such as the glutamate sensor iGluSnFr. We show that putative single and multiquantal release from small hippocampal synapses activate iGluSnFr molecules in a neighborhood with a radius of approximately 2 μm. This neighborhood is much larger than expected based on previous theoretical models of glutamate spread in the neuropil following synaptic release (Rusakov and Kullmann 1998; Barbour 2001). In fact, when we used these models and added iGluSnFr molecules according to Helassa et al. (2018 and Armbruster et al. (2020), a single vesicle is predicted to generate a local iGluSnFr response of less than 1% DF/F at a distance of 1500 nm (Supplementary Fig. 4) whereas we experimentally determined an iGluSnFr response of approximately 5.4% DF/F at 1500 nm (cf Fig. 2). This means that our experimental results exceed the theoretical predictions by a factor of approximately 5. Responses at this distance are sufficiently far away not to be contaminated by fluorescent light originating from the activated synaptic cleft, as evidenced by the spatial restriction of the signal in the red channel in Figure 1. Further, the spatial gradients of the signals at that distance are relatively flat and compare well to the optical resolution such that the local iGluSnFr response amplitudes should be well resolved that far away from a synapse. Thus, our optical recordings suggest that glutamate after vesicular release may penetrate much further into the perisynaptic tissue than previously reported and may also imply a larger synaptic cross-talk component. This view of an unexpectedly large spread of synaptic glutamate into the extracellular hippocampal neighborhood is supported by our scavenger experiments, which suggested that even AMPA-R mediated synaptic communication, to a small extent, is carried out by synaptic cross-talk (Fig. 7).

We further used 2P-glutamate uncaging to quantitatively determine distance-dependent activation of AMPA and NMDA receptors situated on dendritic spines. It is inherent to this approach that the uncaging laser spot

is much larger than a synaptic cleft, and the laser pulse releases more glutamate than contained in a single vesicle and the duration of the laser pulse (0.6 ms) is longer than the time it takes to empty a synaptic vesicle. Therefore, a question arises what uncaging experiments can tell us about synaptic cross-talk and how do these differences affect our conclusions?

The differences between synaptically generated glutamate gradients occurring on and very near a spine and those induced by uncaging on or close to a spine are particularly large: vesicular glutamate is released faster (vesicle content liberated within ~0.1–0.3 ms; Wahl et al. 1996) and is initially confined to the synaptic cleft. This difference can be most clearly seen when considering that uncaging at 0 nm (at the spine) equals the AMPA-R amplitude caused by a single vesicle (~12 pA, average mEPSC amplitude) whereas we photo-release the equivalent of approximately five vesicles. Thus, uncaging amplitudes close to the source are smaller than they would be if the same amount of glutamate was liberated in the synaptic cleft only and for this reason the distance-dependent curves we measured appear "flatter" than they really are. Therefore, λ values cannot directly be taken to describe the relative spatial decay of synaptic cross-talk responses.

However, a meaningful comparison can be made between the remote action of synaptic and uncaging sources of glutamate. Synaptically released glutamate escapes the synaptic cleft and spreads within the neuropil like a progressively enlarging cloud and reaches the target spine/synapse with some delay. Thus, even after fast and very local vesicular release, the wave of glutamate arriving at a remote target synapse will be slowed, broadened, and diluted (and reduced by transporters). It is instructive to compare the glutamate concentration profiles arriving at a remote synapse, for example, at 500 nm, after a brief vesicle release (<0.1 ms) and after uncaging release from a 3D PSF for 0.6 ms. For this comparison, we simulated the two types of release of 5000 glutamate molecules and the ensuing diffusion in neuropil according to the standard approaches used by Rusakov and Kullmann (1998) and Barbour (2001). Supplementary Figure 5A clearly shows that after vesicular release, glutamate concentrations reached a approximately 2-fold higher peak at 500 nm (e.g., at the nearest neighbor synapse) when compared to prolonged 0.6 ms release from a PSF volume (x/y FWHM = 280 nm, $\omega_z \sim 3.5\ \omega_{x,y}$). This is mainly due to the fact that the brief and point-like release of glutamate from a synapse generates a sharper wave of glutamate and is less broadened when arriving at 500 nm. Adding AMPA-receptors to the simulation at 500 nm (following Rusakov and Kullmann 1998 and Barbour 2001) demonstrated that synaptic release accordingly causes an approximately 2-fold stronger glutamate receptor opening when compared to uncaging the same amount of glutamate (Supplementary Fig. 5B). Thus, uncaging glutamate at 500 nm likely underestimates the AMPA-R-mediated cross-talk following synaptic release of the same number of glutamate molecules (5000) at the same distance.

In our uncaging experiments, we release the glutamate content of approximately five vesicles (~35 000 molecules) and this generated an AMPA-R-mediated uEPSC of approximately 4.6 pA at a distance of approximately 500 nm (cf Figs 3 and 4). With the reasoning above, this means that synaptic release of five vesicles would produce a similar or larger current response at its nearest neighbor synapse equaling approximately 40% of the average quantal amplitude (>4.6 pA/12 pA). Furthermore, when glutamate transporters are blocked (tfb-TBOA, Fig. 4D), our uncaging data suggest that a five-vesicle release event results in a cross-talk current approximately 55% of the quantal amplitude (~6.4 pA).

Such large AMPA-R responses to remote uncaging spots in comparison to the quantal amplitude go clearly beyond the predictions by standard models of glutamate diffusion in the neuropil. To illustrate this, we followed the modeling approach of (Barbour 2001). In this model, the release of a single vesicle filled with 7000 molecules of glutamate generates an AMPA-R open probability (P_o) of approximately 0.172 in the synaptic cleft (quantal response, with and without transporters). To calculate the predicted open probability in response to a remote uncaging stimulus, we added a 3D, PSF-shaped and 0.6 ms-lasting source of 35 000 molecules of glutamate (five vesicles) at a distance of 500 nm (Supplementary Fig. 5C). It can be seen that this model predicts a P_o in response to uncaging of approximately 0.022 (Supplementary Fig. 5C, in the absence of transporters), which represents only approximately13% of the quantal response (0.172/0.022), whereas the uncaging response in our experiments reached approximately 55% of the quantal response (as above). Thus, our experimental data on AMPA-R activation also exceeds the theoretical estimates by a factor of approximately 4. It is worth noting that other models of neuropil diffusion predict a much higher P_o for synaptic AMPA-Rs (up to 0.7; Rusakov and Kullmann 1998), which would make the difference to our experimental observations even larger.

A similar line of arguments can be made for the activation of NMDA-Rs, as remote uncaging accurately estimates remote synaptic receptor activation. Our data (Fig. 3C–G) indicate that the neighboring synapses in a sphere with a radius approximately 1.5 μm (λ_{NMDA}) around a multivesicular release site may become activated by cross-talk if depolarization of the postsynaptic neurons permits opening of the NMDA-Rs. This sphere, on an average, will contain 20–30 synapses (~14 μm^3) and the degree of the activation of their NMDA-Rs will depend on how many vesicles are released. As mentioned above, there is a strong and growing evidence that many synapses, if not all, release up to five vesicles (Oertner et al. 2002; Christie and Jahr 2006; Jensen et al. 2019; Kusick et al. 2020; Maschi and Klyachko 2020) emphasizing the physiological relevance of our

conclusions based on the photo-release of approximately 36 000 molecules of glutamate. Multivesicular release from and cross-talk between Schaffer collateral synapses is consistent with our glutamate scavenger experiments in this pathway (Fig. 7).

Our finding of remote action of glutamate on AMPA-Rs and NMDA-Rs contradicts previous modeling studies, which predict negligible activation of AMPA-Rs at more than 500 nm, even for multivesicular release, and a much weaker activation of NMDA-Rs (Rusakov and Kullmann 1998; Barbour 2001; Rusakov 2001; Zheng et al. 2008; Zheng and Rusakov 2015). To some extent this difference could be explained by more recent estimates of certain biological parameters such as a higher glutamate content of synaptic vesicles (7000–8000 molecules; Budisantoso et al. 2012; Wang et al. 2019), a wider synaptic cleft (≥24 nm; Lučić et al. 2005; Zuber et al. 2005; Kinney et al. 2013) and a deeper understanding of glutamate transporter reaction schemes (Kortzak et al. 2019). The "porous medium" approach used to approximate diffusible signaling on the nanoscale in the brain may be another shortcoming of existing modeling studies. This approach has been developed and successfully validated to describe the spread of molecules in the brain over larger distances (>10 μm; Syková and Nicholson 2008) but it may not be well suited to describe the initial diffusion on a scale of less than 1 μm (Nicholson and Phillips 1981; Hrabe et al. 2004).

The fraction of glutamate photoconverted by our uncaging laser pulse, ε, is a critical parameter for estimating how much glutamate we released but it is not precisely known. We estimated ε to be approximately 0.3 as we noted that by only slightly elevating laser power, we could easily increase AMPA-R mediated uEPSC currents (cf Fig. 6C) up to approximately 40 pA (not shown). If ε was significantly larger than 0.3, such strong amplitude increases are difficult to explain as we bathed the slices only in 5 mM MNI-glutamate (K_d AMPA-R ~ 500 μM). On the other hand, the rapid rise of the uncaging excitatory postsynaptic current (EPSC) suggested that at least several hundred μM glutamate acted as AMPA-Rs on the spine head. If we assumed a substantially lower fraction, for example, $\varepsilon \sim 0.1$, much slower rise times would be expected (e.g., Barbour 2001; Fig. 7), which would not be consistent with our observations. If ε was larger than assumed, then we would have released proportionally more glutamate. For example, if ε was 0.6, one uncaging pulse would correspond to approximately 10 rather than approximately 5 vesicles. Even such a strong deviation in ε would not severely affect our main conclusion because as previously discussed, uncaging is only approximately half as effective in opening AMPA-Rs when compared to brief synaptic release (Supplementary Fig. 5).

Is glutamate capable of saturating glutamate uptake mechanisms or their binding sites? λ_{AMPA} did not decrease when the amount of glutamate released by uncaging was reduced (cf Fig. 6C) as would be expected if transporters were overloaded. Similarly, small synaptic iGluSnFr responses (selected small and spontaneous events) showed a glutamate spread comparable to large responses (Figs 1 and 2). On the other hand, the λ_{AMPA} and λ_{NMDA} were slightly enhanced when we uncaged more glutamate (Fig. 6), indicating that a higher glutamate load cannot be handled with the same efficiency and that the uptake system operates close to the border of leaving linearity when challenged by the standard uncaging pulse. This scenario explains why applying three uncaging spots simultaneously led to a glutamate spread that was supra-additive (Fig. 5). The spread of glutamate is likely to be facilitated by glutamate transporters becoming overburdened as a result of the high local glutamate load.

Can synaptic activity generate such a local glutamate load? In our uncaging experiment the spine head integrated glutamate release equivalent to approximately 15 vesicles (3 uncaging spots, each of 5 vesicles) within a radius of approximately 0.75 μm corresponding to a volume of approximately 1.8 μm^3. This volume of neuropil on average contains approximately 3–4 synapses (2 synapses/μm^3) each of them being able to release up to five vesicles. Thus, if a handful of neighboring synapses are active together and undergo multivesicular release, the synaptic current can be increased by approximately 30%, as observed during the uncaging experiment. The physiological boost could even be greater because synaptic activity can occur simultaneously while uncaging pules in our experiment were limited to a synchrony of approximately 2 ms for technical reasons. Further, when keeping in mind, as argued above, that following uncaging lower glutamate concentrations are reached due to the PSF-shaped source and the prolonged release time (0.6 ms), even fewer (<15) coreleased synaptic vesicles may generate the same level of amplification as seen during uncaging. Such high density of active synapses is unlikely to be achieved across a larger region typically recruited for experimentally stimulated compound synaptic responses, which may explain the conclusion that transporters are not overwhelmed by synaptic activity in the previous work (Diamond and Jahr 2000).

What exactly is the role of astroglial glutamate uptake in limiting the action range of glutamate around a synapse, on the scale of less than 2 μm and below 2 ms? Blocking glutamate transport competitively by tfb-TBOA strongly increased λ_{AMPA} by approximately 75% demonstrating that glutamate transporters are important for limiting the spread of glutamate. However, the intracellular translocation of glutamate by transporters of hippocampal astrocytes shows a high temperature sensitivity (Q10 ~ 2.5; Bergles and Jahr 1998) but λ_{AMPA} modestly decreased by approximately 15% when elevating the recording temperature from 20 to 32 °C. This indicates that the intracellular translocation of glutamate does not play a significant role in limiting λ_{AMPA}. One possible explanation is that the translocation process itself is too slow, even at near-body temperature, to efficiently remove glutamate molecules on the scale

of 2 μm and below 2 ms. Rather, it appears likely that transporters limit λ_{AMPA} not by translocating glutamate but by binding glutamate and by successfully competing with glutamate receptors for binding to the ligand, as has been proposed for glutamate dynamics within the synaptic cleft (Diamond and Jahr 1997) and at Bergmann glial membranes (Dzubay and Jahr 1999). Binding by transporters is rapid, precedes translocation and is competitively blocked by tfb-TBOA, which is most consistent with our experimental observations. This scenario suggests that the number of transporter binding sites exposed to the extracellular space in the microenvironment of a spine is sufficiently high to reduce λ_{AMPA} even without translocation of glutamate (cf. Fig. 5; Barbour 2001) but also that those binding sites can be partially depleted if the local density of active synapses grows high (see above). Conversely, it can be concluded that if the local transporter density is slightly up- or down-regulated, this will result in a shorter or larger action range of glutamate. Local glutamate transporter density has been shown to be affected by activity-induced immobilization of glutamate transporters or by increasing their surface expression through recycling (Murphy-Royal et al. 2015; Michaluk et al. 2021). This connection puts astrocytes in an ideal position to tune synaptic cross-talk through AMPARs by strategically positioning glutamate transporter molecules on their membranes. This has recently been proposed to happen albeit for the activation of NMDA-Rs after the induction of LTP (Henneberger et al. 2020).

Another major aspect of our work is the finding of supra-additive spread of glutamate caused by coincidental activity of nearby synapses. This finding suggests a new mechanism by which astrocytes can regulate synaptic integration on the millisecond time scale through acting on the extracellular space. While intracellular calcium signaling or gliotransmitter release by astrocytes is very slow and happens within seconds, astrocytes could tune the local volume density of glutamate transporters (Murphy-Royal et al. 2015; Michaluk et al. 2021) and thus regulate high-frequency neuronal activity: the density of transporters will set the degree and regionality of supra-additivity of kHz coincident neuronal activity and foster pseudoclustered activity along the same and across different dendrites. Taken together, our results suggest that a deep functional understanding of neuronal circuits and behaviors not only calls for deciphering synaptically connected pairs of neurons in the brain but may also require considering the immediate spatial neighborhood of neurons and their synapses on the submicrometer scale.

Supplementary Material

Supplementary material can be found at *Cerebral Cortex* online.

Funding

Deutsche Forschungsgemeinschaft (SFB 1089 to A.B., C.H., D.D., S.S., E.A.M., SPP1757 to C.H., D.D., and S.S., INST1172 15, DI853/3-5, DI853/3-7 to D.D., SCHO 820/4-1, SCHO 820/6-1, SCHO 820/7-1, SCHO 820/5-2 to S.S., FOR 2715 to A.J.B.); the European Union's Seventh Framework Program (FP7/2007-2013) under grant agreement no. 602102 (EPITARGET; A.J.B., S.S.); Bundesministerium für Bildung und Forschung (01GQ0806 to S.S.; the EraNet DeCipher to A.J.B.); National Institute of Mental Health (R01 MH66198) to E.T.K.; NRW-Rückkehrerprogramm to C.H.; the BONFOR program of the Medical Faculty of the University of Bonn (to J.P., A.J.B., S.S., D.D., W.S., V.S.); Verein zur Förderung der Epilepsieforschung (to S.S., A.J.B.) and CONNECT-GENERATE (FKZ01GM1908C to A.J.B.).

Notes

We are grateful for the assistance of the Viral Core Facility of the Medical Faculty of the University of Bonn, supported in part by SFB1089 (funded by the D.F.G.). We thank Sabine Opitz for her excellent technical assistance.

Conflict of Interest: None declared.

References

Abbott LF, Regehr WG. 2004. Synaptic computation. *Nature*. 431: 796–803.

Anders S, Minge D, Griemsmann S, Herde MK, Steinhauser C, Henneberger C. 2014. Spatial properties of astrocyte gap junction coupling in the rat hippocampus. *Phil Trans R Soc B Biol Sci*. 369:(1654):20130600.

Armbruster M, Dulla CG, Diamond JS. 2020. Effects of fluorescent glutamate indicators on neurotransmitter diffusion and uptake. *Elife*. 9:10404–10426.

Arnth-Jensen N, Jabaudon D, Scanziani M. 2002. Cooperation between independent hippocampal synapses is controlled by glutamate uptake. *Nat Neurosci*. 5:325–331.

Asztely F, Erdemli G, Kullmann DM. 1997. Extrasynaptic glutamate spillover in the hippocampus: dependence on temperature and the role of active glutamate uptake. *Neuron*. 18:281–293.

Barbour B. 2001. An evaluation of synapse independence. *J Neurosci*. 21:7969–7984.

Barbour B, Keller BU, Llano I, Marty A. 1994. Prolonged presence of glutamate during excitatory synaptic transmission to cerebellar Purkinje-cells. *Neuron*. 12:1331–1343.

Benna MK, Fusi S. 2016. Computational principles of synaptic memory consolidation. *Nat Neurosci*. 19:1697–1706.

Bergles DE, Jahr CE. 1998. Glial contribution to glutamate uptake at Schaffer collateral-commissural synapses in the hippocampus. *J Neurosci*. 18:7709–7716.

Bourne JN. 2013. Presynaptic ultrastructural plasticity along CA3→CA1 axons during long-term potentiation in mature hippocampus. *J Comp Neurol*. 521:3898–3912.

Boyer C, Schikorski T, Stevens CF. 1998. Comparison of hippocampal dendritic spines in culture and in brain. *J Neurosci*. 18:5294–5300.

Bridges RJ, Esslinger CS. 2005. The excitatory amino acid transporters: pharmacological insights on substrate and inhibitor specificity of the EAAT subtypes. *Pharmacol Ther*. 107:271–285.

Budisantoso T, Harada H, Kamasawa N, Fukazawa Y, Shigemoto R, Matsui K. 2012. Evaluation of glutamate concentration transient in the synaptic cleft of the rat calyx of held. *J Physiol*. 591:219–239.

Carter AG, Regehr WG. 2000. Prolonged synaptic currents and glutamate spillover at the parallel fiber to stellate cell synapse. *J Neurosci*. 20:4423–4434.

Christie JM, Jahr CE. 2006. Multivesicular release at Schaffer collateral-CA1 hippocampal synapses. *J Neurosci*. 26:210–216.

Danbolt NC, Furness DN, Zhou Y. 2016. Neuronal vs glial glutamate uptake: resolving the conundrum. *Neurochem Int*. 98:29–45.

Diamond JS. 2001. Neuronal glutamate transporters limit activation of NMDA receptors by neurotransmitter spillover on CA1 pyramidal cells. *J Neurosci*. 21:8328–8338.

Diamond JS, Jahr CE. 1997. Transporters buffer synaptically released glutamate on a submillisecond time scale. *J Neurosci*. 17: 4672–4687.

Diamond JS, Jahr CE. 2000. Synaptically released glutamate does not overwhelm transporters on hippocampal astrocytes during high-frequency stimulation. *J Neurophysiol*. 83:2835–2843.

DiGregorio DA, Nusser Z, Silver RA. 2002. Spillover of glutamate onto synaptic AMPA receptors enhances fast transmission at a cerebellar synapse. *Neuron*. 35:521–533.

Dürst CD, Wiegert JS, Helassa N, Kerruth S, Coates C, Schulze C, Geeves MA, Torok K, Oertner TG. 2019. High-speed imaging of glutamate release with genetically encoded sensors. *Nat Protoc*. 14:1401–1424.

Dzubay JA, Jahr CE. 1999. The concentration of synaptically released glutamate outside of the climbing fiber-Purkinje cell synaptic cleft. *J Neurosci*. 19:5265–5274.

Helassa N, Dürst CD, Coates C, Kerruth S, Arif U, Schulze C, Wiegert JS, Geeves M, Oertner TG, Torok K. 2018. Ultrafast glutamate sensors resolve high-frequency release at Schaffer collateral synapses. *Proc Natl Acad Sci*. 115:5594–5599.

Henneberger C, Bard L, Panatier A, Reynolds JP, Kopach O, Medvedev NI, Minge D, Herde MK, Anders S, Kraev I, et al. 2020. LTP induction boosts glutamate Spillover by driving withdrawal of Perisynaptic Astroglia. *Neuron*. 108(5):919–936.

Hrabe J, Hrabětová S, Segeth K. 2004. A model of effective diffusion and tortuosity in the extracellular space of the brain. *Biophys J*. 87:1606–1617.

Hrabětová S. 2005. Extracellular diffusion is fast and isotropic in the stratum radiatum of hippocampal CA1 region in rat brain slices. *Hippocampus*. 15:441–450.

Hubbard JA, Szu JI, Yonan JM, Binder DK. 2016. Regulation of astrocyte glutamate transporter-1 (GLT1) and aquaporin-4 (AQP4) expression in a model of epilepsy. *Exp Neurol*. 283:85–96.

Jensen TP, Zheng K, Cole N, Marvin JS, Looger LL, Rusakov DA. 2019. Multiplex imaging relates quantal glutamate release to presynaptic Ca^{2+} homeostasis at multiple synapses in situ. *Nat Commun*. 10:1–14.

Kasai H, Matsuzaki M, Noguchi J, Yasumatsu N, Nakahara H. 2003. Structure–stability–function relationships of dendritic spines. *Trends Neurosci*. 26:360–368.

Kavalali ET, Klingauf J, Tsien RW. 1999. Activity-dependent regulation of synaptic clustering in a hippocampal culture system. *Proc Natl Acad Sci USA*. 96:12893–12900.

Kinney GA, Overstreet LS, Slater NT. 1997. Prolonged physiological entrapment of glutamate in the synaptic cleft of cerebellar unipolar brush cells. *J Neurophysiol*. 78:1320–1333.

Kinney JP, Spacek J, Bartol TM, Bajaj CL, Harris KM, Sejnowski TJ. 2013. Extracellular sheets and tunnels modulate glutamate diffusion in hippocampal neuropil. *J Comp Neurol*. 521: 448–464.

Kopach O, Zheng K, Rusakov DA. 2020. Optical monitoring of glutamate release at multiple synapses in situ detects changes following LTP induction. *Mol Brain*. 13:1–10.

Kortzak D, Alleva C, Weyand I, Ewers D, Zimmermann MI, Franzen A, Machtens J-P, Fahlke C. 2019. Allosteric gate modulation confers K^+ coupling in glutamate transporters. *EMBO J*. 38:e101468.

Kusick GF, Chin M, Raychaudhuri S, Lippmann K, Adula KP, Hujber EJ, Vu T, Davis MW, Jorgensen EM, Watanabe S. 2020. Synaptic vesicles transiently dock to refill release sites. *Nat Neurosci*. 23: 1329–1338.

Lakowicz JR. 2009. *Principles of fluorescence spectroscopy*. 3rd ed. Boston, MA: Springer, XXVI, 954. https://doi.org/10.1007/978-0-387-46312-4.

Lozovaya NA, Kopanitsa MV, Boychuk YA, Krishtal OA. 1999. Enhancement of glutamate release uncovers spillover-mediated transmission by N-methyl-D-aspartate receptors in the rat hippocampus. *Neuroscience*. 91:1321–1330.

Lučić V, Yang T, Schweikert G, Förster F, Baumeister W. 2005. Morphological characterization of molecular complexes present in the synaptic cleft. *Structure*. 13:423–434.

Marvin JS, Borghuis BG, Tian L, Cichon J, Harnett MT, Akerboom J, Gordus A, Renninger SL, Chen T-W, Bargmann CI, et al. 2013. An optimized fluorescent probe for visualizing glutamate neurotransmission. 10:162–170.

Marvin JS, Scholl B, Wilson DE, Podgorski K, Kazemipour A, Muller JA, Schoch S, Quiroz FJU, Rebola N, Bao H, et al. 2018. Stability, affinity, and chromatic variants of the glutamate sensor iGluSnFR. *Nat Methods*. 15:936–939.

Maschi D, Klyachko VA. 2020. Spatiotemporal dynamics of multivesicular release is determined by heterogeneity of release sites within central synapses. *Elife*. 9:279–220.

Matsuzaki M, Ellis-Davies GC, Nemoto T, Miyashita Y, Iino M, Kasai H. 2001. Dendritic spine geometry is critical for AMPA receptor expression in hippocampal CA1 pyramidal neurons. *Nat Neurosci*. 4:1086–1092.

Michaluk P, Heller JP, Rusakov DA. 2021. Rapid recycling of glutamate transporters on the astroglial surface. *Elife*. 10. https://elifesciences.org/articles/64714.

Min MY, Rusakov DA, Kullmann DM. 1998. Activation of AMPA, kainate, and metabotropic receptors at hippocampal mossy fiber synapses: role of glutamate diffusion. *Neuron*. 21:561–570.

Mishchenko Y, Hu T, Spacek J, Mendenhall J, Harris KM, Chklovskii DB. 2010. Ultrastructural analysis of hippocampal neuropil from the connectomics perspective. *Neuron*. 67:1009–1020.

Murphy-Royal C, Dupuis J, Groc L, Oliet SHR. 2017. Astroglial glutamate transporters in the brain: regulating neurotransmitter homeostasis and synaptic transmission. *J Neurosci Res*. 95: 2140–2151.

Murphy-Royal C, Dupuis JP, Varela JA, Panatier A, Pinson B, Baufreton J, Groc L, Oliet SHR. 2015. Surface diffusion of astrocytic glutamate transporters shapes synaptic transmission. *Nat Neurosci*. 18: 219–226.

Nagy A, Wu J, Berland KM. 2005. Observation volumes and;-factors in two-photon fluorescence fluctuation spectroscopy. *Biophys J*. 89: 2077–2090.

Nicholson C, Phillips JM. 1981. Ion diffusion modified by tortuosity and volume fraction in the extracellular microenvironment of the rat cerebellum. *J Physiol*. 321:225–257.

Oertner TG, Sabatini BL, Nimchinsky EA, Svoboda K. 2002. Facilitation at single synapses probed with optical quantal analysis. *Nat Neurosci*. 5:657–664.

Overstreet LS, Kinney GA, Liu YB, Billups D, Slater NT. 1999. Glutamate transporters contribute to the time course of

synaptic transmission in cerebellar granule cells. *J Neurosci*. 19: 9663–9673.

Pankratov YV, Krishtal OA. 2003. Distinct quantal features of AMPA and NMDA synaptic currents in hippocampal neurons: implication of glutamate Spillover and receptor saturation. *Biophys J*. 85:3375–3387.

Pitsch J, Kuehn JC, Gnatkovsky V, Muller JA, van Loo KMJ, de Curtis M, Vatter H, Schoch S, Elger CE, Becker AJ. 2019. Anti-epileptogenic and anti-convulsive effects of Fingolimod in experimental temporal lobe epilepsy. *Mol Neurobiol*. 56:1825–1840.

Reiner A, Levitz J. 2018. Glutamatergic Signaling in the central nervous system: ionotropic and metabotropic receptors in concert. *Neuron*. 98:1080–1098.

Rossi DJ, Alford S, Mugnaini E, Slater NT. 1995. Properties of transmission at a giant glutamatergic synapse in cerebellum: the mossy fiber-unipolar brush cell synapse. *J Neurophysiol*. 74:24–42.

Rusakov DA. 2001. The role of Perisynaptic glial sheaths in glutamate Spillover and extracellular Ca^{2+} depletion. *Biophys J*. 81: 1947–1959.

Rusakov DA, Kullmann DM. 1998. Extrasynaptic glutamate diffusion in the hippocampus: ultrastructural constraints, uptake, and receptor activation. *J Neurosci*. 18:3158–3170.

Savtchenko LP, Rusakov DA. 2005. Extracellular diffusivity determines contribution of high-versus low-affinity receptors to neural signaling. *NeuroImage*. 25:101–111.

Scimemi A, Scimemi A, Fine A, Kullmann DM, Rusakov DA. 2004. NR2B-containing receptors mediate cross talk among hippocampal synapses. *J Neurosci*. 24:4767–4777.

Shimamoto K, Lebrun B, Yasuda-Kamatani Y, Sakaitani M, Shigeri Y, Yumoto N, Nakajima T. 1998. DL-threo-beta-benzyloxyaspartate, a potent blocker of excitatory amino acid transporters. *Mol Pharmacol*. 53:195–201.

Silver RA, Cull-Candy SG, Takahashi T. 1996. Non-NMDA glutamate receptor occupancy and open probability at a rat cerebellar synapse with single and multiple release sites. *J Physiol*. 494: 231–250.

Syková E, Nicholson C. 2008. Diffusion in brain extracellular space. *Physiol Rev*. 88:1277–1340.

Szapiro G, Barbour B. 2007. Multiple climbing fibers signal to molecular layer interneurons exclusively via glutamate spillover. *Nat Neurosci*. 10:735–742.

Thomas CG, Tian H, Diamond JS. 2011. The relative roles of diffusion and uptake in clearing Synaptically released glutamate change during early postnatal development. *J Neurosci*. 31: 4743–4754.

Uppal N, Puri R, Yuk F, Janssen WGM, Bozdagi-Gunal O, Harony-Nicolas H, Dickstein DL, Buxbaum JD, Hof PR. 2015. Ultrastructural analyses in the hippocampus CA1 field in Shank3-deficient mice. *Mol Autism*. 6:1–10.

van Loo KMJ, Schaub C, Pitsch J, Kulbida R, Opitz T, Ekstein D, Dalal A, Urbach H, Beck H, Yaari Y, et al. 2015. Zinc regulates a key transcriptional pathway for epileptogenesis via metal-regulatory transcription factor 1. *Communications*. 6:12.

Varshney LR, Sjöström PJ, Chklovskii DB. 2006. Optimal information storage in noisy synapses under resource constraints. *Neuron*. 52: 409–423.

Wahl LM, Pouzat C, Stratford KJ. 1996. Monte Carlo simulation of fast excitatory synaptic transmission at a hippocampal synapse. *J Neurophysiol*. 75:597–608.

Wang Y, Fathali H, Mishra D, Olsson T, Keighron JD, Skibicka KP, Cans A-S. 2019. Counting the number of glutamate molecules in single synaptic vesicles. *J Am Chem Soc*. 141: 17507–17511.

Wohland T, Rigler R, Vogel H. 2001. The standard deviation in fluorescence correlation spectroscopy. *Biophys J*. 80:2987–2999.

Yuste R. 2015. From the neuron doctrine to neural networks. *Nat Rev Neurosci*. 16:487–497.

Zheng K, Rusakov DA. 2015. Efficient integration of synaptic events by NMDA receptors in three-dimensional neuropil. *Biophys J*. 108: 2457–2464.

Zheng K, Scimemi A, Rusakov DA. 2008. Receptor actions of Synaptically released glutamate: the role of transporters on the scale from nanometers to microns. *Biophys J*. 95: 4584–4596.

Zipfel WR, Williams RM, Webb WW. 2003. Nonlinear magic: multiphoton microscopy in the biosciences. *Nat Biotechnol*. 21: 1369–1377.

Zuber B, Nikonenko I, Klauser P, Muller D, Dubochet J. 2005. The mammalian central nervous synaptic cleft contains a high density of periodically organized complexes. *Proc Natl Acad Sci USA*. 102:19192–19197.

nature communications

Article

https://doi.org/10.1038/s41467-023-36070-6

Subcellular analysis of blood-brain barrier function by micro-impalement of vessels in acute brain slices

Received: 19 June 2021

Accepted: 13 January 2023

Published online: 30 January 2023

Check for updates

Amira Sayed Hanafy[1,2,6], Pia Steinlein[1,2,6], Julika Pitsch[3,4], Mariella Hurtado Silva[5], Natascha Vana[1], Albert J. Becker[3], Mark Evan Graham[5], Susanne Schoch[3], Alf Lamprecht[2] ✉ & Dirk Dietrich[1] ✉

The blood-brain barrier (BBB) is a tightly and actively regulated vascular barrier. Answering fundamental biological and translational questions about the BBB with currently available approaches is hampered by a trade-off between accessibility and biological validity. We report an approach combining micropipette-based local perfusion of capillaries in acute brain slices with multiphoton microscopy. Micro-perfusion offers control over the luminal solution and allows application of molecules and drug delivery systems, whereas the bath solution defines the extracellular milieu in the brain parenchyma. Here we show, that this combination allows monitoring of BBB transport at the cellular level, visualization of BBB permeation of cells and molecules in real-time and resolves subcellular details of the neurovascular unit. In combination with electrophysiology, it permits comparison of drug effects on neuronal activity following luminal versus parenchymal application. We further apply micro-perfusion to the human and mouse BBB of epileptic hippocampi highlighting its utility for translational research and analysis of therapeutic strategies.

In vertebrates, the vascular system constitutes the main pathway to metabolically connect organs throughout the body by delivering nutrients and by collecting and transporting metabolites to the excreting organs via the transport medium blood[1]. The vascular system is enclosed by a continuous cell-based barrier surrounding its lumen. This barrier not only assures an efficient stream of blood but also strongly restricts the free exchange of molecules between blood and tissue and thereby compartmentalizes the milieu of the vascular system from other tissues of the body[2]. However, rather than being generally impermeable, the barrier selectively and actively regulates the passage of molecules in both directions to meet the regional requirements of the nurtured tissue[2].

The brain is the organ with the most tightly and actively regulated vascular barrier called the blood-brain-barrier (BBB)[3]. This likely reflects the brain's strict requirements for a constant milieu of electrolytes and metabolites, despite strongly varying states of neuronal activity, and a partial separation of the brain's immune system from the rest of the body[4]. Maintenance and development of the BBB is regulated by an interaction of three types of cells, endothelial cells (ECs), pericytes (PCs) and astrocytes, which are together with neurons referred to as the neurovascular unit (NVU)[3]. ECs in the brain contiguously border the vascular lumen and are intricately linked to each other by tight junctions, such that they form the primary barrier, which cannot be crossed by most small molecules and water[5]. PCs form a

[1]Department of Neurosurgery, University Hospital Bonn, Bonn, Germany. [2]Department of Pharmaceutics, Institute of Pharmacy, University of Bonn, Bonn, Germany. [3]Section for Translational Epilepsy Research, Dept. of Neuropathology, University Hospital Bonn, Bonn, Germany. [4]Department of Epileptology, University Hospital Bonn, Bonn, Germany. [5]Synapse Proteomics, Children's Medical Research Institute, The University of Sydney, Sydney, Australia. [6]These authors contributed equally: Amira Sayed Hanafy, Pia Steinlein. ✉e-mail: alf.lamprecht@uni-bonn.de; dirk.dietrich@uni-bonn.de

https://doi.org/10.1038/s41467-023-36070-6

loose mesh on top of ECs and regulate outgrowth of vessels and the development of the BBB[6]. Astrocytes regularly but not contiguously touch ECs with their endfeet while the remainder of their cellular processes extend into the brain parenchyma. Astrocytes sense neuronal activity, have a homeostatic function in the brain parenchyma and regulate the capillary diameter in response to neuronal activity[7].

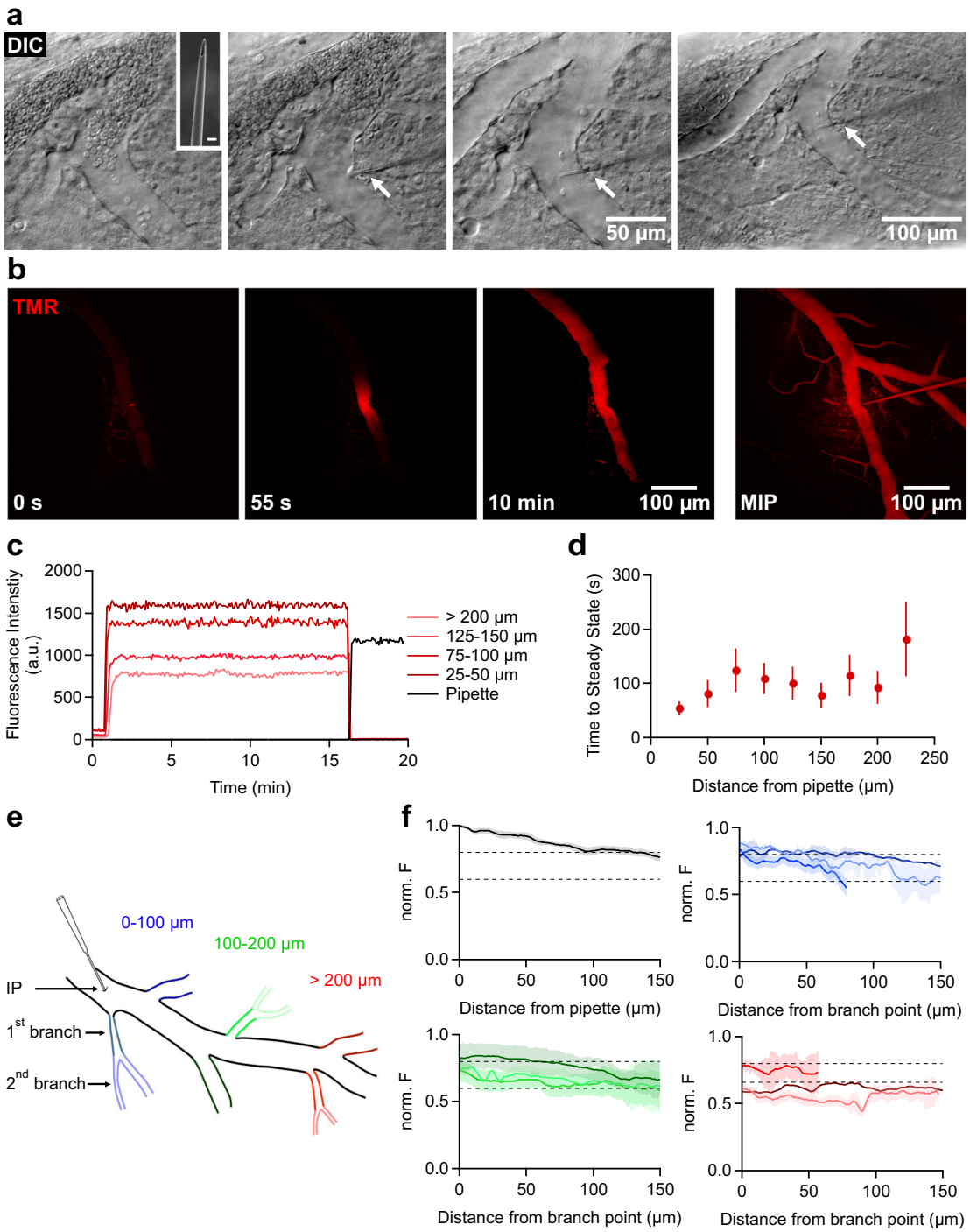

Fig. 1 | Micro-pipette-based perfusion of capillaries provides control of the composition of the luminal solution and pressure. a Representative light microscopic (differential interference contrast, DIC) images showing the penetration of a vessel with a glass capillary (4 experiments). Arrow points toward the tip of the pipette. Inset: raster electron micrograph of the beveled tip (scale bar 5 µm). Also see Suppl. movie 1 illustrating the flushing of the vascular lumen. **b** 2P-scans representative of at least 15 experiments. MIP; maximum intensity projection. **c** Intravascular fluorescence. Numbers denote the distance of the measurement from the point of impalement. **d** Luminal steady-state tracer concentration, as assessed by fluorescence measurements, are reached within ~100 s. Data obtained from 15 injections/9 animals; number of assessed ROIs: $n_{IP} = 15$; $n_{0-25\mu m} = 15$; $n_{25-50\mu m} = 14$; $n_{50-75\mu m} = 12$; $n_{75-100\mu m} = 10$; $n_{10-125\mu m} = 8$; $n_{125-150\mu m} = 7$; $n_{150-175\mu m} = 5$; $n_{175-200\mu m} = 5$; $n_{>200\mu m} = 5$. Data are presented as mean values +/- SEM. **e** Schematic classification of analyzed compartments of the vascular tree for assessing intravascular fluorescence intensities. Intensities measured within ROIs in the compartments and are shown in (f) (11 injections/6 animals). **f** Normalized intravascular fluorescence intensity profiles measured along the injected blood vessels (black) and vessels branching off at 0–100 µm (blue), 100–200 µm (green) and >200 µm (red) from the injection point. Dark lines represent the moving average of 5 measurements, shaded regions represent SEM. Data obtained from 11 injections/5 animals. Source data to panels of Fig. 1 are provided as a Source Data file.

It is now understood that the BBB is not just a constant filter for specific molecules entering and leaving the brain parenchyma but that transport is regulated in a very dynamic manner, depending on the biological states of the body: it is bidirectionally linked to neuronal activity, stress, sleep, changes of nutrition and it is coupled to the immune system[3]. Therefore, it is not surprising that disease-associated changes of the BBB are receiving increasingly more attention and causal roles of BBB alterations have, for example, been suggested for Alzheimer's disease and epilepsy[8,9]. Coupling of transport and BBB permeability to body states and systems-level functions is likely based on blood-borne signaling[10].

While significant progress on this topic has been made in recent years[11–15], a number of major questions regarding this dynamic regulation of the BBB and the specific facilitation of the passage of some molecules versus others are still mainly unresolved: a) What are the key molecules and pathways essential for the dynamic and pathological alterations of the BBB?, b) how and when are immune cells recruited across the BBB, c) do ECs and BBB properties differ between brain regions and across the smaller vessels between arterioles, venules and capillaries, d) which pattern of neuronal activity influences the transport and permeability of the BBB, e) conversely, how does the regulated transport of metabolites and neuroactive molecules at the BBB influence the activity of neurons in health and disease?

A more detailed understanding of BBB properties is not only fundamental to biology but has also great translational potential for improving drug delivery to the brain. Many CNS-active molecules fail to reach the brain parenchyma following oral or intravenous administration as they do not pass or are extruded at the BBB[16]. Moreover, pathophysiological changes can strongly impact drug transport into the brain. Therefore, defining modes of hindrance and extrusion at the BBB and identifying ways to modulate them for improved drug delivery holds great promise to advance medical treatment of CNS diseases[17]. Current approaches to improve CNS drug delivery successfully concentrated on altering EC properties and capitalized on their transcytotic pathways to overcome the BBB[18–20] rather than risking a general leakage by weakening the ECs' intercellular tight junctions or a metabolic imbalance by blocking BBB transporters. Validation of these strategies in the human brain vasculature would be desirable, as well as more detailed understanding on the regulation of intracellular trafficking towards transcytosis, recycling back to the bloodstream or degradation[7]. Further, it has recently been discovered that in inflammatory diseases where the endothelial BBB is disturbed astrocytes respond and re-build a second barrier by expressing tight junctions[21] potentially complicating drug delivery in the disease condition.

With the currently available methodology, answering these open questions is rather difficult. Approaches are required that allow analysis of the native BBB, which has been in interaction with the healthy or the diseased brain and was under the control of systemically circulating signaling molecules. Furthermore, experimentally controlling the intra-luminal solution is of paramount importance in order to apply or interfere with BBB-activating molecules, cells, drug candidates or fluorescent tracers. Suitable experimental approaches should be applicable to various brain regions in different species, to capillaries, venules and arterioles and also to other organs for comparative studies of the BBB. Addressing the interdependence of the BBB and neuronal activity requires combining BBB analysis with recording and stimulating neuronal activity[7]. Ideally, experimental approaches should allow the visualization of cellular and sub-cellular details of the NVU in situ with high spatial and temporal resolution to study the barrier-forming intercellular interfaces of ECs as well as of BBB-penetrating immune cells and to optically track BBB permeation of labelled molecules[22]. In particular, it will be important to visualize the cytoplasm of ECs to analyze the different transcytotic pathways, as the regulation of transcytosis[23] is emerging as a critical mechanism of maintaining BBB integrity and facilitating drug targeting[24].

Many useful and sophisticated in vitro models of the BBB based on cultured cells have been developed and successfully used to address specific questions[25]. However, as BBB properties are not intrinsic to ECs but arise from an interaction with both the brain and the rest of the body via circulating factors or cells, it is clear that such models, while certainly very useful for specific questions, are limited in their ability to replicate many aspects of the healthy and diseased BBB.

In vivo approaches to study the BBB with high-resolution imaging on the other hand provide a gold standard in looking at the healthy or diseased native BBB in its physiological environment[26]. However, not all brain regions and developmental stages are amenable to intravital microscopy and optical resolution at subcellular levels is difficult to achieve[27]. The bloodstream can be supplemented with drugs, tracers and signaling molecules in vivo by intravenous injection but it is usually difficult to maintain their intraluminal concentration at a constant level due to systemic metabolism and excretion[28]. Furthermore, if experimental substances are applied systemically, it is hard to precisely define how, where and when they entered the brain parenchyma[29]. Finally, the possibilities to systematically alter the composition of the intraluminal and brain interstitial solutions is limited, as blood flow and oxygen content are crucial for brain vitality during observation and the extracellular solution of the brain parenchyma is not easily accessible, respectively.

Taken together, for the currently available approaches to study the BBB there is a general trade-off between experimental controllability and accessibility on the one hand and biological validity on the other, hampering the ability to answer fundamental biological and pressing translational questions.

Here, we report an approach to study the native BBB in situ, which unites systematic accessibility with high validity and flexibility. This approach is based on combining micro-perfusion of capillaries in acute brain slices with high-resolution multiphoton microscopy. It allows to systematically study BBB transport, permeation of cells and molecules in real-time, resolves subcellular details of cells of the NVU and offers control over luminal solution stream and pressure. We furthermore showed that this approach can be combined with cellular electrophysiology to record and evoke neuronal activity and allowed comparison of drug activity following luminal versus parenchymal application. We validated and applied this approach to human and murine brain under healthy, diseased and damaged conditions.

Results

To systematically and quantitatively study regional properties and locally restricted mechanisms of the native BBB, we aimed at controlling the composition of the solutions on both sides of the barrier in acutely prepared mouse cortical brain slices. While the parenchymal side of the BBB is easily and routinely controlled in a brain slice recording chamber via the perfusion medium, the lumen of the vascular system remained experimentally inaccessible and capillaries collapse in the absence of the blood or a solution stream. We achieved access to the luminal side of the BBB by inserting glass capillaries into vessels which enabled us to re-establish a solution stream in the vascular system of a brain slice and gave us full control of the composition of the luminal solution. To this end, we beveled injection pipettes to a ~3 μm diameter and a sharp flat-angled tip (Fig. 1a). Under microscopic control (Fig. 1a, b), dye-filled pipettes (100 μM biocytin-tetramethylrhodamine, TMR) were carefully inserted into an acute brain slice (300 μm) and moved towards the border of a vessel with the help of micro-manipulators (for images of the setup see Suppl. Figure 1a–d). The type of vessels approached (artery, arteriole, capillary, venule, vein) could clearly be discerned in the DIC or Dodt image, based on

https://doi.org/10.1038/s41467-023-36070-6

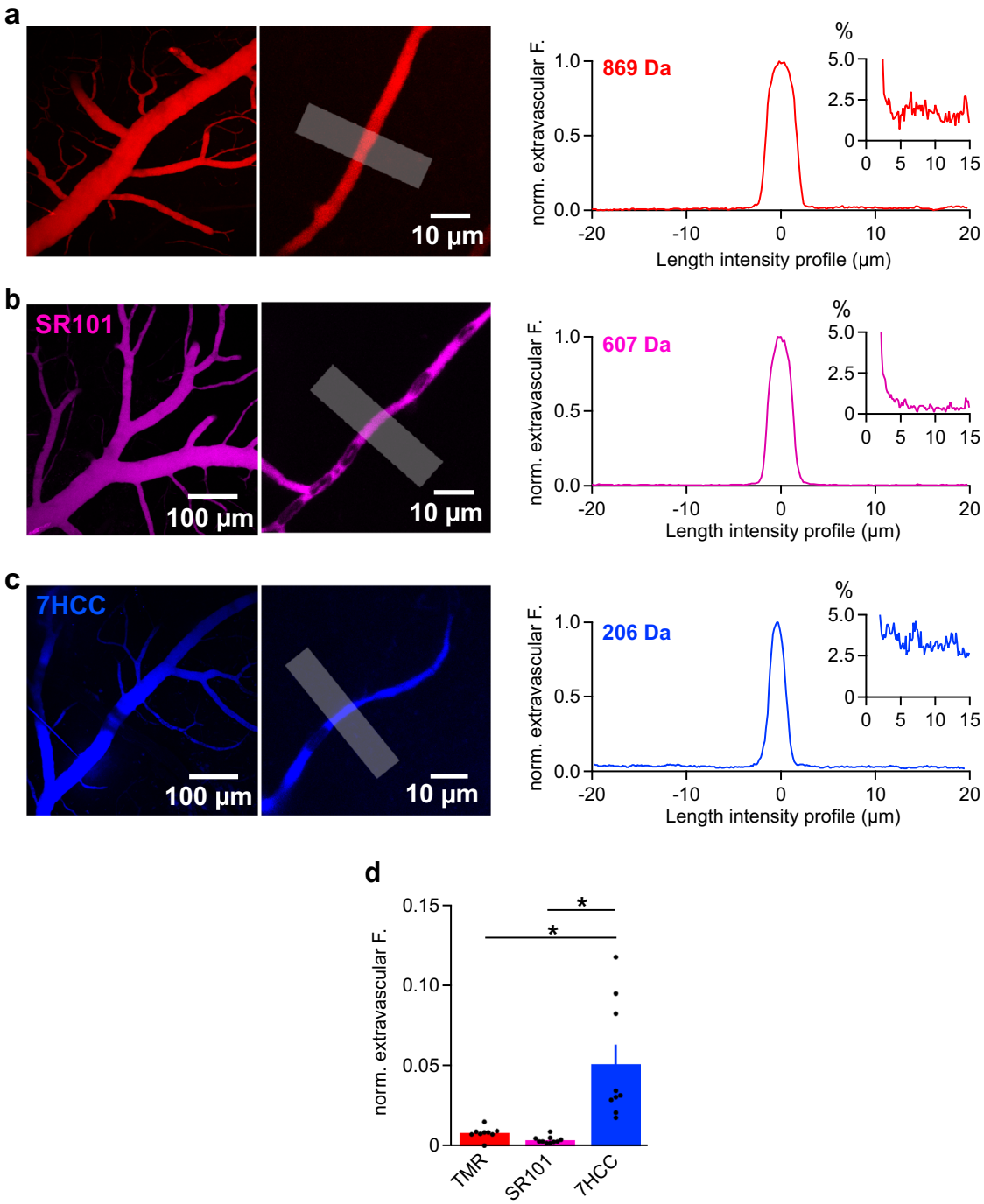

Fig. 2 | Tracers of variable molecular size show differential diffusion rates across the BBB. a MIP of TMR-injected vascular tree and a single frame of a capillary (left) and the spatial fluorescence profile of an ROI (white line) across a capillary at 30 min (left) with less than 2% extravascular fluorescence (see inset). Images represent 9 experiments. **b** MIP at t_{30} of SR101 injection (left) and the line profile of an ROI across a capillary (right) showing an extravascular fluorescence below 1% (see inset). Images are representative of 5 experiments. **c** MIP of the vascular tree and a single frame of a capillary recorded at t_{30} of 7HCC injection (left) and the spatial fluorescence profile of an ROI (white line) across the capillary at 30 min (right) showing 3–4% extravascular fluorescence (see inset). Images are representative of 5 experiments. **d** Comparison of fluorescence intensities measured within ROIs placed on single frames of capillaries at 30 min after normalization to the intravascular fluorescence. Data are graphed as mean ± SEM from 19 injections/8 animals, ROIs: $n_{TMR} = 9$, $n_{SR101} = 9$, $n_{7HCC} = 10$. Statistical significance was calculated using a one-way ANOVA with Tukey's post *hoc* test (*, $P < 0.05$). The P values between TMR/7HCC and SR101/7HCC were 0.0006 and 0.0001, respectively. Source data to panels of Fig. 2 are provided as a Source Data file.

their diameter and thickness of the wall[30]. In general, all types of vessels could be penetrated when approached from the side by the tip of the injection pipette, except capillaries. Capillaries were too elastic and could be pushed for several hundred µm through the brain slice without rupture and without penetration by the pipette tip. Arterioles could be penetrated but the success rate was low (<20%) as often the tip of the glass pipette broke at or in the wall of the vessel. Therefore, we chose venules (diameter 20–50 µm) which yielded a high success rate (~80–90%) for experiments. The piercing was done at a slice depth of 30–50 µm which still permitted a good visualization of the pipette tip with wide-field microscopy (DIC or Dodt contrast) but the dye-filled arborization of the vascular system was followed deep into the brain

slice with two-photon (2 P) microscopy (Fig. 1b). After pushing the tip of the pipette ~5–10 μm into the lumen of the venule, a slight pressure (~100 mmHg) was applied to the back of the pipette. This resulted in an immediate perfusion of the vessel system, thereby flushing away blood cells (Suppl. Movie 1) and filling capillaries and the venous system, causing them to reach their full diameter (approx. +20%, Fig. 1a). The luminal spread of the dye could be observed simultaneously with 2 P scanning microscopy (Fig. 1b). Within a minute, steady-state fluorescence levels were achieved and a multitude of vascular branches became visible (Fig. 1b–d). Near the injection point, the dye concentration in the lumen was comparable to that in the pipette (relative fluorescence 118 ± 7.5%) and then dropped with distance due to vascular branching and the resulting increase in total vascular diameter (Fig. 1e, f). Note that the dye concentrations remained constant in large and small vessels as long as pressure was applied (Fig. 1c). The fluorescence of the TMR-filled vascular system appeared with a high contrast against the brain parenchyma, suggesting that BBB integrity was well maintained in acute slices and that tight junction protein complexes do not allow a polar tracer such as TMR to cross the BBB[31].

We perfused a range of tracer molecules and tested whether they cross the BBB by quantifying the fraction of extravascular fluorescence nearby the vessel (Fig. 2). The extravascular fluorescence of TMR (869 Da) steeply dropped to ~1% of the luminal fluorescence across the vascular wall (Fig. 2a, d). Similar results were obtained for the slightly smaller tracer sulforhodamine 101 (SR101, 607 Da, 400 μM, Fig. 2b, d) indicating that these two tracer molecules are too large to permeate the BBB[32]. In contrast, the small tracer 7-hydroxycoumarin-3-carboxylic acid (7HCC, 206 Da, 500 μM) reached significantly higher levels outside the vessel (~5-fold, Fig. 2c, d) suggesting that it is able to cross the BBB paracellularly.

We next tested whether molecules integrating in the endothelial cell membrane can bypass the tight junctional complex at the interface of neighboring ECs via membrane-delimited diffusion. For this, we perfused the styryl dye FM1-43 (40 μM) into the vascular lumen. FM1-43 becomes fluorescent when it integrates into cell membranes. Integration into membranes is reversible and membranes de-stain within minutes after removal of FM1-43. This probe cannot cross phospholipid bilayers and only partitions into the outer leaflet of the membrane (when applied from outside) while freely diffusing laterally within the outer leaflet (Fig. 3a)[33–36]. FM1-43 strongly stained the luminal walls of smaller and larger vessels (Fig. 3b). Higher magnification of the fluorescent image and superposition onto the Laser-Dodt channel to visualize cells showed that the abluminal membrane of ECs did not stain within the first minutes (Fig. 3c, i vs ii and Suppl. Figure 2a) suggesting that tight junction complexes slow down membrane-delimited diffusion. However, extended live cell imaging demonstrated that after ~30 min the abluminal membrane started to stain and accumulated FM1-43 fluorescence (Fig. 3c, d and Suppl. Figure 2a). When we applied 400 μM FM1-43 (i.e. 10-fold increase), the abluminal walls were stained much earlier and became clearly visible already after 5 min (Fig. 3e, f). We neither observed fluorescent punctae nor stained organelles in ECs as would be expected if FM1-43 reached the abluminal membrane by either transcytosis[23] or intracellular diffusion. In further experiments, we perfused DyLight 488-labelled Lycopersicon esculentum agglutinin (tomato lectin) into the vasculature. Tomato lectin binds to glycoproteins containing complex-type and high mannose-type N-glycans present on the luminal membrane of ECs[37] and produced a similar luminal membrane staining as FM1-43 (Fig. 3g). However, we did not observe labelling of the abluminal membrane of ECs even after 30 min (Fig. 3g). This was expected as, unlike FM1-43, the tomato lectin target cannot undergo free lateral diffusion and is integrated in the luminal endothelial glycocalyx[38]. Thus, the data indicates that intra-membrane diffusion across the junctional complexes linking ECs occurs and that molecules with amphiphilic properties similar to FM1-43 might be utilized as shuttles for drug delivery to the brain. To assess whether FM1-43 unbinds from the lipids of the abluminal membrane of ECs and can be found in tissue surrounding vessels, we quantified the average FM1-43 fluorescence intensity in regions defined along vessels and normalized it on the brightness of the luminal membrane. For comparison we performed the same analysis following staining with tomato lection which was only found on the luminal membrane. As shown in Suppl Fig. 2b and c, FM1-43 reached significantly higher levels in the brain parenchyma supporting the view that this molecule enters the brain tissue after bypassing junctional complexes by membrane-delimited diffusion. Note that cells selected for the analysis of FM1-43 diffusion to the abluminal membrane showed a flat shape largely contained within the outline of capillaries (Fig. 3c, e, h). This appearance is characteristic of ECs whereas PCs show a rounder and more bulky shape clearly protruding from capillaries (Fig. 4h and Suppl Fig. 2d).

Perfusion of both FM1-43 and tomato lectin revealed a rhombic mesh of fluorescent strings along the luminal walls of ECs which could be most easily identified on larger vessels (Fig. 3h (left) and j). A similar staining pattern was observed upon immunolabelling of adherens junctions with VE-cadherin primary antibody (Fig. h, fixed tissue, right). Thus, these fluorescent strings likely represent regions where FM1-43-stained membranes of neighboring ECs are in contact and parallel to each other and are connected by tight and adherens junction proteins. This supports the view that visualizing these strings by intraluminal FM1-43 application may be used to assess the extent of ECs and trace the path of the line of junctional complexes in between them (Fig. 3i). The area and shape of individual ECs in the BBB has, to the best of our knowledge, not been systematically reported before. In FM1-43-stained vessels, we determined the average surface area of ECs to be 182 ± 26.4 μm^2 and 384 ± 46.2 μm^2 in capillaries and venules, respectively (Fig. 3j, k, see methods for details of the calculation). The calculated surface areas using tomato lectin staining were very comparable (153 ± 17.2 μm^2 and 368 ± 15.6 μm^2 in capillaries and venules, respectively) (Fig. 3j, k). The luminal cellular surface area is a key parameter as it determines the rate of diffusion of membrane-permeable molecules from the blood into ECs and thereby the extrusional transport load per cell. Knowing this area also permits to estimate transporter densities from cellular transport rates or from quantifying the number of transporters per length of a vessel. When compared to the surface area of the venule, ECs consistently cover ~19% of the unit surface area of capillaries (Fig. 3). This implies that ~8 ECs are required to maintain the BBB along a ~83 μm segment of capillaries. Single ECs are on average ~2-fold larger in venules but occupy a smaller fraction of the vessel's luminal surface area (~5%). The size of ECs in venules grows with the vessel's diameter (and thus surface area) linearly but not proportionally, as observed for capillaries (Fig. 3k).

A number of membrane-permeable molecules, which generally permeate cells, cannot pass the BBB because ECs strongly express efflux mechanisms at their luminal membrane[16] that potently and actively extrude such molecules back into the lumen of the vessel (Fig. 4). The ATP-binding cassette (ABC) transporters ABCB1/MDR1, ABCG2/BCRP1 and ABCC1/MRP-1 are considered the most prominent transporters in ECs of the BBB[39]. It has so far remained difficult to quantitatively study the regional and cellular potency of these efflux pumps in ECs of the native BBB. Here, we developed three assays to study the functionality of ABC transporters in live ECs in the combined brain slice and capillary perfusion model (Fig. 4).

For the first assay, we intraluminally perfused the membrane-permeable fluorescent dye rhodamine123 (15 μM), which potently stains mitochondria when applied at nanomolar concentrations[40–42]. However, under control conditions rhodamine123 did not label mitochondria in ECs even after perfusion of the vasculature for 30 min with 15 μM (Fig. 4a). This suggested that ECs possess remarkably potent rhodamine123 extrusion mechanisms, which keep

https://doi.org/10.1038/s41467-023-36070-6

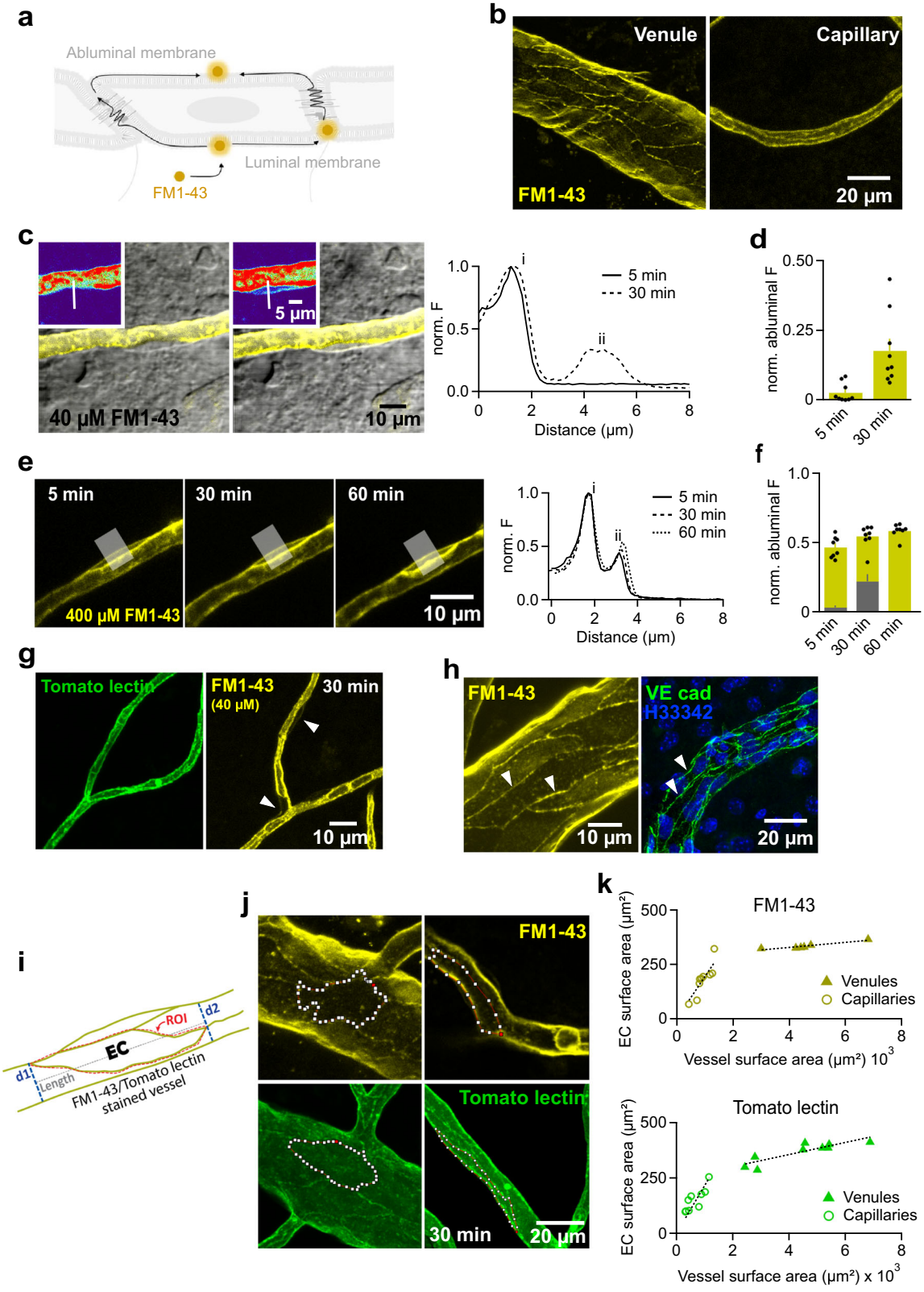

the intra-endothelial cell concentration well below the nanomolar range despite continued application of the dye such that it did not accumulate in mitochondria. Rhodamine123 is a substrate of the ABCB1[43], ABCC1[44] and ABCG2[45] transporters. ABCB1 and ABCC1[46] can be inhibited by verapamil[47]. Bath application of verapamil (200 µM, pre-applied for 15 min) drastically changed the experimental outcome in this assay. Already early during the experiment, a patchy staining of ECs along both capillaries and venules was clearly visible, which continuously increased during the recording time (Fig. 4b, left). The patchy staining of the walls of the vessels likely represented labelled mitochondria in ECs as another mitochondrial stain (MitoTracker Orange CMTMRos 50 µM) produced quantitatively and qualitatively a very similar labelling pattern under the same conditions (Fig. 4b, right).

Fig. 3 | Membrane dyes outline endothelial cells and can be used to measure their surface area across the vascular tree. a Schematic representation of how FM1-43 incorporates into the outer leaflet of the luminal and abluminal membranes. **b** MIPs of a FM1-43 perfused venule (left) and capillary (right) at 30 min. **c**, FM1-43 fluorescence (yellow and false color, inset) in the luminal and abluminal membranes of a capillary EC. FM1-43 fluorescence is superimposed on a laser Dodt scan. Right panel shows the spatial fluorescence profile at 5 and 30 min. **d** Summary of fluorescence intensity of the abluminal membrane normalized to the luminal membrane (n_{ROI}=10). **e** A 400 μM FM1-43 injection outlines an EC in a capillary at a faster rate. The right panel shows the spatial fluorescence profiles at the times indicated of an line ROI (white line). **f** Quantified fluorescence intensity in the abluminal membrane (n_{ROI} = 8). **g** Tomato lectin outlines ECs across capillaries at 30 min in a pattern similar to that obtained with the FM1-43 probe (in 40 μM concentration). **h** MIPs of a FM1-43-injected blood venule showing EC borders (arrowheads)(left). Images are representative for 10 injections in slices of 4 animals. Right, immunofluorescent labelling of adherens junctions (VE-cad) outlining the ECs (arrowheads) (Hoechst 33342 counterstain). The image is representative of 6 slices/3 animals. **i** Cartoon illustrating how the surface area of EC was computed based on the outline of an EC (region of interest, ROI). **j** Outlined ECs in FM1-43 (top) and tomato lectin (bottom) -labelled venules (left) and capillaries (right) can morphometrically be analyzed (see methods for details). **k** The surface area of ECs plotted versus the surface area of the vessels (top panel, slope 0.195) and tomato lectin (bottom panel, slope 0.216). Source data to panels of Fig. 3 are provided as a Source Data file. Data are presented as mean values + /- SEM.

Secondly, we assayed the transport activity of ECs using calcein-AM. Calcein-AM is membrane permeable and non-fluorescent until the AM group is cleaved off by intracellular esterases, releasing fluorescent calcein that cannot pass membranes anymore. Calcein-AM is a known substrate of ABCB1 and ABCC1, while fluorescent calcein is a substrate of only ABCC1[48]. Similar to the rhodamine123 experiments, intraluminal application of calcein-AM (20 μM) in the absence of ABC transporter inhibitors did not lead to accumulation of green fluorescence in ECs (Fig. 4c). In contrast, when blocking ABCB1/ABCG2[49] and ABCC1 with Elacridar (1 μM[50]) and Probenecid (1 mM[51]), respectively, ECs strongly accumulated calcein along capillaries and venules (Fig. 4c, d). Application of Elacridar alone, but not of probenecid, was sufficient to induce staining of ECs (Fig. 4e) suggesting that ABCB1 (calcein-AM is not transported by ABCG2[52]) is the primary transporters extruding calcein-AM from ECs. In contrast, the transport rate of ABCC1 alone was not sufficient to prevent accumulation of calcein in ECs.

Not only ECs but also PCs are found along vessels. To assess whether some of the cells which accumulate calcein may represent PCs, we labelled PCs with a PC-specific live cell tracer, neurotrace 500/525[53] (1:250), and perfused a red-shifted calcein-AM version (20 μM) in the presence of Elacridar (1 μM) and probenecid (0.6 mM) to induce calcein accumulation in ECs. As shown in Fig. 4f, the red-shifted calcein selectively accumulated in ECs and not in PCs.

The third assay was based on the membrane-permeable DNA stain Hoechst33342 (Hoechst) that has a picomolar affinity for double-stranded DNA[54]. Hoechst was bath-applied at high concentrations (5-10 mM) and combined with intraluminal FM1-43 application to visualize the outline of ECs. However, while Hoechst strongly stained nuclei of neurons and glial cells it never stained ECs (Suppl. Figure 3a), demonstrating that ECs can generate and maintain very high and very local dye concentrations across their membranes. Only after we subjected slices to chemical fixation, which inactivates all transporters, were the nuclei of ECs and other cells clearly stained by Hoechst (Suppl Fig. 3b).

We further explored the suitability of our approach of microperfusion of capillaries to detect, track and quantify acute chemical or physical damage of the BBB in real-time. For this purpose, we introduced a spatially restricted and acute physical lesion of a capillary branch by exposing its wall to strong laser illumination (see methods). While normally TMR is highly restricted to the lumen, after the lesion we observed immediate and profound extravasation of the dye. The parenchymal fluorescence strongly increased within seconds and remained elevated for the duration of the experiment (Fig. 5a). This increase in extra-vascular parenchymal fluorescence was confined to the site of the laser damage while other capillaries were unaffected (Fig. 5a).

DMSO induces a concentration-dependent chemical lesion of the BBB such that intravenously injected proteins (>40 kDa) can pass through the BBB and were found in the extracellular space of the brain parenchyma[55]. While DMSO treatment has been experimentally considered as a potential way to improve CNS drug delivery[56,57], the mechanism of its action is still not fully resolved. DMSO-induced damage is thought to be caused either by enhanced transcytosis or altered integrity of tight junctions[55]. To observe the action of DMSO during live-cell high resolution imaging, we micro-perfused fluorescently-labelled bovine serum albumin (BSA-Alexa488, 66.5 kDa) into the vasculature. Under control conditions, BSA-Alexa488 was only detected within the vascular lumen (Fig. 5b). In contrast, when 10% DMSO was co-micro-perfused with BSA-Alexa488, we detected clustered droplets of BSA-Alexa488 in the CNS parenchyma in the vicinity of smaller and larger vessels indicating that the protein had crossed the BBB (Fig. 5b, c). However, we never found ECs labelled with BSA-Alexa488 and their cytoplasm remained invisible and free of fluorescent vesicles, suggesting that BSA may have reached the parenchyma by passing through DMSO-weakened tight junctions rather than by increased transcytosis via ECs. The droplets showed little mobility and progressively accumulated over time indicating that they could have been phagocytosed by resident cells. Immunohistochemical staining of microglial cells (TMEM119[58]) did not reveal a co-localization of BSA-Alexa488 and showed unaltered microglial cell densities between the control and DMSO condition (Fig. 5d). In contrast, labelling for the F4/80 antigen (putative macrophages[59,60], see for discussion[59]), which normally is not found in the healthy brain (Fig. 5e), revealed a clear co-localization with BSA-Alexa488 (Fig. 5d) and showed that the DMSO treatment potently induced F4/80-positive cells within 30 min (Fig. 5e). The morphology of F4/80 labelled cells closely resembled that of perivascular macrophages which are known to phagocytose material of the size of BSA[60–62]. These myeloid cells have been reported to normally reside in the perivascular space of venules and arterioles, phagocytose material of 10–70 kDa and play multiple roles in cerebral diseases[60]. In time-lapse imaging, we did not observe diffuse leakage of BSA-Alexa488 into the brain parenchyma under DMSO application but rather a progressive appearance of clusters of fluorescent droplets. This observation is most consistent with a scenario in which putative macrophages in the perivascular space effectively phagocytosed BSA-Alexa488 material that diffused across DMSO-injured tight junctions and thereby prevented a diffusive appearance of the labelled proteins in the extracellular space. Weakening of tight junctions by DMSO is also suggested by our observation of a small but consistent spatial leakage gradient of TMR into the parenchyma (Fig. 5e, f). This leakage is much smaller than the one observed after laser damage but clearly exceeds levels around untreated vessels under control conditions (Fig. 5g). Our data also showed that at least for a time frame of 30–60 min, BSA-Alexa488 is not phagocytosed by TMEM119-positive microglial cells (Fig. 5d, e).

The DMSO experiments demonstrate damage to the BBB which might be explained by a partial opening of tight junctions but they do not directly reveal the mechanism causing this damage. To lend support to the view that DMSO affects the tightness of junctional protein complexes, we perfused a hyperosmolar mannitol solution (15%) for comparison. Hyperosmolar mannitol is known to temporarily open tight junctions by a combination of vasodilation and shrinkage of ECs[63,64]. Within 10 min, mannitol induced a similar progressive appearance of clusters of BSA-Alexa488 along vessels

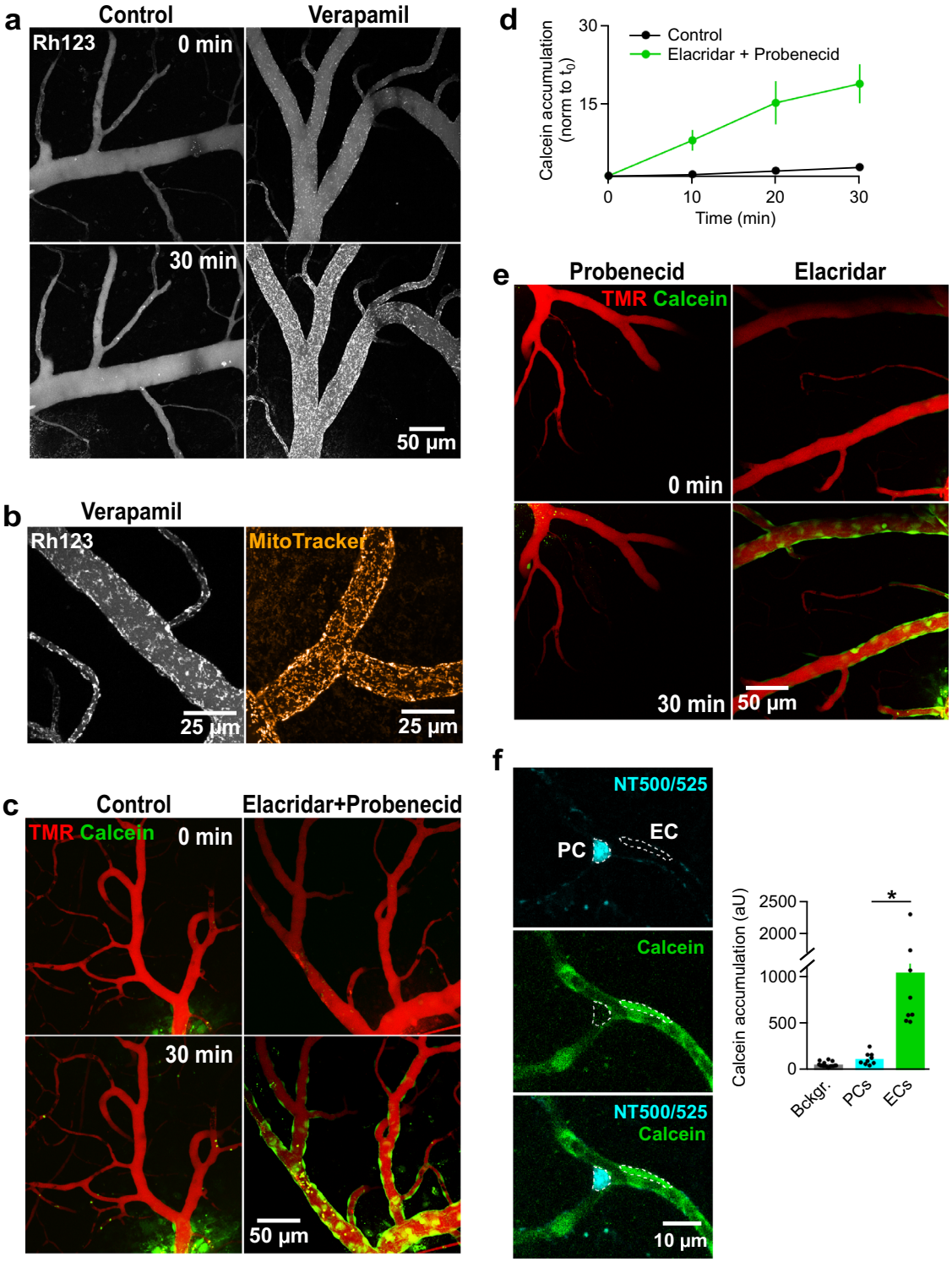

(Fig. 6a). After 30 min, the clusters became dense and clearly marked the cells they were contained in. Cells containing BSA-Alexa488 were most frequently found along venules when compared to capillaries (Fig. 6b). As observed following DMSO application, cells which had taken up BSA-Alexa488 were stained by anti-F4/80 antibodies (Fig. 6c) suggesting the same origin. When we co-applied TMR and mannitol, we found a similar small but consistent leakage across the BBB and extravasation of this tracer (Fig. 6d, e). To assess the osmotic effect of mannitol, we tracked the diameter of blood vessels upon perfusing mannitol. The diameter of capillaries significantly increased after 30 min mannitol perfusion by 8.4 ± 2.5% compared to the diameter at the beginning of the experiment (after 5 min perfusion, n = 8). In the absence of mannitol, the diameter remained unchanged upon perfusing TMR solely (1.3 ± 2.2%, n = 7). The diameter of venules did not change significantly under the same conditions (1.9 ± 0.4, n = 10, and 2.0 ± 1.1, n = 6, with and without mannitol, respectively). Taken together, hyperosmolar mannitol closely reproduced the findings detected after perfusion of DMSO suggesting, but not proving, that the two manipulations act via the same mechanism and partially open tight junctions.

Breakdown of the BBB in epileptic patients and animal models of epilepsy has been previously reported but the regionality and degree

Fig. 4 | Assessing cellular transport rates of endothelial efflux systems. a MIPs recorded at t_0 (top) and t_{30} (bottom) under control conditions (left) and ABCB1 inhibition with verapamil (right). Accumulation of rhodamine123 (Rh123) in mitochondria of endothelial cells is only visible when verapamil is applied. Rhodamine123 is hardly seen in cells around the vessel likely because the endothelial cell cytoplasm already contains a low Rhodamine123 concentration due to remaining extrusion activity and there is a strong dilution of the dye in the surrounding 3D environment. Images are representative of 11 experiments. **b** MIPs acquired at t_{30} after rhodamine123 and MitoTracker injections. Note the very similar staining pattern of both dyes. Images are representative of 5 experiments. **c** MIPs recorded at t_0 (top) and t_{30} (bottom) under control conditions (left) and simultaneous efflux protein inhibition of ABCB1/ABCC1 with 1 μM Elacridar and 1 mM probenecid (right). Only in the presence of ABC-transport inhibition did calcein accumulate in endothelial cells. Images are representative of 10 experiments. **d** Quantification of the endothelial fluorescent signal over time. Plot represents the mean normalized fluorescence measured in capillary endothelial cells (n_{ROI}=19, 9 injections/9 animals). Data are presented as mean values + /- SEM. **e** MIPs recorded at t_0 (top) and t_{30} (bottom) under individual ABCC1 (left) or ABCB1 (right) inhibition with probenecid and Elacridar, respectively. Images are representative of 6 experiments. **f**, Quantification of calcein accumulation in pericytes (PC) at 30 min after calcein-red-orange injection under protein inhibition of ABCB1/ABCC1 with 1 μM Elacridar and 0.6 mM probenecid. PC were prelabeled with Neurotrace 500/525 (NT500/525) (cyan). The recorded individual channels show little to no overlap between calcein and NT500/525 within the PC. The graph shows quantification of the mean fluorescence intensity of the calcein signal within EC (n_{ROI} = 9) and PC (n_{ROI} = 9) in the calcein detection channel compared to the background (Bckgr.) signal (n_{ROI} = 18) (± SEM, 7 injections/3 animals). Statistical significance was calculated using a two-tailed Student's *t* test (*; P = 0.0004). Source data to panels of Fig. 4 are provided as a Source Data file.

of BBB damage could not be precisely determined[65,66]. To address this issue, we employed the pilocarpine-induced status epilepticus (SE) model[67,68], in which SE initiates a process termed epileptogenesis that finally leads to chronic recurrent seizures and temporal lobe epilepsy[69]. In this animal model of epilepsy, BBB breakdown has been assessed histologically following systemic in vivo administration of tracers[70]. Mice were taken into the experiment 2 h following pilocarpine induced SE (Fig. 7a) and tested for tightness of junctions and leakage across the BBB by micro-injection of the tracer TMR. After 14 injections (n = 3 mice), a small leakage similar to that induced by DMSO or mannitol treatment (Fig. 7b, c) was consistently observed indicating that the integrity of tight junctions was similarly affected after pilocarpine-induced SE in mice.

As it was reported previously that BSA after systemic injection is found in the mouse brain following SE, we also micro-perfused BSA-Alexa488 2 and 24 h after the status (3 and 4 mice, respectively). However, we did not observe extravasation of BSA-Alexa488 resembling that seen under DMSO or mannitol treatment in any of the mice (Fig. 7d).

We further evaluated BBB properties of human epileptic hippocampi (7 patients). Hippocampi were removed for surgical control of medically intractable chronic temporal lobe epilepsy (TLE)[71] and transferred from the operating room to the laboratory in cooled ACSF within 10–15 min. Once in the lab, human tissue underwent identical slicing and experimental procedures as murine tissue. Micro-perfusion was well applicable to human tissue albeit the walls of human vessels appeared sturdier and turned out to be more difficult to penetrate than mouse vessels. Similar to the mouse tissue, BSA-Alexa488 fluorescence was confined to the human vasculature and we did not detect fluorescent droplet-loaded macrophages suggesting the protein does not reach the brain parenchyma (Fig. 7e, f). These data show that the approach of vascular micro-perfusion in brain slices is well applicable to diseased tissue across species and suggest that a single SE in the murine model can cause a lasting leakage for small molecules (TMR) across the BBB. However, the BBB is sufficiently intact to avoid detectable BSA extravasation in the mouse model and human chronic epilepsy.

Previous work reported up-regulated expression of ABCB1 at the BBB post SE[72]. Therefore, we assessed the functionality of ABCB1/ABCC1 transporters in our murine model 2 h post SE. In both sham- and pilocarpine treated mice, perfusing calcein-AM in the vasculature did not result in any noticeable calcein accumulation in ECs suggesting that in both groups there is no relevant reduction in calcein-AM transport rate compared to control mice reported above (Fig. 7g, left column). To test for increased calcein-AM transport rates we partially blocked ABC transporters (0.6 μM Elacridar, 0.6 mM probenecid) to induce a small degree of accumulation of calcein in ECs in the beginning of the experiment (at t_0, Fig. 7g, middle column). In ECs of sham-injected mice, the fluorescent levels of calcein increased to more than 4-fold over 30 min (Fig. 7h). In contrast, ECs in slices prepared from pilocarpine-injected mice accumulated only little additional fluorescence over the same period (Fig. 7h), pointing to a substantial increase in the functional activity of the transporters extruding calcein-AM from ECs (ABCB1/ABCC1).

We assessed whether the protein levels of ABC transporters were altered after SE by performing a proteomic analysis of hippocampal tissue from sham- and pilocarpine-injected mice. A number of transporters were detected in samples obtained 4 and 24 h post SE including ABCB1(MDR1) and ABCG2(BCRP1) (Fig. 7i). ABCC1(MRP1), which appeared to play a minor role in calcein-AM extrusion, was not detected. We only measured small changes in ABC-transporter protein levels and counts in post-SE mice fell within ±12% of sham mice (Fig. 7i). Only at 24 h post-SE, some of these alterations reached the level of statistical significance. As the relative changes in the ABC protein levels were small, the proteomic data suggest that the observed 3-4-fold-increase in calcein-AM extrusion rate of ECs from pilocarpine-treated mice can hardly be explained by increased protein expression but rather is due to a functional regulation such a dynamic redistribution of ABC proteins from an intracellular pool to the cell membrane[73].

So far in this study, we have optically monitored interactions at the BBB but in some instances, it might be desirable to monitor a functional response, for example neuronal activity, to assess whether a micro-injected molecule crosses the BBB to a sufficient degree. Measuring a functional response allows to determine whether the drug/signaling molecule reaches the target receptor and if it does so at the relevant concentration. Furthermore, as the brain slice system allows to apply a drug at a defined concentration, both directly to the parenchyma ("bath application") and to the vascular system ("micro-perfusion"), an equivalence dose-ratio at the BBB can be calculated at which both routes of application reach the same effect. We demonstrate this approach by studying BBB permeation of caffeine and its antagonistic effect on presynaptic adenosine receptors (A1)[74]. We monitored synaptic transmission with field potential (fEPSPs) recordings of Schaffer collateral-evoked synaptic responses while perfusing TMR in the vasculature to assess the injection quality and follow the vascular tree (Fig. 8d). These synapses express inhibitory A1 receptors and we first applied the A1-receptor agonist N^6-cyclopentyladenosine (CPA, 15 nM) to activate A1 receptors and observed the expected reduction in fEPSPs (Fig. 8a). Bath application of 300 μM caffeine in the continued presence of CPA antagonized the activation of A1 receptors and increased fEPSPs responses (Fig. 8a). In a separate experiment we also pre-applied CPA to activate A1 receptors but additionally applied caffeine by micro-perfusion of capillaries at a later time point (Fig. 8b). Consistent with its BBB permeation, caffeine also antagonized the inhibitory action of CPA and increased fEPSP within ~15 min. The extent of antagonisms was slightly (but not significantly) lower than when bath-applied (Fig. 8c) despite the fact that we injected 30 mM caffeine, suggesting an equivalence dose-ratio of ~100.

https://doi.org/10.1038/s41467-023-36070-6

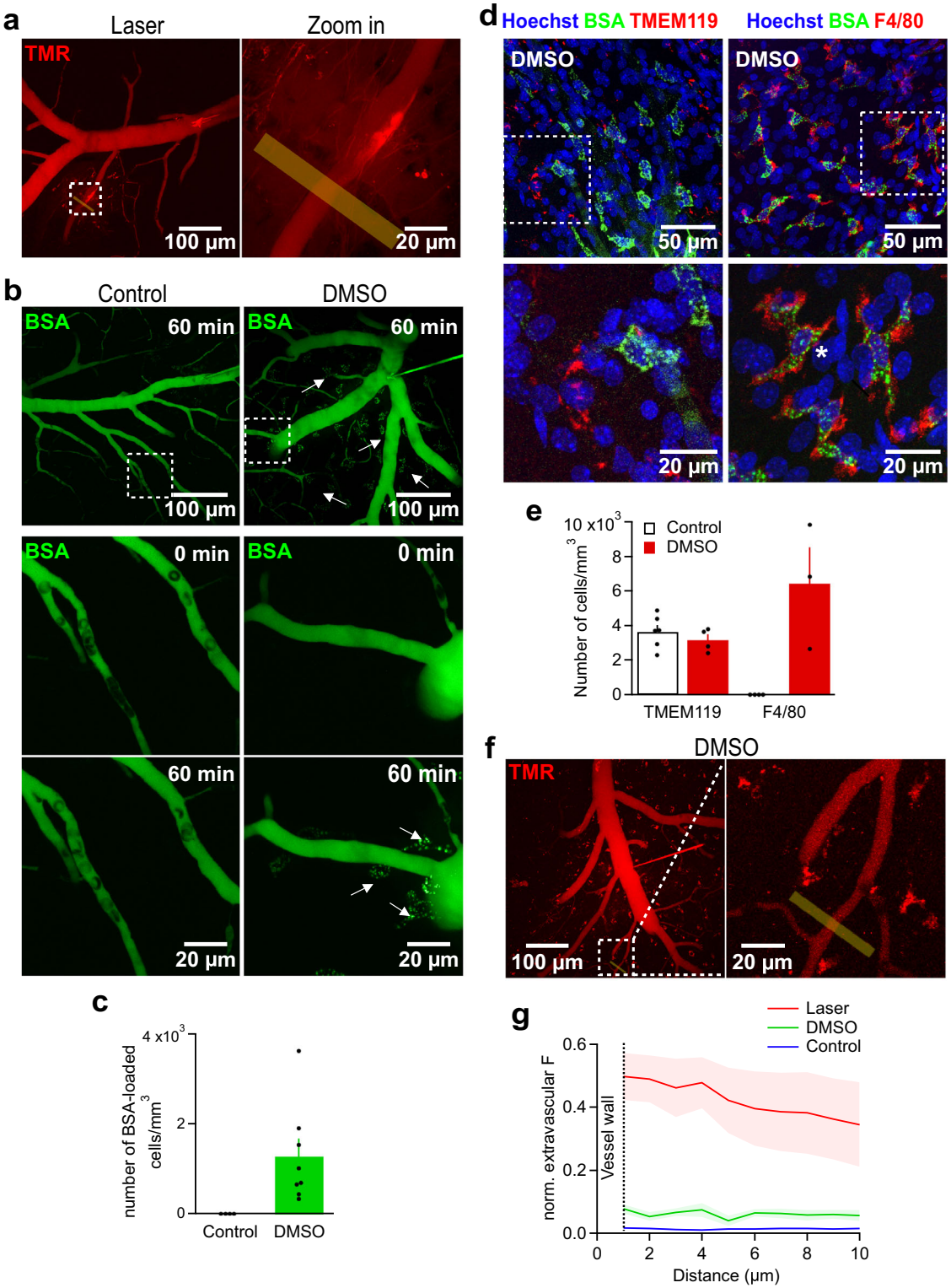

Discussion

Here, we report the development, characterization and broad applicability of an in situ BBB model based on acute brain slices, micro-perfusion of capillaries and multi-photon imaging (ISMICAP, in situ micro-perfusion of capillaries). ISMICAP overcomes several limitations of previous models and offers a number of additional advantages. We build on the traditional and long-established technique of preparing acute brain slices for electrophysiological recordings. Decades of research have demonstrated that neurons remain viable for many hours after preparation of the slice. Our results clearly show that the viability of neurons, their electrophysiological properties and the functionality of ABC-transporters functionality are preserved. Calcein-AM, rhodamine and Hoechst were found to be potently extruded from ECs throughout the entire experimental window (up to 8 h following slicing). In fact, when comparing our results to previous assays applied to cultured ECs, it turns out that the activity of ABC transporters is much stronger in ECs in our slices: we did not detect any accumulation of the three ABC transporter substrates mentioned above over a period of at least 60 min and they only became visible after blocking ABC transporters. In contrast, previous studies[75–77] reported that even

https://doi.org/10.1038/s41467-023-36070-6

Fig. 5 | Quantifying physical and chemical lesions to the BBB. a Overview (left) and close-up (right) of a laser-damaged capillary with subsequent tracer diffusion into the surrounding neuronal tissue. **b** MIPs of BSA-Alexa488 (BSA)-injected microvasculature in an overview at t_{60} (top), zoomed-in views of the regions enclosed in dashed squares acquired at t_0 (middle) and t_{60} (bottom) under control conditions (left column) and after the addition of DMSO (right column). Arrows indicate extravascular BSA-Alexa488 accumulations. Images are representative of 5 experiments. **c** Quantification of the extravascular BSA-loaded cells potentially referring to macrophages under control conditions (5 injection/5 animals) and after exposure to DMSO (8 injections/6 animals, $n_{ROI} = 8$). **d** Immunofluorescent labelling of microglia (left column, TMEM119) and macrophages (right column, F4/80). White dashed squares indicate zoomed-in regions (below) showing that BSA-Alexa488 only co-localizes with macrophages but not with microglial cells. Micrographs are representative of 5 experiments. **e** The microglial cell density around vessels does not change after DMSO injection, but macrophages, normally absent from the brain parenchyma, are strongly recruited. Cellular densities for microglia under control conditions (7 injections/3 animals, $n_{ROI} = 6$) and DMSO exposure (4 injections/3 animals, $n_{ROI} = 4$) are compared to macrophage densities under control conditions (7 injections/3 animals) and DMSO exposure (3 injections/2 animals, $n_{ROI} = 3$). **f** DMSO induces a slight leakage of TMR into the parenchyma. The level of leakage is so small that it cannot visually be identified in the image but only became clear upon quantification of fluorescent gradients across the vascular wall (see g). Images are representative of 5 experiments. **g** Fluorescent gradients across the vascular wall normalized to the luminal fluorescence. Note the strong accumulation of dye in the extracellular space of the brain following laser-induced damage of the BBB. TMR accumulation is much weaker after DMSO application when compared to laser-induced damage but clearly stronger than under control conditions. Source data to panels of Fig. 5 are provided as a Source Data file. Data are presented as mean values +/- SEM.

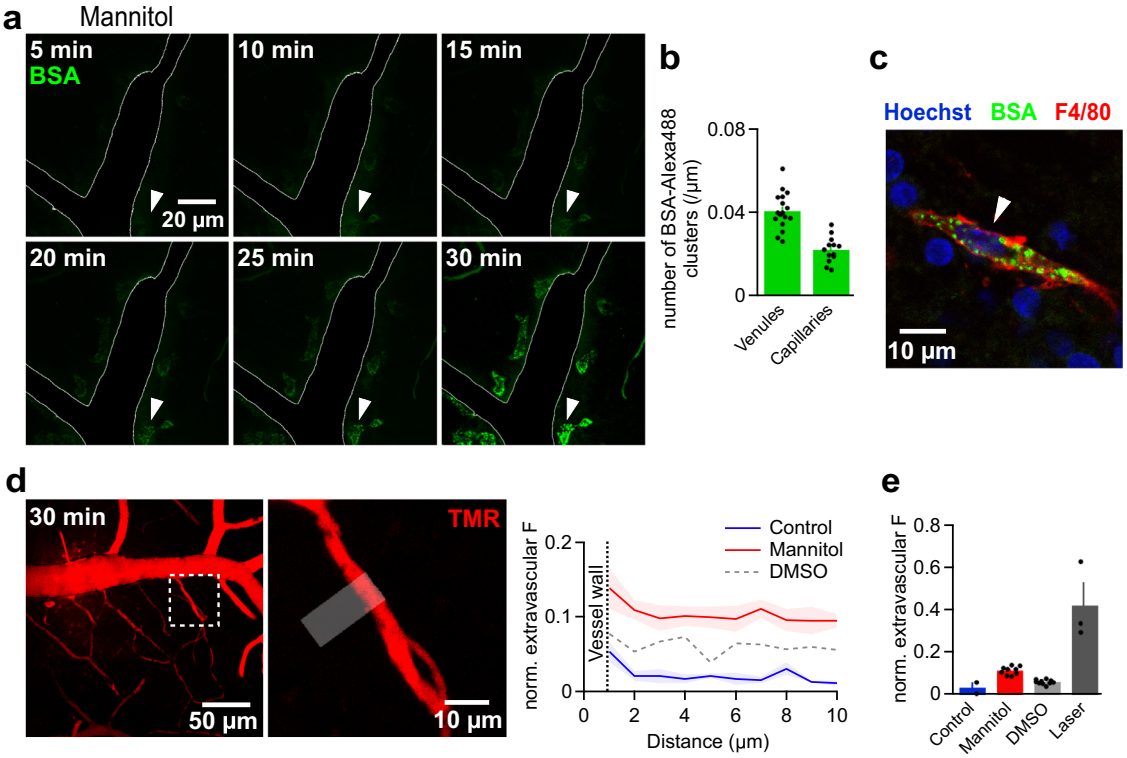

Fig. 6 | Hyperosmolar mannitol enhances TMR and BSA extravasation to the parenchyma. a Time lapse images showing the gradual extravasation and subsequent accumulation of BSA-Alexa488 (BSA) in macrophages recruited upon perfusing 15% mannitol into vasculature, which was verified by immunofluorescent labelling (see c). For better clarity of BSA clusters, the intravascular fluorescence was deliberately removed using Fiji software and the vessel was outlined manually. Images are representative of 4 experiments. **b** The number of BSA-Alexa488 clusters within macrophages (per µm length) in the vicinity of venules is twice as high as that next to capillaries (12 injections/ 4 animals, n_{ROI} for venules = 17, n_{ROI} for capillaries = 13). **c** Immunofluorescent labelling of macrophages (F4/80) showing BSA-Alexa488 accumulation within them upon perfusing the vessels with mannitol. The micrograph is representative of 3 experiments. **d** MIPs of the vascular tree (left) and an enlarged capillary (right) 30 min after co-injection of TMR and 15% mannitol solution. Images are representative of 3 experiments. The graph shows the fluorescence gradients across the vascular wall normalized to the luminal fluorescence (white line) of a capillary compared to that in absence of mannitol (and DMSO, dashed line). **e** Perfusing mannitol for 30 min led to a significantly higher extravascular fluorescence of TMR, normalized to the luminal fluorescence signal (n_{ROI}=9, 4 injections/2 animals) at control conditions, yet it was much less than the leakage caused by laser damage. Source data to panels of Fig. 6 are provided as a Source Data file. Data are presented as mean values +/- SEM.

without blockers a clear accumulation of the substrates occurred at a level ~25% of that seen after ABC-transporter inhibition. As ABC transporters are highly ATP-dependent, this means that ECs in our slice preparation can generate ATP for extended periods of time and likely also express more functional transporters than their in vitro counterparts. As a consequence, ISMICAP can significantly reduce the risk of underestimating efflux phenomena during drug discovery research.

Many useful and sophisticated in vitro models of the BBB ideally suited for certain purposes are currently available and they often provide the advantage of applicability for high throughput analyses[78]. However, an obvious limitation of in vitro models is that they are not composed of native tissue and as a consequence it is hard to achieve and prove the validity of in vitro models in all aspects. In vitro, a BBB is grown with a reduced cellular microenvironment, in the absence of normally circulating factors and without dynamic exchange with the rest of the body. Furthermore, in vitro models lack a solution stream and intravascular pressure, which is important for several physiological responses and the regulation of the NVU[79–81]. Finally, studying the role of the BBB in specific pathological contexts would require to completely

https://doi.org/10.1038/s41467-023-36070-6

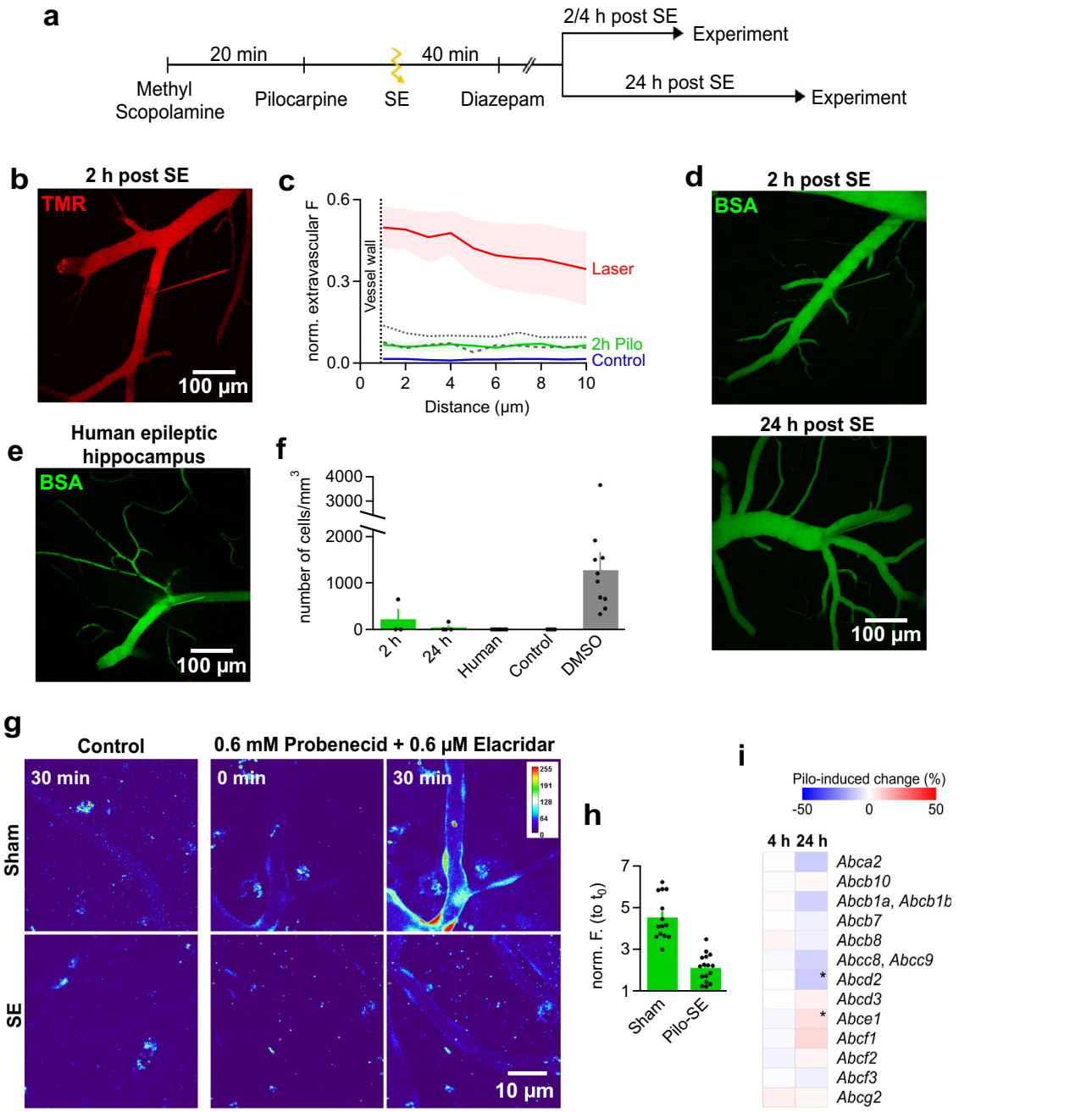

Fig. 7 | BBB in temporal lobe epilepsy. a Timeline of pilocarpine experiments. **b** MIP after TMR injection at 2 h post SE, quantified in (c). **c**, Fluorescent profiles across walls of capillaries. Comparison across conditions, mannitol (dotted line), DMSO (dashed line). **d** MIPs of BSA-Alexa488 (BSA)-injected brain microvasculature assessed 2 h (top) and 24 h (bottom) post SE. **e** MIP of BSA-filled microvasculature within a human hippocampal brain slice. Image is representative of 7 injections performed in hippopcampi of 5 TLE patients who underwent neurosurgical treatment of their epilepsy. **f** Quantification of BSA-Alexa488-loaded macrophages in the murine epileptic condition at 2 h ($n = 3$) and 24 h ($n = 4$). Data are compared to those obtained from human ($n = 7$), control ($n = 4$) and DMSO ($n = 10$) samples. **g**, MIPs of capillaries of sham (top row) and 2 h post SE murine slices (bottom row) without preincubation with blockers (control) at t_{30} and under full ABCC1/partial ABCB1 inhibition with 0.6 mM probenecid and 0.6 µM Elacridar, respectively, at t_0 and t_{30}, quantified (see h). Images are representative of 4 experiments. **h**, Calcein signal at t_{30}, normalized to that at t_0 (norm. F.), 11 injections/ 6 animals, n_{ROI} of control = 14, n_{ROI} of SE = 16. **i**, Heat map of percentage change in protein levels for ABC transporter proteins at 4 and 24 h after pilocarpine treatment of mice relative to sham treatment, as determined by mass spectrometry. Percentage is an average of 4 measurements ($n = 4$ mice per condition). "*" designates significant changes (P value < 0.05). The P values denoting the significance of Abcd2 and Abce1 transporters relative to sham treatment were 0.003574 and 0.047767, respectively. Source data to panels of Fig. 7 are provided as a Source Data file. Data are presented as mean values +/- SEM.

replicate the disease in vitro, which is not possible if the disease itself is not fully understood or complex.

In vivo models on the other hand work with the native BBB and can be combined with animal models and represent an optimal combination in this respect. However, in vivo models systematically differ from our model in applicability and possible read-outs. In vivo (injection) models broadly fall into two classes: a) sacrificing the experimental animal before analyzing uptake of the test substance into the brain and b) analyzing *uptake* in vivo in the living organism (e.g. 2 P in vivo imaging, PET imaging[82]). For the former, usually a

https://doi.org/10.1038/s41467-023-36070-6

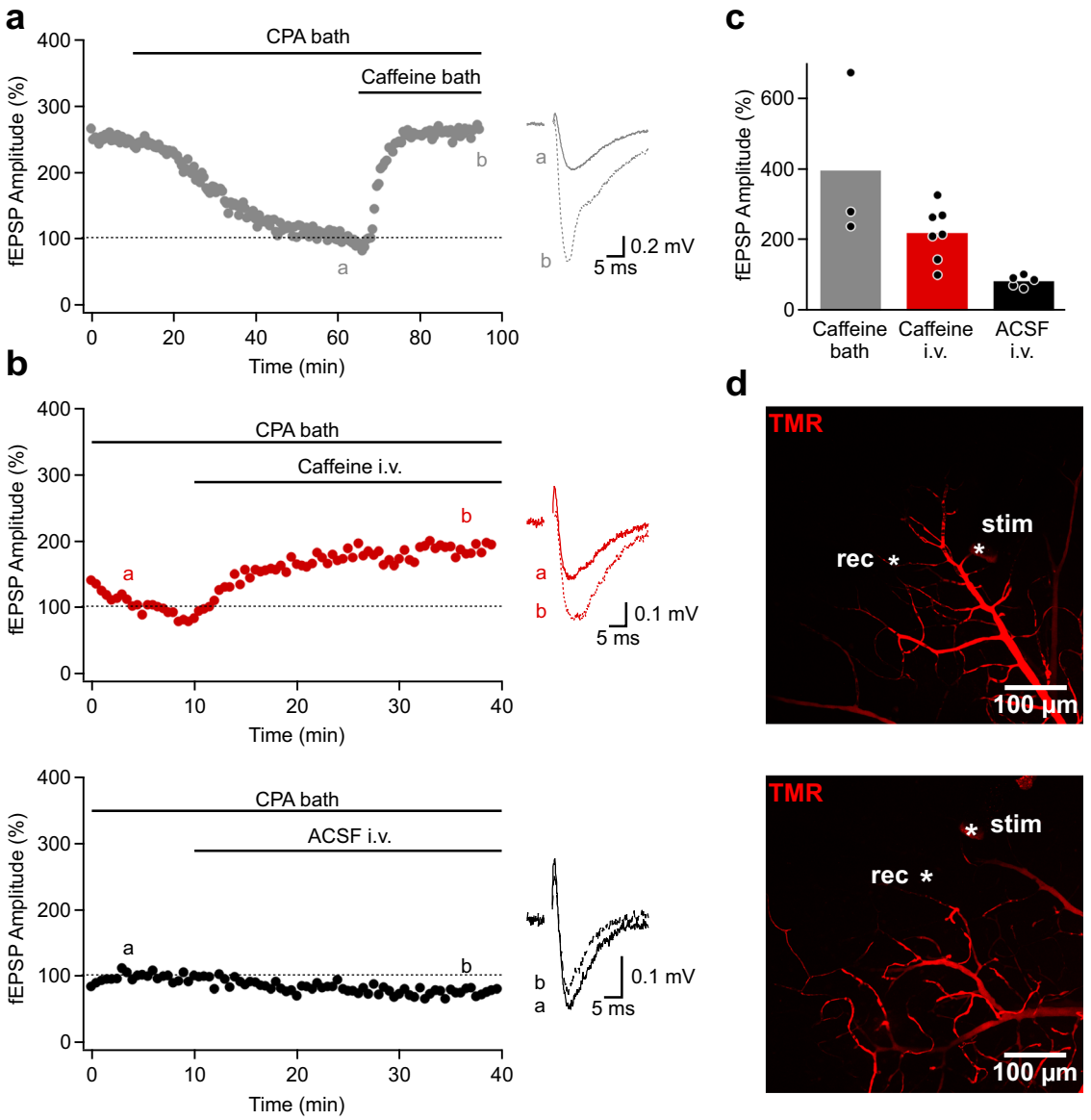

Fig. 8 | Monitoring the pharmacological effect on neuronal responses after drug passage through the BBB. a Time course of an example experiment of fEPSP recordings in the hippocampal area CA1. The adenosine A1-receptor CPA reduces synaptic responses. This effect is antagonized by co-application of caffeine. Inset shows recordings (average of 5 traces) from times indicated by lower case letters. **b** Top panel: Intravascular (i.v.) application of caffeine also antagonizes the effect of CPA (pre-applied) and increases synaptic responses. Note the different time scale of the x-axis when compared to **a**). Bottom panel: Control intravascular injection of ACSF does not alter synaptic responses. **c** Summary of percentage fEPSP amplitude changes after caffeine bath application ($n = 3$ from 2 injections/2 mice), intravascular caffeine application ($n = 5$ from 3 injections/4 mice) and intravascular ACSF application ($n = 5$ from 3 injections/3 mice). Bar graph shows mean ± SEM. **d** MIPs of caffeine (top) and sACSF (bottom) injected vascular tree. The asterisks denote the positions of the stimulating (stim) and recording (rec) pipettes. Images are representative of 10 experiments. Source data to panels of Fig. 8 are provided as a Source Data file.

biochemical or histochemical readout of BBB function is used and permeating test molecules are quantified per volume or weight of brain tissue, but the extracellular concentration, relevant for neurons and glial cells, remains imprecisely known as it depends on the subcellular distribution of the test molecule (e.g. intra- vs extracellular, membrane- vs. lipid-bound). Furthermore, it is difficult to exclude or identify changes of test molecule distribution caused during fixation of the tissue or occurring post-mortem. Of all approaches, the second class of in vivo models employing high resolution 2 P in vivo imaging as read-out have the closest and most realistic look at the BBB. However, due to movements of the living brain and strong light scattering at high imaging depths, it is difficult to obtain very high image resolution (e.g. for quantifying fluorescence of EC membranes) and certain experiments or experimental combinations are not possible or very demanding. For example, some brain regions (e.g. medulla oblongata, thalamus), some organs (e.g. heart) and early developmental stages (e.g. embryonic) are not readily accessible for in vivo imaging. In addition, while local imaging is the rule, intravenously applied test molecules will distribute in the whole circulation and reach all parts of the brain. This makes it difficult to monitor where and when substances enter the brain (veins, capillaries, arteries, choroidal membranes, lymphatic system) and to control the effective concentration in cerebral blood vessels near the imaging site as excretion, metabolism and binding to blood components are hard to control confounding factors. Finally, combining imaging in vivo with compound and drug injection as well as cellular electrophysiology for physiological recordings is very challenging.

ISMICAP offers precise control of both luminal (capillary perfusion) and parenchymal (bath perfusion) concentrations of drugs and tracers and constant concentrations are maintained as long as the vascular system is perfused. This made it possible to quantitatively compare the accumulation of calcein in the presence of several ABC-transporter blockers and to show that ABCC1 shows a much weaker calcein-AM extrusion rate compared to ABCB1. The precise control of the concentrations on both sides of the BBB together with subcellular optical or cellular physiological recordings offer the unique opportunity to obtain a dose-effect titration directly at the blood barrier as we illustrated for the case of caffeine.

In a slice preparation, the brain tissue including the vasculature and the NVU are fed with oxygen and nutrients (such as glucose) via the bath perfusion medium. This provides the experimental freedom to modify the luminal solution, such as removing blood cells or changing the chemical or cellular composition, without the danger of damaging the NVU or the nervous tissue as in vivo imaging approaches would be faced with. This allowed us to flush out cellular components from the vasculature and apply the fluorescent membrane dye FM1-43. Only because cellular components were removed, we obtained a clear and unobstructed view of the stained EC boundaries and could visualize the shape and boundaries of living ECs and quantify their surface area. This is an important parameter to assess the cellular transport load at the BBB.

Establishing a solution stream through the vessel system of brain slices also advances the applicability of slice experimentation, for example to physiological studies. Responses of the NVU unit depend on the actual diameter and/or the intracapillary pressure, but conventional brain slice preparations lack capillary perfusion resulting in a collapse of capillaries and venules. Lack of capillary perfusion in brain slices may be even more important for studying potassium buffering and clearing by astrocytes in brain slices. While brain slices are optimally suited to accurately measure the local potassium concentration, to stimulate, manipulate and record neuronal activity and the uptake capabilities of astrocytes, one important component of potassium homeostasis is missing: the removal of potassium through astrocytic endfeet into the circulation. ISMICAP now experimentally re-generates this potassium sink by clamping intracapillary potassium levels and allowing astrocytes to release the neuronal potassium they have been collecting in the parenchyma during periods of neuronal activity into the vascular lumen.

ISMICAP also comes with certain limitations. The controllability of luminal and parenchymal solutions may also be a disadvantage when studying effects of endogenous molecules on the BBB. For ISMICAP, the endogenous solutions are removed, whereas they are maintained in in vivo models. Further, while the slices used for the approach presented here had been in contact with the circulation and the rest of the organism, they are isolated during the experiment. Thus, any acute effects of e.g. the composition of the blood on the BBB are (almost) impossible to study in a slice model. Finally, the advantage of working with native tissue can represent a disadvantage if the goal is to study the effect of differences in the composition of the NVU or surrounding tissue. While in vitro models do allow an engineering of the experimental tissue and provide a certain level of control of the cellular environment this is not possible with acute brain slices and also difficult with cultured slices.

The usage of 2 P microscopy is key to the experimental flexibility of ISMICAP. 2 P microscopy vs. other excitation methods is necessary to follow the arbors of the vascular tree, which penetrate deeply into the tissue (>100 μm). Only this high-resolution live cell imaging approach enabled us to firstly observe the slow, membrane-delimited diffusion of FM1-43 beyond endothelial tight junctions, the extravasation of wall-resident perivascular macrophages upon strong damage of the BBB and to exclude strong transcytosis of fluorescently-labelled proteins through ECs after DMSO treatment and status epileptics.

The fact that ISMICAP is based on a slice preparation delivers the advantage of universality. Almost any tissue and organ from many species can be cut into slices and kept in a recording chamber for micro-perfusion of the contained capillaries. In this study, we demonstrate this versatility by examining BBB properties of an animal model of epilepsy and by analyzing the native human BBB in a disease context supporting the translational value of ISMICAP.

Methods

All experiments with specimens of murine origin were performed in accordance with the guidelines of the University of Bonn Medical Centre Animal-Care-Committee. All efforts were made to minimize pain and suffering and to reduce the number of animals used, according to the ARRIVE guidelines. Animals were provided with nesting material, water and food ad libitum and kept under control of an alternating 12-hour light-dark-cycle (light-cycle 7am–7pm), in a temperature (22 ± 2 °C) and humidity (55 ± 10%) controlled environment.

Hippocampal tissue of pharmacoresistant TLE patients was neurosurgically removed for seizure control in the context of the local epilepsy surgery program[71]. Tissue from 5 individuals were analyzed (3 males 27, 61, 21 years old, 2 females 40 and 14 years old). For human tissue sampling, it was ensured that each patient gave written consent for the scientific use of her or his tissue and permission was obtained from the Ethics Committee of the University of Bonn. All procedures adhered to national and institutional ethical requirements and were conducted in accordance with the Declaration of Helsinki.

Manufacturing of injection-pipettes

Glass capillaries were horizontally pulled (Sutter Instruments) and subsequently underwent abrasive treatment at an angle of approximately 30–40° (World Precision Instruments). Pipettes with tip-openings >3 μm or contaminated with debris were excluded from experiments. Randomly selected pipettes were visualized via scanning electron microscopy (Hitachi). Samples were carefully mounted on modelling clay, sputter coated with gold (Quorum Technologies) and imaged at 5–10 kV under high vacuum conditions. Secondary electrons were detected with a SE-detector.

Acute brain slices preparation

Post-natal 25–35-day old C57bl/6NCrl male mice (Charles River Laboratories) or mice from the pilocarpine-induced mesial TLE model were used. After anesthetizing with isoflurane, mice were decapitated, the brain was removed from the skull and rapidly submerged into ice-cold modified artificial cerebrospinal fluid (mACSF) containing (in mM): 87 NaCl, 2.5 KCl, 1.25 NaH_2PO_4, 7 $MgCl_2$, 0.5 $CaCl_2$, 25 $NaHCO_3$, 25 glucose, and 75 sucrose (saturated with 95% O_2/5% CO_2). Horizontal cortical or hippocampal slices (300 μm) were prepared on a vibratome (HM650 V, Thermo Fisher Scientific, Waltham, USA). Subsequently, slices were quickly transferred to a submerged chamber containing mACSF at 35 °C for 30 min before stored at room temperature in standard artificial cerebrospinal fluid (sACSF) containing (in mM): 124 NaCl, 3 KCl, 1.25 NaH_2PO_4, 2 $MgCl_2$, 2 $CaCl_2$, 26 $NaHCO_3$, 10 glucose (saturated with 95% O_2/5% CO_2). Experiments were not started earlier than 30 min after dissection. During the experiment, perfusion solutions were constantly aerated with a mixture of O_2/CO_2 (95%/5%) and the pH was verified before each experiment to ensure sufficient pre-bubbling to reach the equilibrium pH of 7.4 (at RT) (Suppl. Figure 1). During perfusion, the beakers were partially covered to improve gassing of the solution. In general, slices were used for the span of 6–8 h following their preparation and the BBB properties explored in this study appear stable within that period.

Intravascular injections were performed on brain slices in a submerged specimen chamber of a two-photon laser scanning microscope (Suppl. Figure 1a, b) either from Nikon (A1R MP), Scientifica (2PIMS-PMT-20) or Bruker Scientific (Olympus BX51WI), each equipped with one or two chameleon vision II lasers (Coherent) and with NIS-Elements AR 4.13.01, Scanimage r3.8 or Prairie View 5.4 software for scanning and acquisition, respectively. Slices were constantly perfused with carbogenated sACSF at a flow rate of 1–2 ml/min. Perfusion-pipetted were filled with 5 µl of the respective test solution, inserted into a pipette holder mounted to a micromanipulator (Luigs & Neumann) and connected to a pressure container regulated by a patch perfusion system (ALA Scientific Instruments) (Suppl. Figure 1c, d). Under optical control, pipette tips were lowered into the tissue and approached to a venous vessel membrane in 20–50 µm depth. Next, vessel membranes were punctured by the cannula-like pipette tip. Subsequent application of 100 mmHg pressure flushed the vascular system with the pipette solution. Pressure on the injection-pipette was kept constant throughout the experiment. Successful injections were indicated by absence of intense dye leakage around the injection point (IP).

Biocytin tetramethylrhodamine (TMR, Sigma Aldrich) was perfused into cortical and hippocampal vessels at a concentration of 100 µM in sACSF. Single frame time series over 20 min (1 frame/5 s), as well as z-stacks (plane distance 0.25–1 µm) were recorded. If non-fluorescent molecules were injected into the vasculature, TMR was added to the injection solution at a concentration of 100 µM as an indicator for a successful piercing and perfusion.

Time to reach steady state was assessed on time series. For quantification, fluorescence intensities were determined within regions of interests (ROIs) positioned at nine distances to the IP. 'Steady state' of intravascular dye fluorescence was defined 95% of the plateau level of fluorescence reached at >5 min (cf. Figure 1c). The elapsed time from starting pressure application to reaching this at each of the nine distances is plotted in Fig. 1d and was called "time to steady state".

Spatial intravascular gradients of TMR were assessed by intensity profiles taken from maximum intensity projections (MIPs). Two profiles were taken along the punctured primary vessel starting at the IP until a distance of at least 150 µm (Fig. 1f). Additional intensity profiles were taken from branches of that primary vessel. Profiles from these branches were groups into three categories according to their distance from the IP (< 100, <200, >200 µmcf. Figure 1e). The profiles of each category are shown in 3 separate panels in Fig. 1 f. The color of the lines in all panels codes the order and the diameter (above or below 10 µm) of the measured branch as illustrated by the cartoon in Fig. 1e. All profiles were normalized to the fluorescence reached at the IP.

Estimation of the surface area of individual ECs. Based on the fact that only one longitudinal border of the EC was visible, it could be assumed that an EC in a capillary occupies a quarter of the vessel's 3D surface area. Accordingly, the calculations were adjusted by multiplying the measured 2D surface area of the EC by the factor $[(\pi \times d \times l)/4 \div (d \times l/2)] = \pi/2$, where d and l are the diameter and length of the EC-contained section of a vessel. ECs in venules were fully visible and the measured area was not scaled. Analysis of fluorescent images was performed with the ImageJ platform (1.51 to 1.53).

Dyes were obtained from: 7-hydroxycoumarin-3-carboxylic acid (7HCC), Sigma Aldrich; sulforhodamine 101 (SR101), R&D Systems; Lycopersicon Esculentum Lectin-DyLight 488 (Tomato lectin), Thermo Fisher Scientific; FM1-43/ FM1-43fx, Thermo Fisher Scientific; Rhodamine123 (Sigma Aldrich); MitoTracker CMTM (MitoTracker), Thermo Fisher Scientific; calcein-AM, Thermo Fisher Scientific; Neurotrace 500/525 (NT500/525), Thermo Fisher Scientific; Calcein red-orange (red-shifted calcein), Thermo Fisher Scientific; Hoechst33342, mannitol, Sigma-Aldrich; bovine serum albumin-Alexa Fluor 488 conjugate (BSA-Alexa488), Invitrogen, DMSO (Carl Roth).

MIPs of venules and capillaries 30 min after perfusing the vasculature with FM1-43 or tomato lectin were used for the surface area measurement of ECs. In venules, ECs can be manually fully outlined, while they could only be partially outlined in capillaries as one of their longitudinal borders was hidden in the side wall of the capillary. Therefore, it could be assumed that an EC in a capillary occupies a quarter of the vessel's 3D surface area (if it would be more than a quarter, a second border would have appeared) and part of the EC remains undetectable in the projection. To correct for this error associated with the projection, the calculations were adjusted by multiplying the measured 2D surface area of the EC by the factor $[(\pi \times d \times l)/4 \div (d \times l/2)] = \pi/2$, where d and l are the diameter and length of the EC-contained section of a vessel, respectively.

Adult male C57Bl/6-N mice received a dose of scopolamine methyl nitrate (1 mg/kg, s.c.; Sigma Aldrich) 20 min prior to the administration of pilocarpine hydrochloride (335 mg/kg, s.c.; Sigma Aldrich). Forty min after SE onset, mice received 4 mg/kg s.c. diazepam (Ratiopharm). Control animals were treated identically, but received saline instead of pilocarpine. After pilocarpine injection, animals exhibit several stage 3 (severe seizures with rearing without falling) and stage 4 seizures (severe seizures with rearing and falling)[83]. Behavioral SE was clearly identified using a modified seizure scheme, with persistent immobilization, postural loss and sustained generalized convulsions[84]. Among pilocarpine-injected animals, only those that developed SE (SE-experienced) were further used for analysis. For calcein accumulation assay, it was conducted as previously described. However, slices were pre-incubated and constantly perfused with 0.6 mM probenecid and 0.6 µM Elacridar.

Preparation of hippocampal tissue from pilocarpine-treated mice for proteomics analysis

Male C57Bl6/N mice were either sham- or pilocarpine injected as described above. Both hemispheres of the hippocampus were extracted at 4 or 24 h post-pilocarpine injection and frozen on dry ice. Sixteen mice were injected allowing for four mice per time point. The hippocampal tissue was homogenized in 500 µl PBS and 125 µl lysis buffer was added consisting of 2% sodium dodecyl sulphate, 50 mM trisaminomethane/HCl pH 7.4, 2 mM ethylene glycol-bis(β-aminoethyl ether)-N, N, N0, N0-tetraacetic acid, 2 mM ethylenediaminetetraacetic acid, Complete Protease Inhibitor Cocktail (Roche), 2 mM phenylmethylsulfonyl (Sigma), 5 mM NaF (Sigma), 2 mM beta-glycerophosphate (Sigma), Phosphatase Inhibitor Cocktail 2 (1:1000) and PhosSTOP (Roche). Lysates were incubated at 85 °C for 10 min, sonicated for 3 × 10 s, frozen and lyophilized. Samples were resuspended in 100 µL of 10 mM tris(2-carboxyethyl) phosphine, reduced for 10 minutes at 85 °C and alkylated in 25 mM iodoacetamide at 22 °C. Proteins were precipitated from the samples using chloroform-methanol extraction and air dried. The precipitates were dissolved in 20 µL solution containing 7.8 M urea, 50 mM triethylammonium bicarbonate and 5 µg of Lys-C (FUJIFILM Wako Pure Chemical Corporation) for an 8 h digestion at 25 °C, then diluted with a solution containing 170 µL 100 mM 4-[2-hydroxyethyl]-1-piperazineethanesulfonic acid (HEPES) (pH 8) and 5 µg TrypZean trypsin (Sigma Life Sciences) for subsequent digestion at 37 °C for 4 h. The trypsin digestion was twice repeated[85]. Two TMT-10plex kits (Thermo Fisher Scientific) were used to label 400 µg of peptide to generate two 8-plex sets, one for each time point. The 4 h TMT sample set consisted of: sham replicate 1, 128 N; sham replicate 2, 128 C; sham replicate 3, 129 N; sham replicate 4, 129 C; pilocarpine replicate 1, 130 N; pilocarpine replicate 2, 130 C; pilocarpine replicate 3, 131 N; pilocarpine bio-replicate 4, 131 C. The 24 h TMT sample set consisted of: pilocarpine replicate 1, 128 N; pilocarpine replicate 2, 128 C; pilocarpine replicate 3, 129 N; pilocarpine replicate 4, 129 C;

sham replicate 1, 130 N; sham replicate 2, 130 C; sham replicate 3, 131 N; sham replicate 4, 131 C (lot numbers TB266076 and TA265136). The TMT labelled samples were diluted to 2 mL with 0.1% trifluoracetic acid and desalted using a Sep-Pak tC18 3cc Vac cartridge (200 mg sorbent, Waters), then fractionated by hydrophilic interaction liquid chromatography using a Dionex UltiMate 3000 HPLC system (Thermo Fisher Scientific) controlled by Chromeleon 6.8 software with a TSKgel Amide-80 1 mm inside diameter x 250 mm long column (Tosoh Bioscience). Samples were injected in 150 µL in 90% acetonitrile, 9.9% water, 0.1% trifluoracetic acid (HILIC Buffer A) at a flow rate of 60 µL/min with buffer A at 100% for 10 min. The gradient was from 100% HILIC buffer A 100% to 40 % HILIC buffer B (99.9% water and 0.1% trifluoracetic acid) for 35 minutes at a flow rate of 50 µL/min, then to 80% buffer B for 3 minutes then back to 100% buffer A for 12 minutes. Sample fractions were collected in 60 s intervals into a 96-well plate using a Probot (LC Packings) controlled by µCarrier 2.0[85].

LC-MS/MS was performed on each fraction using an Ultimate 3000 RSLC nano system and Q Exactive Plus hybrid quadrupole-orbitrap mass spectrometer (Thermo Fisher Scientific). The TMT sets were pre-screened for ABC transporter peptides by data-dependent acquisition as described previously[85]. Then, the identified ABC transporter peptides were targeted for re-analysis using an inclusion list, incorporating precursor mass-to-charge ratio, precursor charge state and elution time. A total of 124 peptide sequences corresponding to twenty-five ABC transporter proteins and two standard cytoskeletal proteins (Dynein heavy chain 1 and alpha-tubulin), as loading controls, were targeted by LC-MS/MS. Samples were loaded directly onto a 300 × 0.075 mm column packed with ReproSil Pur C18 AQ 1.9 µm resin (Dr Maisch, Germany). A column oven (PRSO-V1, Sonation lab solutions, Germany) integrated with the nano flex ion source (Thermo Fisher Scientific) maintained the column at 50 °C with an electrospray operating at 2.3 kV. The S lens radio frequency level was 60 and capillary temperature was 250 °C. A The samples were loaded in 5 µL at 300 nL/min for 25 min, then the gradient was from 5% to 25% buffer B in 74 min, then to 35% buffer B in 8 min and to 99% buffer B in 1 min, held at 99% B for 2 min, then to 1% B in 1 min and held at 1% B for 8 min. MS/MS scans were acquired using parallel reaction monitoring at a resolution of 35,000 full width at half maximum with an isolation width of 0.8 m/z for a maximum ion time of 400 ms and automatic gain control target of 50,000 counts.

Processing of mass spectrometry data

LC-MS/MS data output was processed with MaxQuant v1.6.7.0[86]. The Mus musculus reference proteome was downloaded March 14, 2022 and contained 63,628 canonical protein isoform entries. Reporter mass tolerance was 0.005. Filtering by product ion fraction was 0.6. Variable modifications allowed were oxidation of Met, acetylation of the protein N-terminus and deamidation of Gln/Asn. Carbamidomethylation of Cys was a fixed modification. The enzyme specificity was Trypsin/P and three missed cleavages were allowed. The minimum peptide length was 6 and the maximum peptide mass was 6,000 Da. Modifications were not allowed in the protein quantification. Unmodified counterpart peptides were discarded. Second peptide were allowed. All other MaxQuant parameters were default. The proteinGroup text file from the MaxQuant output was processed in Microsoft Excel. The intensities of the ABC transporter proteins, dynein heavy chain 1 and alpha-tubulin were log2 transformed across the 8 channels for both the 4 h and 24 h sets. The ABC transporter intensities were then normalized using the combined dynein heavy chain 1 and alpha-tubulin intensities. The normalized values were then statistically compared using GraphPad Prism 9. Two comparisons were made: i) 4 h pilocarpine treated against 4 h sham treated and ii) 24 h pilocarpine treated against 24 h sham treated. Proteins with <2 unique peptides at both 4 h and 24 h were excluded from the analysis. A t-test was performed, which was adjusted for multiple comparisons using a false discovery rate of 1%. The heatmap of the percentage change was generated using Morpheus v1 (https://software.broadinstitute.org/morpheus). The proteinGroups file and annotated MS/MS spectra for the ABC transporter peptides are supplied as supplementary material (MS files.zip). The mass spectrometry proteomics data have been deposited to the ProteomeXchange Consortium via the PRIDE [1] partner repository with the dataset identifier PXD037454 and 10.6019/PXD037454.

BSA-Alexa488 and FM1-43 injected brain slices were post-processed after time-lapse recordings by overnight incubation at 4 °C in a 24-well plate with 4 % paraformaldehyde solution (PFA; Sigma Aldrich). Control brain slices (500 µm) were incubated overnight at 4 °C in 4% PFA immediately after slicing. Afterwards, all slices were washed thrice for 10 min with TRIS-buffered saline (TBS; 0.1 M). The slices were embedded in 3% agar (Sigma Aldrich) and trimmed to 50 µm thin sections. For cell specific staining, slices were incubated overnight with primary antibodies in TBS at 4 °C (in 0.06–0.1% Triton-X). After 3 10-min washing steps with TBS, slices were incubated with secondary antibodies (in 0.06–0.1% Triton-X) for 3 h at 35 °C then washed as described. For nuclear labelling, the slices were incubated with Hoechst33342 (20 µg/ml; Sigma Aldrich) for 20 min then washed. The slices were mounted on slides and subsequent image acquisition was performed by confocal laser scanning microscopy (Nikon).

The following primary antibody were used: TMEM119 (rabbit, 1:100; Abcam), VE-cadherin (rabbit, 1:200; Abcam), F4/80 (rat, 1:100; Novus Biologicals). Secondary antibodies: Alexa 488-conjugate (anti-rabbit, 1:100; Abcam), rhodamine red X-conjugate (antirabbit, 1:200; Jackson Immune Research Laboratories), Alexa 568-conjugate (antirat, 1:200; Invitrogen).

For the combination of micro-perfusion and field potential recording, first, stimulation and recording electrodes (glass pipettes) were lowered into the stratum radiatum of the hippocampal CA1 region. Next, the perfusion pipette was lowered into the tissue and venules were perforated near the hippocampal fissure. Field potentials signals were amplified with a field potential amplifier EXT-02F/2 (npi electronic GmbH, Tamm, Germany) and a post-amplifier BF-48DGX (npi electronic GmbH, Tamm, Germany). Signals were filtered at 3 kHz (by postamplifier), digitized with a sampling frequency of 10 kHz (NI USB-6229 National Instruments, Austin, TX, USA) and recorded using the IGOR Pro software (version 5–7, Wavemetrics, Portland, OR, USA). fEPSP amplitudes were determined from the baseline prior to stimulation to the maximum of the negative deflection. Amplitudes were normalized (100%) on the level achieved in CPA (cf. Figure 8).

Data are represented as mean ± standard error of the means (SEM). For comparison of two groups, two-tailed Student's *t*-test was used. For comparison of more than two groups, one-way analysis of variance (ANOVA) test was applied (two-tailed) coupled with Tukey's post *hoc* test for correction of pairwise multiple comparisons. Differences were accepted as statistically significant at $P < 0.05$. Statistical analysis was conducted using GraphPad Prism 9.0.2 (GraphPad Software, CA, USA). All statistical tests applied were two-sided.

Reporting summary

Further information on research design is available in the Nature Portfolio Reporting Summary linked to this article.

Data availability

Source data are provided with the paper. Mass spectrometry data generated in this study has been deposited and made publicly available at the PRIDE database with the accession code PXD037454. Source data are provided with this paper.

References

1. Monahan-Earley, R. et al. Evolutionary origins of the blood vascular system and endothelium. *J. Thromb. Haemost.* **11**, 46–66 (2013).
2. Potente, M. & Mäkinen, T. Vascular heterogeneity and specialization in development and disease. *Nat. Rev. Mol. Cell Biol.* **18**, 477–94. (2017).
3. Segarra, M. et al. Blood–Brain Barrier Dynamics to Maintain Brain Homeostasis. *Trends Neurosci.* **44**, 393–405 (2021).
4. Chow, B. W. & Gu, C. The molecular constituents of the blood-brain barrier. *Trends Neurosci.* **38**, 598–608 (2015).
5. Saunders, N. R. et al. Barriers in the brain: a renaissance? *Trends Neurosci.* **31**, 279–286 (2008).
6. Sweeney, M. D. et al. Pericytes of the neurovascular unit: key functions and signaling pathways. *Nat. Neurosci.* **19**, 771–783 (2016).
7. Kaplan, L. et al. Neuronal regulation of the blood–brain barrier and neurovascular coupling. *Nat. Rev. Neurosci.* **21**, 416–432. (2020).
8. Zlokovic, B. V. Neurovascular pathways to neurodegeneration in Alzheimer's disease and other disorders. *Nat. Rev. Neurosci.* **12**, 723–738 (2011).
9. Shlosberg, D. et al. Blood–brain barrier breakdown as a therapeutic target in traumatic brain injury. *Nat. Rev. Neurol.* **6**, 393–403 (2010).
10. García-Cáceres, C. et al. Role of astrocytes, microglia, and tanycytes in brain control of systemic metabolism. *Nat. Neurosci.* **22**, 7–14 (2019).
11. Hartz, A. M. et al. 17-β-Estradiol: a powerful modulator of blood-brain barrier BCRP activity. *J. Cereb. Blood Flow. Metab.* **30**, 1742–1755 (2010).
12. Kirst, C. et al. Mapping the Fine-Scale Organization and Plasticity of the Brain Vasculature. *Cell* **180**, 780–95.e25 (2020).
13. Nishihara, H. et al. Intrinsic blood-brain barrier dysfunction contributes to multiple sclerosis pathogenesis. *Brain* **145**, 4334–4348 (2022).
14. Steinfort, M. et al. Transforming growth factor-beta signaling alters substrate permeability and tight junction protein expression at the blood-brain barrier during inflammatory pain. *Brain* **29**, 1084–1098 (2009).
15. Vanlandewijck, M. et al. A molecular atlas of cell types and zonation in the brain vasculature. *Nature* **554**, 475–480 (2018).
16. Löscher, W. & Potschka, H. Drug resistance in brain diseases and the role of drug efflux transporters. *Nat. Rev. Neurosci.* **6**, 591–602 (2005).
17. Banks, W. A. From blood–brain barrier to blood–brain interface: new opportunities for CNS drug delivery. *Nat. Rev. Drug Discov.* **15**, 275 (2016).
18. Terstappen, G. C. et al. Strategies for delivering therapeutics across the blood–brain barrier. *Nat. Rev. Drug Discov.* **20**, 362–383 (2021).
19. Kariolis, M. S. et al. Brain delivery of therapeutic proteins using an Fc fragment blood-brain barrier transport vehicle in mice and monkeys. *Sci. Transl. Med.* **12**, eaay1359 (2020).
20. Ullman, J. C. et al. Brain delivery and activity of a lysosomal enzyme using a blood-brain barrier transport vehicle in mice. *Sci. Transl. Med.* **12**, eaay1163 (2020).
21. Horng, S. et al. Astrocytic tight junctions control inflammatory CNS lesion pathogenesis. *J. Clin. Investig.* **127**, 3136–3151. (2017).
22. Neuwelt, E. A. et al. Engaging neuroscience to advance translational research in brain barrier biology. *Nat. Rev. Neurosci.* **12**, 169–182 (2011).
23. Andreone, B. J. et al. Blood-Brain Barrier Permeability Is Regulated by Lipid Transport-Dependent Suppression of Caveolae-Mediated Transcytosis. *Neuron* **94**, 581–94.e5 (2017).
24. Ayloo, S. & Gu, C. Transcytosis at the blood–brain barrier. *Curr. Opin. Neurobiol.* **57**, 32–38 (2019).
25. Bhalerao, A. et al. In vitro modeling of the neurovascular unit: advances in the field. *Fluids barriers CNS* **17**, 22 (2020).
26. Stanimirovic, D. B. et al. Blood–brain barrier models: in vitro to in vivo translation in preclinical development of CNS-targeting biotherapeutics. *Expert Opin. drug Discov.* **10**, 141–155 (2015).
27. Soulet, D. et al. Multiphoton intravital microscopy in small animals: Motion artefact challenges and technical solutions. *J. Microsc.* **278**, 3–17 (2020).
28. Warren, K. E. Beyond the blood: brain barrier: the importance of central nervous system (CNS) pharmacokinetics for the treatment of CNS tumors, including diffuse intrinsic pontine glioma. *Front. Oncol.* **8**, 239 (2018).
29. Syková, E. & Nicholson, C. Diffusion in brain extracellular space. *Physiol. Rev.* **88**, 1277–1340 (2008).
30. Hirsch, S. et al. Topology and hemodynamics of the cortical cerebrovascular system. *J. Cereb. Blood Flow. Metab.* **32**, 952–967 (2012).
31. Knowland, D. et al. Stepwise recruitment of transcellular and paracellular pathways underlies blood-brain barrier breakdown in stroke. *Neuron* **82**, 603–617 (2014).
32. On, N. H. et al. Modulation of blood–brain barrier permeability in mice using synthetic E-cadherin peptide. *Mol. Pharm.* **11**, 974–981 (2014).
33. Bertrand, C. A. et al. Methods for Detecting Internalized, FM 1-43 Stained Particles in Epithelial Cells and Monolayers. *Biophys. J.* **91**, 3872–3883 (2006).
34. Betz, W. et al. Activity-dependent fluorescent staining and destaining of living vertebrate motor nerve terminals. *J. Neurosci.* **12**, 363–375 (1992).
35. Kay, A. R. et al. Imaging Synaptic Activity in Intact Brain and Slices with FM1-43 in C. elegans, Lamprey, and Rat. *Neuron* **24**, 809–817 (1999).
36. Schote, U. & Seelig, J. Interaction of the neuronal marker dye FM1-43 with lipid membranes. *Biochim. Biophys. Acta Biomembr.* **1415**, 135–146 (1998).
37. Robertson, R. T. et al. Use of labeled tomato lectin for imaging vasculature structures. *Histochem. cell Biol.* **143**, 225–234 (2015).
38. Suzuki, A. et al. Form follows function: The endothelial glycocalyx. *Transl. Res.* **247**, 158–167 (2022).
39. Mahringer, A. & Fricker, G. ABC transporters at the blood–brain barrier. *Expert Opin. drug Metab. Toxicol.* **12**, 499–508 (2016).
40. Emaus, R. K. et al. Rhodamine 123 as a probe of transmembrane potential in isolated rat-liver mitochondria: spectral and metabolic properties. *Biochim. Biophys. Acta Bioenerg.* **850**, 436–448 (1986).
41. Huang, M. et al. Mitochondrial Inner Membrane Electrophysiology Assessed by Rhodamine-123 Transport and Fluorescence. *Ann. Biomed. Eng.* **35**, 1276 (2007).
42. Johnson, L. V. et al. Localization of mitochondria in living cells with rhodamine 123. *Proc. Natl Acad. Sci.* **77**, 990–994 (1980).
43. Fontaine, M. et al. Use of rhodamine 123 to examine the functional activity of P-glycoprotein in primary cultured brain microvessel endothelial cell monolayers. *Life Sci.* **59**, 1521–1531 (1996).
44. Zaman, G. et al. The human multidrug resistance-associated protein MRP is a plasma membrane drug-efflux pump. *Proc. Natl Acad. Sci.* **91**, 8822–8826 (1994).
45. Shen, S. & Zhang, W. ABC transporters and drug efflux at the blood-brain barrier. *Rev. Neurosci.* **21**, 29 (2010).
46. Perrotton, T. et al. (R)-and (S)-verapamil differentially modulate the multidrug-resistant protein MRP1. *J. Biol. Chem.* **282**, 31542–31548 (2007).
47. Gottesman, M. M. & Pastan, I. Biochemistry of Multidrug Resistance Mediated by the Multidrug Transporter. *Annu. Rev. Biochem.* **62**, 385–427 (1993).
48. Essodaïgui, M. et al. Kinetic Analysis of Calcein and Calcein–Acetoxymethylester Efflux Mediated by the Multidrug Resistance Protein and P-Glycoprotein. *Biochemistry* **37**, 2243–2250 (1998).
49. de Bruin, M. et al. Reversal of resistance by GF120918 in cell lines expressing the ABC half-transporter, MXR. *Cancer Lett.* **146**, 117–126 (1999).

50. Hubensack, M. et al. Effect of the ABCB1 modulators elacridar and tariquidar on the distribution of paclitaxel in nude mice. *J. cancer Res. Clin. Oncol.* **134**, 597–607 (2008).
51. Stefan, S. M. & Wiese, M. Small-molecule inhibitors of multidrug resistance-associated protein 1 and related processes: A historic approach and recent advances. *Med. Res. Rev.* **39**, 176–264 (2019).
52. Szabó, E. et al. A new fluorescent dye accumulation assay for parallel measurements of the ABCG2, ABCB1 and ABCC1 multidrug transporter functions. *PLoS One* **13**, e0190629 (2018).
53. Damisah, E. C. et al. A fluoro-Nissl dye identifies pericytes as distinct vascular mural cells during in vivo brain imaging. *Nat. Neurosci.* **20**, 1023–32. (2017).
54. Shapiro, A. B. et al. P-glycoprotein-mediated Hoechst 33342 transport out of the lipid bilayer. *Eur. J. Biochem.* **250**, 115–121 (1997).
55. Broadwell, R. D. et al. Morphologic effect of dimethyl sulfoxide on the blood-brain barrier. *Science* **217**, 164–166 (1982).
56. Nasrallah, F. A. et al. Modulation of brain metabolism by very low concentrations of the commonly used drug delivery vehicle dimethyl sulfoxide (DMSO). *J. Neurosci. Res.* **86**, 208–214 (2008).
57. Kleindienst, A., et al. Effect of dimethyl sulfoxide on blood-brain barrier integrity following middle cerebral artery occlusion in the rat. In: Hoff J. T., Keep R. F., Xi G., Hua Y., editors. Brain Edema XIII. Acta Neurochirurgica Supplement: Springer. p. 258–62, 2006.
58. Bennett, M. L. et al. New tools for studying microglia in the mouse and human CNS. *Proc. Natl Acad. Sci. USA* **113**, E1738–E46 (2016).
59. Butovsky, O. & Weiner, H. L. Microglial signatures and their role in health and disease. *Nat. Rev. Neurosci.* **19**, 622–635 (2018).
60. Yang, T. et al. Brain perivascular macrophages: Recent advances and implications in health and diseases. *CNS Neurosci. Ther.* **25**, 1318–1328 (2019).
61. Mato, M. et al. Tridimensional observation of fluorescent granular perithelial (FGP) cells in rat cerebral blood vessels. *Anat. Rec.* **215**, 413–419 (1986).
62. Mato, M. et al. Involvement of specific macrophage-lineage cells surrounding arterioles in barrier and scavenger function in brain cortex. *Proc. Natl Acad. Sci.* **93**, 3269–3274 (1996).
63. Al-Sarraf, H. et al. Time course of hyperosmolar opening of the blood-brain and blood-CSF barriers in spontaneously hypertensive rats. *J. Vasc. Res.* **44**, 99–109 (2007).
64. Rapoport, S. I. Osmotic opening of the blood-brain barrier: principles, mechanism, and therapeutic applications. *Cell. Mol. Neurobiol.* **20**, 217–230 (2000).
65. Michalak, Z. et al. Spatio-temporally restricted blood–brain barrier disruption after intra-amygdala kainic acid-induced status epilepticus in mice. *Epilepsy Res.* **103**, 167–179 (2013).
66. Van Vliet, E. et al. Blood–brain barrier leakage may lead to progression of temporal lobe epilepsy. *Brain* **130**, 521–534 (2007).
67. Pitsch, J. et al. Circadian clustering of spontaneous epileptic seizures emerges after pilocarpine-induced status epilepticus. *Epilepsia* **58**, 1159–1171 (2017).
68. Van Loo, K. M. et al. Zinc regulates a key transcriptional pathway for epileptogenesis via metal-regulatory transcription factor 1. *Nat. Commun.* **6**, 1–12 (2015).
69. Becker, A. Animal models of acquired epilepsy: insights into mechanisms of human epileptogenesis. *Neuropathol. Appl. Neurobiol.* **44**, 112–129 (2018).
70. Löscher, W. & Friedman, A. Structural, molecular, and functional alterations of the blood-brain barrier during epileptogenesis and epilepsy: a cause, consequence, or both? *Int. J. Mol. Sci.* **21**, 591 (2020).
71. Borger, V. et al. Resection of piriform cortex predicts seizure freedom in temporal lobe epilepsy. *Ann. Clin. Transl. Neurol.* **8**, 177–189 (2021).
72. Bauer, B. et al. Seizure-induced up-regulation of P-glycoprotein at the blood-brain barrier through glutamate and cyclooxygenase-2 signaling. *Mol. Pharmacol.* **73**, 1444–1453 (2008).
73. McCaffrey, G. et al. P-glycoprotein trafficking at the blood–brain barrier altered by peripheral inflammatory hyperalgesia. *J. Neurochem.* **122**, 962–975 (2012).
74. Karcz-Kubicha, M. et al. Involvement of adenosine A 1 and A 2A receptors in the motor effects of caffeine after its acute and chronic administration. *Neuropsychopharmacology* **28**, 1281–1291 (2003).
75. Puech, C. et al. Assessment of HBEC-5i endothelial cell line cultivated in astrocyte conditioned medium as a human blood-brain barrier model for ABC drug transport studies. *Int. J. Pharm.* **551**, 281–289 (2018).
76. Kuo, Y.-C. & Lu, C.-H. Expression of P-glycoprotein and multidrug resistance-associated protein on human brain-microvascular endothelial cells with electromagnetic stimulation. *Colloids Surf. B: Biointerfaces* **91**, 57–62 (2012).
77. Voirin, A.-C. et al. Inflammatory stress induced by a combination of cytokines (IL-6, IL-17, TNF-α) leads to a loss of integrity on bEnd. 3 endothelial cells in vitro BBB model. *Brain Res.* **1730**, 146647 (2020).
78. Hanafy, A. S. et al. Blood-brain barrier models: Rationale for selection. *Adv. Drug Deliv. Rev.* **176**, 113859 (2021).
79. Mishra, A. et al. Astrocytes mediate neurovascular signaling to capillary pericytes but not to arterioles. *Nat. Neurosci.* **19**, 1619–1627 (2016).
80. Hartmann, D. A. et al. Brain capillary pericytes exert a substantial but slow influence on blood flow. *Nat. Neurosci.* **24**, 633–645 (2021).
81. Cohen-Salmon, M. et al. Astrocytes in the regulation of cerebrovascular functions. *Glia* **69**, 817–841 (2021).
82. Chowdhury, E. A., et al. Understanding the brain uptake and permeability of small molecules through the BBB: A technical overview. *J. Cereb. Blood Flow Metabol.* **41**, 1797–1820 (2021).
83. Racine, R. J. Modification of seizure activity by electrical stimulation: II. Motor seizure. *Electroencephalogr. Clin. Neurophysiol.* **32**, 281–294 (1972).
84. Pitsch, J. et al. The presynaptic active zone protein RIM1α controls epileptogenesis following status epilepticus. *J. Neurosci.* **32**, 12384–12395 (2012).
85. Müller, J. A. et al. A presynaptic phosphosignaling hub for lasting homeostatic plasticity. *Cell Rep.* **39**, 110696 (2022).
86. Tyanova, S. et al. The MaxQuant computational platform for mass spectrometry-based shotgun proteomics. *Nat. Protoc.* **11**, 2301–2319 (2016).

Acknowledgements

Supported by the Deutsche Forschungsgemeinschaft (SFB 1089 to AB, DD, SS, SPP1757 to DD and SS, INST1172 15, DI853/3-5&7 to DD, SCHO 820/4-1, SCHO 820/6-1, SCHO 820/7-1, SCHO 820/5-2 to SS, FOR 2715 to AJB), the BONFOR program of the Medical Faculty of the University of Bonn (to ASH, JP, AJB, SS, DD), the European Union's Seventh Framework Program (FP7/2007-2013) under grant agreement n°602102 (EPITARGET; AJB, SS), Bundesministerium für Bildung und Forschung (the EraNet DeCipher to AJB), Verein zur Förderung der Epilepsieforschung (to SS & AJB), CONNECT-GENERATE (FKZ01GM1908C to AJB), Else Kröner-Fresenius-Foundation (Promotionskolleg 'NeuroImmunology' to AJB, 2016_A05 to JP), The Alexander-von-Humboldt Foundation via a Georg Forster postdoctoral fellowship (to ASH).

Author contributions

A.S.H. and P.S. carried out experiments in brain slices and analyzed and graphed data. J.P. and A.J.B. provided status epilepticus model mice and input thereof. M.E.G. and M.HS. performed proteomics, mass spectrometry and related bioanalyses. N.V. assisted with Dodt scan acquisition. D.D. and A.L. conceived the study and designed the experiments. A.S.H., P.S., S.S., M.E.G., A.L., A.J.B., J.P., N.V. and D.D. wrote the manuscript.

Funding

Open Access funding enabled and organized by Projekt DEAL.

Competing interests
The authors declare competing interests.

Additional information
Supplementary information The online version contains supplementary material available at https://doi.org/10.1038/s41467-023-36070-6.

Correspondence and requests for materials should be addressed to Alf Lamprecht or Dirk Dietrich.

Peer review information *Nature Communications* thanks the anonymous reviewers for their contribution to the peer review of this work. Peer reviewer reports are available.